Istituto Italiano di Tecnologia – Graphene Labs

Università di Genova – Dipartimento di Chimica e Chimica Industriale

Corso di: Scienze e Tecnologie della Chimica e dei Materiali

Curriculum: Nanochemistry

XXXI cycle

Science and technology of graphene-based inks for polymer-composite applications

PhD student: Emanuele Lago

IIT supervisors: Dr. F. Bonaccorso, Prof. V. Pellegrini

UniGe supervisor: Prof. O. Cavalleri

List of publications and contributions

Original publications on ISI Journals:

1) **E. Lago**, P. S. Toth, G. Pugliese, V. Pellegrini, and F. Bonaccorso, "Solution blending preparation of polycarbonate/graphene composite: boosting the mechanical and electrical properties", **RSC Advances, 6 (2016) 97931**

2) A. E. Del Rio Castillo, V. Pellegrini, H. Sun, J. Buha, D. A. Dinh, **E. Lago**, A. Ansaldo, A. Capasso, L. Manna, F. Bonaccorso, "Exfoliation of few-layer black phosphorus in low-boiling-point solvents and its application in Li-ion batteries", **Chemistry of Materials, 30 (2018) 506**

3) E. Petroni, **E. Lago**, S. Bellani, D. W. Boukhvalov, A. Politano, B. Gürbulak, S. Duman, M. Prato, S. Gentiluomo, R. Oropesa-Nuñez, J.-K. Panda, P. S. Toth, A. E. Del Rio Castillo, V. Pellegrini, F. Bonaccorso, "Liquid-Phase Exfoliated Indium–Selenide Flakes and Their Application in Hydrogen Evolution Reaction", **Small 14 (2018) 1800749**

4) A. E. Del Rio Castillo, V. Pellegrini, A. Ansaldo, F. Ricciardella, H. Sun, L. Marasco, J. Buha, Z. Dang, L. Gagliani, **E. Lago**, N. Curreli, S. Gentiluomo, F. Palazon, M. Prato, R. Oropesa-Nuñez, P. S. Toth, E. Mantero, M. Crugliano, A. Gamucci, A. Tomadin, M. Polini and F. Bonaccorso, "High-yield production of 2D crystals by wet-jet milling", **Materials Horizons 5 (2018) 890**

5) **E. Lago**, Peter S. Toth, S. Gentiluomo, S. B. Thorat, V. Pellegrini, and F. Bonaccorso, "Enhanced polycarbonate mechanical performances by the addition of few-layers boron nitride with tuneable morphology", **submitted**

6) **E. Lago**, F. Bonaccorso, S. Gentiluomo, A. E. Del Rio Castillo, N. M. Pugno, R. Cingolani, P. S. Toth, and V. Pellegrini, "Exploiting the ideal properties of two-dimensional fillers for the mechanical reinforcement of polymer nanocomposites", **submitted**

7) **E. Lago**, A. E. Del Rio Castillo, P. S. Toth, S. B. Thorat, R. Oropesa-Nuñez, S. Colonna, A. Fina, V. Pellegrini and F. Bonaccorso, "On-demand tuning of physical properties of poly(lactic acid) through the addition of 2D crystals", **submitted**

Communications at Conferences

Oral communications:

1) **E. Lago**, P.S. Toth, S. Gentiluomo, S. B. Thorat, V. Pellegrini and F. Bonaccorso, "Unravelling the boron nitride flakes morphology to enhance polycarbonate performances" presented at **ImagineNano 2018 - GraphIN**, Bilbao (Spain) March 13-15, 2018

2) S. Gentiluomo, P. S. Toth, **E. Lago**, S.Thorat, M. Prato, V. Pellegrini, and F. Bonaccorso "Application of functional polymer inks: two-dimensional crystals production and enhancement of their polymer composites properties" presented at **MRS 2017 Fall Meeting**, Boston (USA) November 26-December 1, 2017

3) **E. Lago**, P.S. Toth, V. Pellegrini, and F. Bonaccorso, "Effects of 2D crystals addition on the physical properties of polycarbonate-based composite", presented at **GrapheneCanada2016** conference, Montreal (Canada) October 18-20, 2016

Poster Communications:

1) **E. Lago**, P. S. Toth, S. Gentiluomo, S.B. Thorat, V. Pellegrini and F. Bonaccorso, "Unravelling the boron nitride flakes morphology to enhance polycarbonate performances", presented at **MRS 2017 Fall Meeting**, Boston (USA) November 26-December 1, 2017

2) **E. Lago**, P. S. Toth, G. Pugliese, V. Pellegrini, and F. Bonaccorso, "Solution blending preparation of polycarbonate/graphene composite: boosting the mechanical and electrical properties", presented at **Graphene2016** conference, Genoa (Italy) April 19-22, 2016

3) **E. Lago**, P.S. Toth, S. Gentiluomo, S.B. Thorat, V. Pellegrini, and F. Bonaccorso, "Enhancing polycarbonate performances by adding environmentally friendly liquid-phase exfoliated boron nitride flakes", presented at **materials.it** conference, Aci-Castello (Italy), December 12-16, 2016

4) **E. Lago**, P.S. Toth, S. Gentiluomo, S.B. Thorat, V. Pellegrini and F. Bonaccorso, "Unravelling the boron nitride flakes morphology to enhance polycarbonate performances", presented at **Graphene2017** conference, Barcelona (Spain) March 28-31, 2017

TABLE OF CONTENTS

Abstract

Many of our modern technologies require materials with unusual combinations of properties that cannot be met by the conventional metal alloys, ceramics, and polymeric materials. This is especially true for materials that are needed for aerospace, underwater, and transportation applications. For example, researchers, engineers and material scientists are increasingly searching for structural materials that have low densities, are strong, stiff, as well as abrasion and impact resistant, in addition not to be easily corroded. Material property combinations and ranges have been, and are yet being, extended by the development of composite materials.

Polymer-based composites are the combinations of two or more organic and inorganic materials, mixed together to create a new material, the composite, with enhanced physical cumulative properties of the constituents. The polymer acts as the matrix, while the filler is dispersed in order to improve the physical properties of the final composite.

Polymer matrices and fillers are chosen to create composites with tailored properties; *e.g.*, high-modulus but brittle carbon fibres are added to low-modulus polymers to create a stiff, lightweight composite with increased toughness compared to the bare polymer. Recently, however, researchers have reached the limits of optimizing composite properties of traditional micrometre-scale composite fillers, because the properties achieved usually involve compromises: stiffness is traded for toughness, or toughness is obtained at the cost of optical transparency. In addition, macroscopic defects due to regions of the high or low volume fraction of filler often lead to breakdown or failure. Recently, a large window of opportunities has opened to overcome the limitations of traditional micrometre-scale polymer composites: nanoscale filled polymer composites, in which the filler is <100 nm in at least one dimension. Examples of nanoscale fillers are carbon black, carbon nanotubes (CNTs), exfoliated clays, and two-dimensional (2D) crystals, such as graphene.

In particular, graphene has a Young's Modulus of 1 TPa and intrinsic strength of 130 GPa, electrical conductivity, σ, of up to 10^8 S m^{-1}, thermal conductivity of ~ 5×10^3 W $m^{-1}\cdot K^{-1}$, and a specific surface area of 2630 m^2 g^{-1}, being, therefore, a promising filler for polymer matrices.

Graphene/polymer composites possess not only increased stiffness and strength, compared to the pristine matrices, but can be useful for multi-functional applications such as in the electronic field, as wearable strain sensors, printed electrodes, conductive adhesives, and supercapacitors.

Other 2D crystals, with their own and peculiar properties, can be used as fillers for different kind of applications. As an example, hexagonal-boron nitride (*h*-BN) has similar mechanical and thermal properties compared to those of graphene, but it is an electrical insulator. Therefore, *h*-BN/polymer composites can cover applications in which high electrical conductivity is undesirable, *e.g.* for thermal management or food packaging. Whereas, 2D semiconductors, such as Black Phosphorous (BP) and transition metal dichalcogenides (TMDs), can be exploited as fillers for developing composites useful for optoelectronic applications, such as pulsed fibre lasers and photo-actuators.

In spite of the recent development of 2D crystals/polymer composites, there are many questions yet to be answered. In particular, many technical barriers involving structure control, dispersion of 2D crystals in the matrix, the interfacial interaction between 2D crystals and matrix, and re-aggregation issues between 2D crystal flakes must be taken into account to target the wide applications of these advanced composites.

The aim of my PhD work, presented in this Thesis, was indeed to investigate 2D crystals as potential fillers for the development of future polymer-based composites, trying to meet the requirements set by the aforementioned open-questions, linking the morphology of the 2D crystals and their dispersion in the polymer matrix to the final properties of the as-produced composites.

In my PhD work, I focused my attention, particularly on graphene, *h*-BN, and WS_2. The 2D crystals used in this work have been synthesized exploiting sonication-assisted LPE and wet-jet milling (WJM)-assisted LPE, the latter being a completely novel approach developed in our group that allows an industrial rate production of 2D crystals, meeting the demand of large-scale filler production required for the composite field. The morphology of the as-synthesized 2D crystals, in terms of surface area (A), lateral size (l) and thickness (t), has been tuned by exploiting sedimentation-based separation (SBS).

The size-sorted 2D crystals are subsequently used as fillers in polymer composites, investigating several polymer matrices: polycarbonate (PC), acrylonitrile butadiene styrene (ABS), and polylactic acid (PLA). Composites are produced by means of solution blending technique, allowing a thorough dispersion of the fillers inside the matrix, and then coagulated or cast in order to obtain composite pellets or composite films. Mechanical, thermal and electrical characterizations of composite films have been performed and the obtained results are linked to the morphological properties of the fillers.

In details, the Thesis is organized as follow:

Chapter 1 summarizes the fundamental understanding of 2D crystals as fillers in polymer-based composites, reviewing their production techniques. In this chapter it is presented the theoretical background governing the composite properties modification mechanisms, focusing on the mechanical reinforcement, and electrical, thermal and gas barrier properties, evidencing the effect of the fillers and their morphology.

Chapter 2 displays the production methods and characterization techniques used during my PhD work, for both fillers and composites.

Chapter 3 is dedicated to the structural and morphological characterizations of 2D crystals (graphene, *h*-BN and WS_2). This chapter lays a solid foundation for the understanding of the mechanical performances of composites, which will be discussed in the subsequent Chapters 4, 5 and 6.

Chapter 4 concerns the study of graphene as filler in PC-based composites, giving a first example of the development of a 2D crystal/polymer composite, evidencing the contribution of filler loading and the effect of dispersion and agglomeration of the filler inside the matrix.

Chapter 5 covers the production of *h*-BN flakes with tuned morphology obtained by means of an environmentally friendly approach and its use as a reinforcing agent in the PC matrix.

Chapter 6 describes the effects of morphological parameters of different 2D crystals, *i.e.* graphene, *h*-BN and WS_2, in the mechanical properties of ABS-based composites, giving new insights in the exploitation of fillers in the composite field.

Chapter 7 presents the use of graphene and *h*-BN, produced by WJM approach, as fillers in PLA matrix, giving a comprehensive study on the mechanical, electrical and thermal properties of composites and also exploiting synergistic effects due to the simultaneous use of both graphene and *h*-BN as fillers in a hybrid, three-phase, composite.

Chapter 8 summarizes the most important insights achieved in the research topics of 2D crystals, from material to morphological characterization, and their use as fillers in polymer-based composites. I will also provide some hints for the future exploitation of these materials in the composite field.

CHAPTER 1

Introduction

1.1 2D crystals for polymer composites

Two-dimensional (2D) crystals [1,2], *i.e.* crystals with atomic thickness, are nowadays at the centre of an ever-growing research effort due to their unique physical and chemical properties, often superior with respect their bulk three-dimensional counterparts, interesting for both fundamental science and applications [1,3]. From the 2D crystals family (Figure 1.1), the most known and studied is certainly graphene (Figure 1.1a), a defect-free carbon monolayer in which atoms are arranged in honeycomb lattice, that was isolated for the first time in 2004 by A. Geim and K. Novoselov [4], then awarded in 2010 with the Nobel Prize in Physics for their "*groundbreaking experiments regarding the two-dimensional material graphene*" [5]. Graphene is indeed at the centre of an ever-growing research effort due to its unique properties. In particular, it possesses a Young's Modulus of 1 TPa and intrinsic strength of 130 GPa [6], a room temperature (RT) mobility (μ) of 2.5×10^5 cm^2 V^{-1} s^{-1} [7], electrical conductivity, σ, of up to 10^8 S m^{-1} [8], thermal conductivity of ~ 5×10^3 W m$^{-1}\cdot$K^{-1} [9], and a specific surface area of 2630 m^2 g^{-1} [10].

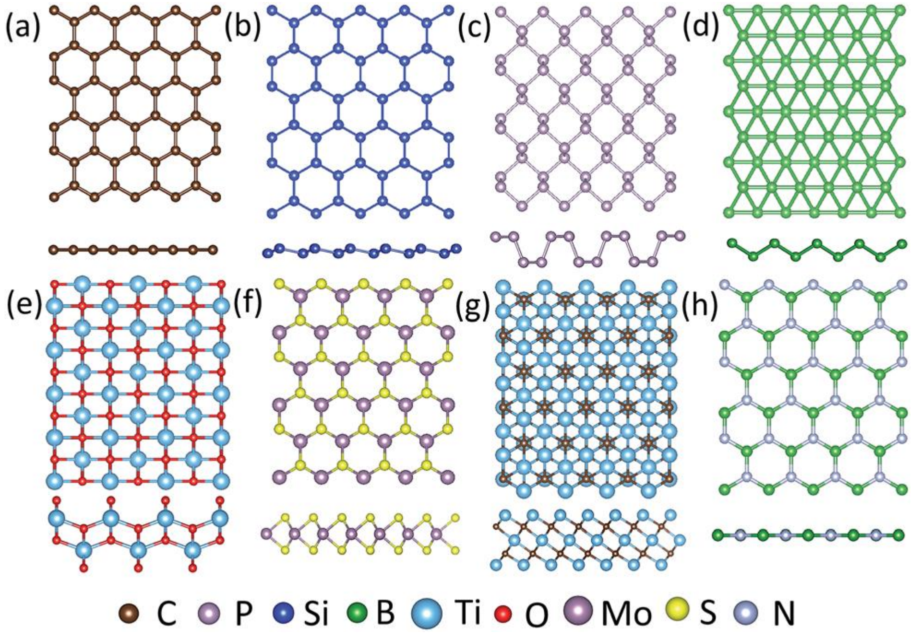

Figure 1.1. Top and side view of the atomic structure of some 2D crystals: (a) graphene, (b) silicene, (c) phosphorene, (d) borophene, (e) TiO_2, (f) MoS_2, (g) Ti_3C_2 and (f) *h*-BN. Image taken from [11].

However, nature offers a very broad class of 2D crystals with characteristic and properties complementary to those of graphene [1]. From an electronic point of view, for example, MoS_2 (Figure 1.1f), WS_2, $MoSe_2$ and WSe_2 (part of the family of transition metal dichalcogenides, TDMs) are semiconductors [12], Bi_2Se_3 and Bi_2Te_3 are topological insulators with thermoelectric properties [13], hexagonal-boron nitride (*h*-BN, Figure 1.1h) is an insulator [14], just to cite a few [1]. Above all, *h*-BN is structurally similar to graphene, having a honeycomb lattice composed of alternating boron (B) and nitrogen (N) atoms. This structure makes *h*-BN mechanically strong as graphene [15].

Therefore, 2D crystals are expected to have a major impact in several technological fields due to the new applications enabled by their properties [1], ranging from electronics, to energy, to polymer composites [1]. To have an idea of the technological outputs of these materials, in Figure 1.2 is presented an analysis of Intellectual Property activity concerning graphene in terms of number of patent applications (Figure 1.2a) and divided by sector (Figure 1.2b) [1]. It is worth noting that composites field represent a large share of the graphene industrial interest (17% of overall patent applications) and nowadays graphene-based composites are currently the only application of graphene already commercialized on a large scale [16]. Some examples are the motorcycle graphene-based helmet by MomoDesign and Fondazione Istituto Italiano di Tecnologia [17,18] and the graphene-based racquet by Head [19].

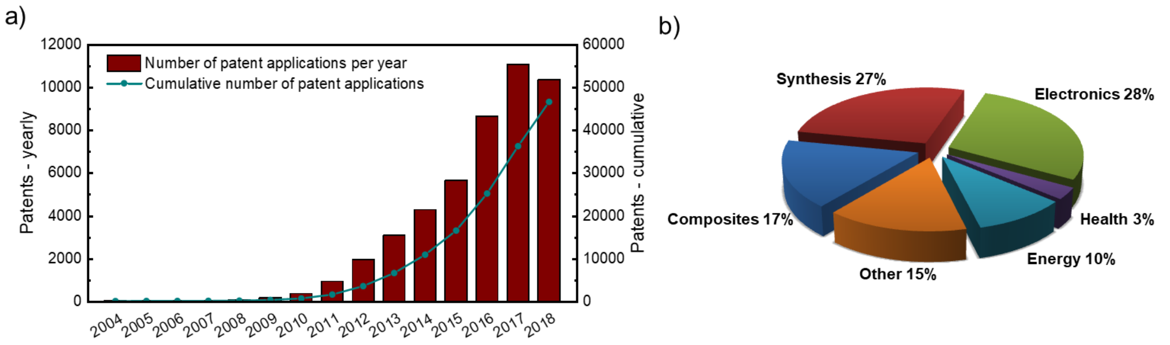

Figure 1.2. a) Patent applications on graphene as a function of application year (data from Web of Science™). b) Proportion of overall graphene patents by sectors, adapted from [1].

What makes 2D crystals interesting specifically used as fillers in polymer composites, besides their intrinsic mechanical, electrical or thermal properties, with respect fillers of different geometries, is their specific surface for given volume (Figure 1.3). In fact, platelet-like geometry (Figure 1.3a), inherent to 2D crystals but also to exfoliated clays, allow the maximum specific surface, outperforming the one-dimensional (1D. Figure 1.3b) tube-like structure, inherent *e.g.* to carbon nanotubes (CNTs), and the spherical zero-dimensional (0D. Figure 1.3c) nanoparticles (NPs). Maximizing the specific surface area of the fillers results in an increase of interactions between the fillers and the polymer matrix. For this reason, before the advent of graphene and 2D crystals, exfoliated clays have dominated the nanocomposite field [20,21], starting from the pioneering work of Toyota researchers which successfully fabricated nylon-6/montmorillonite nanocomposites [22]. In fact, montmorillonite, one of the most used filler in polymer-based composite amongst clay family, [23,24] has a predicted Young's Modulus of ~ 270 GPa [25] in its single layer form. This value is roughly ¼ of that of graphene (1 TPa) [6] or *h*-BN (1 TPa) [15], therefore, as a matter of principle, the same enhancement in Young's Modulus in a composite filled with montmorillonite can be obtained by using four times less loading of either graphene or *h*-BN.

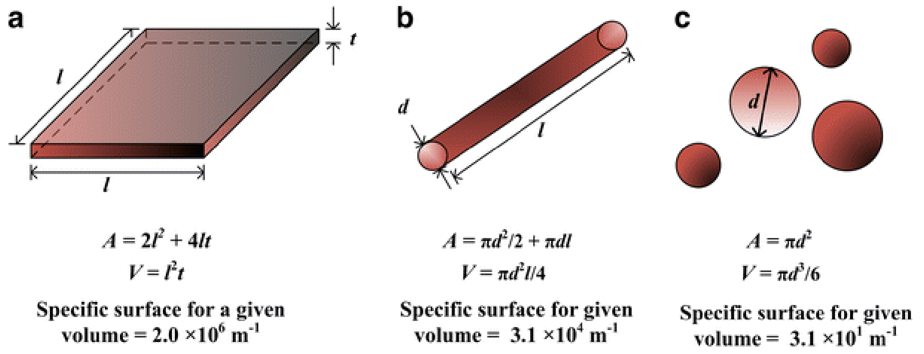

Figure 1.3. Geometry and specific surface for given volume of nanostructured fillers, adapted from [23].

1.2 2D crystals production methods

The implementation of graphene and 2D crystals in the composite field is still a challenge and one of the most important problems lies in the preparation of high-quality crystals in bulk quantities. For this reason, several production strategies, both bottom-up and top-down, have been proposed [1,26]. Moreover, different production routes yield 2D crystals with different morphologies and aspect ratios, the latter a parameter extremely important in composite science, as discussed in section 1.3.

Mechanical exfoliation (Figure 1.4a) is the simplest of the preparation methods and involves using adhesive tape to peel thin layers from bulk crystals, *e.g.* graphite, and depositing them on a silicon substrate [26]. By repeatedly using this method, the bulk crystals can be split into increasingly thinner pieces, eventually resulting in monolayer exfoliation [26]. This preparation method makes the highest quality crystals, but is only useful for lab-scale experiments and prototyping as it is not possible to scale-up the process [26]. Only few examples of the use of mechanically exfoliated graphene in polymer composites have been proposed and only for proof of concept experiments [6–8].

Chemical vapour deposition (CVD, Figure 1.4b) is a bottom-up approach and one of the most useful methods to prepare 2D crystals in single layer form, as well as their heterostructures [27], of high structural quality [26–28]. This route involves the decomposition of a gas precursor, *e.g.*, hydrocarbon gases for graphene [28], borazine or ammonia borane for *h*-BN [29,30], or solid precursors, *e.g.*, transition metal oxides (*e.g.*, MoO_3, WO_3) or chlorides ($MoCl_5$) as metal (molybdenum or tungsten) sources while S or Se elemental powders as the source of sulphur or selenium, in the case of TMDs production [27,31–33]. A process gas, *e.g.*, hydrogen or argon, catalyses a reaction forming 2D crystals layers on a metal substrate, typically copper or nickel [26,28,30], or SiO_2 [32,33]. In terms of scaling-up, graphene film of 30 inches has been produced exploiting roll-to-roll process [34], but the high energy-demand required from this technique restricts CVD technology to high-value applications, *i.e.* in the electronic field. As for mechanical exfoliation, graphene produced by CVD has been used as filler in polymer composites for proof of concept applications [9].

The properties of 2D crystals can be exploited for applications where, rather than a monolayer on a substrate, as can be obtained by either mechanical exfoliation or CVD, large quantities are processed from solution or melt to be included into polymers. For this reason, liquid phase exfoliation (LPE) of layered crystals emerged as one of the most promising techniques for the upscaling of 2D crystals production and their exploitation in the polymer composite field. The LPE consists in three main steps [3,5]: dispersion of a layered material in a solvent, exfoliation, by means of ultra-sonication [14] or shear forces [4], and purification, generally performed by centrifugation, separating the non-exfoliated crystals from the exfoliated ones [5,15,16]. During the purification process, the exfoliated crystals can be sort according to their morphological differences, this is attractive for their use as filler in composites since theoretical [22] and experimental [23] works suggest that tuning the lateral size-thickness ratio is essential to obtain composites with targeted mechanical, electrical, or thermal properties. [3] Even more, having 2D crystals dispersed in a liquid medium makes possible the chemical modification of the crystal surface or edges, by introducing functional groups [24–26], thus enhancing the mechanical-stress-transfer between the filler and the polymer matrix [27–29]. This method, because of its importance in view of applications in polymer composite field, will be described in detail in the next section.

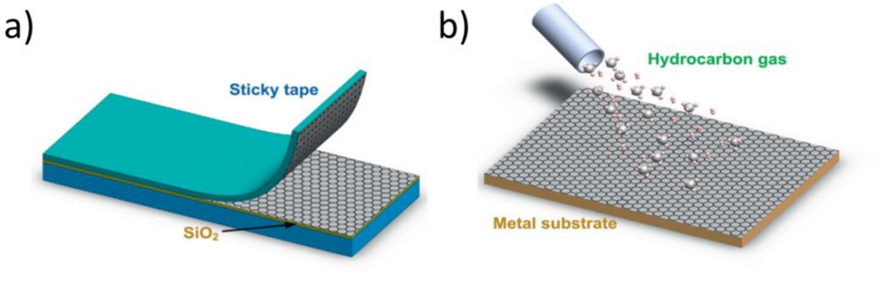

Figure 1.4. Schematic illustration of some of the main 2D crystal production techniques: (a) micromechanical cleavage, (b) chemical vapour deposition for graphene production. Adapted from [26].

1.2.1 Liquid phase exfoliation of graphite and other layered materials

As mentioned, LPE method involves three steps [26], summarized in Figure 1.5. The first one is the dispersion of the bulk layered material in a suitable solvent. Then, the exfoliation of layered materials in the solvent is usually realized by ultra-sonication [35–37], or others external driving forces [26], such as shear forces [38], in the second step. During the ultra-sonication process, propagation of cavitons [26,39], *e.g.*, the growth and subsequent collapse of bubbles or voids in solvents due to pressure fluctuations [26], creates hydrodynamic shear-forces which act on layered materials, inducing exfoliation [26]. After exfoliation, the solvent/2D crystal flakes interaction needs to balance the inter-sheet attractive van der Waals forces [26]. This means that the Gibbs free energy (ΔG) of the mixture solvent/2D crystals must be minimized [35,40]. This condition can be endorsed if the surface tension (γ) of the solvent is equivalent to the surface free energy of the 2D crystal [35]:

$$\gamma = E_{Surface}^{Solvent} - TS_{Surface}^{Solvent} \tag{1.1}$$

in which E is the solvent surface energy, T is the absolute temperature and S is the solvent surface entropy (which generally takes a value of ~ 10^{-3} J m^{-2} K^{-1} [35,37,41]). Moreover, the matching of the Hansen or Hildebrand parameters of the solvent with the ones of the layered material facilitates the exfoliation process [35,40,42,43]. The Hildebrand parameter (δ_T) is widely used in polymer science, and is defined as the square root of the cohesive energy density [42]:

$$\delta_T = \sqrt{\frac{\Delta H_v - RT}{V_m}} \tag{1.2}$$

in which ΔH_v is the enthalpy of vaporization, R is the ideal gas constant, and V_m the molar volume. The Hildebrand parameter is used to evaluate the solubility or dispersibility of a material in a known solvent [42]. However, in some specific cases, the Hildebrand parameter is not sufficient to describe and evaluate the dispersibility of a material in a solvent. For example, the δ_T of graphene is ~ 23

MPa$^{1/2}$ [44], thus a solvent with this δ_T value, *e.g.* 2-propanol (IPA) with $\delta_T \sim 23.8$ [40] should form a stable dispersion of graphene which, however, has not been experimentally demonstrated. The reason lies in the fact that δ_T does not consider the hydrogen bonding and polar interactions [40]. In contrast, the Hansen solubility parameters (HSPs) splits the cohesive energy ($\delta^2{}_T$) into three components: the polar contribution (δ_p), the dispersive component (δ_d) and the hydrogen-bonding (δ_h) [40]:

$$\delta_T^2 = \delta_d^2 + \delta_p^2 + \delta_h^2 \tag{1.3}$$

Unfortunately, in the case of graphene, the majority of solvents that fulfill these thermodynamic constraints have high boiling-point (*i.e.* above 150 °C [26]) and are toxic [1,45], such as N-methyl-2-pyrrolidone (NMP) [37,46,47], N,N-dimethylformamide (DMF) [37,48] and ortho-dichlorobenzene (DCB) [37,49]. An alternative route to the solvent exfoliation [39] relies on the use of either surfactants [50,51] or polymers, [52,53] which aid the exfoliation of graphite in water [54] or low boiling-point solvents, such as ethanol [55], tetrahydrofuran (THF) [56], and chloroform[56], stabilizing the exfoliated flakes against re-aggregation [1,50–54]. However, the residual of either surfactants or polymer increases the inter-flake contact resistance [1]. On the other hand, several 2D crystals can be obtained exploiting LPE in environmentally benign and low-boiling-point solvents, as we have demonstrated for the cases of black phosphorous with acetone [57] and indium selenide with 2-propanol (IPA) [58]. After the ultra-sonication process, an ultra-centrifugation step is required to remove thick and un-exfoliated flakes from the as-prepared dispersion [46,59–61]. This last step will be discussed more in detail in section 1.2.2.

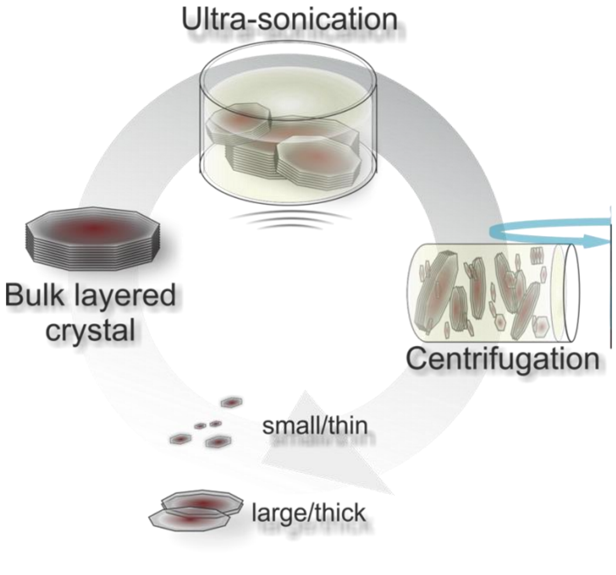

Figure 1.5. Production of graphene sheets by LPE with graphite as raw materials.

Liquid phase exfoliation is a versatile technique and can be exploited not only for the exfoliation of pristine graphite into graphene but also for the exfoliation of graphite oxide (GrO) [26]. The production of graphene oxide (GO) is based on the Hummer's method and its modification in which graphite (Figure 1.6a) is intercalated and oxidized in the presence of strong acids (generally sulphuric acid) and oxidizing agents (sodium nitrate and potassium permanganate) [62,63]. This processes disrupt the sp^2-bonded network and covalently functionalizes both basal planes and edges with oxygen-containing groups (Figure 1.6b), such as hydroxyl, carboxyl, and epoxide groups [64,65]. Eventually, GO flakes can be easily exfoliated from GrO via sonication [66] or thermal expansion [67] (Figure 1.6c). The presence of functional groups makes GO strongly hydrophilic, allowing its dispersion in pure water [66], as well as in organic solvents [26,68] However, although large GO single-layer flakes, up to several microns [69], can be produced, they are defective [65,70] and insulating [65,70,71].

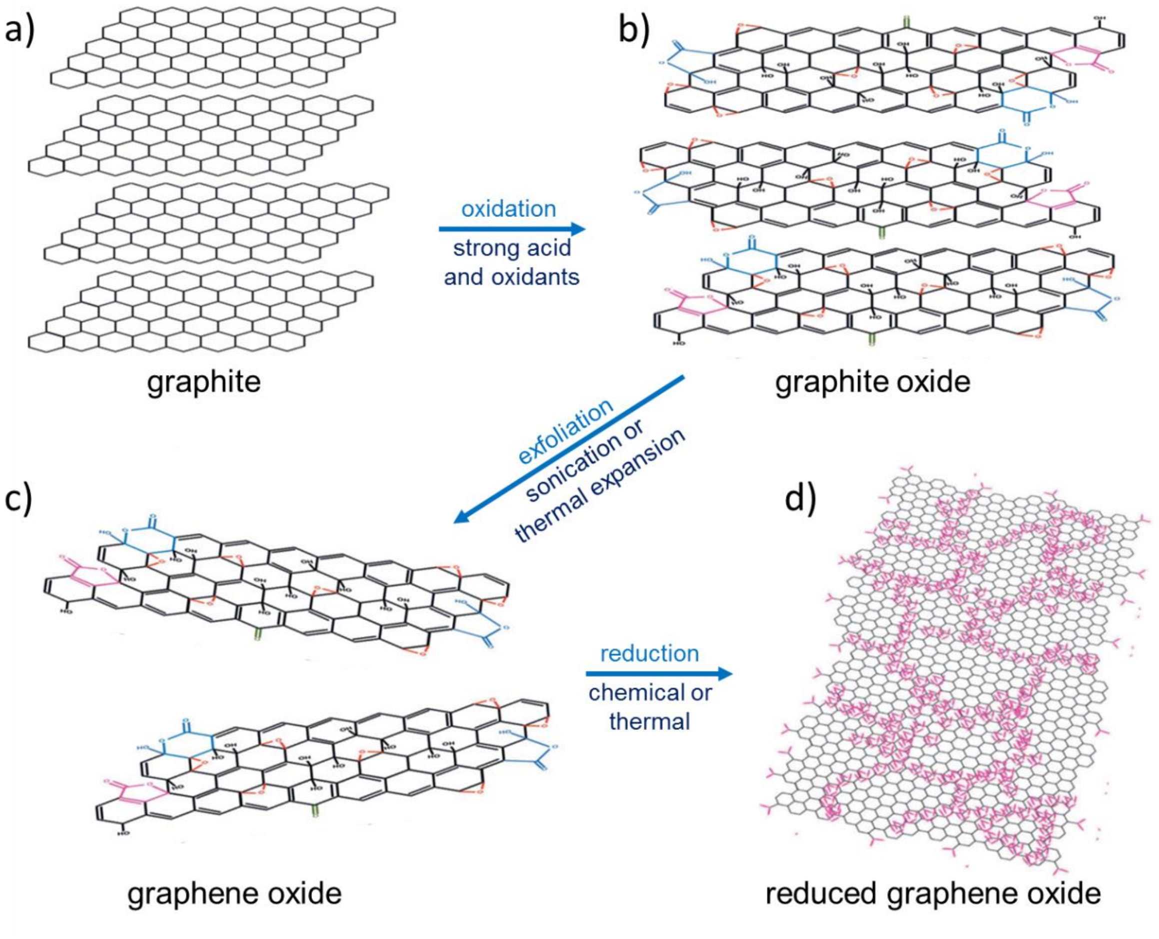

Figure 1.6. Production of GO and reduced graphene oxide (RGO) from parental graphite. Adapted from [26].

Several processes have been developed to chemically or thermally reduce GO flakes (Figure 1.6d), *i.e.* decrease the oxidation state of the oxygen-containing groups and restore the sp^2-conjugated network, in order to re-establish the structure and the electrical and thermal conductivities as close as possible to pristine graphene [69]. Thermal annealing has demonstrated to be one the most effective method to reduce GO, decreasing the oxygen content down to 5 % [72]. Despite this, the crystalline structure of graphene is not fully recovered, making the mechanical, thermal and electrical properties of RGO inferior compared to the physical performance of non-defective graphene, *e.g.*, the Young’s modulus of RGO is ~ 250 MPa [73], and its electron mobility is ~ 200 $cm^2\ V^{-1}\ s^{-1}$ [72].

1.2.2 Morphology tuning of 2D crystals

Whatever is the process used for the exfoliation of layered crystals, after this step, the as-produced dispersions have a heterogeneous composition of 2D flakes both in lateral size and thickness [1,35,39], a condition that is not ideal to fully exploit the properties of the exfoliated 2D crystals [39].

In view of the application of the as-exfoliated flakes in the polymer composite field, having a control on the morphology of the flakes is of paramount importance, as evidenced by the strong influence of the aspect ratio of fillers in the final properties of composites [74–78]. Thus, ultra-centrifugation methodologies emerged not only as purification strategies of the dispersion, *i.e.* for the removal of the un-exfoliated flakes but also as a useful tool for sorting of 2D flakes morphology [1,39,61,79].

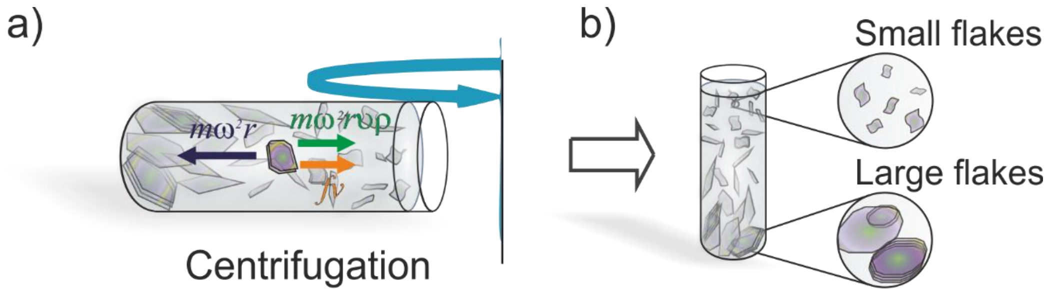

Figure 1.7. Schematic illustration of 2D crystals sorting by SBS.

The most simple and common method is the sedimentation-based separation (SBS, Figure 1.7), based on the ultra-centrifugation in a uniform medium [80]. The exploitation of SBS permits to separate particles and/or flakes in a solvent, under a force field, on the basis of their sedimentation rate [80]. The forces acting in the SBS are (Figure 1.7a): (*i*) the centrifugal force $F_c = m_p\omega^2 r$, proportional to the mass of the particle itself (m_p), the distance from the rotational axes (r), the square of the angular velocity (ω); (*ii*) the buoyant force, $F_b = -m_s\omega^2 r$, the force deriving from the Archimedes’ principle that is proportional to the mass of the displaced solvent (m_s) and the centrifugal acceleration; and (*iii*) the frictional force $F_f = -f_v$, the force acting on the particles while moving with a sedimentation velocity (v) in a fluid, proportional to the friction coefficient (f) between the solvent and the particle itself. The net sum of the forces acting on the dispersed flakes is [80]:

$$F_{tot} = F_c + F_b + F_f \tag{1.4}$$

The volume of the particle or flake can be calculated as its mass (m_p) divided by its density (ρ_p), thus the displaced solvent can be calculated as $m_s = m_p \cdot \rho_s / \rho_p$, where ρ_s is the density of the solvent. Substituting each force in the Eq. 1.4:

$$F_{tot} = m_p \omega^2 r - m_p \omega^2 r \frac{\rho_s}{\rho_p} - fv \tag{1.5}$$

Considering that at equilibrium the net sum of the forces acting on the flake is zero, it is possible to define the ratio of sedimentation, or sedimentation coefficient (S) as the ratio between the sedimentation velocity and the particle acceleration, obtaining [80]:

$$S = \frac{v}{\omega^2 r} = \frac{m_p \left(1 - \frac{\rho_s}{\rho_p}\right)}{f} \tag{1.6}$$

As expressed by Equation 1.5, the sedimentation of 2D sheets depends on their mass and the frictional coefficient [39,57,61,79]. Thick and large sheets, having larger mass, sediment faster with respect to small and thin sheets, having a smaller mass, which are thus retained in dispersion during the ultra-centrifugation process [39,57,61,79]. Therefore, by tuning the experimental ultra-centrifugation parameters, it is possible to retain flakes with different lateral sizes and thickness in dispersion (Figure 1.7b).

1.3 Theoretical background of composite properties modification

1.3.1 Mechanical reinforcement

One of the simplest relationships that have been developed to describe the reinforcement achieved from a high-modulus filler, such as 2D crystals, in a low-modulus matrix, such as polymers, is the so-called "rule of mixtures", in which the modulus of the composite E_c is given by [81,82]:

$$E_c = \varphi_f E_f + \varphi_m E_m \tag{1.7}$$

where E_f and E_m are the moduli of the filler and the modulus of the matrix and φ_f and φ_m are the volume fractions of the filler and the matrix, respectively [81,82]. This model assumes perfectly aligned semi-infinite fillers (Figure 1.8a) and perfect stress transfer between the filler and the matrix [81,82]. However, despite its simplicity, it has been found to accurately predict the modulus of the composites, especially at low loadings [78,83]. At higher filler contents, the unavoidable aggregation of the filler is not taken into account from this linear equation and in most cases this model is not applicable [78,83–85], still providing an upper bound [78,81–83]. A modified version of the simple rule of mixtures has been proposed in order to take into account the effects of both orientation and filler's aspect ratio α, *i.e.* lateral size over thickness of the 2D crystal [78,86]:

$$E_c = \eta_0 \eta_l \varphi_f E_f + \varphi_m E_m \tag{1.8}$$

where η_0 is the Krenchel orientation factor, which depends on the average orientation of the filler with respect to the applied stress, while η_l is the length distribution factor, directly linked to α, *i.e.*, η_l approaches 1 with increasing the α value [78,86]. The Krenchel factor for a composite with aligned fillers (Figure 1.8b) is equal to 1, while it has been shown that for a material reinforced with randomly aligned platelets, such as 2D crystals, is equal to 8/15 [78,86]. Hence, the random orientation of the 2D crystals inside the matrix (Figure 1.8c) should cause a reduction of the modulus by almost a factor of two, with respect the case of aligned 2D crystals in the matrix. Noteworthy, the effect of mechanical reinforcement by the inclusion of 2D crystals is higher than that obtained by using fillers such as fibres or CNTs since for these materials a random orientation causes a reduction of the modulus by a factor of five (η_0 = 1/5) [86,87].

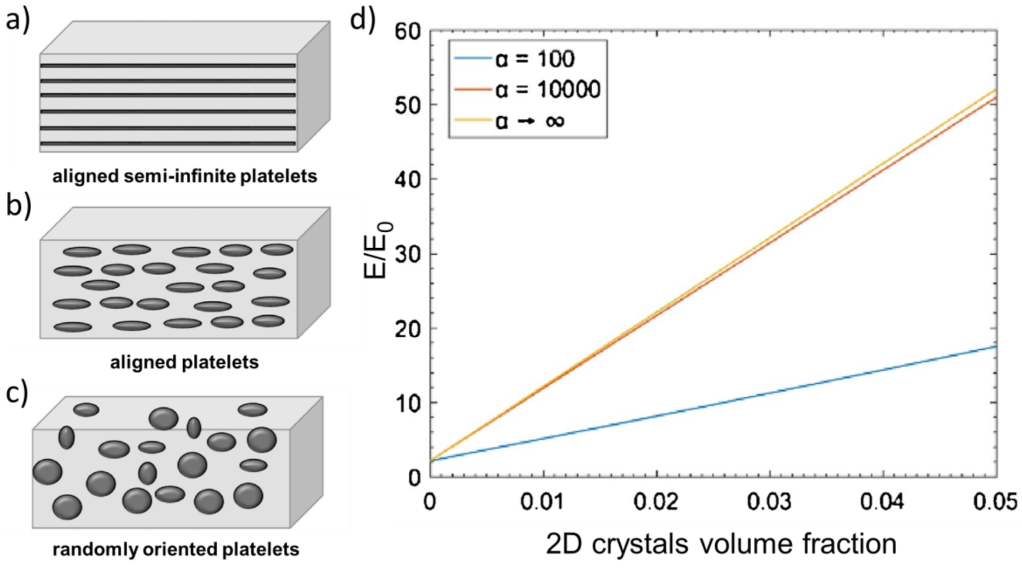

Figure 1.8. Composites with (a) aligned semi-infinite platelets; (b) aligned platelets; (c) randomly oriented platelets. d) Effect of aspect ratio of 2D crystals on mechanical stiffness enhancement of composite. Adapted from [74].

The Halpin-Tsai semi-empirical model [88] is a more complicated model that considers the distribution of 2D aligned anisotropic fillers as well as 3D randomly oriented fillers with different geometries [74,78,88,89]. For composite materials with parallel aligned short platelets, it gives Young's modulus of the composite in the longitudinal direction ($E_{\|}$) as [74,88]:

$$E_{\|} = \frac{1 + 2\alpha\eta_{\|}\varphi_f}{1 - \eta_{\|}\varphi_f} E_m, \qquad \text{where} \qquad \eta_{\|} = \frac{E_f/E_m - 1}{E_f/E_m + 2\alpha} \tag{1.9}$$

The effect of 2D crystals α on the final stiffness of the composite is evidenced in Figure 1.8d [74]. When α→∞, the Halpin-Tsai equation converges to the Eq. 1.8, but the reinforcement approaches this limit already when a > 10000 [74].

1.3.2 Gas barrier

Impermeability to gases is important for food or electronic packaging applications [90]. The barrier properties of polymers can be significantly enhanced by the inclusion of impermeable platelet-like fillers, such as clays [91,92], graphene [90,93], and *h*-BN [94], in order to alter the diffusion path of gas-penetrant molecules [90]. The presence of the filler makes the diffusing molecules to follow longer and more tortuous pathways to pass through the composite film, thus reducing the overall gas permeability (Figure 1.9) [90].

The gas permeation in a polymer (Figure 1.9a), as well as in a composite, film is governed by a diffusion-solubility mechanism [95] and it occurs due to a pressure gradient across the film [95]. According to the diffusion-solution model, the permeability (P) of a gas molecule in a composite film can be expressed as a product of the diffusivity, related to the kinetic aspect of the transport, and solubility, related to the thermodynamic aspect of the transport, *i.e.* the penetrant affinity between the gas molecule and the composite [90,95].

For polymer composites with 2D crystal fillers oriented perpendicular to the diffusion path (Figure 1.9b), the relative permeability (P/P_0, where P_0 is the permeability of the pure polymer matrix) is given by the relation [90]:

$$\frac{P}{P_0} = \frac{1 - \varphi_f}{\tau} \tag{1.10}$$

where τ is the tortuosity factor, which depends on the aspect ratio of the fillers and their orientation. In a dilute regime ($\varphi_f < 0.01$) of flakes aligned perpendicularly to the gas flow (Figure 1.9b) the relative permeability can be described by the Nielsen model [96]:

$$\frac{P}{P_0} = \frac{1 - \varphi_f}{1 + \alpha\varphi_f} \tag{1.11}$$

Here, $\tau = 1 + \alpha\varphi_f$. The importance of the aspect ratio of 2D crystal fillers is evidenced in Figure 1.9c. As an example, a reduction of ~ 80% in gas permeability can be obtained with a volume fraction of

0.0005, if the filler has an aspect ratio of ~ 1000, whereas if the filler has an aspect ratio of 10000, the reduction in permeability at the same volume fraction reaches 98%.

The Nielsen model can be modified in order to take into account the orientation of the 2D crystals inside the polymer matrix, introducing the parameter S into the definition of τ [97]:

$$\tau = 1 + \frac{2\alpha\varphi_f}{3}\left(S + \frac{1}{2}\right) \tag{1.12}$$

where $-1/2 \leq S \leq 1$. In particular, $S = 1$ describes the condition of oriented 2D crystals as assumed in the Nielsen model (note that in this case Eq. 1.12 converges into Eq. 1.11), $S = 0$ describes the condition of 2D crystals randomly oriented inside the polymer matrix and $S = -1/2$ describes the condition of 2D crystals aligned towards the gas flow, thus not contributing to the tortuosity [90,97].

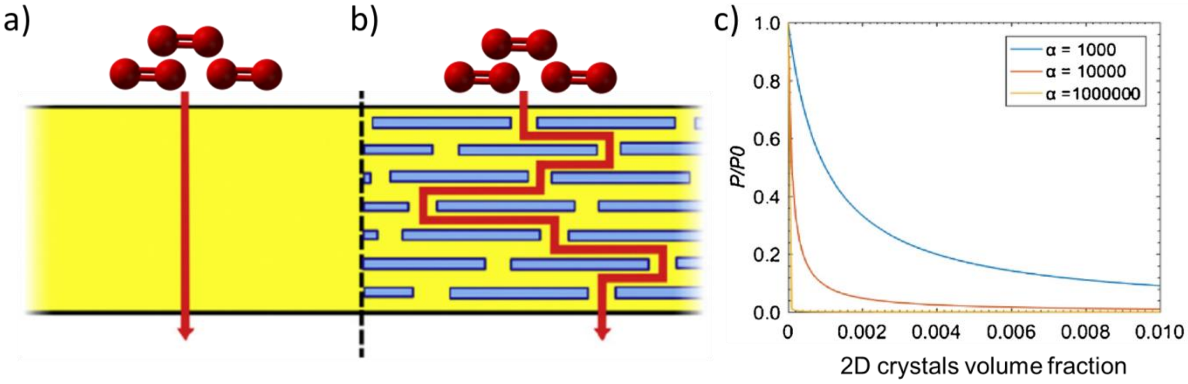

Figure 1.9. Illustration of the tortuous pathway created by incorporation of aligned 2D crystals into a polymer matrix film and consequent variation of barrier properties. a) In a polymer film, diffusing gas molecules, in this case O_2, migrate via a pathway that is perpendicular to the film orientation; b) in a composite, diffusing molecules navigate around impenetrable 2D crystals platelets through a more tortuous pathway; c) change in relative permeability of composites for different aspect ratio of 2D crystals. Adapted from [90], [98] and [74].

1.3.3 Electrical conduction

Electrically conductive composites can be achieved by adding a conductive filler, such as graphene [8], to the polymer matrix, generally insulating [77]. These composites can be useful for many applications, including conductive adhesives [99], strain sensors [100,101], and electromagnetic shielding [102].

The electrical conduction mechanism in a composite is described by the percolation theory [103–105], and it can be divided into three stages, as evidenced in Figure 1.10a. For filler loadings below the so-called percolation threshold (φ_c), *i.e.* the loading in which the fillers form a conductive network no charge can flow, and the composite remains insulating. On the other hand, if the filler forms a directly connected network, electrons can move through this network, and the composite is conductive. Between these two extremes, conduction takes place when the fillers are not in direct contact but are connected via electrons tunnelling through an interface formed between the filler and the matrix; the conductivity, in this case, is lower than that where a direct network has been formed. This tunnelling conduction is a quantum phenomenon where the contribution between the nearest neighbours is the most dominant [77,106,107], therefore the tunnelling resistance is the limiting factor in the composite conductivity [108].

The variation of electrical conductivity of composites with the filler loading follows a power-law relation (valid for $\varphi > \varphi_c$) [105]:

$$\sigma = \sigma_0 \left(\frac{\varphi - \varphi_c}{1 - \varphi_c} \right)^s \tag{1.13}$$

where σ_0 is the intrinsic conductivity of the filler and s is the critical exponent, related with system dimensionality, *i.e.* geometrical pathways [105,109] *e.g.* for two-dimensional pathway s assumes values in the range 1.1–1.3, and ~ 2 for three-dimensional systems [105,109]. Both simulations and experiments have shown that fillers with larger aspect ratios lead to reduced percolation thresholds (Figure 1.10b) [107,110,111]. Assuming disc-shaped particles oriented two- or three-dimensionally and randomly in a polymer matrix, the percolation threshold can be expressed by the following equations [110]:

$$\varphi_{c(2D)} = \frac{2\pi D^2 t}{(D + D_{IP})^3} \tag{1.14}$$

$$\varphi_{c(3D)} = \frac{27\pi D^2 t}{4(D + D_{IP})^3} \tag{1.15}$$

where D is the diameter of the disk, t the thickness of the platelet, and D_{IP} is the inter-particle distance [110]. The effects of D_{IP} on the percolation threshold are negligible for $D/t > 500$ [110]. Moreover, it has been shown that fillers with higher aspect ratio lead to a higher final conductivity of the composite [112,113], because fillers with large aspect ratios form a network with fewer junctions than those with smaller aspect ratios, and fewer junctions reduce the total resistance of the network [77,112,113].

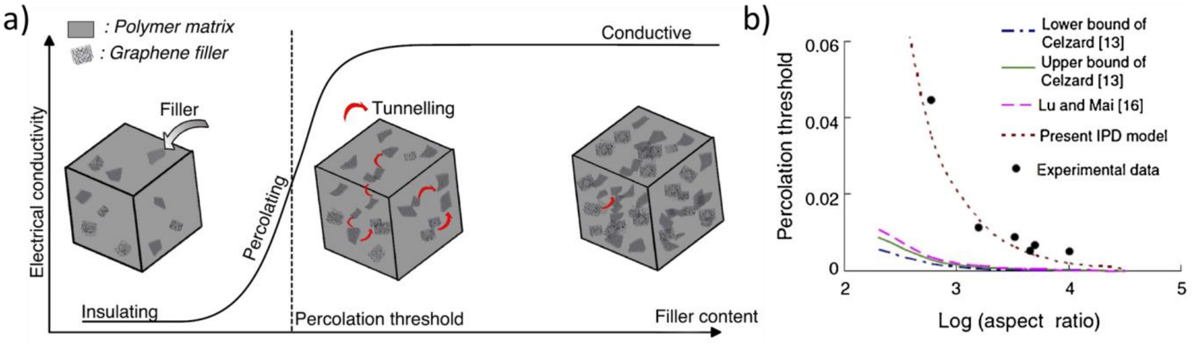

Figure 1.10. Electrical conduction in graphene-based composites. a) A schematic of conduction mechanisms in a composite with increasing graphene loading: at no graphene loading, the polymer is insulating, and remains insulating while the loadings are low; as the graphene loading is increased to the percolation threshold, a conductive network begins to form; at loadings higher than the percolation threshold an efficient network has been formed and the conductivity is saturated. b) Percolation threshold of electrical conduction of polymer nanocomposites with graphene at different aspect ratios. Adapted from [77] and [110].

1.3.4 Thermal conduction

In polymers, phonons are the primary mechanism of heat conduction since free movement of electrons is not possible [114,115]. In view of theoretical prediction, the Debye equation is frequently used to calculate the thermal conductivity (λ) of polymers [114,115]:

$$\lambda = \frac{c_p v' \Lambda}{3} \tag{1.16}$$

where c_p is the specific heat capacity per unit volume, v' is the phonon group velocity, and Λ is the phonon mean free path [114]. For amorphous polymers, Λ is an extremely small constant (*i.e.* a few angstroms) due to phonon scattering from numerous defects, leading to a low thermal conductivity in polymers (usually < 0.4 W m^{-1} K^{-1}) [114,116].

Many applications would benefit from the use of polymers with enhanced thermal conductivity [115,117]. For example, when used as heat sinks in electric or electronic systems, composites with a thermal conductivity approximately from 1 to 30 W m^{-1} K^{-1} are required [118]. The thermal conductivity of polymers has been traditionally enhanced by the addition of thermally conductive fillers [119], including graphite [120,121], carbon black [122,123], carbon fibres [124,125], ceramic [126] or metal particles [127], and more recently by CNTs [115,128,129] and 2D crystals *e.g.* graphene [123,130–132] or *h*-BN [133–135].

Thermal conduction in an isotropic, two-phase composite with low filler volume fraction is well represented by the Maxwell model (Figure 1.7a) [136]:

$$\lambda_c = \frac{2\lambda_m + \lambda_f + 2\varphi_f(\lambda_f - \lambda_m)}{2\lambda_m + \lambda_f - \varphi_f(\lambda_f - \lambda_m)}\lambda_m \tag{1.17}$$

where λ_c, λ_f and λ_m are the thermal conductivities of the composite, of the filler, and of the matrix, respectively [136]. The Maxwell model assumes that the filler particles are spherical, isolated, and randomly distributed within the matrix [136]. The validity and accuracy of the Maxwell model breaks down for high filler volume fractions, *i.e.* for $\varphi_c > 0.3$ [74,123,136]. In this case, percolation theory may be applied also in thermal transport, leading to the expression (Figure 1.11a) [136]:

$$\lambda_c = \lambda_f\left(\frac{\lambda_p}{\lambda_f}\right)^{\left[\frac{1-\varphi}{1-\varphi_c}\right]^n} \tag{1.18}$$

where λ_p is the thermal conductivity at the percolation threshold and n is the percolation exponent, usually in the range 0.3–0.8 [136], which depends upon filler's shape, size and distribution [136].

However, despite the case of electrical conductivity enhancement, the high intrinsic thermal conductivity of the filler is usually not well exploited in composites [117]. In fact, heat would quickly diffuse through the crystalline filler, whereas it is considerably slowed by the polymer because of phonon scattering at the interfaces [117]. For this reason, having continued, high-aspect-ratio fillers are beneficial for the thermal conductivity improvement.

Polymer matrices are thermally homogeneous, *i.e.*, each polymer chain or component will display similar low thermal conductivity. Therefore, heat diffuses slowly and uniformly through the matrix (Figure 1.11b). In the case of a composite filled with spherical nanoparticles, heat diffusion is locally facilitated, but the overall thermal diffusion is hindered by a large number of nanoparticle/matrix interfaces (Figure 1.11c). Following this hypothesis, a composite with anisotropic fillers appears to be more suitable to improve thermal conductivity. Considering the same loading as in the nanoparticle-based composite, better heat transfer is expected due to far fewer filler/matrix interfaces (Figure 1.11d). Fillers with a higher aspect ratio can further reduce those distances and build better thermal paths to achieve higher thermal conductivities in the final composite because mean inter-filler distance, detrimental for good thermal transfer, are further reduced (Figure 1.11e) [117].

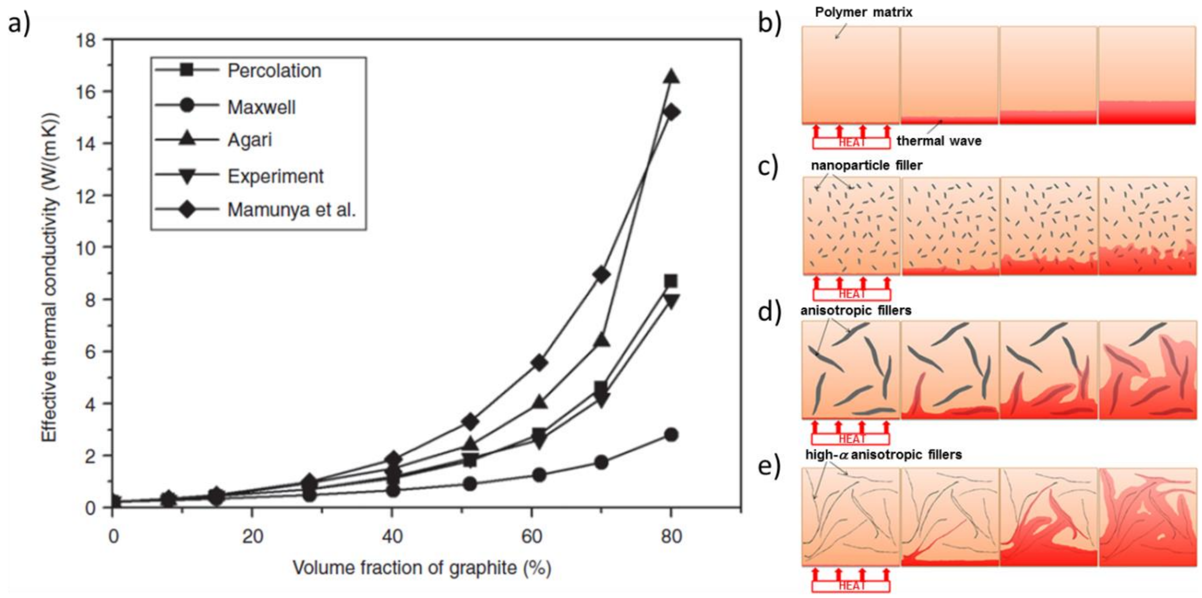

Figure 1.11. a) Results for the effective thermal conductivity of a graphite-based composite as a function of graphite volume fraction as obtained from experiment and modeling. b-e) Heat transfer mechanisms in composites, as a function of size and aspect ratios of fillers. Adapted from [136] and [117].

1.4 Using 2D materials in a 3D world

Currently, graphene-based composites are the only application of graphene already commercialized on a large scale [17–19]. Nevertheless, the performance of such products is not comparable to that of pristine graphene [16]. A key reason for this difference in properties is that it is not yet fully understood how graphene-based, and in general 2D crystal-based, composites work at the nanoscale level and what is the ultimate performance (mechanical, electrical, etc.) that can be achieved when they are included in a bulk material [16].

A key requirement, apart from the 2D crystal morphology, as evidenced by the importance of the aspect ratio of filler in the previous section, to obtain improvements with respect pristine polymer in the properties of the final composite material is the optimal dispersion of the graphene flakes in the polymer matrices [74,78]. The molecular interactions between the 2D crystals and polymer chains are essentially due to weak van der Waals forces [137], π–π stacking [137,138], and hydrophobic-hydrophobic interactions [137]. These interactions hinder efficient connections between the 2D crystals and the polymer chains, so 2D crystals usually do not form homogeneous composites [139–141]. In contrast, the functional groups present on the basal plane of GO [63,70] and also partially in RGO [66,72] can interact with the polymer chains. Therefore, their use as a filler in the polymer-based composites is widely reported in the literature [1,139,141,142]. As aforementioned, the presence of these groups acts as defects, reducing the mechanical and electrical properties of GO and RGO flakes compared to graphene flakes [66,139,143,144]. Besides, the dispersion of the 2D crystals inside the polymer matrix is strongly dependent on the processing techniques used for the production of the composite itself. Some of the most common processes for polymer composite preparation are melt blending [145,146], solution blending [47,147,148], and in situ polymerization.[149] Melt blending is industrially attractive due to its scalability and low-cost, while solution blending provides better mixing than melt blending between the exfoliated 2D crystals flakes and the polymer matrix [93,150,151]. Moreover, strong shear forces produced during melt mixing are able to break the larger flakes to smaller sizes, thus reducing their aspect ratio [146,152], whereas other issues such as thermal degradation, often observed during melt mixing, and feeding difficulty are also still challenges necessary to overcome [146].

CHAPTER 2

Experimental procedure

2.1 Liquid phase exfoliation of 2D crystals

During the research activity, LPE, presented in the previous chapter, has been exploited as a production technique for the preparation of 2D crystals i.e. graphene, *h*-BN, MoS_2, and WS_2.

Two exfoliation methodologies have been followed: sonication-assisted LPE [35] and WJM [153]. The WJM technique has been developed in our laboratories as a synthesis method for 2D crystal able to produce flakes with higher aspect ratio and higher production rate compared to the sonication-assisted LPE [154], targeting the needing of gram-scale production rates required for the full exploitation of 2D crystals as fillers in polymer composites.

2.1.1 Sonication-assisted LPE of graphite

500 mg of graphite flakes (Sigma-Aldrich, +100 mesh) are dispersed in 50 mL of NMP (Sigma-Aldrich, Reagent Plus®, 99%) and exfoliated by ultra-sonication in a sonic bath (VWR Ultrasonic Cleaner USC-THD) for 6 hours. The resulting dispersion is then ultra-centrifuged at 10000 rpm (17000 g) in a Beckman Coulter Optima ™ XE-90 equipped with a SW32Ti rotor, for 30 minutes at 15°C, to remove thick flakes and un-exfoliated graphite. After the ultracentrifugation process, 80% of the supernatant is collected by pipetting, thus delivering a graphene dispersion in NMP.

2.1.2 Sonication-assisted LPE of layered materials and size sorting

500 mg of bulk material (graphite flakes, Sigma-Aldrich, +100 mesh, WS_2, Sigma-Aldrich, 2 μm particle size powder, and *h*-BN, Sigma-Aldrich, 1 μm particle size powder) are dispersed in 50 mL of NMP and exfoliated by ultra-sonication in a sonic bath for 6 hours. The supernatant is collected by pipetting after the ultra-centrifugation process. Different angular velocity is applied at 1000, 2500, 5000, 7500, 10000 rpm, corresponding to different g-forces, *i.e.*, 170g, 1000g, 4250g, 9500g, 17000g, respectively. In order to further tune the morphology of the 2D crystals, we performed cascade ultra-centrifugations [61], using multiple ultra-centrifugation steps in sequence, collecting and processing the supernatant for all cases. We started with an as-prepared LPE dispersion of 2D crystals, where any un-exfoliated bulk materials had been removed by the centrifugation at 170 g. This dispersion is then centrifuged at a higher speed (4250 g) and the supernatant is collected again. Afterwards, the

dispersion is again centrifuged at 170 g, and subsequently a second, and a third 170g centrifugation steps are added, collecting supernatant at each step.

2.1.3 Environmentally-friendly sonication-assisted LPE of *h*-BN and size sorting

500 mg of *h*-BN powder (1 µm particle size) are dispersed in 50 mL of water/surfactant solution concentrated at 2 wt % and exfoliated in an ultrasonic bath for 6 hours. The surfactant herein used is Kolliphor® P188, a triblock copolymer. More details on it structure and function will be given in the next chapter. Then, the obtained dispersion (Figure 2.1a) is ultra-centrifuged at 1000 rpm (200 g) for 30 min at 15 °C with an ultra-centrifuge, to remove un-exfoliated and thicker flakes (Figure 2.1b). The supernatant is collected and ultra-centrifuged again at 2400 rpm (1000 g) for 30 min at 15 °C. Both supernatant and precipitate (re-dispersed in a freshwater/surfactant solution) are collected and named as "*h*-BN-s" and "*h*-BN-p", where "s" and "p" correspond to "supernatant" and "precipitate", respectively (Figure 2.1c).

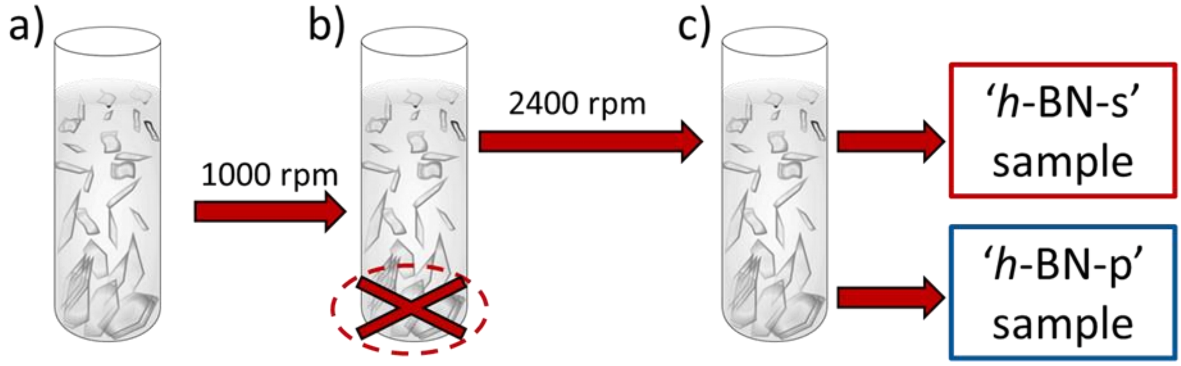

Figure 2.1. Scheme of size selection of *h*-BN flakes. a) Heterogeneous *h*-BN dispersion after exfoliation; b) first ultra-centrifugation step (1000 rpm for 30 min) to remove un-exfoliated and thick flakes; c) second ultra-centrifugation step (2400 rpm for 30 min) for the selection of *h*-BN flakes with different morphology.

2.2 Wet-jet mill exfoliation of layered materials

Seeking for industrially relevant approaches, *i.e.* the time, weight-yield and a cost-effective production of the 2D crystals without compromising the crystalline-integrity, our group developed the WJM exfoliation technique, a promising method to produce 2D crystals exfoliated from their bulk layered materials. Particularly, the WJM allows obtaining single- and few-layers 2D crystal flakes with concentrations up to 10 g L^{-1}, with no material loss, *i.e.* the weight ratio between the final processed material and the starting layered material flakes is one. Additionally, the WJM guarantees a production capability of 2.35 L h^{-1}, *i.e.* the time required to produce one gram of exfoliated graphite is only 2.55 min, thus outperforming other proposed LPE-based synthesis approaches such as shear exfoliation [38] and micro-fluidization [155]. In the WJM the solvent/layered-crystal mixture is forced to pass through a nozzle with an adjustable diameter (0.3-0.1 mm) by applying high pressure (180 – 250 MPa) creating jet streams and shear forces between the layered material and the solvent. The shear forces generated by the solvent when passing through the nozzle is the main phenomenon that promotes the exfoliation of layered-crystals into 2D crystals [154].

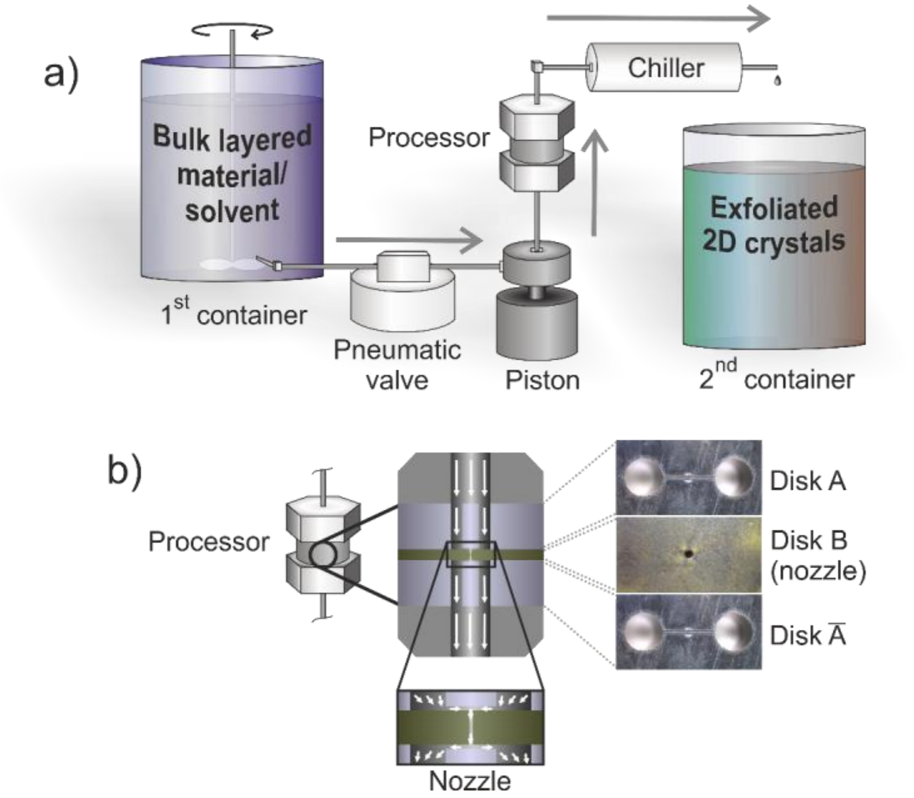

Figure 2.2. a) Scheme of the WJM system, the arrows indicate the flow of the solvent through the WJM; b) Close-up view of the processor. The zoomed image in (b) shows the channels configuration and the disks arrangement. The solvent flow is indicated by the white arrows. On the right side a top view of the holes and channels on each disk. The disks A and Ā have two holes of 1 mm in diameter, separated by a distance of 2.3 mm from centre to centre and joined by a half-cylinder channel of 0.3 mm in diameter. The thickness of the A and Ā disks is 4 mm. The disk B is the core of the system; the image (b, disk B) shows the 0.10 mm nozzle. It can be changed to 0.10, 0.20, and 0.30 mm nozzle diameter disks according to the size of the bulk layered crystals. The thickness of the B disk is 0.95 mm. Adapted from [154].

The WJM apparatus is schemed in Figure 2.2a. A hydraulic mechanism and a piston supply the pressure (up to 250 MPa) in order to push the sample into a set of 5 different perforated and interconnected disks, see Figure 2.2b, named processor, where jet streams are generated. The pulverization is obtained mainly by collision of the pressurised streams of the particle liquid dispersions. The collision takes place between the disks A and B (Figure 2.2b). In contrast, for the exfoliation of layered crystals, the shear force generated by the solvent when the sample passes through the disk B is the main phenomenon promoting the exfoliation.

2.2.1 Wet-jet mill exfoliation of layered crystals

A mixture of the bulk layered crystals (natural graphite flakes, Sigma-Aldrich, +100 mesh; or MoS_2, Sigma-Aldrich, <2 μm particle size powder; or WS_2, Sigma-Aldrich, 2 μm particle size powder; or hBN, Sigma-Aldrich, 1 μm particle size powder; or *h*-BN, Alfa Aesar, +325 mesh) and NMP (concentration of bulk materials in the solvent is kept at 10 g L^{-1}) is prepared. The mixture is placed in the container and mixed with a mechanical stirrer (Eurostar digital Ika-Werke). The dispersion formed by either graphite/NMP or *h*-BN (325 mesh)/NMP is forced to pass through 0.30, 0.15 and 0.10 mm nozzles consecutively, obtaining a dispersion of the exfoliated material. The processed dispersion is then dried, removing the NMP by rotary evaporation and re-dispersed in dimethyl sulfoxide (DMSO, Sigma-Aldrich, ReagentPlus®, ≥99.6%) at a concentration of 30 g L^{-1}. Finally, the dispersion is lyophilized (Martin Christ Alpha 2-4 LSC plus) obtaining wet-jet milled graphene (WG) and *h*-BN (W*h*BN) in the powder form.

For the others layered materials, *i.e.*, *h*-BN (1 µm powder form), MoS_2, and WS_2, since their starting crystallite size is much smaller, it is possible to perform the exfoliation directly with the 0.10 mm nozzle diameter.

2.3. Material characterization techniques

2.3.1. Optical extinction spectroscopy

The Optical extinction spectroscopy is carried out in a Cary Varian 5000 UV-vis spectrophotometer. The extinction spectra are acquired using a 1 mL quartz glass cuvette. The extinction spectra of the solvents used are subtracted from each spectrum.

2.3.2. Raman spectroscopy

Raman spectroscopy is carried out using a Renishaw inVia confocal Raman microscope, with a laser excitation wavelength of 514.5 nm at an incident power of ~1 mW and a 100× objective. For the measurements, dispersions of exfoliated 2D crystals are drop cast onto Si/SiO_2 wafer (Si-Mat Silicon Materials) substrate and dried under vacuum overnight.

2.3.3 Transmission electron microscopy

Transmission electron microscopy (TEM) images of samples are acquired with a JOEL JEM-1011 microscope, operating at 100 kV. High-resolution TEM (HRTEM) is performed using a 200 kV field emission gun, a CEOS spherical aberration corrector for the objective lens, enabling a spatial resolution of 0.9 Å, and an in-column image filter (Ω-type). For the measurements, dispersions of exfoliated 2D crystals are drop cast onto ultrathin C-film on holey carbon 400 mesh Cu grids (Ted Pella Inc.) and dried under vacuum overnight.

2.3.4 Atomic Force Microscopy

Atomic Force Microscopy (AFM) images are acquired with Bruker Innova AFM in tapping mode using silicon probes (f = 300 kHz, k = 40 Nm^{-1}). Images of 5×5 μm^2 were collected with 512 data points per line and the working set point was kept above 70% of free oscillation amplitude and measurements were taken at a scan rate of 0.7 Hz. The AFM instrument was calibrated using the Bruker Platinum-coated grating for AFMs: 100 nm depth, 1 µm pitch. For the measurements, dispersions of exfoliated 2D crystals are drop cast onto a Si/SiO_2 wafer (Si-Mat Silicon Materials) substrate and dried under vacuum overnight.

2.3.5 X-ray Photoelectron Spectroscopy

X-ray photoelectron spectroscopy (XPS) characterization was carried out on a Kratos Axis UltraDLD spectrometer, using a monochromatic Al Kα source (15 kV, 20 mA). The spectra were acquired over an area of 300 µm × 700 µm. Wide scans were collected with constant pass energy of 160 eV and an energy step of 1 eV. High-resolution spectra were acquired at constant pass energy of 10 eV and an energy step of 0.1 eV. The binding energy scale was calibrated to the C 1s peak at 284.8 eV. For the measurements, dispersions of exfoliated 2D crystals are drop cast onto Si wafer (Si-Mat Silicon Materials) substrates and dried under vacuum overnight.

2.4 Composites preparation

2.4.1 Graphene/Polycarbonate composites

The graphene/polycarbonate (PC, MAKROLON®2405) (PC/G) composites are produced by exploiting the solution blending technique. Figure 2.3a shows a schematic representation of the composite preparation. Firstly, PC pellets are dissolved in 1,3-dioxolane (Sigma-Aldrich, Reagent Plus®, 99%) at a concentration of 150 mg mL^{-1} by stirring for 3 h using a magnetic stirrer. Then, the graphene dispersions in NMP are exchanged *via* rotary evaporation (Heidolph Hei-Vap) and re-dispersed in 1,3-dioxolane at a concentration of 10 mg mL^{-1}. Subsequently, graphene dispersion and

PC dispersion are mixed together at different weight fractions, specifically between 0 wt % and 10 wt % compared to PC weight. The resulting composite dispersions are mixed by means of ultra-sonication for 1 h, maintaining the temperature in the range 25–40 °C, in order to obtain a thorough mixing. The composite dispersion, in 1,3-dioxolane, is then dripped into distilled water (volume ratio of 1,3-dioxolane/distilled water is 1:4). The PC/G mass is therefore immediately coagulated forming pellets (Figure 2.3b), because water is a non-solvent for PC. Finally, composite pellets are dried in a vacuum oven (Binder VDL 115) at 80 °C for 12 h and compression moulded, by hot pressing at 225°C at 2 tons for 5 minutes using a Madatec Atlas T8 press, forming composite films.

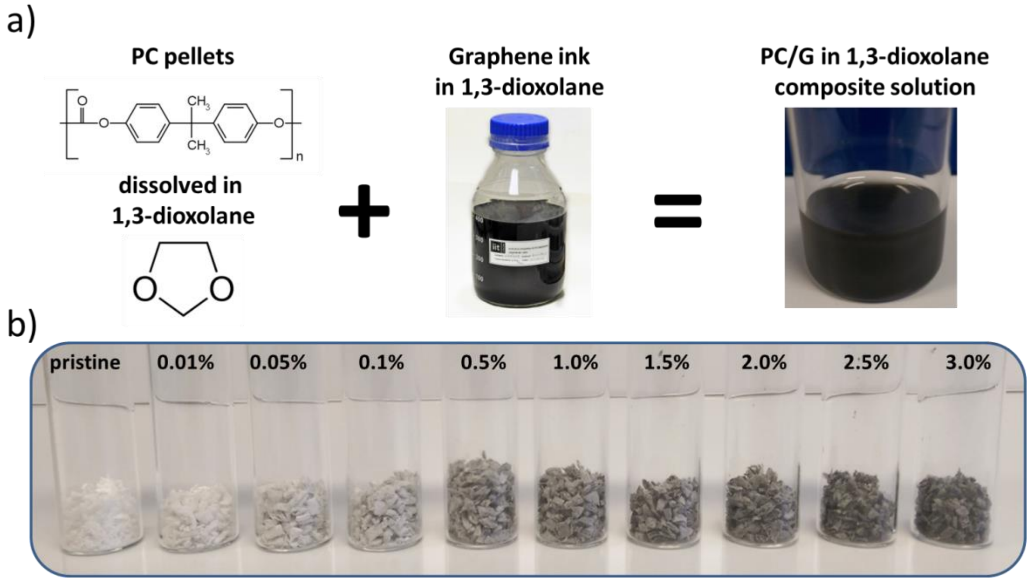

Figure 2.3. a) Scheme of solution blending preparation of PC/G composites. b) Photograph of PC/G composites pellets at different loadings of graphene-based flakes. Adapted from [47].

2.4.2 *h*-BN/Polycarbonate composites

The *h*-BN/PC composites are produced by exploiting the solution blending technique. Briefly, PC pellets are dissolved in 1,3-dioxolane, at a concentration of 150 mg mL^{-1}, by stirring for 3h using a magnetic stirrer. *h*-BN-s and *h*-BN-p dispersions in water surfactant are exchanged, washed and re-dispersed in 1,3-dioxolane in order to perform the blending. Thus, specified amounts of either *h*-BN-s or *h*-BN-p flakes dispersed in 1,3-dioxolane at a concentration of 10 mg mL^{-1} are mixed with PC dispersions, obtaining composite dispersions for both samples ranging from 0 to 5 wt % of filler with respect to the polymer weight. After mixing, composite dispersions are subsequently sonicated for 1 h obtaining a thorough mixing and then coagulated forming composite pellets by pouring into water, using a similar procedure descripted in section 2.4.1. Composite pellets are then dried in a vacuum oven at 80 °C for 12 h and finally hot pressed at 2 tons at 225 °C for 5 minutes in order to produce composite films.

2.4.3 2D crystals/ABS composites

Acrylonitrile butadiene styrene (ABS) pellets (Terluran® GP-22) are dissolved in acetone (Sigma-Aldrich, ACS Reagent, ≥99.5%) at a concentration of 240 mg mL^{-1}. 2D crystals, either graphene, or *h*-BN, or WS_2, exfoliated in NMP are exchanged and re-dispersed in acetone at a concentration of 10 mg mL^{-1}. ABS and 2D crystal dispersions in acetone are mixed together according to different ABS/2D crystal weight fractions, ranging from 0.01 to 1 wt %. Composite dispersions are sonicated for 1 h in order to obtain a thorough mixing. The composite dispersion is coagulated/precipitated forming pellets by pouring water. Finally, composite pellets are dried in a vacuum oven at 80 °C for 12 h and compression moulded, by hot pressing at 215°C at 1 ton for 5 minutes, forming composite films.

2.4.4 WJM-exfoliated 2D crystals/PLA composites

Polylactic-acid pellets (Natureworks Ingeo 4043D) are dissolved in 1,3-dioxolane at a concentration of 100 mg mL^{-1} by stirring for 8 h. Calculated masses, corresponding to 0.1, 0.5, 1, 2, 5 and 10% in volume of the total composite mass, of WG and WhBN powders into the PLA dispersions are mixed by ultra-sonication for 1 h, forming the composite dispersions. Three-phase composites are produced with a similar procedure at 0.1, 0.5, 1, 2, 5 and 10% in volume keeping the ratio between WG and WhBN 1:1. After mixing, the composite dispersions are sonicated for 1 h and then cast into polytetrafluoroethylene Petri dishes. Composite dispersions are dried in air overnight, then dried in a vacuum oven at 80 °C for 12 h and finally hot pressed applying 2 tons at 180 °C for 5 minutes in order to produce composite films of c.a. 80 µm thickness (Mitutoyo micrometre 293).

The conversion from mass fraction (w) to volume fraction (φ) of the fillers is made by considering $\varphi = w_f \rho_m/(w_f \rho_m + w_m \rho_f)$ [82], where w_f and w_m are the weight fractions and ρ_f and ρ_m are the densities of fillers and PLA matrix, respectively. Densities of 2.2 g cm^{-3} for graphene [84], 2.3 g cm^{-3} for *h*-BN [85] and 1.24 g cm^{-3} for PLA [156] have been used.

2.5 Composites characterization

2.5.1 Scanning electron microscopy

Scanning electron microscopy (SEM) images of cryo-fractured cross-sections of pristine polymer matrices and composites are taken using a field-emission scanning electron microscope (Jeol JSM-

7500 FA) at the operating voltage of 10 kV. Before image acquisition, samples are first coated with ~ 10 nm of gold layer in order to avoid charging effect due to insulating nature of polymer matrices.

2.5.2 Raman spectroscopy

Raman spectroscopy of cryo-fractured cross-sections of pristine polymer matrices and composites is carried out using a Renishaw inVia confocal Raman microscope, with a laser excitation wavelength of 514.5 nm at an incident power of ~1 mW and a 100× objective.

2.5.3 Thermogravimetric analysis

Thermogravimetric analysis (TGA) is carried out with a TGA Q500-TA Instrument. During TGA, the samples are heated from 30 °C to 800 °C at a heating rate of 10 °C min^{-1} under nitrogen atmosphere set at a flow rate of 50 mL min^{-1}.

2.5.4 Tensile testing

Mechanical properties of materials, either metals, ceramics, polymers and composites, can be analysed *via* tensile testing. This process involves applying a uniaxial tensile stress to a sample, in form of dog-bones, of known geometry at a predetermined rate and examining the force required to elongate and ultimately cause a fracture in the material. The output of such a tensile test is recorded as load (or force, F) *vs.* deformation (or elongation). These load-deformation characteristics are dependent on the specimen size. To minimize the geometrical factors, load and elongation are normalized to the respective parameters of stress and strain [157,158]. Stress (σ) [MPa] is defined by the relationship [157,158]:

$$\sigma = \frac{F}{A_0} \tag{2.1}$$

in which F [N] is the instantaneous load applied perpendicular to the specimen cross-section and A_0 [m^2] is the original cross-sectional area. Strain (ε) [%] is defined by the relationship [157,158]:

$$\varepsilon = \frac{l_i - l_0}{l_0} = \frac{\Delta l}{l_0} \tag{2.2}$$

in which l_0 is the original length before any load is applied, and l_i is the instantaneous length.

Therefore, a stress-stain curve can be obtained (Figure 2.4). Important parameters that can be obtained by the tensile test (Figure 2.4a) are: (1) the Young's Modulus, evaluated as the slope of the curve in the elastic region, *i.e.*, the deformation is non-permanent, which means that when the applied load is released the sample returns to its original shape; (2) the yield strength (σ_Y), *i.e.*, the value of stress corresponding to the proportional limit of stress and strain, in which the deformation is no more elastic (reversible) but plastic (irreversible); (3) the ultimate tensile strength (σ_U), *i.e.*, the maximum value of stress recorded during the test and corresponds to the formation of a necking in the sample and its consequent fracture; and (4) elongation at break (ε_B), *i.e.*, the elongation, usually expressed in percentage, at which sample failure (or fracture) occurs [157,158].

Concerning polymeric materials, as well as and their composites, three typical stress-strain behaviours are expected, as schematized in Figure 2.4b.

In this thesis, mechanical properties of the pristine polymer and composite films are measured, performing tensile tests using an Instron dual column tabletop universal testing System 3365, with 5 mm min^{-1} cross-head speed. The tensile measurements are carried out at least on five different specimens for each film according to ASTM D 882 Standard Test Methods for Tensile Properties of Thin Plastic Sheeting [159]. Dogbone specimens used have overall length of ~ 74 mm, gauge length of ~ 25 mm, width of ~ 4 mm and thickness of ~ 100 µm.

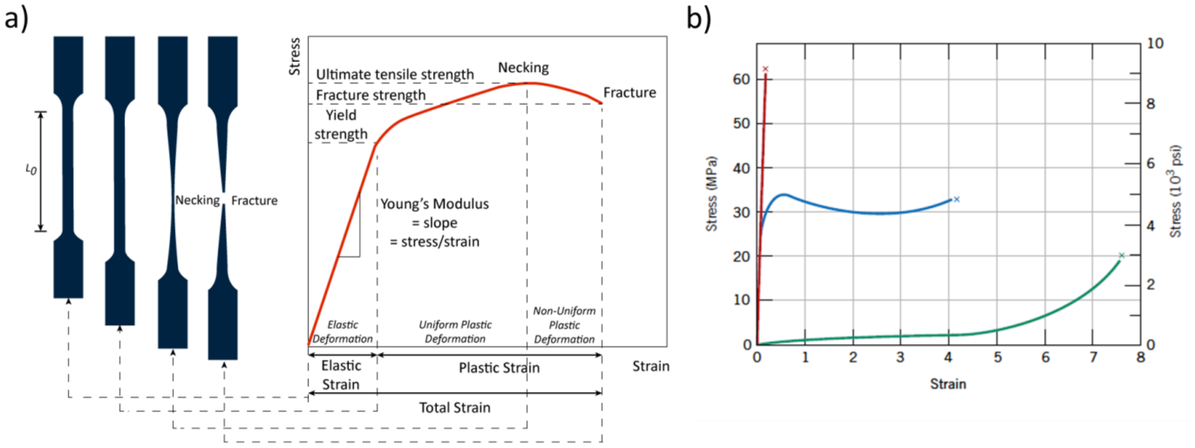

Figure 2.4. a) Analysis of a stress-strain curve, with reference to structural shape evolution of the sample (dogbone) during the tensile test; b) Typical stress-strain curve for brittle (red), ductile (blue) and elastic (green) polymers. Adapted from [158].

2.5.5 Electrical conductivity

Electrical conductivity was measured by using a four-point-probe station (Signatone 1160 probe station) connected to a Keithley source-measurement unit in DC regime on 1 cm × 0.5 cm pieces of the compression-moulded pristine polymer or composite films. Measurements are carried out applying voltages ranging from –1 to 1 V and acquiring current values. From the linear interpolation of the acquired I–V curves electrical resistance is extracted and linked to the electrical conductivity [160].

2.5.6 Thermal conductivity

In-plane and through-plane thermal conductivity has been evaluated by measuring room-temperature thermal diffusivity ($\bar{\alpha}$) of composites by light flash technique (Netzsch LFA 467 Hyperflash) which is related to the thermal conductivity by the relation $\lambda = \bar{\alpha}\rho c_p$, where ρ is the density of the composites and c_p the specific heat capacity [161]. The rule of mixtures has been used for estimating both ρ and c_p of the composites, considering the respective values of the polymer matrix and the fillers, both taken from literature.

CHAPTER 3

Characterization of 2D crystals

This chapter provides a detailed morphological and structural characterization of 2D crystals (graphene, *h*-BN, MoS_2, and WS_2) exfoliated by exploiting both sonication-assisted LPE and WJM-assisted LPE. Different techniques have been used in order to investigate the physical and chemical properties of the samples. The morphology of 2D crystals has been evaluated in terms of lateral size (TEM), surface area (TEM), and thickness (AFM). The structural properties of all samples are revealed by Raman spectroscopy. In addition, XPS is carried out to evaluate the surface chemical composition of 2D crystals and the possibility of oxidative processes occurring during exfoliation.

The information obtained from the aforementioned characterization techniques enables a comprehensive evaluation of the material properties, in particular providing an insightful understanding of their morphological properties that are of paramount importance for the exploitation of 2D crystals as fillers in polymer composites.

3.1 2D crystals exfoliated by sonication-assisted LPE

3.1.1 Characterization of graphene flakes exchanged in 1,3-dioxolane

In order to exploit graphene flakes as fillers in PC-based composites, natural graphite flakes are exfoliated in NMP exploiting sonication-assisted LPE, and purified by SBS (see section 2.1.1 for experimental details). The obtained graphene flakes are subsequently exchanged from NMP to 1,3-dioxolane, which is the solvent used for dissolving PC, and characterized by TEM, AFM, and Raman spectroscopy.

A representative TEM image of graphene flakes in 1,3-dioxolane is depicted in Figure 3.1a. The electron diffraction pattern (DP) image (inset to Figure 3.1a) confirms the typical lattice reflections present in a graphene flake, the expected honeycomb lattice, and pristine crystallinity [162]. The statistical analysis of lateral sizes (Figure 3.1b) shows a distribution of lateral size in the 200 – 600 nm range. The statistic is fitted by a log-normal distribution with a mode of lateral size peaked at 295 nm and log-normal standard deviation (lg-sd) of 0.34.

A representative AFM image and statistical analysis of graphene dispersion are shown in Figure 3.1c and Figure 3.1d, respectively. More than 70 % of the measured thicknesses are in the range 0.7–1.4

nm, corresponding to 1–3 layers of graphene flakes, considering that the first layer on SiO_2 substrate has a height of ~0.7 nm [163,164]. The mode occurs at 1.05 nm (with a lg-sd of 0.35).

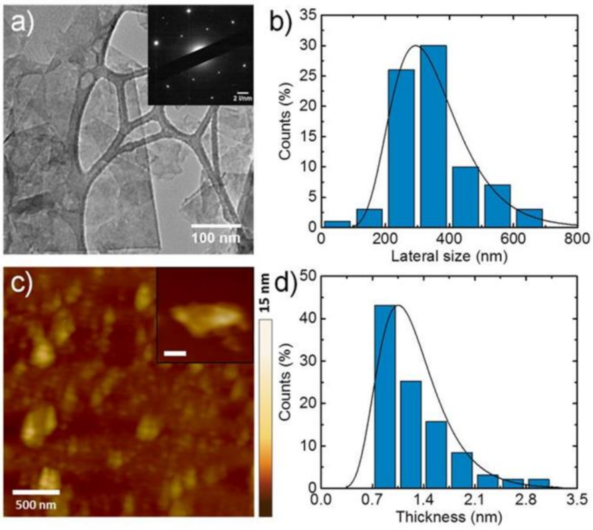

Figure 3.1. Morphological characterization of graphene dispersion in 1,3-dioxolane. (a) TEM image of selected graphene flakes; in the upper inset, the electron DP image of graphene flakes is depicted. (b) Statistical analysis from TEM images of the flakes lateral size. (c) AFM image of graphene flakes cast; the upper inset shows a higher magnification image of a graphene flake (scale bar corresponds to 100 nm). (d) Statistical analysis of the flake thickness. A total of ~ 100 flakes per sample have been evaluated to perform the statistical analyses. Adapted from [47].

Figure 3.2 shows the Raman spectroscopy results obtained investigating graphene dispersion in 1,3-dioxolane, where a representative Raman spectrum is depicted in Figure 3.2a. The Raman fingerprints of graphene are the G (~1580 cm^{-1}) and 2D (~2700 cm^{-1}) peaks [165–168]. If graphene flakes have defects, a D peak (~1350 cm^{-1}) also appears.[165–168] The G peak corresponds to the E_{2g} phonon at the Brillouin zone centre.[166] The D peak is due to the breathing modes of sp^2 rings and requires defects for its activation, the 2D peak is the second order of the D peak and is always visible, even without the presence of defects.[169,170] Statistical analysis shows 2D peak position (Pos(2D)) (Figure 3.2b) in the 2688 – 2700 cm^{-1} range. The analysis of 2D peak in position, width (full width at half maximum, FWHM, Figure 3.2c) and intensity (respect to the G peak, I_{2D}/I_G, Figure 3.2d), gives information about the numbers of layers of the graphene flakes [165–167]. The FWHM (2D) is in average ~70 cm^{-1}, while the I_{2D}/I_G ratio is higher than 0.5, which represents the reference value of graphite [165]. These results suggest that the dispersion is composed by a combination of both single (SLG) and few-layer graphene (FLG) flakes [37,167], in agreement with the AFM data reported. The

I_D/I_G ratio, which gives information about the presence of defects [37,165,166], is in the range 0.6 – 1.6 (Figure 3.2e), but the lack of correlation between I_D/I_G and FWHM(G) (Figure 3.2f) proves that these defects are related to the edges of sub-micrometre flakes, according to the TEM analysis, rather than to the presence of structural defects [37,169].

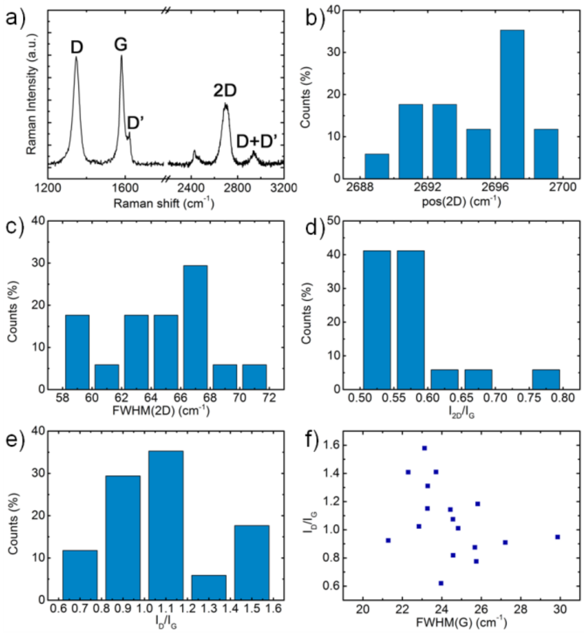

Figure 3.2. (a) Representative Raman spectrum of graphene flakes dispersed in 1-3 dioxolane. (b – f) Statistical analysis on the acquired Raman spectra ($<N_{RAMAN}>$ = 15): (b) Pos(2D), (c) FWHM(2D), (d) I_{2D}/I_G, (e) I_D/I_G, and (f) I_D/I_G as a function of FWHM(G). A total of 15 spectra have been acquired to perform the statistical analyses. Adapted from [47].

3.1.2 Characterization of *h*-BN flakes obtained by environmentally friendly sonication-assisted LPE

As discussed in section 1.2.1, for many 2D crystals suitable solvents for exfoliation, such as N-methyl-2-pyrrolidone (NMP) [1,35,39], dimethylformamide (DMF) [1,35,39], and ortho-dichlorobenzene (oDCB) [1,35,39,171], have surface tension in the 35 – 40 mN m^{-1} range [1,35]. Unfortunately, the majority of these solvents have high boiling points, *i.e.* more than 150 °C [26], experiencing also toxicological issues [1]. Pure water, due to its surface tension value (72 mN m^{-1}) [137], is generally not suitable for the dispersion of 2D-crystals [1]. In fact, although a few attempts for its use in a LPE process have been undertaken [172,173], the achieved concentrations are very low compared to the aforementioned organic solvents. In fact, ~ 0.1 mg mL^{-1} has been reported for the case of *h*-BN with 25h sonication time [172] and ~ 0.0065 mg mL^{-1} and ~ 0.018 mg mL^{-1} in the case of graphene and *h*-BN, respectively, by using temperature control during the ultra-sonication process [173]. As for example, it has been shown that the stability of exfoliated SLG/FLG flakes in pure water depends on the balance of repulsive (electrostatic, due to ion absorption) and attractive (van der Waals and hydrophobic interactions) forces [174]. Attractive forces intensify with the increase of the layers number, thus FLG flakes are less stable in water with respect to SLG ones [174]. Exfoliation yield, defined as the ratio between the weight of dispersed flakes and that of the starting bulk material [26], in water can be increased using additives, such as surfactants [51], which stabilizes exfoliated flakes against re-aggregation [51,175–177]. Therefore, I carried out the exfoliation of bulk *h*-BN powder in a water/surfactant solution, selecting Kolliphor® P188 as a surfactant. Kolliphor® P188, also referred as Pluronic® F68 or Lutrol® F68, according to different suppliers, is a triblock copolymer of the family of poloxamers [178,179] composed by a hydrophobic poly(propylene oxide) (PPO) central chain, that is attracted to the *h*-BN basal plane through hydrophobic interactions [177], surrounded by two hydrophilic poly(ethylene oxide) (PEO) chains, which stabilize the exfoliated flakes by steric hindrance [177]. After the exfoliation process, a heterogeneous dispersion of *h*-BN flakes is obtained. Then, the exfoliated *h*-BN flakes have been sorted by aspect ratio by means of SBS [1,47,59,60] using a cascade centrifugation [61], obtaining two population of flakes with different morphology, *i.e.* lateral size and thickness.

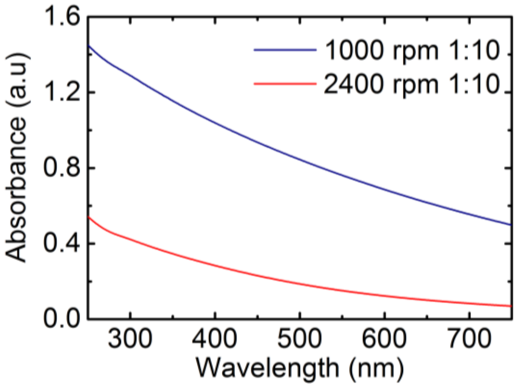

Figure 3.3. Extinction spectra of *h*-BN flakes in water/surfactant solution, diluted 1:10, after the ultra-centrifugations. Blue curve: supernatant after ultra-centrifugation at 1000 rpm (200 *g*); red curve: supernatant after ultra-centrifugation at 2400 rpm (1000 *g*).

Firstly, to assess the effectiveness of exfoliation in a water/surfactant solution, the concentration of the dispersed *h*-BN flakes was evaluated. The measured extinction, or absorbance, (Σ) is correlated to the concentration of the 2D-crystal flakes by the Lambert-Beer law: $\Sigma = \varepsilon l c$, where l [m] is the light path length, c [g L^{-1}] is the concentration of dispersed flakes, and ε [L g^{-1} m^{-1}] is the extinction coefficient. The extinction coefficient for *h*-BN has been calculated by Coleman and co-workers to be 2367 mL mg^{-1} m^{-1} at 300 nm wavelength [35]. Extinction spectra of the collected supernatants after the ultra-centrifugation are shown in Figure 3.3. The calculated concentration of *h*-BN flakes is therefore 0.62 g L^{-1} after the first ultra-centrifugation step (red curve in Figure 3.3) and 0.19 g L^{-1} after the second one (blue curve in Figure 3.3).

In order to exploit the solution blending technique for the production of the composite, both polymer matrix and inorganic fillers have to be dispersed in the same solvent and mixed together [47,151]. Therefore, *h*-BN-s and *h*-BN-p flakes have been re-dispersed in 1,3-dioxolane, the solvent used for dissolving the PC matrix, and their aspect ratio is evaluated measuring lateral size and thickness of the flakes using TEM and AFM (Figure 3.4). Figure 3.4a and 3.4c show the representative transmission electron micrographs of *h*-BN-s and *h*-BN-p flakes, respectively, whereas the corresponding statistical analyses on lateral size are shown in Figure 3.4b and 3.4d. The statistics are fitted by a log-normal distribution [180] with a mode of lateral size peaked at 340 nm for *h*-BN-s flakes and 410 nm for *h*-BN-p flakes.

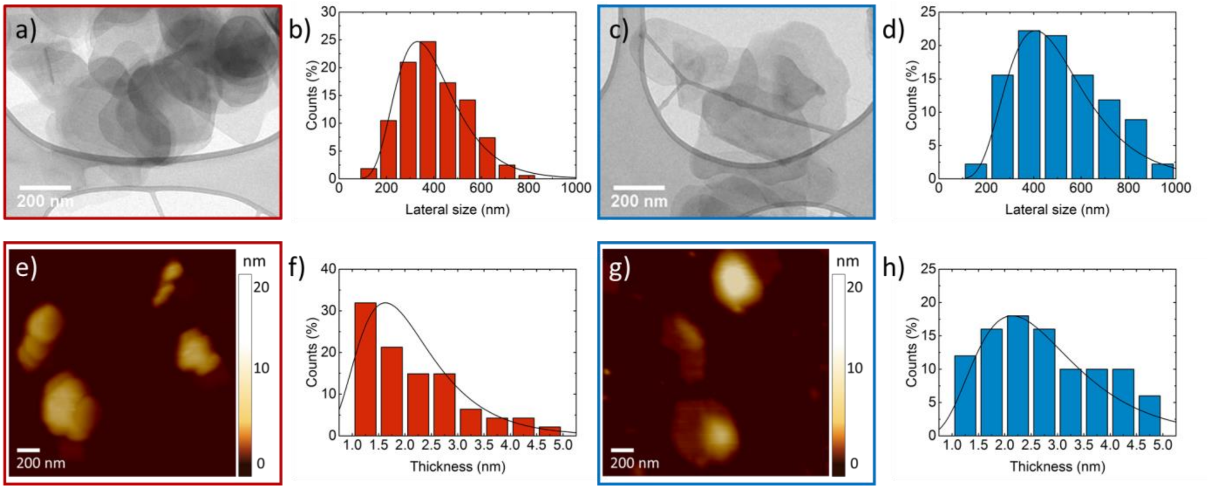

Figure 3.4. Morphological characterization of *h*-BN flakes. (a) Representative TEM micrograph of *h*-BN-s flakes re-dispersed in 1, 3-dioxolane; (b) statistical analysis from TEM micrographs of the *h*-BN-s flakes lateral size; (c) representative TEM micrograph of *h*-BN-p flakes re-dispersed in 1,3-dioxolane and (d) statistical analysis from TEM micrographs of the *h*-BN-p flakes lateral size; (e) representative AFM image of *h*-BN-s flakes re-dispersed in 1,3-dioxolane; (f) statistical analysis from AFM images of the *h*-BN-s flakes lateral size; (g) representative AFM image of *h*-BN-p flakes re-dispersed in 1,3-dioxolane and (h) statistical analysis from AFM images of the *h*-BN-p flakes lateral size. A total of ~ 100 flakes per sample have been evaluated to perform the statistical analyses.

In Figure 3.4e and 3.4g, the representative AFM images are shown for the *h*-BN-s and *h*-BN-p samples, respectively, and relative statistical analyses of thickness are shown in Figure 3.4f and 3.4h. The statistics are fitted by a log-normal distribution with a mode of thickness peaked at 1.6 nm for *h*-BN-s flakes and 2.3 nm for *h*-BN-p flakes. Liquid phase exfoliated *h*-BN single layer has an apparent height of ~ 1 nm on Si/SiO$_2$ wafer [35,172], whereas theoretical spacing between *h*-BN layers is 0.33 nm [14,172]. Based on the aforementioned considerations, we can estimate the average number of the layer for each sample from their AFM thickness being ~ 3 for *h*-BN-s and ~ 5 for the *h*-BN-p sample. Using the lateral size values obtained by TEM analysis, the calculated aspect ratios are, consequently, ~ 350 for *h*-BN-s and ~ 250 for *h*-BN-p.

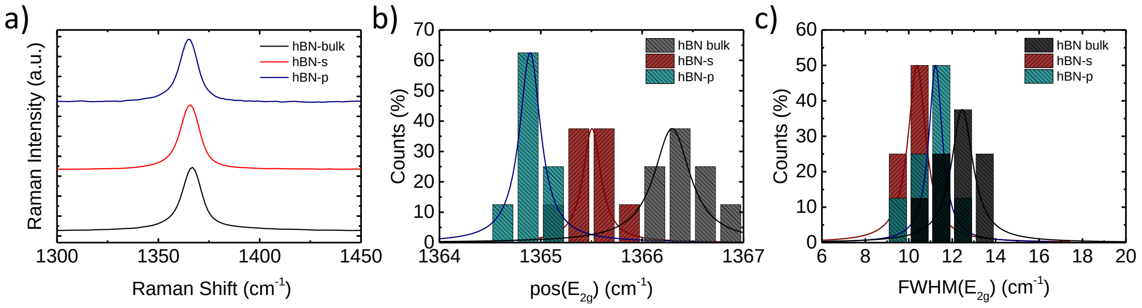

Figure 3.5. Raman spectroscopy on *h*-BN flakes. (a) Raman spectra of bulk *h*-BN (black), *h*-BN-s sample (red) and *h*-BN-p sample (blue); (b) statistical analysis on Pos(E$_{2g}$); c) statistical analysis on (c) FWHM(E$_{2g}$). A total of 15 spectra per sample have been acquired to perform the statistical analyses.

In spite of the similar structure to graphene, *h*-BN flakes do not show a Raman 2D band due to the lack of the Kohn anomaly, but Raman spectroscopy is still widely used to characterize *h*-BN flakes [181–184]. In-plane atomic displacements give origin to two Raman active E$_{2g}$ modes in *h*-BN [184], a low-frequency mode at 49 - 52.5 cm^{-1} [184,185], attributed to shear-type rigid layer mode of the crystal [184,185], and a high-frequency mode at 1366 cm^{-1} [182,184]. For example, in the case of *h*-BN monolayer produced by micromechanical cleavage (MC), a blue shift up to 4 cm^{-1} has been observed, due to the hardening of E$_{2g}$ phonons [182,184], with possible red shifts due to strain by the MC preparation method, which eventually further red shifts for the bilayer *h*-BN (by ~ 1 – 2 cm^{-1}) [182,184]. In Figure 3.5 is presented the Raman analysis carried out on the *h*-BN dispersions. Figure 3.5a shows representative spectra acquired on bulk *h*-BN (black trace), *h*-BN-s sample (red trace) and *h*-BN-p sample (blue trace) in which the E$_{2g}$ peaks around 1366 cm^{-1}. The statistical analysis on the shift in the position of high-frequency E$_{2g}$ peak (Pos(E$_{2g}$)) is reported in Figure 3.5b. The redshifts of exfoliated samples respect to the bulk *h*-BN reveals the formation of few-layer *h*-BN flakes [182,186], in which in particular Pos(E_{2g}) of *h*-BN-s sample centred at 1365 cm^{-1} is attributed to the presence of mostly bilayer and tri-layer flakes for liquid phase exfoliated *h*-BN [186], confirming the results of AFM microscopy. The red-shift in few-layer *h*-BN is attributed to the elongation of B-N bonds due to interlayer interactions that involve a softening of the phonons [182,184,186]. The FWHM of the E_{2g} peak (Figure 3.5c) reduces with the decrease of the flake thickness, starting from 12.5 cm^{-1} for the *h*-BN bulk powder to 11 cm^{-1} and 10 cm^{-1} for the *h*-BN-p and *h*-BN-s samples, respectively. This reduction in E_{2g} peak line-shape is consistent with a decrease in the superposition of multiple peaks due to a more homogeneity of the flakes size with respect the bulk powder, subsequent to the exfoliation and purification process [186].

3.1.3 Characterization of 2D crystals size selected by SBS

As aforementioned, LPE of bulk layered-materials is a cost-effective method to produce high-concentration of 2D crystals directly dispersed in a solvent [1,35]. However, the as-produced 2D crystals have a broad distribution of both thicknesses (from monolayer flakes to un-exfoliated material) and lateral size (from few nanometres to micrometres scale) [39] preventing to identify the impact of their aspect ratio for mechanical reinforcement. To overcome these issues, we prepared dispersions of 2D crystal, namely graphene, *h*-BN and WS_2 flakes, using LPE, tailoring their morphological properties and increase the content of monolayers by exploiting iterative ultra-centrifugation cascades [61] (see section 2.1.2 for details), a process still compatible with large-scale applications.

Figure 3.6 shows the TEM and AFM images of graphene flakes, as well as their statistical analyses. The five samples, prepared by using different g-forces, have five different surface area and thickness values. In particular, the 170g (sample FLG-1), 1000g (sample FLG-2), 4250g (sample FLG-3), 9500g (sample FLG-4), 17000g (sample FLG-5) ultra-centrifugation processes give around 0.078, 0.059, 0.052, 0.013, and 0.008 μm^2 for area, and 4.2, 3.8, 2.2, 2.1, and 0.9 nm for thickness, respectively. To further sort the samples (Figure 3.7) using cascade centrifugation steps by 170-4250-170g, 170-4250-170-170g, and 170-4250-170-170-170g, producing samples in Figure 3.7a, 3.7b and 3.7c, respectively. Because of the heavier mass, FLG flakes are removed in each step of the cascade, the resultant supernatants become eventually single-layer enriched, still having a similar surface area [61]. The area and thickness sizes distributions of the *h*-BN, and WS_2 flakes is depicted in Figure 3.8, and Figure 3.9, respectively. The 170g (sample *h*-BN-1), 1000g (sample *h*-BN-2), and 4250g (sample *h*-BN-3) ultra-centrifugation processes give flakes of 0.062, 0.041, and 0.039 μm^2 area, and 1.5, 1.4, and 1.1 nm thickness, respectively, for *h*-BN flakes. For what concern WS_2, the 170g (sample WS_2-1), 1000g (sample WS_2-2), and 4250g (sample WS_2-3) ultra-centrifugation processes give flakes of

0.009, 0.015, and 0.008 μm^2 for the area, and 2.8, 2.2, and 1.9 nm for the thickness, respectively. Table 3.1 summarises surface area (*A*), *t*, and *A/t*^{2} morphological properties for all samples, whereas a graphical summary of the morphological properties of the 2D crystals obtained by the size selection is in Figure 3.10.

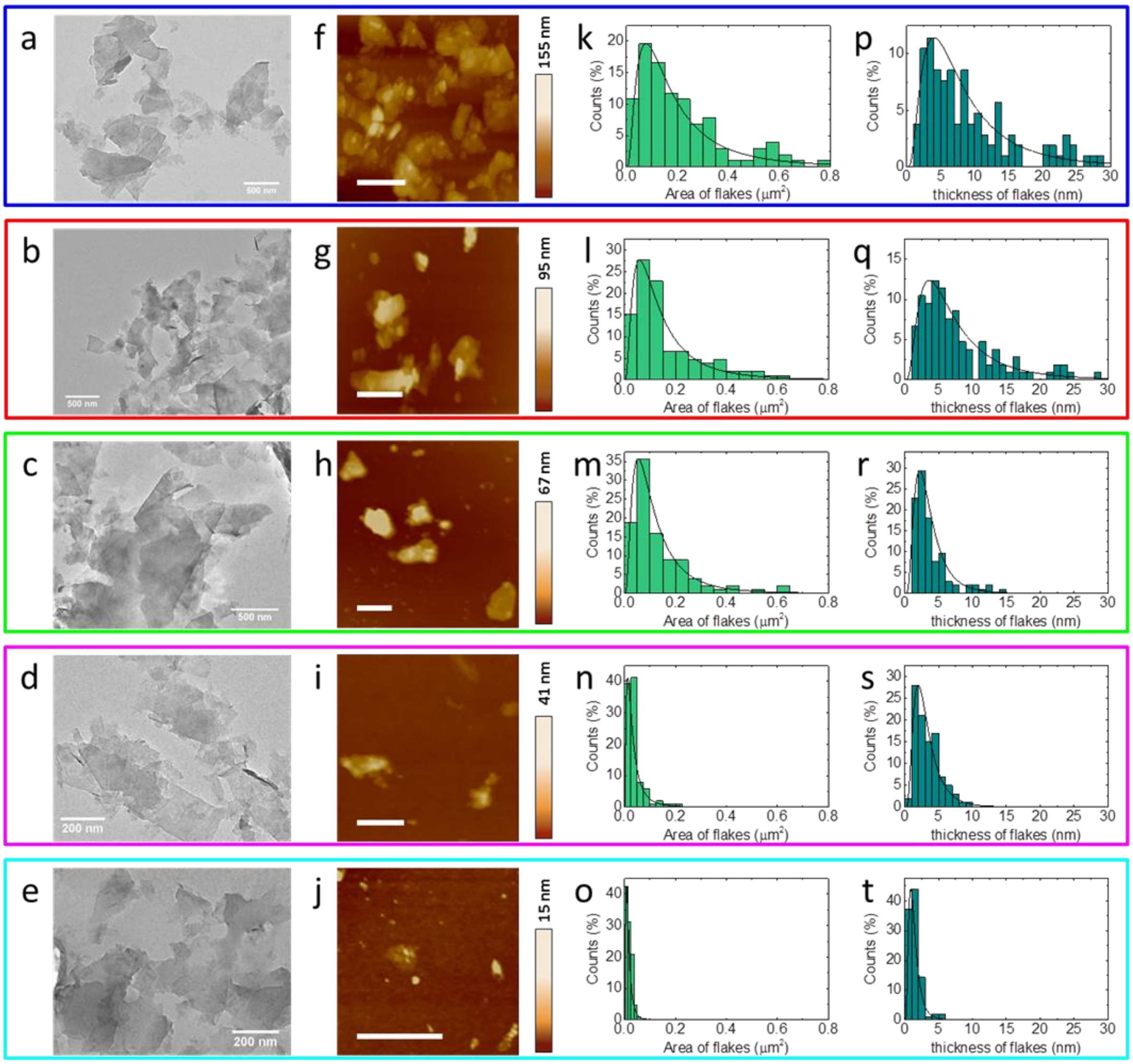

Figure 3.6. Morphological characterization of the graphene flakes obtained by tuning ultra-centrifugation g-forces. a-e) TEM images, and (f-j) AFM images of selected flakes (scale bars correspond to 500 nm). Statistical analysis of surface area (k-o) and thickness (p-t) of different graphene flake dispersions. Blue box: FLG-1 sample (170g), red box: FLG-2 sample (1000g), green box: FLG-3 sample (4250g), magenta box: FLG-4 sample (9500g), cyan box: FLG-5 sample (17000g). A total of ~ 100 flakes per sample have been evaluated to perform the statistical analyses.

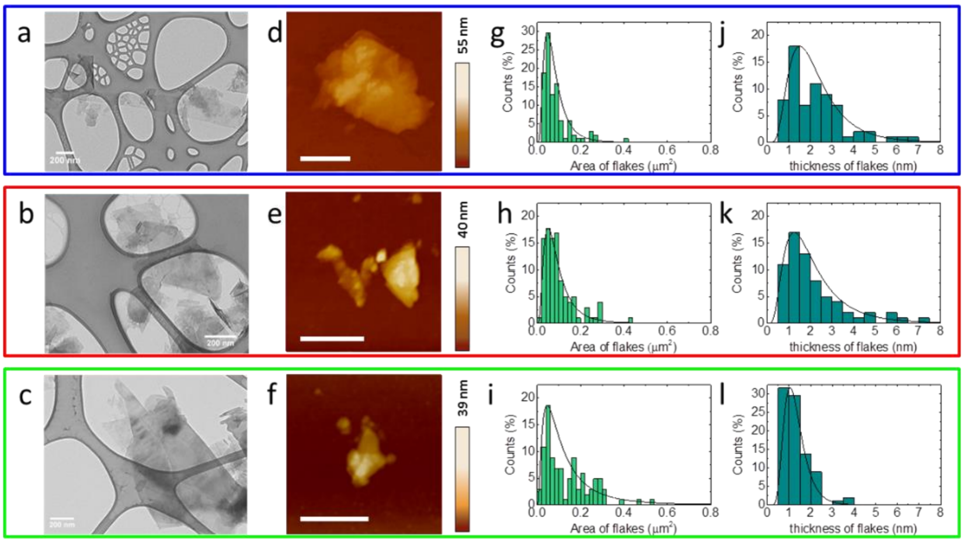

Figure 3.7. Morphological characterization of the 4250g cascade ultra-centrifugation-related graphene flakes. a-c) TEM images, and (d-f) AFM images of selected flakes (scale bars correspond to 500 nm). Statistical analysis on (g-i) surface area and (j-l) thickness of different graphene flakes dispersions. Blue box: FLG-6 sample (170-4250-170g), red box: FLG-7 sample (170-4250-170-170g), green box: FLG-8 sample (170-4250-170-170-170g). A total of ~ 100 flakes per sample have been evaluated to perform the statistical analyses.

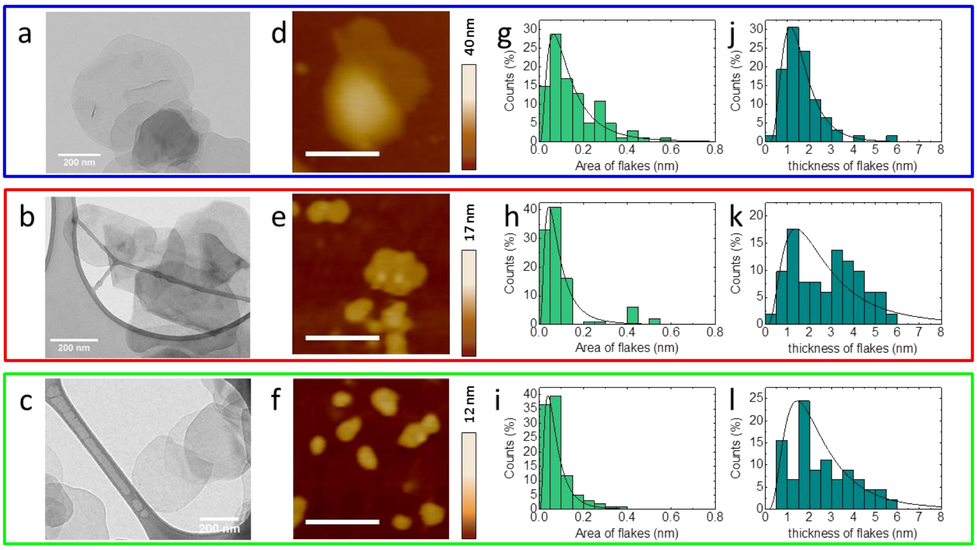

Figure 3.8. Morphological characterization of the *h*-BN flakes. a-c) TEM images, and (d-f) AFM images of selected *h*-BN flakes (scale bars correspond to 500 nm). Statistical analysis on (g-i) area and (j-l) the thickness of the *h*-BN flakes dispersions. Blue box: *h*-BN-1 sample (170g), red box: *h*-BN-2 sample (1000g), green box: *h*-BN-3 sample (4250g). A total of ~ 100 flakes per sample have been evaluated to perform the statistical analyses.

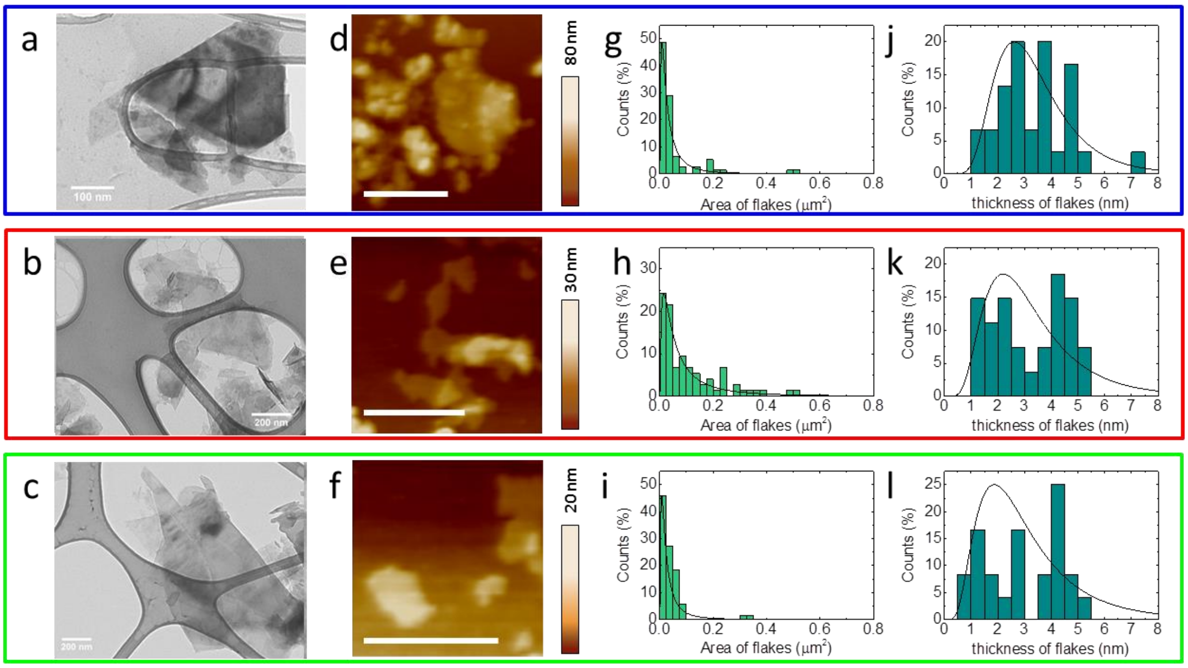

Figure 3.9. Morphological characterization of the WS_2 flakes. a-c) TEM images, and (d-f) AFM images of selected WS_2 flakes (scale bars correspond to 500 nm). Statistical analysis on (g-i) area and (j-l) the thickness of the WS_2 flakes dispersions. Blue box: WS_2-1 sample (170g), red box: WS_2-2 sample (1000g), green box: WS_2-3 sample (4250g). A total of ~ 100 flakes per sample have been evaluated to perform the statistical analyses.

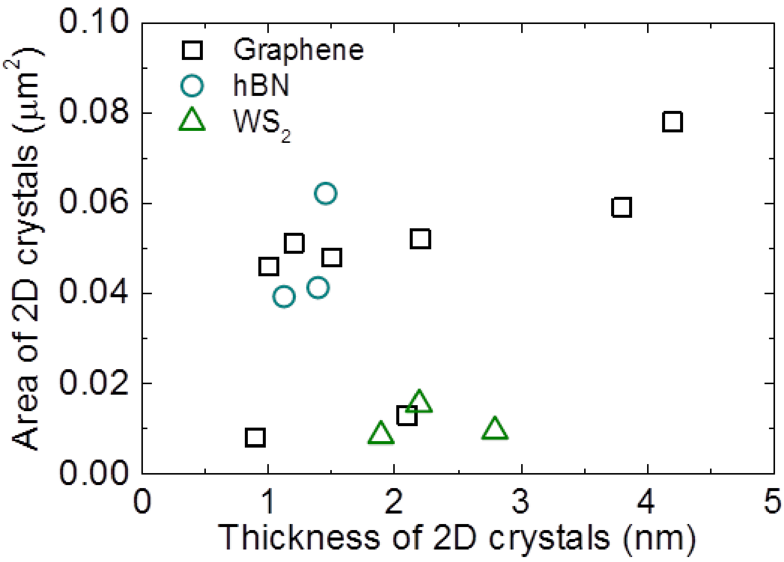

Figure 3.10. Summary of the measured surface area *vs.* thickness of exfoliated 2D crystals flakes.

Table 3.1. The *A*, *t*, and A/t^2 morphological properties for all LPE produced 2D crystal samples.

sample	***A*** (μm^2)	***t*** (nm)	$\boldsymbol{A/t^2}$
FLG-1	0.078	4.2	4421.8
FLG-2	0.059	3.8	4085.9
FLG-3	0.052	2.2	10743.8
FLG-4	0.013	2.1	2947.8
FLG-5	0.008	0.9	9876.5
FLG-6	0.046	1.0	46000.0
FLG-7	0.051	1.2	35416.7
FLG-8	0.048	1.5	21333.3
***h*-BN-1**	0.062	1.5	29086.1
***h*-BN-2**	0.041	1.4	20918.4
***h*-BN-3**	0.039	1.1	30542.7
WS_2-1	0.009	2.8	1148.0
WS_2-2	0.015	2.2	3099.2
WS_2-3	0.008	1.9	2216.1

X-ray photoelectron spectroscopy survey spectra (a) and high-resolution XPS spectra of FLG (b), *h*-BN (c, d), and WS_2 (e, f) samples are shown in Figure 3.11. While, pristine graphene basal-plane lattice (C 1s peak at a binding energy of 284.0 eV) exhibits pure sp^2 hybridization, the defects, edges, and functional groups alter the sp^2 hybridization [187,188] (Figure 3.11b). The high-resolution *h*-BN sample XPS spectra are displayed in Figure 3.11c and 3.11d, showing individual elements of nitrogen and boron, fitting the N 1s (at 398.0 eV) and B 1s (at 192.5 eV) peaks [189] by single Lorentzian components. The high resolution XPS spectra of S 2p (at 162.5 and 163.8 eV), and W 5p (at 38.4 eV) and 4f (at 35.0, and 32.8 eV) orbitals [190], originated by WS_2 sample, are depicted in Figure 3.11e and 3.11f. The W 4f orbital splits to two sets of doublets corresponding to W^{6+} and W^{4+} oxidation states [190,191]. The presence of both tungsten oxidation states indicates a mild oxidation of the tungsten ions and matches with previously reported work [191].

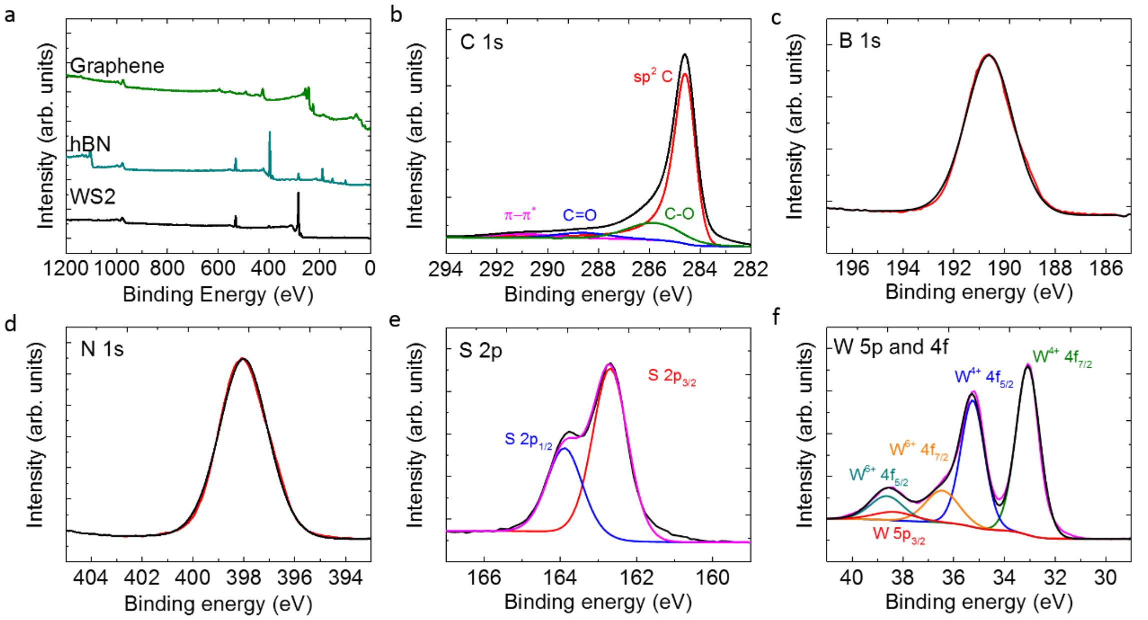

Figure 3.11. XPS analysis of 2D crystals. a) XPS survey spectra of graphene, *h*-BN, and WS_2. High-resolution XPS spectra of (b) graphene, (c-d) *h*-BN, (e-f) WS_2 samples. The sub-orbitals are labelled in all cases.

3.2 2D crystals obtained by WJM-assisted LPE

Among the several liquid-phase approaches for exfoliation, micro-fluidization is the most similar to WJM, in that the whole fluid is forced through a spatial region where the flow becomes turbulent [155,192,193]. In the micro-fluidization case, such region is a microchannel, while in the WJM it corresponds to the channel junctions before and after the nozzle. In this region, turbulent flow results in a high-shear rate [155,192,193], *i.e.* velocity gradient orthogonal to the flow direction.

The resulting shear stress applied to the dispersed flakes induces sliding of the 2D crystal planes, initiating the exfoliation process. For graphene, it has been shown that shear rates in excess of 10^4 s^{-1} are sufficient for the exfoliation process to occur [38]. These values can be achieved through the laminar flow produced by shear-mixers [38], and, more efficiently, in the turbulent flow of micro-fluidizers [155] and WJMs.

A most noticeable difference between the exfoliation process in the WJM and other LPE methods aforementioned is the large pressure drop in time experienced by the crystallites as the dispersion flows through the nozzle, specifically through the disk B. In the following we attribute the high production yield of the WJM to a geometry-induced enhancement of the shear exfoliation rate since we must rule out that the large pressure drop favours an alternative exfoliation pathway.

3.2.1 Characterization of graphene flakes exfoliated by WJM-assisted LPE

In the case of 100+ mesh graphite, the 0.3 mm nozzle diameter has been chosen to start the exfoliation process. Though there is not a preferential ratio nozzle-crystal size, and in principle the exfoliation could be performed with crystals larger than the nozzle diameter, however, it was experimentally observed that starting the exfoliation of such large crystallites with smaller nozzles (<0.3 mm) may cause system clogging. Moreover, it has been noticed that also the reduction of the piston-pressure causes system clogging and increases considerably the processing time. According to this consideration, several combinations with different nozzle diameters (0.30, 0.20, 0.15 and 0.10 mm) are tested. Graphite exfoliation is achieved using the following nozzle diameters sequence: 0.30 mm, 0.15 mm, and twice 0.10 mm. Considering all the four passes, the effective time required to process 10 mL of graphite/NMP (concentration of 10 g L^{-1}), is 15.3 s.

For what concerns the exfoliation of graphite, TEM analysis indicates that the flake lateral size mode decreases from 149 μm (starting graphite material) to 1 μm (lg-sd: 0.53), 0.850 μm (lg-sd: 0.83), and 0.460 μm (lg-sd: 1.18) for WJM0.30, WJM0.15, and WJM0.10, respectively (see Figure 3.12a-c). The lateral-size distribution statistics are reported in the inset to Figure 3.12a-c, obeying a log-normal distribution, which is the typical distribution for fragmented systems [180]. The number of layers in the WJM0.10 sample can be directly visualized on HRTEM in a bent-flake edge [194]. Figure 3.12d shows a representative bent flake with three layers, demonstrating that the WJM0.10 is composed by FLG flakes (other images of representative bent flakes are shown in ESI). At higher magnification (Figure 3.12e) the honeycomb carbon lattice can be observed. The upper inset shows the lattice parameter 0.247 nm of graphite (hexagonal, $p6_3/mmc$, space group 194, with lattices parameters $a = b = 2.4$ Å, $c = 6.70$ Å) [195] with the indexed fast Fourier transform given in the lower inset. Figure 3.12f shows the AFM image of an exfoliated sample WJM0.10, giving a thickness mode of 1.6 nm, demonstrating the production of mainly FLG, *i.e.* 15% of flakes thinner than 1.5 nm (single-layer graphene flakes thicknesses have been reported ranging from 0.4 to 1.5 nm) [164] 54% in the 1.5 to 5.0 nm range, and 31% thicker than 5 nm (see inset to Figure 3.12f).

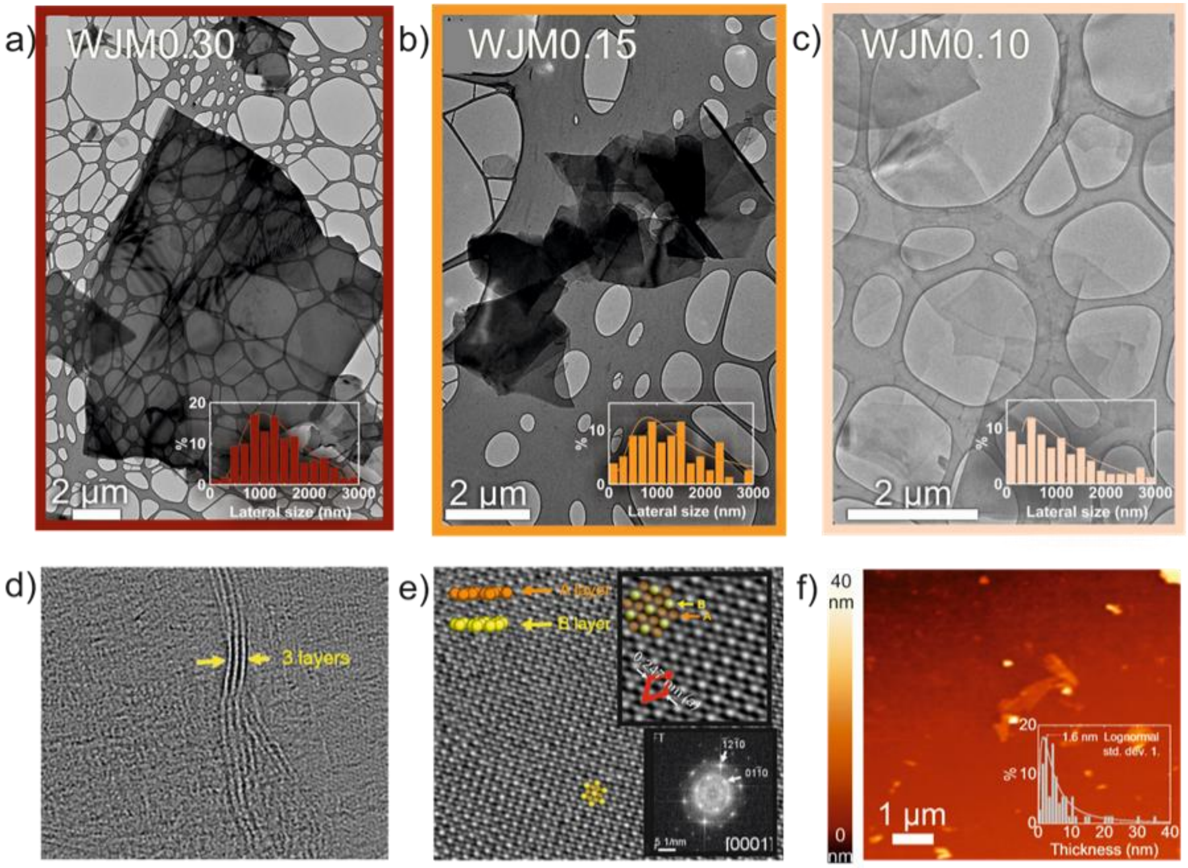

Figure 3.12. TEM images of WJM0.10 (a), WJM0.15 (b) and WJM0.30 samples (c), with the corresponding lateral size distributions in the insets. (d) HRTEM image of a bended three-layer graphene, from sample WJM0.10. (e) HRTEM image of a WJM0.10 flake showing the A-B stacking, depicted by orange and yellow circles on the image. Inset in the upper right corner reports a zoomed area on the same flake where the red diamond indicates the hexagonal unit cell of graphite. The bottom right inset shows the corresponding Fourier transform with the indexed reflections from crystalline planes. (f) AFM image of graphene flakes with the thickness distribution given in the inset. A total of ~ 100 flakes per sample have been evaluated to perform the statistical analyses. Adapted from [154].

The quality of the exfoliated material, in terms of crystalline integrity, is analysed by Raman spectroscopy. Figure 3.13a shows the Raman spectra of the samples WJM0.30, WJM0.15, WJM0.10, and graphite for comparison. All spectra are normalised to the G peak intensity. The intensity variations of the D and D' bands are related to an increase of edge or in-plane defects [168,196]. The statistical analysis shows that I(D)/I(G) ranges from 0.03 to 0.6 for WJM0.30, then the range varies to 0.1 – 1 and 0.1 – 1.2, for WJM0.15 and WJM0.10 samples, respectively (Figure 3.13b). On the contrary, FWHM(G) (Figure 3.13c) are not significantly affected by the nozzle diameter, ranging in all cases from ~14 to ~25 cm^{-1}, with a mode at ~19 cm^{-1}. The plot of I(D)/I(G) *vs.* FWHM(G) in

Figure 3.13d shows that the linear correlation between these parameters becomes scattered (not correlated) when the nozzle diameter is reduced. In fact, the linear correlation is also reduced from 0.748 to 0.289 for WJM0.30 to WJM0.10. This result suggests that the WJM process homogenises the sample by increasing the number of flakes smaller than the laser spot size (1µm). This is in agreement with the TEM measurements.

The normalised intensity ratios $I(2D_1)/I(G)$ *vs.* $I(2D_2)/I(G)$ give an insight on the flake thickness (Figure 3.13e). In general, for graphite, the intensity of $2D_2$ peak [$I(2D_2)$] is roughly double compared to the intensity of $2D_1$ peak [$I(2D_1)$] [168]. Furthermore, the intensity ratio [$I(2D_2)/I(2D_1)$] decreases as the flake thickness is reduced [165,166], until the 2D band can be fitted by a single Lorentzian, highlighting that the flakes are electronically decoupled. The dashed line in Figure 5e represents the multilayer condition ($\sim$5 layers) [197] [$I(2D_1)/I(G) = I(2D_2)/I(G)$] separating the data set, while the points below the line [$I(2D_1)/I(G) < I(2D_2)/I(G)$] are considered graphitic flakes, and the points above the line [$I(2D_1)/I(G) > I(2D_2)/I(G)$] are considered FLG and SLG [165,166]. It is noteworthy that a single Lorentzian component is achieved only for the sample WJM0.10, indicating that the graphite processing through the 0.10 mm nozzle allows getting graphene flakes with electronically decoupled layers. Noteworthy, for graphene flakes obtained by LPE, it is uncommon to find such large intensities for the 2D band, even for SLG [37,51,198,199]. Additionally, the evolution of the 2D band when graphite is processed through the nozzles indicates an effective reduction of flake thickness [165,166].

Figure 3.13f presents the high-resolution XPS C 1s spectrum of WJM0.10. The C 1s spectrum is characterized by the typical asymmetric profiles of graphitic carbon-based materials [187]. The spectrum can be decomposed into different components typical of graphite: a main peak at 284.4 eV for sp^2 carbon [200,201] with the corresponding feature due to π-π^* interactions at 290.8 eV [202], as well as a second peak at 284.8 eV for sp^3 carbon [200,201], probably due to flake edges and solvent residual.

The TEM, AFM, and Raman results demonstrate the successful exfoliation of the layered crystals. The as-produced exfoliated samples consist of a mixture of flakes of different thicknesses, as discussed above. The thick flakes in the sample can be removed by SBS, thus promoting sample enrichment with thin flakes.

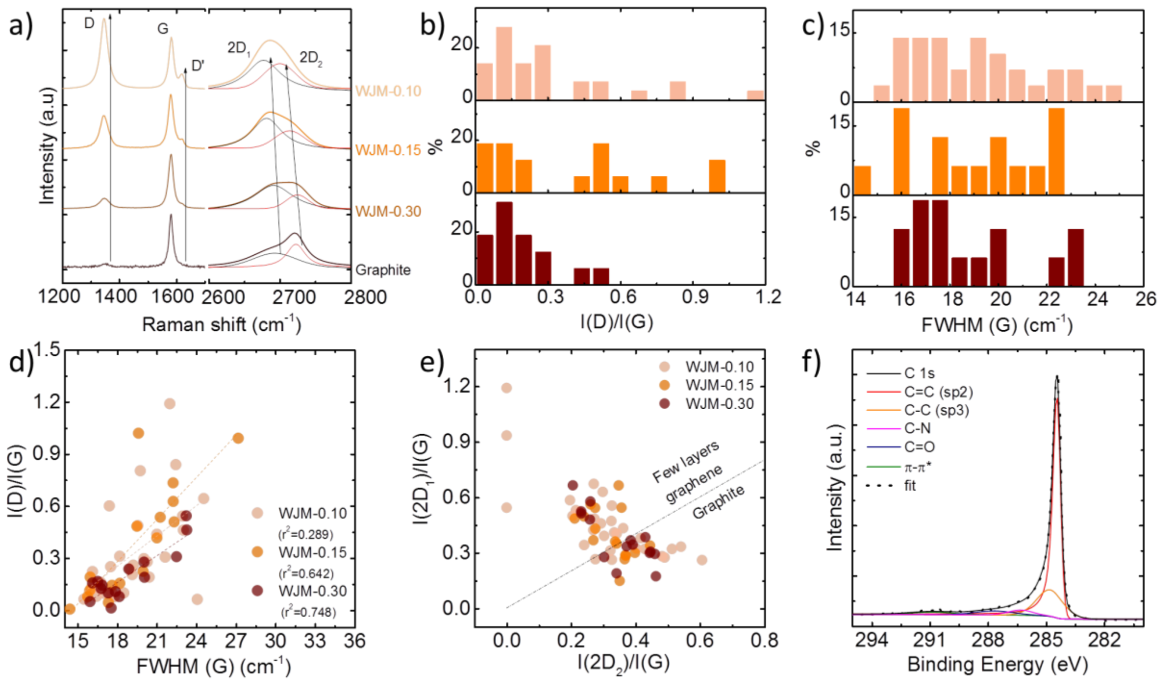

Figure 3.13. (a) Raman spectra of the samples WJM0.10, WJM0.15, and WJM0.30 in pink, orange, and wine, respectively, and graphite spectrum (in black), for the sake of comparison. The black arrows indicate the increase in the integral intensity of the D and D’ peaks and a shift for the $2D_1$ and $2D_2$ peaks when the samples are processed from graphite to WJM0.10. The statistical analyses of the I(D)/I(G) and FWHM(G) of the processed samples are shown in (b) and (c). (d) FWHM(G) vs. I(D)/I(G) and their linear correlation (dashed line) and (e) the normalised integral intensities of the peaks $2D_1$ and $2D_2$ showing the distribution of FLG and graphite. The dashed line represents the condition where $I(2D_1)/I(G) = I(2D_2)/I(G)$. (f) XPS C 1s spectrum of WJM0.10. A total of 30 spectra per sample have been acquired to perform the statistical analyses. Adapted from [154].

The initial *C* of the sample WJM0.10 is confirmed by OES to be ~ 10 g L^{-1} (Figure 3.14a, orange line). After centrifugation, the value of *C* of flakes in dispersion decreases to 1.13 g L^{-1} and 0.31 g L^{-1} for 500 *g* (dark blue line) and 3000 *g* (light blue line), respectively (Figure 3.14a). The physical changes of the WJM0.10 samples after centrifugation are also evident in Raman spectroscopy (Figure 3.14b), from the changes of the normalised intensity ratios $I(2D_1)/I(G)$ vs. $I(2D_2)/I(G)$ band (Figure 3.14c). For the WJM0.10 sample, the points satisfying the condition $I(2D_1)/I(G) < I(2D_2)/I(G)$ (flakes with > 5 layers) decrease from 37% to 7%, for the centrifuged samples. Conversely, the points having $I(2D_2)/I(G) \approx 0$ increase from 10%, for the as-produced WJM0.10 to 40% for the sample centrifuged at 500 *g*, and to 57% for the sample centrifuged at 3000 *g*. These results indicate that the SBS is an effective process to separate graphite-like flakes from FLG.

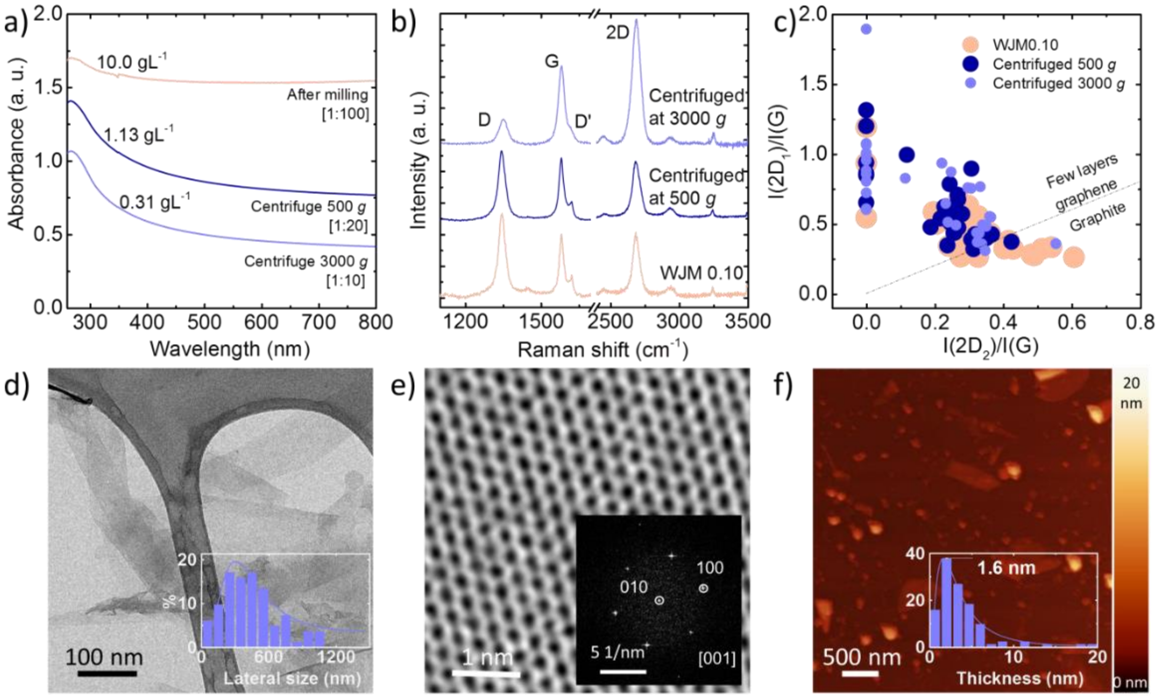

Figure 3.14. (a) Optical absorption spectroscopy and (b) Raman spectra of the sample WJM0.10 and purified after centrifugation at 500 *g* and 3000 *g*. (c) The normalised integral intensities of the 2D$_1$ and 2D$_2$ peaks show the distribution of FLG and graphite in the purified sample at 3000 *g* and, as a comparison, the as-produced WJM0.10 sample. (d) TEM image of the centrifuged sample at 3000 *g*, the inset shows the lateral size distribution. (e) HRTEM image of a flake reported in (d) and its corresponding Fast Fourier Transform of the flake with the indexed reflections from crystalline planes in the inset. (f) AFM image of the sample WJM0.10 and the thickness distribution in the inset. Adapted from [154].

Finally, in order to gain further insight into the quality of the purified samples, we additionally analysed the sample centrifuged at 3000 *g* by TEM and HRTEM (Figure 6d-f). The statistical lateral size distribution, shown in the inset to Figure 3.14d, peaks at 350 nm. It is worth noting that the ln-sd decreases from 1.18 for WJM0.10 to 0.55, meaning that the centrifuged sample has a narrower lateral size distribution than the WJM0.10 [180]. The HRTEM, Figure 6e, of one flake shows the characteristic honeycomb lattice of graphene. The corresponding Fast Fourier Transform (inset to Figure 3.14e) suggests the absence of multi-layered structures or stacked flakes. An AFM image of the sample centrifuged at 3000 *g* is shown in Figure 3.14f. The statistical thickness distribution has a maximum population peaked at 1.6 nm.

In summary, these results indicate that the WJM is an ideal tool to produce gram-scale quantities of FLG flakes, and also SLG, with the use of purification procedures.

3.2.2 Characterization of other 2D crystals exfoliated by WJM-assisted LPE

For the exfoliation of MoS_2, WS_2, and *h*-BN, their crystallite sizes (particle size < 2 µm) allow the direct use of the 0.10 mm nozzle, giving a processing time of 4.5 s per 10 mL of sample.

The MoS_2, WS_2, and *h*-BN flake sizes are also determined by TEM, with the images of the exfoliated flakes shown in Figure 3.15a-c. The lateral-size statistical distribution of the flakes, shown in the insets, displays an average size of 380, 500, and 340 nm for MoS_2, WS_2, and *h*-BN, respectively. The thickness of the processed flakes is analysed by AFM (Figure 3.15d-f). The insets to each AFM image report the statistical distribution of the thicknesses, showing a thickness mode at 6.0, 4.5, and 2.4 nm for MoS_2, WS_2, and *h*-BN, respectively.

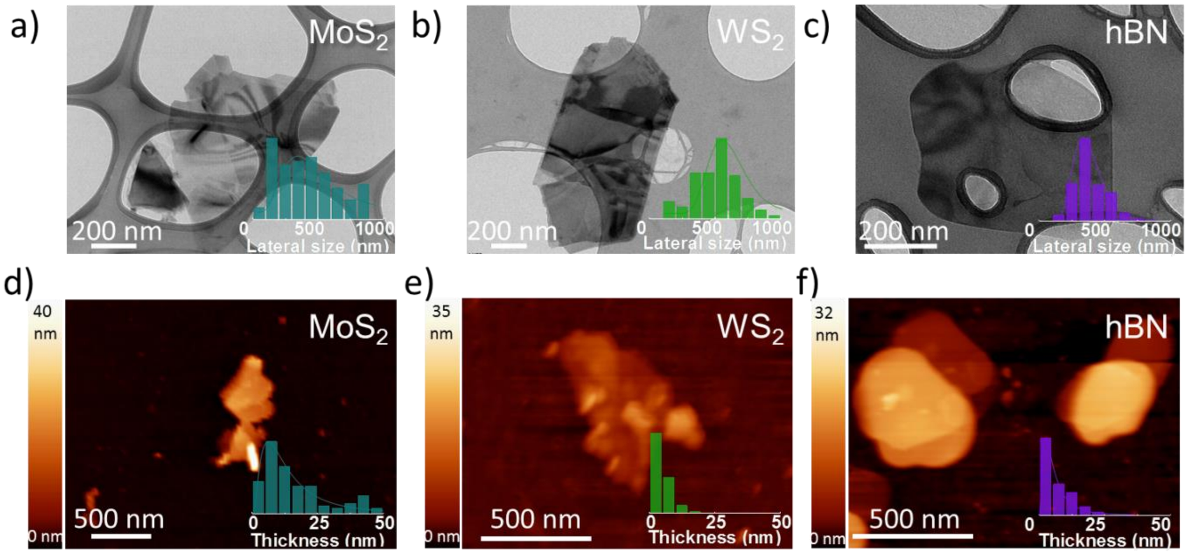

Figure 3.15. TEM images of exfoliated MoS_2 (a), WS_2 (b), and *h*-BN (c) flakes, respectively, and their corresponding statistical lateral size distributions are shown in the insets. AFM images of exfoliated flakes of MoS_2 (d), WS_2 (e), and *h*-BN (f) flakes respectively. Their corresponding thickness distributions are shown in the insets. A total of ~ 100 flakes per sample have been evaluated to perform the statistical analyses. Adapted from [154].

Raman spectroscopy is also used to analyse the physical changes on the exfoliated MoS_2, WS_2, and *h*-BN samples. The Raman spectra of bulk and exfoliated MoS_2, WS_2, and *h*-BN are shown in Figures 3.16a-c, and their corresponding vibrational modes are illustrated in the insets to the corresponding figures. The Raman spectrum of bulk MoS_2 consists of two active peaks, the first one (E_{2g}), at 379 cm^{-1}, corresponds to the mode involving the in-plane vibration of Mo and S atoms [203,204]. The second one (A_{1g}), at 405 cm^{-1}, is due to out-of-plane vibrations [203,204]. The typical Raman spectra of exfoliated MoS_2 show a shift of the E_{2g} and A_{1g} peaks, such that the distance between the peaks goes from 26 cm^{-1} for the bulk case to 19 cm^{-1} in the monolayer limit [203,204]. The MoS_2 Raman spectrum of the exfoliated samples is reported in Figure 3.16a, blue line. The spectrum shows a blue shift for both bands, E_{2g} (3 cm^{-1}) and A_{1g} (4 cm^{-1}), with respect to the bulk case. Similar results have been reported for exfoliated MoS_2 flakes [205,206].

The Raman spectrum of WS_2 consists mainly of three peaks: the E_{2g}, which corresponds to the mode involving the in-plane vibration of W and S atoms [207,208]; the A_{1g}, which is related to out-of-plane vibrations [207,208]; and the second-order longitudinal acoustic mode (2LA) at 350 cm^{-1} [207,208]. The integral intensity of the 2LA peak increases with the decreasing flake thickness [207,208]. The spectrum of exfoliated WS_2 (Figure 3.16b, green line) shows a 7-fold decrease of the integral intensity of the A_{1g} mode and a two-fold increase in the intensity of the 2LA phonon mode, due to the occurrence of a double resonance for exfoliated WS_2 flakes, in agreement with previous studies related with the exfoliation of WS_2 [207,208].

Lastly, the red-shift and the broadening of the E_{2g} peak of exfoliated *h*-BN (Figure 3.16c), compared to bulk material, suggests an effective exfoliation down to few-layers [182,186].

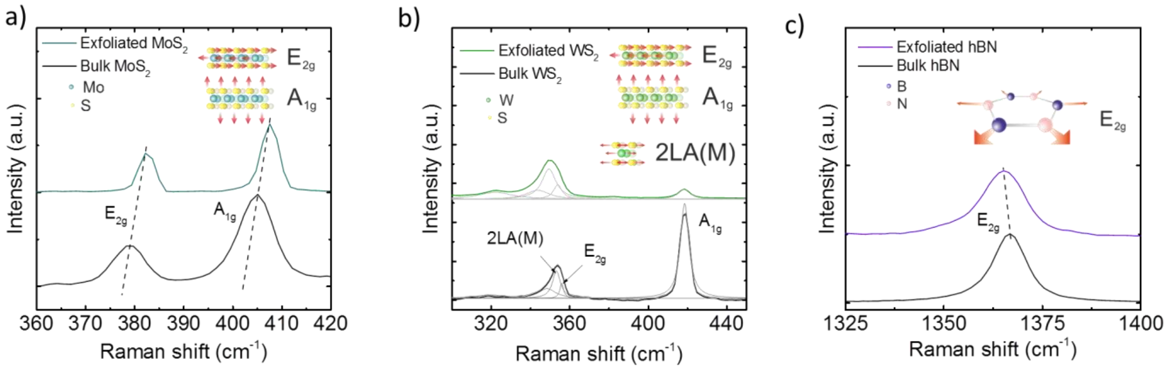

Figure 3.16. Raman spectra of the MoS_2 (a), WS_2 (b) and *h*-BN (c), compared with their bulk counterparts. The Raman active modes are illustrated as insets in each figure. A total of 15 spectra per sample have been acquired to perform the statistical analyses. Adapted from [154].

3.2.3 Characterization of samples WG and W*h*BN obtained by WJM-assisted LPE

In order to exploit the potentialities of 2D crystals produced by WJM-assisted LPE as fillers in polymer composites, the samples WG and W*h*BN have been produced, according to the protocol described in section 2.2.1. The sample WG has been obtained in the same way of the sample

WJM0.10, characterized in section 3.2.1, in fact, the results obtained by TEM, AFM and Raman spectroscopy are similar, evidencing the reproducibility of the WJM exfoliation technique. On the other hand, the sample W*h*BN was obtained using the *h*-BN bulk powder with a crystallite size of ~ 40 µm. This because the aim was to obtain as much larger exfoliated *h*-BN flakes to be used as filler, as evidenced by the importance of aspect ratio in the final properties of composites presented in section 1.3.

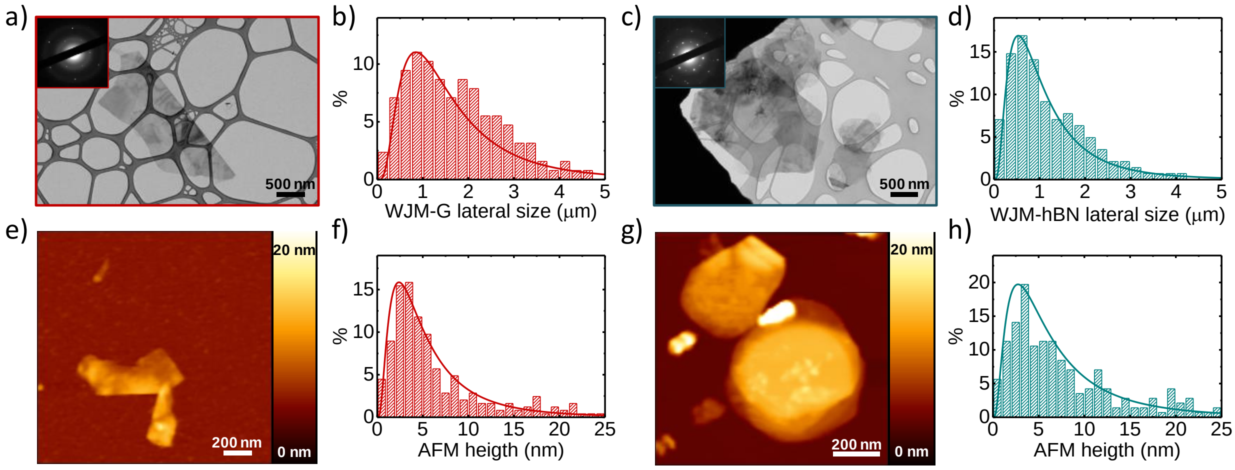

Figure 3.17. Morphological and structural characterization of WG and W*h*BN flakes. TEM images and relative lateral size distribution of samples WG (a-b) and W*h*BN (c-d); AFM images and relative thickness distribution of samples WG (e-f) and W*h*BN (g-h). A total of ~ 100 flakes per sample have been evaluated to perform the statistical analyses.

Representative TEM images of WG and W*h*BN are shown in Figure 3.17a and Figure 3.17c respectively, with top-left insets showing the diffraction patterns that demonstrate the crystallinity and structural integrity of both samples. The statistical analyses of the lateral size obey the log-normal distribution [180], reported in Figure 3.17b and Figure 3.17d. The flakes lateral size decreases from bulk values (~ 150 µm for graphite and ~ 40 µm for *h*-BN) to average values of 850 nm (ln-sd: 0.69) for WG and of 550 nm (ln-sd: 0.74) for W*h*BN, evaluated as the mode (or maximum population) of the log-normal distribution. Moreover, flakes with lateral sizes exceeding 1 µm are ~ 70% in the case of WG and ~ 50% in the case of W*h*BN, thus considerably larger than typical 2D crystal lateral size obtainable by sonication-assisted LPE methods, usually lower than 1 µm [46,47,57,79,209].

The flake thickness is investigated by AFM analysis (Figure 3.17e and Figure 3.17g, with statistical distributions in Figure 3.17f and Figure 3.17h), revealing mode heights of 2.4 and 2.8 nm for WG and W*h*BN flakes, respectively, with ~ 50% of flakes below 5 nm in both cases. Thus, WG and W*h*BN are mainly composed of single- and few-layer flakes.

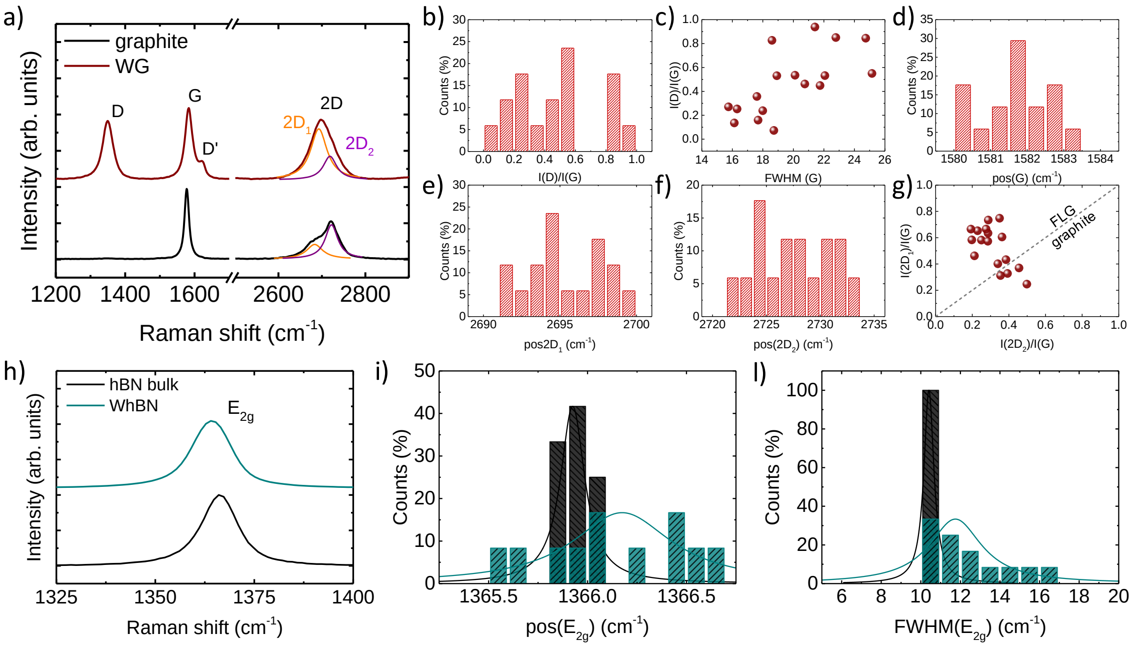

Figure 3.18. Raman spectroscopy analysis on WG and W*h*BN flakes. a) Representative Raman spectra of WG flakes (wine) and graphite (black) as comparison; Raman statistical analysis: b) I(D)/I(G), c) I(D)/I(G) *vs.* FWHM(G), d) Pos(G), e) Pos($2D_1$), f) Pos($2D_2$),and g) I($2D_1$)/I(G) *vs.* I($2D_2$)/I(G); h) representative Raman spectra of W*h*BN flakes (cyan) and bulk *h*-BN (black) as comparison; Raman statistical analysis: i) Pos(E_{2g}), l) FWHM(E_{2g}) A total of 15 spectra per sample have been acquired to perform the statistical analyses.

The evolution of the electronic structure from graphite to few-layers graphene flakes is evidenced by Raman spectroscopy (Figure 3.18). Analysing the intensity ratios (normalized to the G peak intensity) of the $2D_1$, *i.e.* I($2D_1$)/I(G), and $2D_2$, *i.e.* I($2D_2$)/I(G), peaks it is possible to estimate the flake thickness [166,197]. The evolution of the 2D peak of WG sample (Figure 3.18a), compared to the case of graphite, evidences the successful exfoliation. The statistical analysis performed on WG Raman spectra (Figure 3.18b-g) suggests that the sample WG it is composed mainly of FLG. Moreover, the lack of correlation between the intensity of the D peak (I(D)) and the FWHM of the G peak (Figure 3.18c) evidences that the I(D) is not due by the presence of basal plane defects but by edge defects [210].

Regarding the W*h*BN samples, the Raman spectroscopy analysis (Figure 3.18h-l) reveals shifts (Figure 3.18i) and broadening (Figure 3.18l)of the E_{2g} peak, compared to bulk sample, suggesting an effective exfoliation [182,186].

CHAPTER 4

Graphene/Polycarbonate composites

4.1 Introduction

One of the main and most promising applications involving graphene is as filler in polymer-based composites [1,75,138–140,142]. The physical properties of graphene [3,211,212] make it appealing for the composite materials production [1,141]. In fact, graphene-based polymer composites show enhanced mechanical [83,213], thermal [214], and electrical [215] properties compared to pristine polymer matrices, as discussed in chapter 1.

However, large quantities of graphene are needed for exploiting its use in the composite field [1,139], especially in view of industrial scalability. Although several techniques are available for the production of high-quality graphene monolayers on a substrate [26], *e.g.*, MC,[212] CVD [28], and epitaxial growth on SiC substrate [216]. Those approaches are clearly not suitable for composite applications. Nowadays, large-scale production of SLG and FLG flakes by liquid phase exfoliation (LPE) [35,37,39] is among the preferred production routes for the exploitation of graphene as filler in nanocomposites [26,39], as mentioned in section 1.2. In fact, the method allows to obtain SLG and FLG flakes dispersed in a solvent or in powder form and it is offering also the possibility of scalability [1,26,39].

As discussed in sections 1.2.1 and 2.1, in a LPE process, graphene flakes are produced by exfoliation of natural graphite [1,37] in a solvent medium by applying an external driving force, such as ultra-sonication [26,54]. The choice of the solvent for the exfoliation process is crucial [36,37,39]. In this context, suitable solvents have to minimize the interfacial tension between the liquid itself and the graphene flakes, having a surface tension (γ) similar to the surface energy of graphene and matching its HSPs [26,37,44]. Summarizing, the growing demand of the polymer-based graphene composites needs an efficient and scalable production route, which requirements are satisfied by using LPE. However, the LPE produced dispersion has to be purified to obtain stable suspension highly enriched in SLG and FLG flakes, which requires an ultra-centrifugal step. Considering these facts and the up-scalability difficulties of ultra-centrifugation, the only pristine graphene flakes containing dispersions availability on the commercial market is still limited, opening the avenues for novel developments in the scalable production techniques of graphene.

Another key requirement, apart from the graphene flakes morphology, as explained in section 1.3, to obtain improvements with respect pristine polymer in the properties of the final composite material is the optimal dispersion of the graphene flakes in the polymer matrices. The molecular interactions between the graphene flakes and polymer chains are due to weak van der Waals forces [137], π–π stacking [137,138], and hydrophobic-hydrophobic interactions [137]. These interactions hinder efficient connections between the graphene flakes and the polymer chains, so graphene flakes usually do not form homogeneous composites [139–141]. In contrast, the epoxide, hydroxyl, carbonyl, and carboxyl groups present on the basal plane of GO [63,70] and also partially in RGO [66,72] can interact with the polymer chains. Therefore, their use as a filler in the polymer-based composites is widely reported in literature [1,139,141,142]. Nevertheless, the presence of these groups acts as defects, in addition to the structural defects due to the oxidation process in the structure of the flakes [66,143]. The presence of such defects reduces the mechanical and electrical properties of GO and RGO flakes compared to graphene flakes [66,143], *e.g.* GO is an insulator and has Young’s Modulus ranging between 200 and 600 GPa [139,143,144].

Polycarbonate is a thermoplastic polymer with high mechanical stiffness (2.0–2.4 GPa) [217] and optical transparency (over 80% in the visible spectrum, with a refractive index of 1.59) [217], and can be used in a wide range of applications: ranging from automotive and aeronautic industries [217], to data storage (DVDs and CDs) [218], replacing glass [218], and photonics [219,220]. Polycarbonate could also be used as 3D printer filament [221], with higher mechanical and thermal properties with respect to PLA [222] ABS [223], which are the reference materials used in these applications [221]. For instance, the heat deflection temperature, *i.e.* the temperature at which a polymer deforms under a specified load, for PC is in the 135–145 °C range [218], whereas for PLA is ~60 °C [222], while for ABS is ~100 °C [224], making PC suitable for high-temperature required applications. Moreover, the exploitation of ABS or PLA filaments for 3D printing technology has also environmentally implications [225,226], as ultrafine, <100 nm, particle emissions from melt during a 3D printing process is reported [226]. 3D printable graphene-based composites have been firstly reported in the case of PLA [227] and ABS [227]. In order to exploit the aforementioned properties of PC-based graphene composites for their use in 3D printing, further studies are needed. Currently, to the best of our knowledge, there is not reported any PC/graphene (PC/G) composite in which LPE of natural graphite has been exploited, whereas primarily graphene derivatives such as GO or RGO have been previously used [146,228–231]. In particular, for what concerns the solution blending approach, the solvents used for the dissolution of PC are chloroform [229] and THF [228], both suspected of being carcinogenic substances [232,233].

In this chapter, I will present a simple solution blending process to produce PC/G composite pellets using a 1,3-dioxolane-based dispersion, having a two-fold function: acting as a dispersant for the graphene flakes and able to dissolve the PC for the realization of the final polymer composite. Structural characterization is carried out on both graphene flakes dispersion and PC/G composite samples using atomic force, transmission and scanning electron microscopies and Raman spectroscopy. The LPE produced prevalently SLG and FLG flakes with lateral size in the range 200 – 600 nm, and thickness in the 0.7 – 1.4 nm range for 70% of the flakes, respectively. Mechanical tests and electrical conductivity measurements are carried out to investigate the effect of different loadings of SLG and FLG flakes for the reinforcement of the composite's physical properties. If compared to the bare polymer, the as-produced PC/G composite shows a 26 % increment in Young's Modulus at 1 wt % loading and an electrical conductivity of ~10^{-3} S m^{-1} at 10 wt %, the latter representing a seven order of magnitude increment with respect to the pristine polymer.

4.2 Production and characterization of PC/G composites

In order to achieve a homogeneous dispersion of exfoliated graphene flakes into the PC matrix, I exploited solution-blending technique for the production of PC/G composite [150,151]. In a common solution-blending process, both matrix and filler have to be dissolved in the same solvent and then mixed. I selected 1,3-dioxolane as solvent for the solution blending, due to its low-boiling point, *i.e.* 78 °C [234], with a set of solubility parameters (*i.e.* HPS and surface tension) which makes it promising for the dispersion of graphene flakes with respect to, for example, THF and chloroform (see Table 4.1). However, this solvent is not suitable for the direct LPE of graphite because its surface tension, 32.6 mN m^{-1} [235], does not match the surface energy of graphene, that has been estimated to be close to 46.7 mN m^{-1} [37,46]. Thus, LPE of graphite is carried out in NMP [37], by means of low-power ultra-sonication. NMP is one of the best solvent used for the dispersion of graphitic flakes because its surface tension is 41 mN m^{-1} [236], close to the surface energy of graphene [37,46]. The result of the exfoliation process is a heterogeneous dispersion of thin/thick and small/large graphitic flakes [26]. This dispersion is ultra-centrifuged at 10000 rpm (~ 17000*g*), exploiting the SBS process [60,237], and the obtained ink is exchanged from NMP to 1,3-dioxolane, according to sections 2.2.1 and 2.4.1.

The results of the characterization of graphene flakes by TEM, AFM and Raman, presented in section 3.1.1, indicate that the ink is composed by SLG/FLG flakes.

Table 4.1. Summary of HSPs and surface tension at 25 °C for PC [40], 1,3-dioxolane [40][235], chloroform [40][238], THF [40][239], and graphene [37]. For graphene is reported as surface tension the one of a solvent that matches its surface energy.

material	δ_D (MPa$^{1/2}$)	δ_P (MPa$^{1/2}$)	δ_H (MPa$^{1/2}$)	Surface tension (mN m^{-1})
PC	19.1	10.9	5.1	—
1,3-dioxolane	18.1	6.6	9.3	32.6 [235]
Chloroform	17.8	3.1	5.6	27.1 [238]
THF	16.8	5.7	8.0	26.4 [239]
Graphene	18	10	7	~ 46.7 [37]

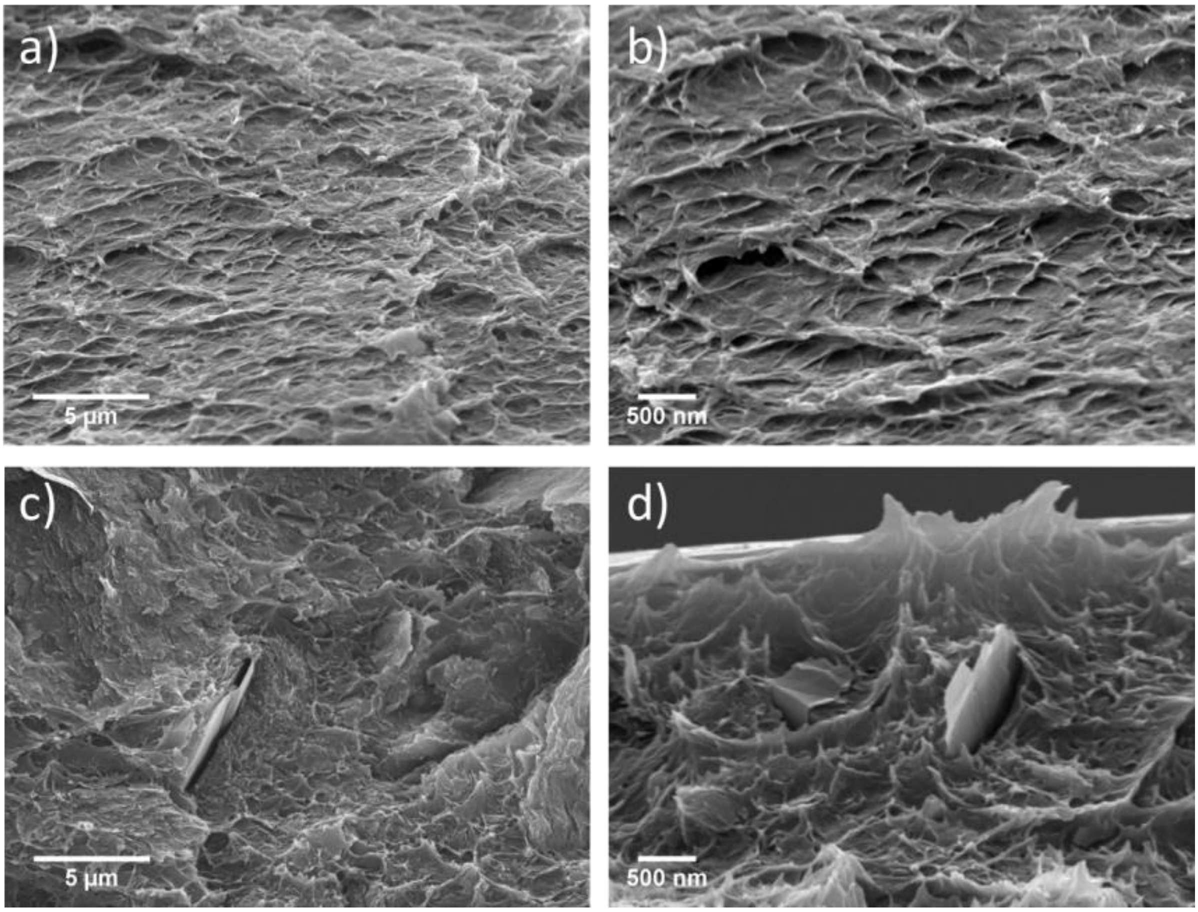

Figure 4.1. SEM images of cross section area of pristine PC, at (a) low and (b) high magnification, and PC/G composite of 1 wt % graphene loading, at (c) low and (d) high magnification. Adapted from [47].

4.2.1 Morphological characterization of PC/G composite

Blend compatibility (*i.e.* expecting macroscopically uniform physical properties), filler dispersion, and the interfacial bond between the polymer matrix and the SLG-FLG flakes are investigated performing SEM measurements on both the pristine PC and PC/G composite. SEM images of the cross-section of pristine PC are shown in Figure 4.1 at low (Figure 4.1a) and high (Figure 4.1b) magnifications, and PC/G composite of 1 wt %, at low (Figure 4.1c) and high (Figure 4.1d) magnifications, respectively. Graphene flakes (the brighter, angular shaped objects) can be clearly seen as uniformly dispersed in the polymer matrix, which is also confirmed by Raman characterization of the PC/G composite.

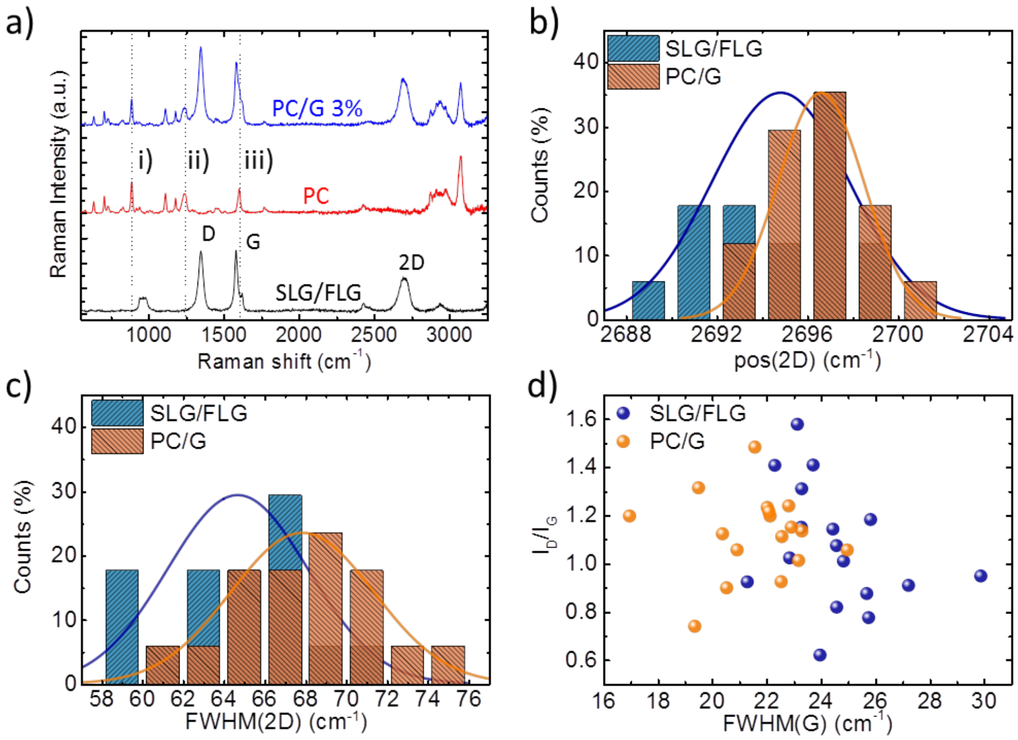

Figure 4.2 (a) Raman spectra of SLG/FLG dispersion (trace black), pristine PC (trace red) and PC /graphene dispersion at 3% of loading (trace blue), (b-d) statistical analysis on Raman spectra of graphene dispersion and composite samples: (b) Pos(2D), (c) FWHM(2D), (d) I_D/I_G respect to FWHM(G). Adapted from [47].

Figure 4.2a shows representative Raman spectra of graphene dispersion (trace black), PC (trace red) and PC/G composite dispersion after blending (trace blue). The Raman spectrum of the PC/G 3 wt % of graphene loading reveals a thorough mixing of the graphene flakes within the polymer matrix; indeed, there is the presence of peaks related to both SLG/FLG and the PC. The dotted lines referred as i), ii) and iii) correspond to C–CH_3 (~889cm^{-1}), C–O (~1235cm^{-1}) and ring stretches (~1606cm^{-1})

of PC [240], respectively. Statistical analysis on Pos(2D) (Figure 4.2b) shows a slight blue shift of the composite compared to the one in pristine PC. In fact, Pos(2D) is in the range 2688–2700 cm^{-1} for the dispersion and 2692–2702 cm^{-1} for the PC/G composite. The blue shift is attributed to π–π interactions between the graphene flakes and the polymer [139,241]. However, the 2D peak in the composite still shows a Lorentzian line-shape differently from graphite (see FWHM(2D) distribution (Figure 4.2c) indicating that FLG flakes are electronically decoupled [60,237]. The lack of correlation between I_D/I_G and FWHM(G) (Figure 4.2d) in the PC/G composite, as for the case of the SLG/FLG dispersion, suggests that no defects in the SLG/FLG flakes are introduced by the solution blending process [242].

4.2.2 PC/G composite enhanced performances

The thermal behaviour of a composite material in view of applications, such as for example 3D printing, has to be known [227]. Therefore, considering the application of the PC/G composite material for 3D printing using Fused Deposition Modelling (FDM) technology, these thermal behaviours are investigated. The FDM is an additive manufacturing technology commonly used for modelling, prototyping, and production of polymer-based objects, and it is one of the most commonly used techniques for 3D printing [243,244]. Using the FDM process, the thermoplastic polymer filament is heated above its glass transition temperature (T_g) and extruded through the nozzle of the 3D printer, then the printed material is cooled down to room temperature forming the product. The TGA and differential TGA (DTGA) analyses on PC (black curve) and PC/G at 1 wt % (red curve) are depicted in Figure 4.3a and Figure 4.3b, respectively. The first loss of weight, of ~5 wt %, occurs at 100–150°C for both pristine PC and the composite and it is attributed to evaporation of residual solvents and/or small organic groups [245]. The pyrolysis, corresponding to the main loss of weight, starts for pristine PC at ~370 °C and is due to the cleavage of the carbonate groups [245], whereas it is reduced in the composite because fillers reduce mobility of polymer chains, so the degradation temperature of the composite loaded with 1 wt % of SLG-FLG flakes, evaluated as the peak in the DTGA curve, increases of ~86 °C. The peak of DTGA, corresponding indeed to the maximum reaction speed in which the sample is degraded, is at ~421 °C for the pristine polymer and at ~507 °C for the PC/G composite 1 wt % loaded. These results show that the presence of graphene flakes increases the thermal stability of the polymer. At 800 °C, residual chars of 20wt % of PC and 21wt % of the composite are found, in agreement with the loading of filler.

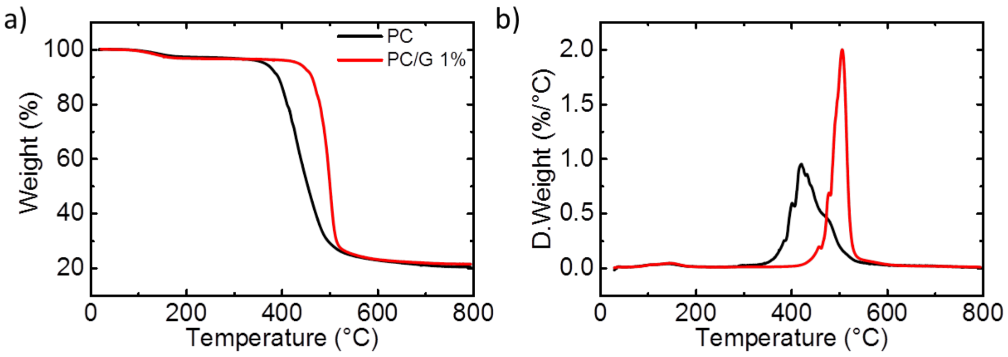

Figure 4.3. (a) TGA analysis of pristine PC (black curve) and PC/G 1 wt % (red curve). (b) DTGA analysis of pristine PC (black curve) and PC/G 1 wt % (red curve). Adapted from [47].

Stress *vs.* strain curves of pristine PC (black curve) and PC/G composite at 1 wt % (red curve) graphene loadings are shown in Figure 4.4a. The Young's Modulus (E) (Figure 4.4b) reaches a maximum value for the 1 wt % content of SLG/FLG flakes of 1455±28 MPa. The increment with respect to pristine PC, having a measured E value of 1151±44 MPa, is ~26%. Increasing the content of filler above 1 wt %, the E value decreases, reaching a minimum value of ~1353 MPa at 1.5 wt %, which, however, still corresponds to ~17% improvement compared to pristine PC (1151±44 MPa).

The decreases of E with a loading of SLG and FLG flakes superior to 1 wt %, could be associated to the occurrence of agglomeration of the flakes [84,148,246], although further studies to ascertain this phenomenon are needed. The presence of SLG and FLG flakes also improves the ultimate tensile strength (σ_U), defined as the higher stress value reached in the stress *vs.* strain curve, Figure 4.4c of the polymer. Contrariwise to the results obtained for E, where exceeding the 1 wt % of loading, there is a sudden decrease, σ_U remains almost constant (~ 60 MPa), as a 'saturation/like' behaviour. The full mechanical characterization data are summarized in Table 4.2 at the end of the chapter.

It is possible to estimate the efficiency of mechanical reinforcement, in terms of E, by comparing the experimental data obtained with the Eq. 1.7. For very low loadings, *i.e.*, < 0.1 wt% (corresponding to ~ 0.055 vol%), data are well aligned with the model, graphically expressed by the grey dashed line in Figure 4.4b, returning from the linear fit a E_F value of 360 GPa for SLG/FLG. This value is comparable with reported values of FLG in literature [83,247].

The increments reported here in mechanical properties are higher than other reported works involving graphene/PC composites. For instance, Kim et al. [146] reported a ~6.7% and ~20.7% increments in E at 1 wt % and 2.5 wt % of functionalized graphene sheets (thermally exfoliated GrO) loading, respectively; Shen et al. [248] reported a 6.8 % increment in E at 10 wt % of thermally RGO loading. The increments in mechanical properties are higher compared to other reported works involving a PC matrix loaded with 1 wt % RGO flakes [146,248], in which composites are produced by melt blending obtaining an increment in E lower than 7%. Mittal et al. [249] reported enhancement of ~ 23% in E but with 7 wt % of loading of RGO flakes.

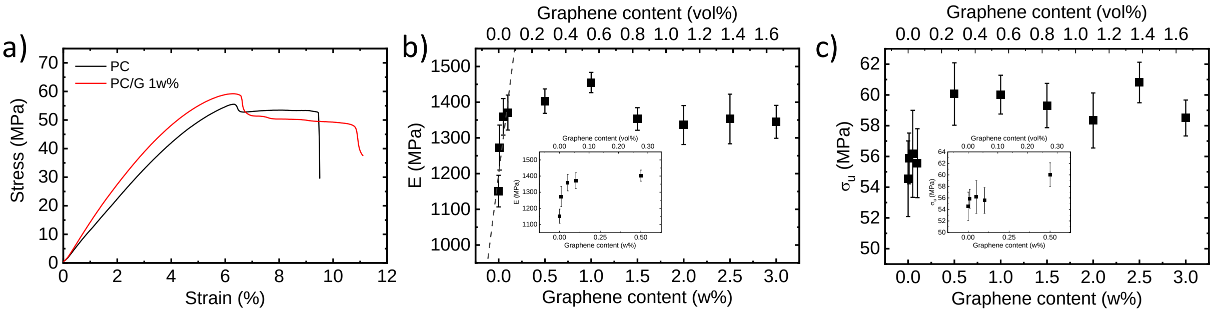

Figure 4.4. Mechanical properties of composites and pristine materials: (a) stress vs. strain curves, (b) Young's modulus (E), and (c) ultimate tensile strength (σ_U), with SLG/FLG content displayed in both wt% (bottom x axis) and vol% (top x axis). Insets represents magnification at very low loadings, i.e. < 0.1wt%. Adapted from [47].

The mechanical properties of the composite material could be additionally enhanced by optimizing the aspect ratio of the graphene flakes (lateral size *vs.* thickness), as reported in the case of PVA [84], where the reported aspect ratio of flakes is ~1900 and the enhancement in E with respect pristine PVA is ~66% at 0.36 vol% of loading (as comparison, our aspect ratio is ~300). Considering this work [84], it seems that the resulting mechanical enhancement of the polymer-based graphene composites is rooted in the differences in the structural and morphological properties of the graphene flakes. However, further systematic studies are needed to verify this hypothesis.

Finally, static electrical conductivity measurements (DC regime) on the composites as a function of SLG/FLG content in the composite material (PC/G), are presented in Figure 4.5. The PC/G composites with SLG and FLG concentrations up to 10 wt % are prepared for this characterization The pristine polymer matrix exhibits DC conductivity of the order of 10^{-11} S m^{-1}, reaching ~10^{-7} S m^{-1} for 1.5 wt % and almost 10^{-3} S m^{-1} at 10 wt % of loading. The improvement on DC electrical conductivity of the composite follows a percolation behaviour [215,228,250], presented in section 1.3.3, with a percolation threshold (φ_c) of ~1 wt % (~0.55 vol%), a value in line compared to other works involving PC/G composites [146,228].

According to Eq. 1.13, from the linear fit of lg(σ) *vs.* lg[($\varphi-\varphi_c$)/($1-\varphi_c$)] shown as inset to Figure 4.5, I found that, $\sigma_0 = 10^{(2.152\pm0.823)}$ S m^{-1} = 141.91 ± 6.65 S m^{-1} and s = 4.027 ± 0.411. Such a high percolation exponent can be related with the presence of a large number of junction resistances between the flakes [251,252]. The percolation threshold could be further lowered increasing the aspect ratio of the filler, facilitating the formation of a conductive path at a lower volume loading [215,253,254].

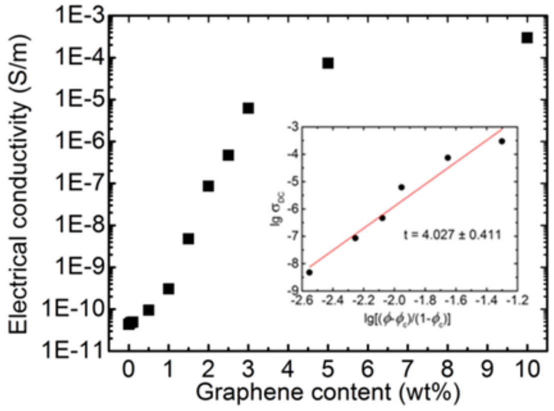

Figure 4.5. Electrical conductivity (σ_{DC}) of composite *vs.* SLG/FLG flakes content showing percolation behaviour. The plot of log(σ_{DC}) *vs.* lg[($\varphi-\varphi_c$)/($1-\varphi_c$)], where φ is the volume content and φ_c the percolation threshold, with a linear fit of experimentally measured points is shown in the inset. Adapted from [47].

4.2.3 Conclusions

In this chapter, I proposed a scalable method for the production of a PC/G composite. Single and few-layers graphene flakes, used as filler, are obtained by means of LPE of pristine graphite. Exfoliation is carried out in NMP and then, by exploiting a solvent exchange process, the graphene flakes are dispersed in 1,3-dioxolane, which is a low-boiling point solvent with a set of solubility parameters which makes it promising for the dispersion of graphene flakes. The final composite is then obtained by mixing the graphene-based dispersion and the polymer solution in 1,3-dioxolane, by means of solution blending. Raman spectroscopy and SEM microscopy have shown the homogeneous dispersion of the SLG and FLG flakes in the PC matrix.

The thermal stability of the PC/G containing 1 wt % of SLG and FLG flakes filler compared to the pristine PC is assessed by TGA analysis demonstrating an upshift of the degradation temperature of ~86 °C. Furthermore, a 26% improvement of Young’s Modulus with respect to pristine PC is reached for 1 wt % content of SLG and FLG flakes. The presence of the fillers also enhances the ultimate tensile strength. The PC/G composite electrical percolation threshold is found at ~1 wt % of graphene loading, reaching electrical conductivity of ~10^{-3} S m^{-1} at 10 wt %.

The as-produced PC/G composite can be the ideal starting material for 3D printing applications in constructing 3D electronics, due to its increased mechanical and electrical properties and thermal stability.

Table 4.2. Summary of mechanical properties of PC/G composite, with standard deviations (s.d.) and relative variation (Δ) in percentage with respect the neat polymer.

SLG/FLG content	E	s.d. E	ΔE	σ_U	s.d. σ_U	$\Delta\sigma_U$
wt %	MPa	MPa	%	MPa	MPa	%
0.00	1151	44	—	55.2	3.4	—
0.01	1273	62	10.6	55.9	2.5	1.3
0.05	1359	51	18.1	56.2	3.8	1.8
0.10	1371	48	19.1	55.6	6.0	0.7
0.50	1403	34	21.9	60.1	0.9	8.9
1.00	1455	28	26.4	60.0	1.1	8.8
1.50	1353	31	17.6	59.3	1.4	7.6
2.00	1226	54	6.5	57.3	2.4	4.0
2.50	1353	69	17.4	60.8	0.2	10.3
3.00	1345	46	16.8	58.5	1.1	6.1

CHAPTER 5

h-BN/Polycarbonate composites: the effect of flakes morphology

5.1 Introduction

In the last years, *h*-BN has attracted increasing attention due to its remarkable properties, complementary to the graphene ones [1,39]. A single layer of *h*-BN has a honeycomb lattice composed by alternating boron (B) and nitrogen (N) atoms, held together by polar covalent bonds [14,184]. This structure makes single layer *h*-BN mechanically strong, *i.e.* its Young's Modulus (E) approaches 1 TPa [15], with a tensile strength of 150 GPa [15] and in-plane stiffness of 267 N m^{-1} [14]. Contrary to graphene, *h*-BN has no optical absorption in the visible region [14] and it is an electrical insulator with a band-gap of ~ 6 eV [14]. This set of properties makes *h*-BN appealing for its use as filler in polymer composites [255]. Polymer reinforcement has already been achieved with *h*-BN flakes, exfoliated by LPE, in cases of several matrices, such as polyvinyl alcohol (PVA) [85], polymethyl methacrylate (PMMA) [133], polyethylene terephthalate (PET) [94], polyvinyl chloride (PVC) [256], and PC [257], in which increments of E are in the range of 20 – 30 % with respect the neat matrixes at filler loadings of 0.1 wt % (0.3 wt % for Ref. [255]). Usually, for loading of *h*-BN flakes higher than 0.1 wt % the mechanical performances of composites saturate or even decrease, probably due to agglomeration of the flakes dispersed in the polymeric matrixes [47,84,85,94]. On the one hand, the occurrence of aggregates, indeed, has been reported in the 0.1 – 0.2 vol% (~ 0.2 – 0.4 wt %) loading range for PVA [85] and PVC [256] based composites, both produced by solvent blending. On the other hand, for composites produced by melt blending, as in the case of Ref. [94], agglomeration of fillers can be observed even at lower concentrations, *i.e.* 0.017 vol% (~ 0.03 wt %).

It is worth noting that in order to produce 2D crystal-based composites with the targeted mechanical reinforcement, both the dispersion of the fillers in the polymer matrix [152,258] and their aspect ratio [75,84,213], *i.e.* lateral size over thickness, are of paramount importance, as shown both by mathematical models [88,259], presented in section 1.3, and experimental evidences obtained in the case of graphene flakes [84,88,259–262]. A study on the reinforcement of a polymer matrix related to the aspect ratio and dispersion of *h*-BN flakes is, however, still lacking. Therefore, I tackled this issue by designing *h*-BN flakes with a different aspect ratio (250 and 350) exploiting LPE in a water/surfactant solution as the dispersing agent. The exfoliated *h*-BN flakes have been sorted by aspect ratio by means of sedimentation-based separation (SBS) [1,47,59,60] using a cascade centrifugation [61], obtaining two population of flakes with different morphology, according to the procedure presented in section 2.1.3. The as-produced flakes are then integrated into PC-based composites, with varying concentration from 0 to 5 wt %, by solution blending, a technique which allows a better dispersion of the flakes in the polymer matrix with respect to melt blending [93,151], by dispersing both PC and *h*-BN flakes in the same solvent, *i.e.*, 1,3-dioxolane. The dispersions are then coagulated in water forming composite pellets, which are finally hot-pressed to produce composite thin films (thickness ~ 100 µm). Mechanical tests on composite films have shown significant reinforcements with respect to the bare PC polymer, with an increment of ~ 22 % in E at 0.1 wt % of loading of *h*-BN flakes with the highest aspect ratio (*i.e.*, 350), while at the same loading the observed increment is of ~ 17 % for the *h*-BN flakes of lower aspect ratio (*i.e.*, 250). A maximum reinforcement of 27 % in E is further obtained by using high-aspect ratio flakes (*i.e.*, 350) at 0.5 wt % of loading, whereas the same increment has been reported by a two-fold loading increase in the case of graphene flakes [47], as evidenced in chapter 4.

5.2 Morphology of *h*-BN/PC composites

In order to understand the impact of the *h*-BN flakes morphology on the mechanical properties of the PC-based composite, we designed and produced *h*-BN-s/PC and *h*-BN-p/PC composites by solution blending technique in 1,3-dioxolane, as detailed in the section 2.1.3. 1,3-dioxolane is a low boiling point solvent (78 °C) [234] with a set of solubility parameters (*i.e.* HPS and surface tension) which makes it promising for the dispersion of *h*-BN flakes with respect to, for example, THF and chloroform (see Table 5.1), other solvents are able to dissolve PC and generally used for the production of solution processed 2D crystals/PC composites [219,228,229,257]. 1,3-dioxolane has HSPs that are in the range of the ones proposed by Coleman and co-worker for exfoliated *h*-BN [35] and a surface tension that is close to the exfoliated *h*-BN surface energy(see Table 5.1). Considering these values, by using 1,3-dioxolane as a solvent for the blending, we expected a thorough mixing of the exfoliated *h*-BN flakes inside the PC matrix.

The results of the characterization of the sorted *h*-BN flakes by TEM and AFM, presented in section 3.1.2, indicate that the *h*-BN-s and *h*-BN-p flakes have an aspect ratio of 350 and 250, respectively.

Table 5.1. Summary of HSPs and surface tension at 25 °C for PC [40], 1,3-dioxolane [40][235], chloroform [40][238], THF [40][239], and *h*-BN flakes [35]. For *h*-BN is reported as surface tension the one of a solvent that matches its surface energy.

material	δ_D (MPa$^{1/2}$)	δ_P (MPa$^{1/2}$)	δ_H (MPa$^{1/2}$)	Surface tension (mN m^{-1})
PC	19.1	10.9	5.1	—
1,3-dioxolane	18.1	6.6	9.3	32.6 [235]
Chloroform	17.8	3.1	5.6	27.1 [238]
THF	16.8	5.7	8.0	26.4 [239]
h-BN	18	10	7	~35 [35]

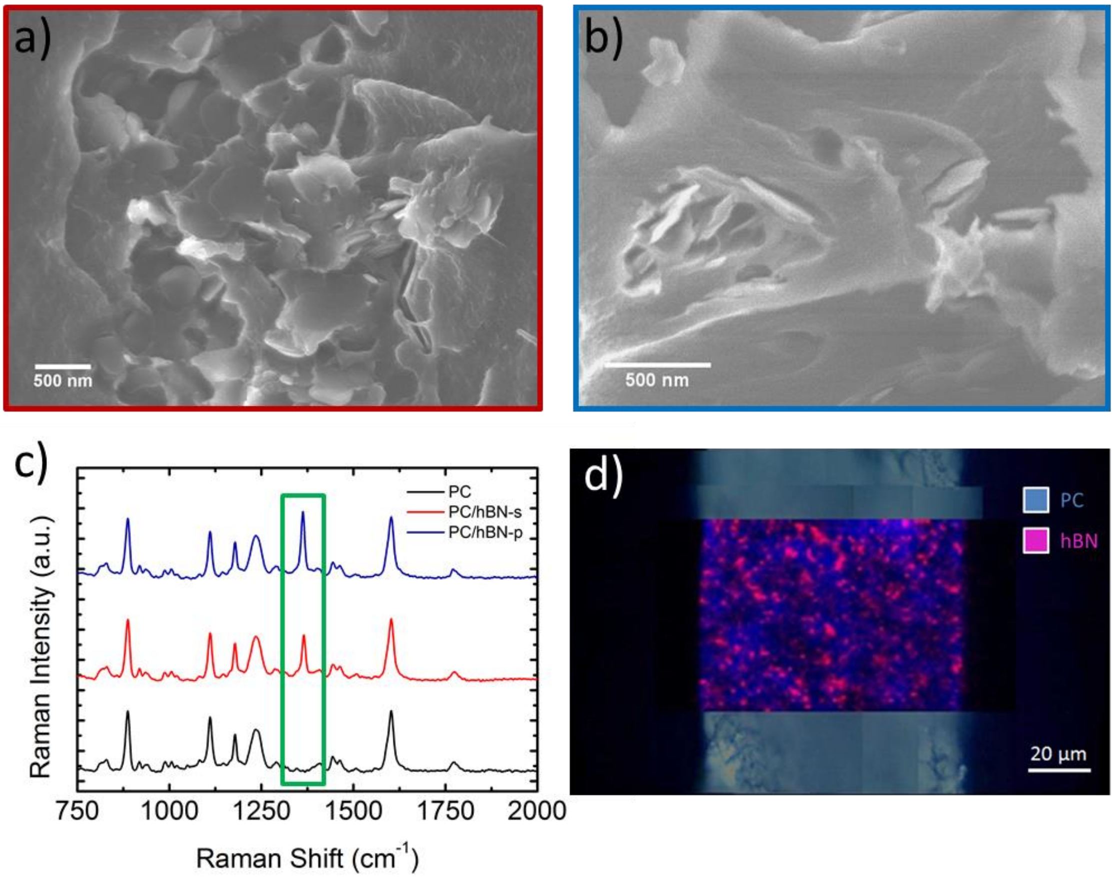

Figure 5.1. Cross-section SEM micrographs of (a) *h*-BN-s/PC 0.5 wt % and (b) *h*-BN-p/PC 0.5 wt %. (c) Raman spectra of pristine PC (black trace), *h*-BN-s/PC 0.5 wt % composite (red trace), *h*-BN-p/PC 0.5 wt % composite (blue trace); in the green box is displayed the high frequency E_{2g} peak of *h*-BN (~ 1366 cm^{-1}). (d) Raman mapping on a cross section of *h*-BN-s/PC 0.5 wt % composite showing the acquired Raman signals of PC (blue) and *h*-BN-s flakes (pink).

The dispersion of *h*-BN flakes in PC matrix is evaluated by scanning electron microscopy (SEM) and Raman spectroscopy (Figure 5.1). Comparison of scanning electron micrographs of the cross-section area of composites with the 0.5 wt % of loading (*h*-BN-s/PC in Figure 5.1a and *h*-BN-p/PC in Figure 5.1b) reveal that fillers – the brighter objects in the images – are uniformly dispersed in the polymeric matrix. Raman spectra on composite films (Figure 5.1c) show the presence of peaks belonging to both *h*-BN (displayed in the green box) and PC, revealing a thorough mixing of the *h*-BN flakes within the polymeric matrix, further confirmed by a Raman mapping made on the film cross-section (Figure 5.1d).

5.3 Effect of the aspect ratio of *h*-BN flakes on mechanical properties of composites

The dispersed *h*-BN flakes improved the mechanical properties of the PC matrix. Results obtained from uniaxial tensile tests on composites are presented in Figure 5.2. With the 0.1 wt % of loading (corresponding to 0.06 vol%), E of PC increased from 1165 ± 56 MPa of the neat polymer to 1370 ± 23 MPa (+ 17 %) and 1426 ± 76 MPa (+ 22 %) using as filler *h*-BN-p and *h*-BN-s flakes, respectively, see Figure 5.2a. It is worth noting that a difference in an aspect ratio of 100 reflects a 5 % (56 MPa) variation in the reinforcement of the composite. By using the rule of mixtures [263], Eq. 1.7, it is possible to evaluate the effective Modulus of the filler (E_F) in the composite. Herein, at this loading, *h*-BN-s flakes and *h*-BN-p flakes show an E_F of 436 GPa and 342 GPa, respectively, values that are less than half of the theoretical value of *h*-BN [15], but, however, in line with the reported literature results [85,94,133,256]. Further increasing the aspect ratio of the flakes, keeping optimized their dispersion in the polymer matrix, can in principle approach E_F to the theoretical value [84]. Moreover, the increment obtained using the *h*-BN-s flakes is comparable to the one obtained by Sainsbury *et al.*, where methoxyphenyl carbamate-functionalized *h*-BN flakes have been used as a reinforcing agent for the PC matrix [257]. Functionalization of flakes is able to increase the interfacial stress transfer between filler and polymer chains [257], and a proper entanglement, *i.e.* their interlocking, can be achieved when the grafted molecules on the flakes are structurally and chemically similar to the matrix [257,264], thus minimizing their enthalpy of mixing [264]. Nevertheless, flake functionalization requires the addition of one or more experimental steps to the process. It is worth noting that in the same work, the authors report that no effective reinforcement has been found using untreated *h*-BN flakes [257]. The enhancements we obtained using un-functionalized *h*-BN flakes can be attributed to the different solvent used for the solution blending process, *i.e.* 1,3-dioxolane instead of THF used in Ref. [257], which does not match the solubility parameters of *h*-BN, as previously explained (see Table 5.1).

Furthermore, a 27 % of increment in E has been found at 0.5 wt % of loading of *h*-BN-s flakes, whereas the same increment is obtained by a two-fold loading increase in the case of graphene [47], reaching a + 35 % of reinforcing at a loading of 5 wt %. For both samples, however, exceeding the 0.5 wt % of *h*-BN flakes loading, the E_F of the flakes suddenly decreases, *e.g.*, is lower than 100 GPa at 1.0 wt % of loading. This behaviour, often observed in literature for low dimensional fillers [47,84,85,94], is attributed to the occurrence of flakes agglomeration [84,265].

The ultimate tensile strength (σ_U), Figure 5.2b, of the composite at 0.1 wt % of *h*-BN-s loading increases of ~ 12 % with respect the neat polymer (60.1 ± 2.1 MPa *vs.* 54.5 ± 1.9 MPa), whereas composite at 0.1 wt % of *h*-BN-p loading has shown an increment of ~ 6 % (57.6 ± 2.6 MPa). Exceeding the loading of 0.5 wt %, for both fillers, there is no more evidence of strength reinforcement in composites and even we report a slight decrease for loadings higher than 1.5 wt %. This fact is consistent with the evoked agglomeration issues found at the same loadings for E.

The *h*-BN-s flakes, with higher aspect ratio with respect to the *h*-BN-p flakes, gave also the highest reinforcements, both in terms of E and σ_U for all the investigated concentrations (0.01 – 5 wt % range). The differences are highlighted in the insets to Figure 5.2a and b that focus the *h*-BN flakes loadings up to 0.1 wt %.

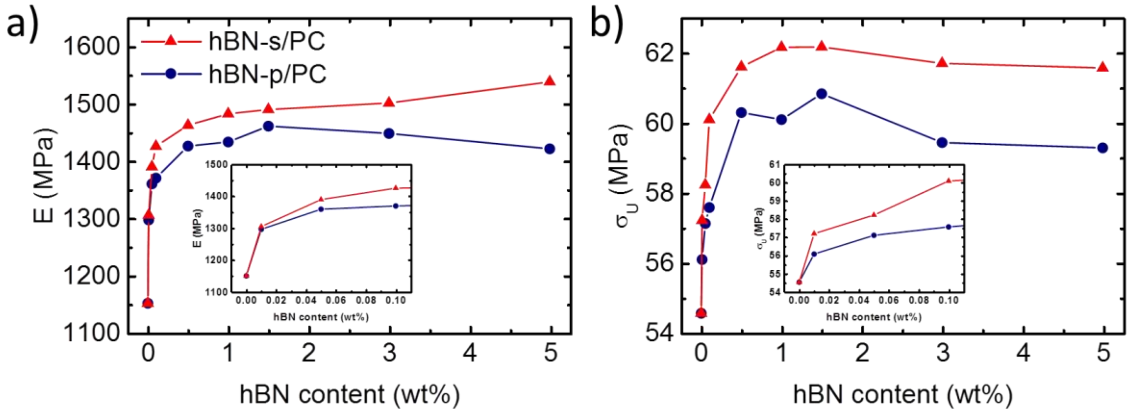

Figure 5.2. Mechanical performances of composites. (a) Young's Modulus (E); (b) ultimate tensile strength (σ_U). Insets to (a) and (b) the *h*-BNcontent in the 0 – 0.1 wt % range.

5.4. Conclusion

The dependence of the *h*-BN flakes morphology, *i.e.*, lateral size and thickness, on the mechanical properties of *h*-BN/PC composites have been demonstrated. Bulk *h*-BN powder has been exfoliated by an environmentally friendly approach exploiting LPE in a water/surfactant solution. *h*-BN flakes have been sorted by the aspect ratio (*i.e.*, lateral size *vs* thickness) using a cascade centrifugation and exploiting the SBS process, obtaining two different specimens *h*-BN-s and *h*-BN-p with aspect ratios of 350 and 250 and an average number of layers of 3 and 5, respectively, as measured by AFM. These flakes have been used as filler for the production of composites with enhanced mechanical properties using PC as a matrix. Composites have been produced by means of solution blending, dissolving PC in 1,3-dioxolane, a solvent with a surface tension and HSPs that match the ones required for *h*-BN exfoliation and stabilization, allowing a thorough dispersion of flakes inside the polymer matrix, as confirmed by SEM and Raman spectroscopy. The differences in the aspect ratio of the fillers reflected in differences in the obtained mechanical reinforcements. The composites produced by using the fillers with higher aspect ratio have shown the highest mechanical performances, both in terms of stiffness (evaluated measuring E, *e.g.* +22 % with respect to the pristine PC matrix obtained at 0.1 wt % of loading of *h*-BN-s flakes *vs.* + 17 % obtained at the same loading of *h*-BN-p flakes) and strength (evaluated measuring σ_{U}, *e.g.* +12 % respect the pristine PC matrix obtained at 0.1 wt % of loading of *h*-BN-s flakes *vs.* + 6 % obtained at the same loading of *h*-BN-p flakes). Moreover, the combination of high aspect ratio fillers and the use of 1,3-dioxolane as a solvent for the blending with the polymeric matrix, allows us to obtain for PC-based composites increments in mechanical properties comparable with the ones of functionalized *h*-BN flakes [257] and even higher if compared with composites having liquid phase exfoliated-graphene flakes as filler [47]. The environmentally friendly, high-yield water/surfactant exfoliation herein proposed, together with the size selection of *h*-BN flakes and their subsequent use as a reinforcing agent in a polymer matrix, can boost the exploitation of 2D crystals for large-scale commercial applications.

CHAPTER 6

2D crystals/ABS composites: beyond theoretical limit of mechanical reinforcement

6.1 Introduction

Although an industrial-scale production process of pure pristine one-atom thick 2D crystals is not yet available, a few methods currently allow for a low-cost, large-scale production of few-layer flakes of different morphologies [35,38,154], *i.e.* surface area (A) and thickness (t). In this chapter, by using liquid phase exfoliated 2D crystals loaded in an acrylonitrile butadiene styrene matrix, I unravel the dependence of stiffness enhancement as a function of the filler content and flakes morphology. I demonstrate the nearly linear relation between the mechanical reinforcement and A/t^2 ratio for three representative 2D fillers, *i.e.*, graphene, *h*-BN, and WS_2. Additionally, is revealed the existence of an ultra-high efficiency regime emerging at a 2D crystals loading below 0.1 wt %, further expanding as A/t^2 increases. In these conditions, the mechanical reinforcement of the composite unexpectedly exceeds the ideal stiffness of the corresponding 2D monolayers, implying a synergic effect between the flake and the surrounding polymer matrix. These results, coupled with the up-scalability of their production by solution processing, define the route towards the practical use of 2D crystals as mechanical reinforcement in the manufacturing industry.

For commercial applications, the mechanical reinforcement of polymers is currently realized by using inorganic fillers [266], *e.g.* mineral fillers [23,267] and micro fibres such as glass fibres (GFs) [268]. However, the main issue of this technology relies on the high amount of fillers required (10–30 wt %), which consequently determines difficulty in the processing [269]. Additionally, this technology has reached a bottleneck and further improvements of the mechanical properties require different approaches. Recent studies [1,78] have shown improved physical properties of polymer-based composites, with respect to the pristine polymers, by using 2D fillers produced either by CVD [270], or solution processing, *i.e.*, nanoplatelets [213,271] as well as pristine FLG [47,76,84,85], and chemically functionalised-2D materials [141,142,186,272], proposing that the mechanical reinforcement is reached at very low volume fractions of the filler (<1 wt %). At the industrial level, however, this new 2D-crystal-based technology is not yet able to compete with commercially-available solutions. Crucial for further developments of these materials in the mechanical reinforcement of the polymers is the understanding of the effect of lateral size and/or thickness of the exfoliated 2D crystals through scalable approaches. In fact, it has been demonstrated for other systems, *e.g.*, fibre-reinforced polymers [268,273,274], that the dependence of the polymer mechanical properties on the fillers morphology is pivotal. Nevertheless, this is an almost unexplored route for 2D fillers, in which only a few studies, mostly at the lab scale, are reported just for graphene flakes [76,84,213,275].

Here, I provided a set of data that allows linking directly the mechanical reinforcements of a representative common polymer, *i.e.* ABS, with the morphology of the 2D crystals used as fillers and produced in scalable quantities by LPE. I determine a nearly linear relationship between the stiffness of the composites and the A/t^2 *a*spect ratio of the 2D flakes. This behaviour seems to be universal, being independent on the nature of 2D crystals, *i.e.*, it is observed not only with graphene but also for other inorganic 2D fillers, *e.g.*, *h*-BN and WS_2. With the aid of the classical rule of mixture model (Eq. 1.13) [81,84,276], I identify a regime of high stiffness of the composite material occurring at low 2D fillers loading (<0.1%) and large A/t^2 values ($\sim 46 \times 10^3$). In these conditions, the mechanical reinforcement of the composite overcomes the sum of the ideal mechanical properties of its individual components. In particular, the back-calculated stiffness of 2D flakes gives higher values (*e.g.* ≈ 1.28 TPa for graphene) than the theoretical one (1 TPa [6,277]). Exploiting these results, we demonstrate that it is possible to achieve mechanical reinforcement (~36%) comparable to those available with conventional fillers (*e.g.*, GFs), but at much lower filler content, *i.e.* up to 20 times less (*i.e.*, 0.5 wt % *vs.* 10 wt %).

The LPE of bulk layered-materials, is a cost-effective method to produce high-concentration of 2D flakes directly dispersed in a solvent [1,35], as previously explained. However, the as-produced 2D flakes have a broad distribution of both thicknesses (from monolayer flakes to unexfoliated material) and lateral size (from few nanometres to micrometres scale) [39] preventing to identify the impact of their aspect ratio for mechanical reinforcement. To overcome these issues, I prepared dispersions of 2D crystal flakes using LPE, tailoring their morphological properties and increase the content of monolayers by exploiting iterative ultra-centrifugation cascades [61], a process still compatible with large-scale applications. The as-prepared 2D flakes are selected as a function of their structural properties, resulting in small/thin and large/thick flakes. The morphological characterization of the as-prepared 2D crystals flakes used in this work, as well as their labels, can be found in section 3.1.3.

To produce the composites, I have exploited the solution blending process (Figure 6.1), according to section 2.3.4. The size-selected 2D filler is added at different weight fractions in the 0.0 – 1.0 wt % range compared to the ABS weight (Figure 6.1a, reported for graphene as a representative sample).

Subsequently, the as-obtained composite dispersion is coagulated in water, dried, pelletized (Figure 6.1b) and further processed by compression moulding and extrusion obtaining films (Figure 6.1c) and filaments (Figure 6.1d), respectively.

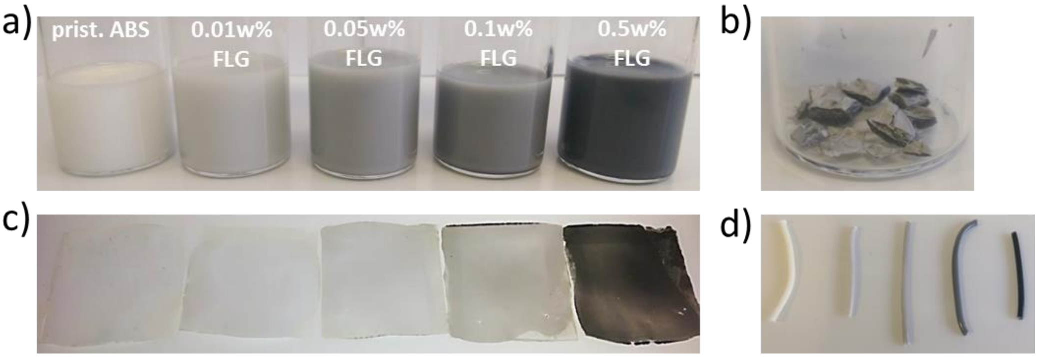

Figure 6.1. Solution blending preparation of FLG/ABS composites. a) dispersions of ABS and FLG/ABS composites in Acetone at different FLG loadings; b) example of pelletized FLG/ABS composite after coagulation; c) composite films obtained by film casting of dispersions; d) composite filaments obtained by extrusion of composite pellets.

Morphology of pristine ABS and FLG/ABS, *h*-BN/ABS, WS_2/ABS composites is investigated by HR-SEM (Figure 6.2, details in the caption), depicting a homogeneous dispersion of 2D crystals thorough the ABS matrix. Further insight into the FLG/ABS interface is obtained by HRTEM analysis. A representative image is shown in Figure 2b for an ABS/Graphene composite at low filling (0.1%). Atomic layers or graphene flakes with a large aspect ratio ($A/t^2 \sim 40$ see below) are clearly visible and they are all well aligned (see white triangles in Fig.2b). The region is also characterized by bright regions, which surround the 2D layers. These bright regions suggest that the polymer becomes softer in the proximity of the 2D fillers enabling an ideal conformation with them. More work and dedicated computational studies are needed to develop further understanding of the observed changes in the polymer matrix close to the interface with the fillers.

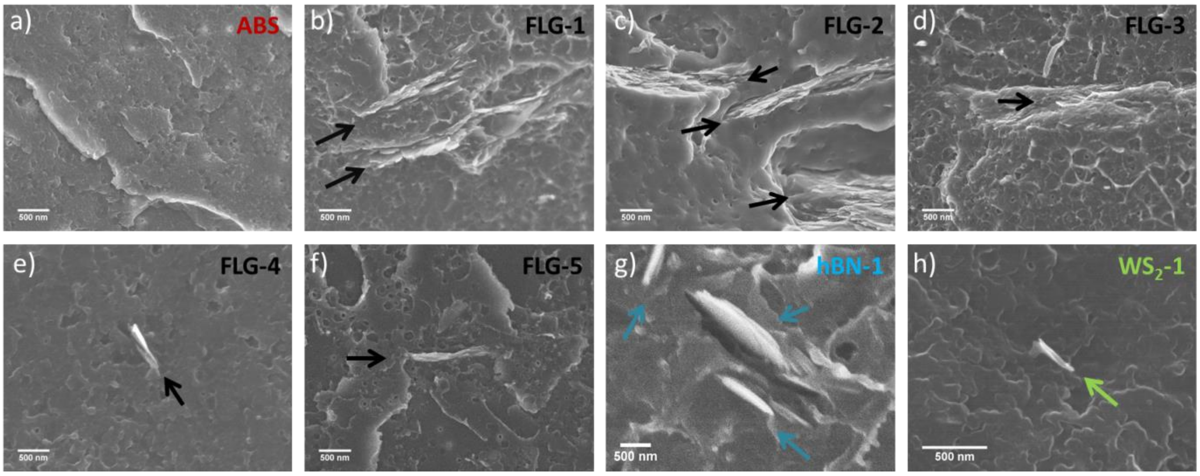

Figure 6.2. Morphological characterization of 2D/ABS composites. HR-SEM analysis of ABS (a), FLG/ABS (b-f), *h*-BN/ABS (g) and WS_2/ABS (h) composites.

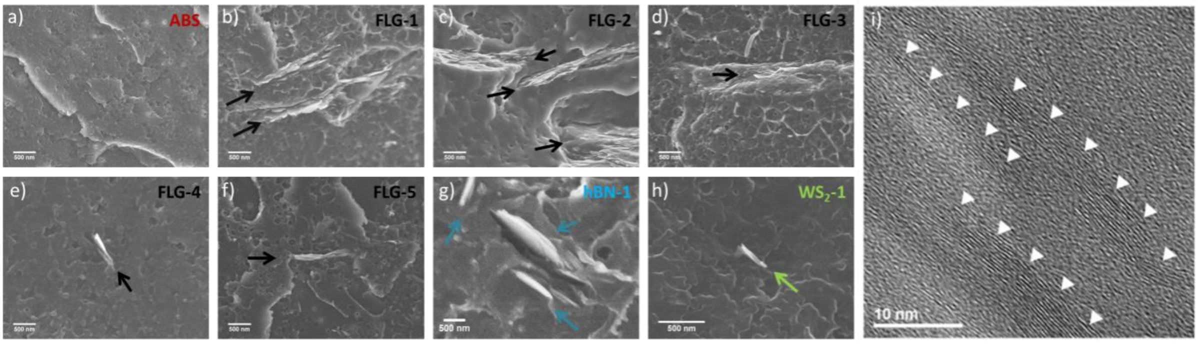

Figure 6.2. Morphological characterization of 2D/ABS composites.HR-SEM images of ABS (a), FLG/ABS (b-f), *h*-BN/ABS (g) and WS_2/ABS (h) composites; i) HRTEM image of FLG/ABS composite.

6.2 Beyond the theoretical limit of mechanical reinforcement

Mechanical tests on both bare ABS and 2D/ABS composites film are performed. Stress *vs.* strain curves are used to determine E, σ_y, and σ_U of the polymers and composites, according to the procedure explained in section 2.5.4.

In particular, E of composites increases with the fillers loading (Figure 6.3), evidencing the beneficial effect of the presence of high-stiffness fillers on the overall stiffness of composites (see Tables 6.1–3 at the end of the chapter for an extensive report of the mechanical properties of composites). Figure 6.3a presents the effects of FLG fillers obtained by using different ultra-centrifugations speeds (samples FLG-1 to FLG-5), whereas Figure 6.3b evidences the difference in FLG fillers obtained by cascade centrifugation starting by the sample FLG-5 (samples FLG-6, FLG-7 and FLG-8). Further details on the parameters used for the production of the samples and their morphological characterisation can be found in sections 2.1.2 and 3.1.3, respectively. Note that with the last samples, composite with only loadings up to 0.1 wt % have been produced, because the cascade centrifugation process lowers the overall yield of 2D crystals that can be obtained. Figure 6.3c and 6.3d are instead related to the composites obtained by using *h*-BN and WS_2 fillers.

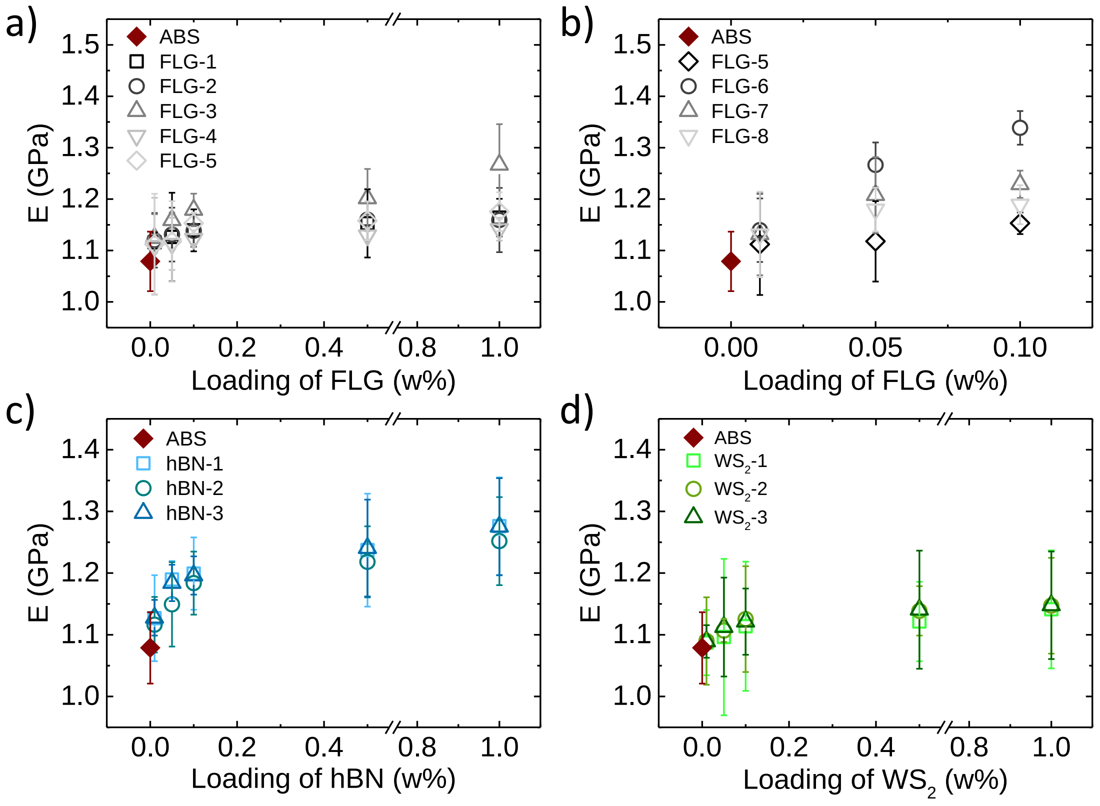

Figure 6.3. Young's Modulus of ABS/2D composites as a function of the filler loading. a and b) Young's Modulus of ABS/FLG composites, c) Young's Modulus of ABS/*h*-BN composites and d) Young's Modulus of ABS/WS_2 composites.

To identify the key-factor of the relationship between the enhancement of the polymer properties induced by 2D fillers and the morphology of the 2D crystals themselves, we investigated *E* of the composites as a function of different representations of aspect ratio: l/t (Figure 6.4 first column), $\sqrt{A}/t$ (Figure 6.4 second column), A/t (expressed in µm, Figure 6.4 third column) and A/t^2 (Figure 6.4 fourth column). All the values of E are reported in graphs for composites produced by using FLG (black points), *h*-BN (cyan points) and WS_2 (green points) with loadings of 0.01 wt % (Figure 6.4 first raw), 0.05 wt % (Figure 6.4 second raw), and 0.1wt % (Figure 6.4 third raw). Exceeding the loading of 0.1 wt %, as extensively reported in the literature, are often present cases of agglomerations of the fillers [47,84,85,94,265] that may cause unexpected results and thus hinder the possibility to identify relationships between the fillers and their morphology.

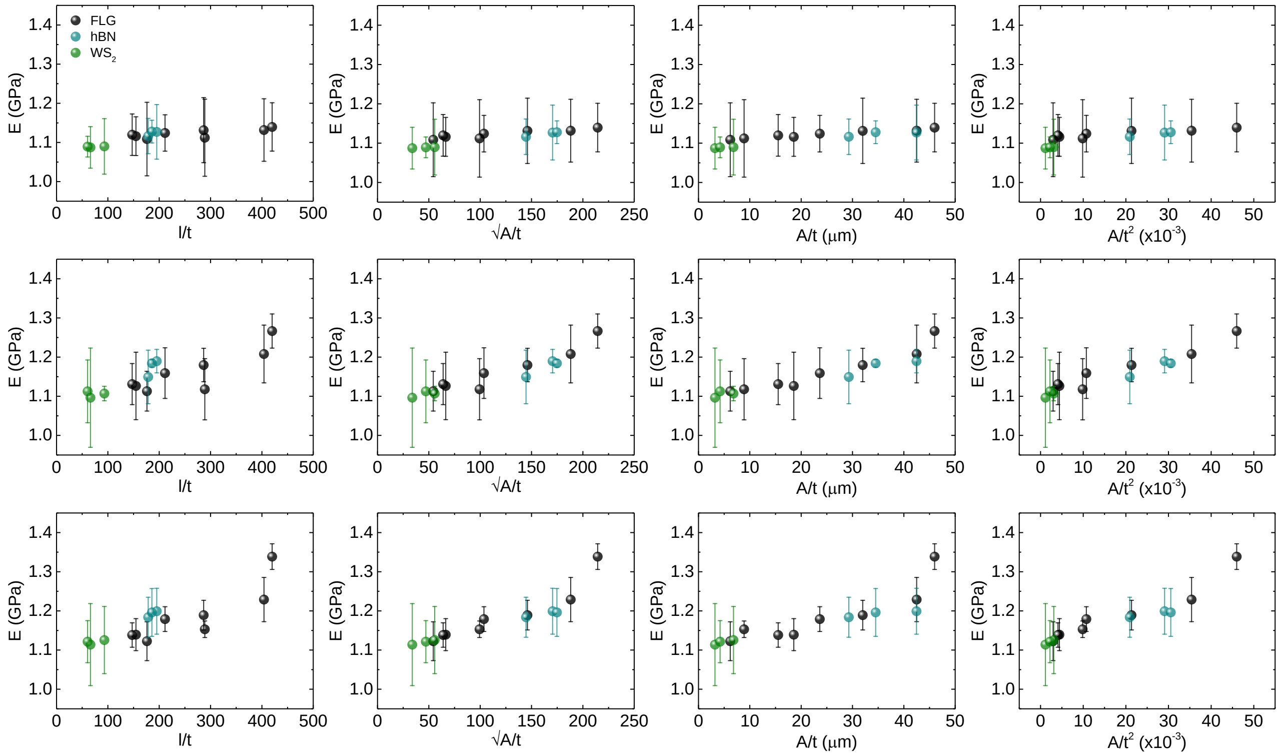

Figure 6.4. Study of Young's Modulus of composites as function of morphological properties, *i.e.*: *l/t* (first column), √*A/t* (second column), *A/t* (expressed in µm, third column) and A/t^2 (fourth column), and loading, *i.e.*: 0.01 wt % (first raw), 0.05 wt % (second raw), and 0.1wt % (third raw), of the fillers (FLG, black points, *h*-BN, cyan points, WS_2, green points).

Examining the graphs in Figure 6.4, a clear trend between *E* and 2D crystals *l/t*, √*A/t*, and *A/t* is lacking, whereas it is possible to linearly relate *E* with the quantity A/t^2. Being quantitative, the linear correlation between the data have been evaluated by considering the Pearson's coefficient, P_r [278], obtained by linearly fitting the values of *E* and the morphological parameters investigated. For a perfect linear correlation between two variables, $P_r = 1$, whereas $P_r = 0$ implies that there is no linear correlation between the variables [278]. Thus, as much P_r tends towards 1, the variables are linearly related [278].

In our case, P_r values obtained considering the parameter A/t^2 are the highest. In particular, for the loadings of 0.05wt % and 0.1wt % P_r is equal to 0.969 and 0.952, respectively, whereas for the parameter l/t, commonly used for linking mechanical properties of composites with the morphology of the fillers, is only 0.799 for the composite at 0.05 wt % loading and 0.769 for the composite at 0.1 wt % loading. This linear relationship can be related to the one predicted by the Cox model [279], which for negligible matrix/filler Young's modulus ratio predicts indeed a linear dependence. It is worth to note that the obtained behaviour is independent of the 2D fillers nature. Therefore, this model can be adapted to describe the relationship between 2D fillers structural properties and the mechanical properties of the polymer matrix and evidence the need to produce 2D fillers development of as much large A/t^2 in order to obtain composites with a high level of reinforcement.

A similar approach can be found in the work of Young et al. [280], in which the authors, starting from the rule of mixture and the shear-lag model [279], propose:

$$E_C \approx \frac{\eta_0 E_m}{12(1+\nu)} \varphi_f^2 \alpha^2 + E_m(1-\varphi_f) \tag{6.1}$$

Where ν is the Poisson's ratio of the matrix (for ABS ~ 0.35) and η_0 is the Krenchel orientation factor already defined for Eq. 1.8. It is worth noting that, in this mode, E_C is independent upon E_F whereas it depends upon $\varphi^2{}_f$ and $\alpha^2 = l^2/t^2 \propto A/t^2$ (equal to A/t^2 for square shaped flakes), the dependence herein proposed.

To underline the importance of using high A/t^2 flakes as fillers, by using 0.5 wt % our size selected FLG (FLG-6, sample with $A/t^2 \approx 46 \times 10^3$) as filler in a ABS matrix, it is possible to obtain the same increment in E obtained by using 10 wt % of glass fibres [268,273]. In fact, the normalised modulus (E/E_0) values are 1.36 and 1.34 for FLG herein used and glass fibres fillers reported in literature, respectively, but with a FLG loading that is 20 times lower with respect the glass fibres one [268,273].

A back-calculation of the effective Young's Modulus of fillers (E_{eff}), exploiting the rule of mixtures (Eq. 1.7), has been performed in order to evaluate the effective individual reinforcements given by the 2D crystals (see Table6.4). In particular, the values of E_{eff} of the flakes in the polymer matrix at 0.01 wt % are ~1.28 TPa, ~1.08 TPa, and ~0.80 TPa for the samples FLG-6 ($A/t^2 = 46 \times 10^3$), *h*-BN-3 ($A/t^2 = 31 \times 10^3$), and WS_2-3 ($A/t^2 = 3 \times 10^3$), respectively. It is worth to note that these values are beyond the theoretical ones of the pristine one-atom-thick 2D flake (*i.e.*, ≈1 TPa, 0.86 TPa, and 0.273 TPa for graphene [84], *h*-BN [85], and WS_2 [281], respectively). Thus, the mechanical properties of the as-prepared composite are better than the sum of the ideal properties of its phases (polymer matrix and 2D fillers), *i.e.* the 2D flakes also can improve E of the surrounding matrix and are able to activate a synergic effect [282]. The full back-calculated data are summarized in Table 6.2. Recently, a few works have reported the mechanical properties of different polymers reinforced with graphene-based materials where the effective Young moduli of the graphene-like fillers are higher than the theoretical one [78].

To identify the key-factor of the relationship between the enhancement of polymer composites mechanical properties induced by few-layer 2D flakes and their own structural morphology, the A/t^2 is plotted as a function of the 2D filler loading. The symbols are empty and filled for those samples where the back-calculated effective modulus of the 2D flake is lower and beyond than the theoretical values, respectively (Fig. 3). In particular, it is important to note that for high A/t^2 values (e.g. > 50 × 10^3 in the case of FLG), it could be possible to extend the "ultra-reinforcement" region to larger volume fractions, where the predicted level of reinforcements can possibly reach the theoretical values of improvement in stiffness, *e.g.* 200% for 0.5 wt % loaded FLG/ABS composite.

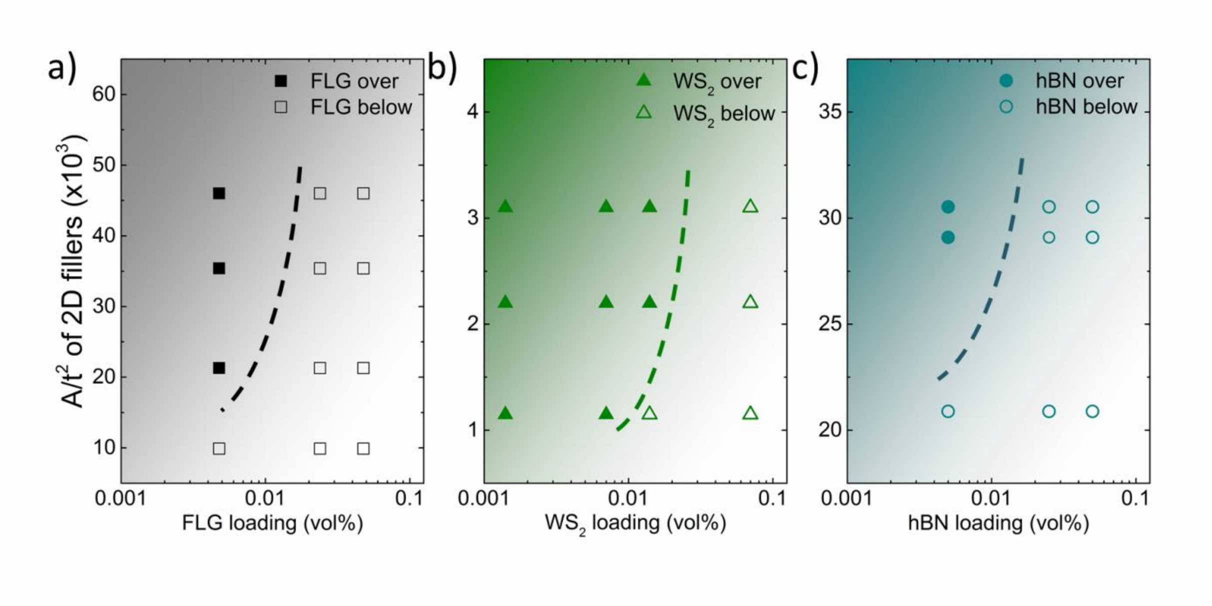

Figure 6.5. The back-calculated Young's moduli (E_{eff}) of 2D fillers as a function of loading and A/t^2 ratio of 2D fillers. a) FLG, b) *h*-BN, c) WS_2. Filled symbols indicate flakes with a E_{eff} over the theoretical limit of flakes stiffness, whereas empty symbols indicate flakes with a E_{eff} over the theoretical limit of flakes stiffness.

6.3 Conclusions

In summary, 2D crystals, namely FLG, *h*-BN, and WS_2 flakes filled ABS-based composites mechanical reinforcements as the function of flakes morphologies and loadings are studied. In agreement with both experimental and back-calculated results, the highest mechanical reinforcement of composites (referred to pristine ABS) is reached with the largest A/t^2 ratio. Thus, in this chapter is studied the relationship between physical properties of polymer composites and morphologies of 2D fillers, namely evaluated the functional parameters, *i.e.* A and t of the 2D crystal flakes to control the mechanical reinforcement of thermoplastics-based composites. As a proof-of-principle demonstration of the universality of the 2D fillers in their polymer-based nanocomposites, tailoring the FLG flakes structural dimensions achieving a 24-36% improvement of tensile modulus at 0.1-0.5 wt % filler loading with highest A/t^2 ratio (46×10^3) without the need of chemical functionalization of the 2D fillers.

Additionally, this work leads to new prospects for nanoscale-related frontiers of materials science, for example, study the shape effect of 2D materials for improved physical properties in their composites, or probing the physical properties by the aspect ratio or *vice versa*. In the long-term, extending the research of this field the investigation of size selection effect of 2D crystals opens new avenues in the exploration of their polymer-based nanocomposites' further physical-chemical properties, *e.g.* gas permeability, electrical-, and thermal conductivities. In a practical viewing, using cheap and large quantity existing few-layer 2D crystals and developing further extrusion-based technologies (*e.g.* plastic film production by blowing), functional materials will be available in packaging, agriculture, and healthcare-related applications selecting the proper 2D filler.

Table 6.2. Comparison of E, σ_Y and σ_U of different FLG flakes filled ABS samples (FLG-1, FLG-2, FLG-3, FLG-4, and FLG-5). The E, σ_Y, and σ_U are 1078.8±57.8 MPa, 18.91±5.48 MPa, and 24.20±4.49 MPa, respectively in the case of pristine ABS. Errors are given as standard deviations (s.d.). All values are in MPa.

loading (wt %)	**FLG-1**		**FLG-2**		**FLG-3**		**FLG-4**		**FLG-5**	
	E	**s.d. E**	**E**	**s.d. E**	**E**	**s.d. E**	**E**	**s.d. E**	**E**	**s.d. E**
0.01	1116.2	19.5	1119.8	53.2	1124.2	46.4	1108.6	93.9	1112.0	98.4
0.05	1126.3	86.1	1131	52.4	1159	14.7	1112.8	50.7	1117.8	78.2
0.1	1139.3	40.8	1138.4	31.1	1178.9	31.6	1122.5	9.61	1153.4	21.1
0.5	1152.8	66.4	1159.9	10.4	1201.4	57.2	1129.3	8.17	1157.8	37.7
1	1164.2	36.6	1159.2	62.5	1266.8	78.9	1141.5	22.2	1175.5	37.9
	σ_Y	**s.d. σ_Y**	**σ_Y**	**s.d. σ_Y**	**σ_Y**	**s.d. σ_Y**	**σ_Y**	**s.d. σ_Y**	**σ_Y**	**s.d. σ_Y**
0.01	20.4	1.0	18.9	5.7	26.3	1.5	24.81	2.0	23.7	2.1
0.05	21.9	2.4	19.1	4.4	25.0	1.6	21.45	5.0	25.29	1.3
0.1	22.2	0.9	20.5	4.5	25.8	2.2	20.99	2.8	24.51	1.5
0.5	25.6	1.2	19.8	7.6	26.4	1.2	22.82	4.6	23.65	0.4
1	24.6	5.1	21.1	4.6	28.4	2.2	25.64	1.4	25.38	0.5
	σ_U	**s.d. σ_U**	**σ_U**	**s.d. σ_U**	**σ_U**	**s.d. σ_U**	**σ_U**	**s.d. σ_U**	**σ_U**	**s.d. σ_U**
0.01	21.1	0.9	25.8	1.5	25.9	0.9	23.7	2.1	25.5	1.3
0.05	22.4	2.8	24.5	0.7	26.0	1.3	25.3	1.3	25.8	1.2
0.1	22.5	0.8	25.2	1.8	27.3	2.3	26.9	0.6	26.1	0.8
0.5	26.4	0.8	27.1	1.3	25.5	0.9	26.5	0.8	26.5	0.1
1	26.8	1.4	27.2	0.6	29.7	2.1	26.9	1.1	26.0	1.1

Table 6.3. Comparison of E, σ_Y, and σ_U of hBN (hBN-1, hBN-2, hBN-3) and WS2 (WS2-1, WS2-2, WS2-3) flakes filled ABS samples. The E, σ_Y, and σ_U of pristine ABS are 1078.8±57.8 MPa, 18.91±5.48 MPa, and 24.20±4.49 MPa, respectively. Errors are given as standard deviations (s.d.). All values are given in MPa.

loading	***h*-BN-1**		***h*-BN-2**		***h*-BN-3**		**WS_2-1**		**WS_2-2**		**WS_2-3**	
(wt %)	**E**	**s.d E**	**E**	**s.d. E**	**E**	**s.d. E**	**E**	**s.d. E**	**E**	**s.d. E**	**E**	**s.d. E**
0.01	1126.9	69.7	1116.3	45.1	1127.7	28.9	1087.3	52.9	1089.9	70.8	1089.2	26.4
0.05	1189.6	30.1	1149.3	68.4	1184.1	9.8	1096.3	126.8	1106.8	18.4	1112.5	80.1
0.1	1199.2	58.6	1183.7	51.1	1196.1	31	1113.8	104.7	1125.4	85.7	1121.3	53.7
0.5	1237.2	91.5	1218.2	57.6	1240.6	78.4	1121.4	64.4	1138.7	40.0	1140.6	95.7
1	1276.1	79.0	1251.8	71.4	1275.2	78.7	1141.2	95.6	1147.1	77.6	1147.8	87.2
	σ_Y	**s.d σ_Y**	**σ_Y**	**s.d σ_Y**	**σ_Y**	**s.d σ_Y**	**σ_Y**	**s.d σ_Y**	**σ_Y**	**s.d σ_Y**	**σ_Y**	**s.d σ_Y**
0.01	24.0	4.6	29.5	1.1	26.1	1.9	28.7	0.8	26.4	2.5	28.8	0.8
0.05	27.6	4.2	30.0	4.1	26.4	0.3	27.7	1.3	28.8	1.0	27.7	1.3
0.1	28.0	5.2	30.2	1.3	26.7	2.5	28.8	2.9	28.9	1.9	28.7	2.2
0.5	29.8	1.0	30.6	0.6	27.0	0.3	29.8	1.5	27.7	0.7	29.2	0.9
1	29.9	1.7	30.8	1.1	25.7	0.6	29.4	1.6	30.1	1.5	29.4	1.6
	σ_U	**s.d σ_U**	**σ_U**	**s.d σ_U**	**σ_U**	**s.d σ_U**	**σ_U**	**s.d σ_U**	**σ_U**	**s.d σ_U**	**σ_U**	**s.d σ_U**
0.01	27.5	3.5	30.6	0.9	28.4	0.6	29.2	0.8	29.8	1.6	29.2	0.8
0.05	29.5	1.4	30.0	3.5	27.1	0.9	29.1	0.7	28.9	0.9	28.4	1.0
0.1	30.9	0.6	30.6	1.1	28.2	1.0	29.7	1.8	29.1	1.9	28.7	2.2
0.5	31.2	1.5	31.0	0.7	27.5	0.5	29.5	0.8	28.4	0.6	30.0	1.4
1	30.0	1.7	31.1	0.8	25.9	0.8	30.3	1.6	30.4	1.3	28.9	1.8

Tables 6.4 The computational back calculated E_{eff} of the 2D flakes from that of the polymer matrix, using the rule of mixture. All values are given in GPa.

loading (wt %)	**FLG-1**	**FLG-2**	**FLG-3**	**FLG-4**	**FLG-5**	**FLG-6**	**FLG-7**	**FLG-8**
0.01	788.6	867.6	960.7	631.7	704.1	1286	1119.4	1111.7
0.05	202.0	221.9	340.4	145.1	166.0	795.2	547.2	428.1
0.1	129.1	127.1	213.0	93.5	158.1	550.6	318.6	234.4
0.5	32.4	35.4	52.9	22.4	34.5	168.2	—	—
1	19.1	18.1	40.8	14.3	21.5	—	—	—

loading (wt %)	***h*-BN-1**	***h*-BN-2**	***h*-BN-3**	**WS_2-1**	**WS_2-2**	**WS_2-3**
0.01	1060.4	827.1	1078.3	612.1	800.1	754.1
0.05	488.9	311.5	464.8	254	405.4	487.3
0.1	266.1	232.2	259.3	253.6	337.4	307.9
0.5	70.9	62.5	72.3	62.6	87.4	90.2
1	44.5	39.2	44.3	46.1	50.3	50.9

CHAPTER 7

WJM-exfoliated 2D crystals/PLA composites

7.1 Introduction

The breaking-through exploitation of 2D crystals as fillers in polymer-based composites relies on the availability of a scalable and industrially relevant synthesis method able to produce defect-free nanosheets [1,38,39,154]. Amongst the several 2D crystal synthesis methods, the LPE of layered crystals has been extensively proposed as an alternative method for the exploitation of 2D crystals, in particular, ideal for the composite field [39,47,89,139,219], as discussed in previous chapters.
Seeking for industrially relevant approaches, *i.e.* the time, weight-yield and a cost-effective production of the 2D crystals without compromising the crystalline-integrity, the WJM, developed in our laboratories, has emerged as a promising method for obtaining 2D crystals [153,154]. Particularly, the WJM allows to obtain 2D crystals with concentrations of 10 g L^{-1} [153,154], and a yield of 100%, (the weight ratio between the final processed material and the starting graphite flakes). Additionally, the WJM guarantees a production capability of 2.35 L h^{-1} [153,154], *i.e.* the time required to produce one gram of exfoliated graphite is only 2.55 min, thus outperforming other proposed synthesis approaches *i.e.* shear exfoliation [38] and micro-fluidization [155,192,193].

In this chapter, the changes in the mechanical, electrical and thermal properties of graphene and *h*-BN exfoliated by WJM as fillers in a PLA matrix will be presented. Interestingly, and with the aim to obtain further knowledge regarding the interaction between the fillers and the polymer matrix, I have developed three-phase hybrid composites using graphene and *h*-BN together as fillers, revealing a synergistic effect that exists for the composite's stiffness.

Graphene and *h*-BN have been extensively used in the composite field as fillers, with the aim to improve the thermal, mechanical or electric properties of the final composite [47,78,85,186]. Recently, PLA is receiving a growing interest in the scientific and industrial community because it is considered as a "green" alternative to other commercial polymers [38]. Additionally, PLA is a compostable, biodegradable thermoplastic made from renewable sources (*i.e.*, corn) [38]. These characteristics make PLA a promising material for packaging [38]. Moreover, the introduction of carbonaceous fillers such as GNPs and GO into PLA matrix revealed no increment of cytotoxicity compared to the pure polymer [283], paving the use of such composites for biomedical applications [283].

Details on the production parameter used for the samples development, *i.e.*, WG and W*h*BN, have been presented in section 2.2 whereas their morphological and structural characterization has been presented in section 3.2.3.

7.2 Composites morphological characterization

The morphology of the composites, which have been produced according to the procedure reported in section 2.4.4, has been evaluated by SEM analysis (Figure 7.1). The fillers in WG/PLA (Figure 7.1a) and W*h*BN/PLA (Figure 7.1b) composites at 0.5% loading appear homogeneously distributed and aligned inside the PLA matrix. The alignment is promoted by the shape of the platelet-like fillers and further endorsed by the hot-pressing process [86,284]. The same is valid for the W(G+*h*BN)/PLA composite (Figure 7.1c) at 0.5% total loading (0.25% WG + 0.25% W*h*BN). For composites with higher fillers concentrations, *i.e.*, the 10% loaded W(G + *h*BN)/PLA composite, agglomeration effects occur, as evidenced in Figure 7.1d. Note that, because of the fillers high specific surface area (~ 2630 m^2 g^{-1} for graphene and *h*-BN single layers, considering their lattice parameters and atoms weight), the fracture surface is covered by the fillers.

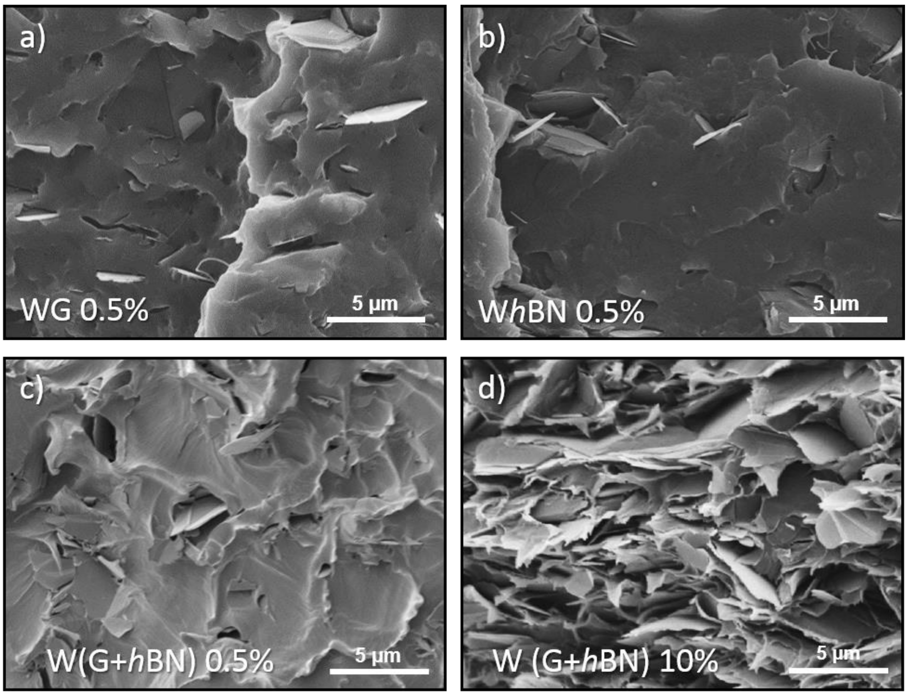

Figure 7.1. Morphological characterization of composites by SEM analysis: a) WG/PLA at 0.5% loading, b) W*h*BN/PLA at 0.5% loading, c) W(G + *h*BN)/PLA at 0.5% loading, d) W(G + *h*BN)/PLA at 10% loading.

7.3 Composites mechanical characterization

Mechanical properties of composite films are measured using an Instron dual column tabletop universal testing System 3365, with 5 mm min^{-1} cross-head speed. The tensile measurements are carried out on five different specimens for each film according to ASTM D 882 Standard Test Methods for Tensile Properties of Thin Plastic Sheeting. Results obtained from uniaxial tensile testing on composites are presented in Figure 7.2, where the Young's Modulus (E), Figure 7.2a, and the ultimate tensile strength (σ_U), Figure 7.2b, are plotted. The former is defined as the slope of the stress vs. strain curve in the elastic region, while the latter is defined as the higher stress value reached in the stress vs. strain curve. Detailed mechanical characterization of composites, with reported standard errors on measurements, can be found in Figure 7.2c-h. The Young's Modulus of composites (Figure 7.2a) increases with the filler concentration, from 1.95 ± 0.06 GPa of neat PLA to 2.30 ± 0.08 GPa (a 18 % increase), 2.35± 0.10 GPa (+ 20 %), and 2.48 ± 0.12 GPa (+ 27 %) at 0.5% loadings of WG, W*h*BN and W(G + *h*BN), respectively. Noteworthy, the values obtained by the composites with double fillers (W(G + *h*BN)/PLA)) are higher than the only-one-filler composites. This synergistic effect can be ascribed to the improved dispersion of the two fillers inside the matrix [78,285], in particular, by the interspace filling of the two fillers that changes the stress distribution and prevents, at low loadings, crack propagations at the interfaces with the polymer matrix [285]. Moreover, as reported in the case of graphene/CNTs [286], the introduction of an extra filler also prevents the aggregation or re-staking of same-type filler, thus further promoting the polymer penetration between filler agglomerates [286]. For a 10% filler loading of (G + *h*BN), E increases to 3.83 ± 0.34, representing a ~ 100 % improvement, whereas for the single filled-composites of increment is of ~ 75 %.

However, 10% loadings are detrimental for σ_U. In fact, σ_U is increased at low concentrations, *i.e.*, at 0.1% mass loading of W*h*BN a 30 % increase σ_U is obtained (63.2 ± 3.1 MPa vs. 48.7 ± 5.8 MPa of pristine PLA). Whereas, the enhancement is reduced at 2% loading, obtaining similar σ_U to pristine PLA. As the filler concentration increases the σ_U continuously decreases, with values lower than the pristine values. Independently from the type of filler, for concentration higher than 2% the composites obtained are stiff but brittle, *i.e.*, their σ_U, elongation-at-break and, therefore, toughness are lower that pristine PLA. This phenomenon is ascribed to fillers aggregation [47,84,85,94].

As previously seen, a useful parameter for the evaluation for the effective stiffness reinforcement made by a filler in a composite is by back-calculating its effective Young's Modulus (E_{eff}) starting from the rule of mixtures, according Eq. 1.7. For 0.1% loading, E_{eff} for WG, W*h*BN and W(G+*h*BN) are 240 GPa, 190 GPa and 250 GPa, respectively.

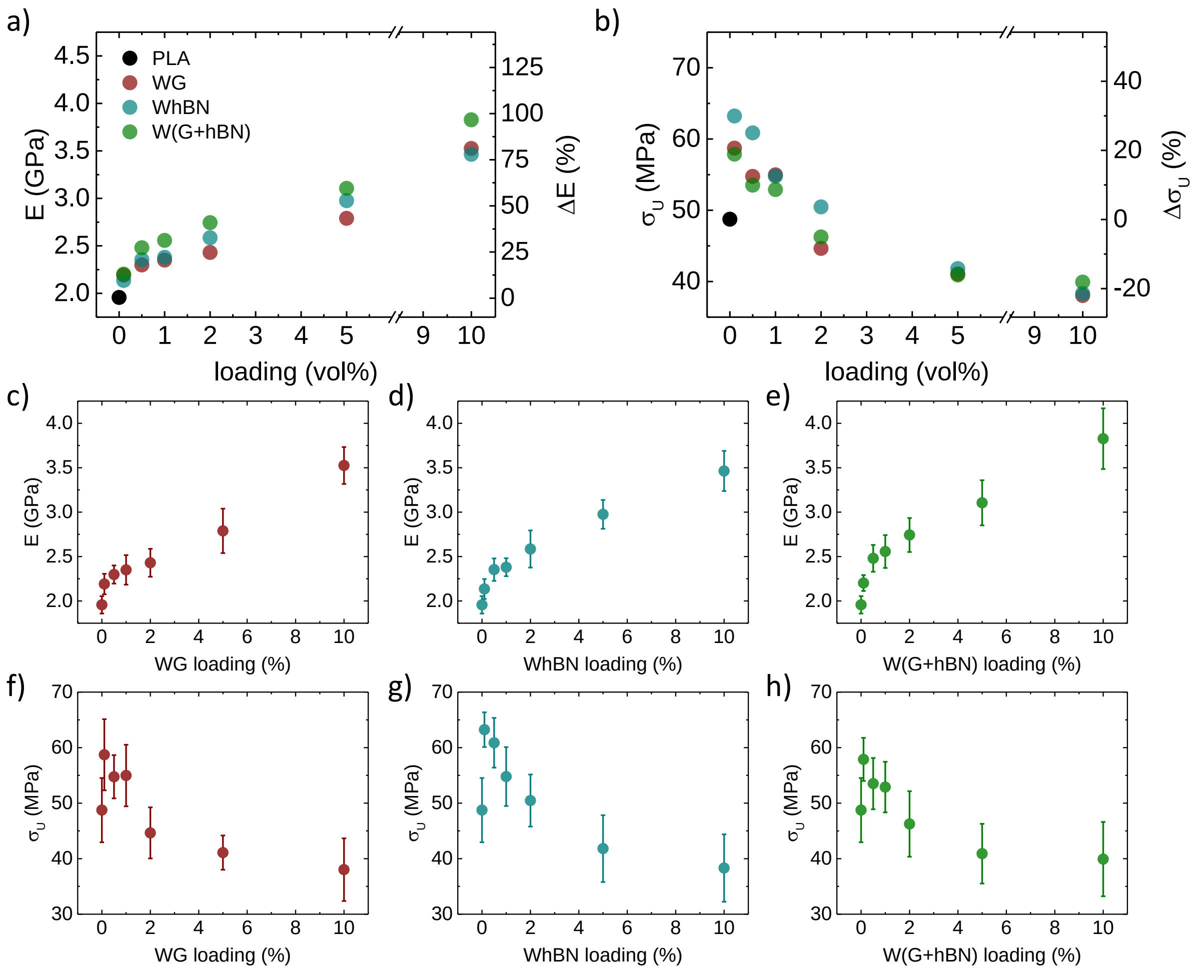

Figure 7.2. Mechanical characterization of composites: a) Young's Modulus and b) ultimate tensile strength of the WG/PLA (red), W*h*BN/PLA (cyan) and W(G+*h*BN)/PLA (green) composites *vs.* fillers loading. c-e) details of Young's Moduli and (f-h) ultimate tensile strength of composites.

7.4 Electrical and thermal conductivity

The exploitation of polymers into the field of electronics is limited to specific tasks due to their low electrical ($<10^{-8}$ Scm^{-1} [109]) and thermal (<0.5 W m^{-1} K^{-1} [115,287]) conductivities, specifically the polymers are used mainly as thermal and electric insulators. In particular, in view of applications as heat sinks for electronic packaging, the development of high thermal conductive polymers is of paramount importance [288–290]. The use of electrical or thermally conductive fillers, such as graphene, CNTs or *h*-BN, allows the development of electrical and/or thermal conductive composites, useful for those applications in which polymers are discriminated [1,109,115]. In fact, graphene has both exceptionally high electrical (up to 10^6 S cm^{-1} [291]) and thermal (in-plane ~ 5000 W m^{-1} K^{-1} [291]) conductivities, while *h*-BN has high thermal conductivity (in-plane ~ 2000 W m^{-1} K^{-1} [14])

but it is an electrical insulator (bandgap ~ 6 eV [14]). The incorporation of graphene into polymer matrices leads to electrically and thermally conductive composites that can be exploited as electromechanical sensors [101], e-textiles [292], and electromagnetic/radio frequency interference shields [293]. Whereas both graphene- and *h*-BN-based polymer composites have been widely used as thermal interface materials [89,109,123,294], the use of *h*-BN instead of graphene is suitable for those applications that require electrical insulation, *e.g.* electronic packaging [295,296].

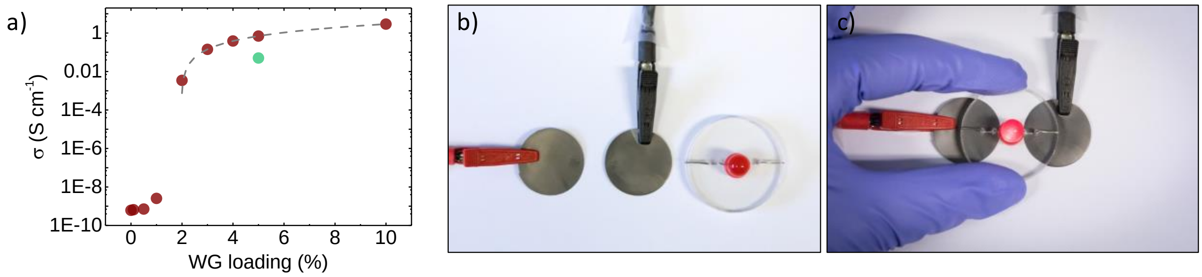

Figure 7.3. Electrical characterization of composites: a) electrical conductivity *vs.* WG loading, and b-c) use of WG/PLA 10% composite as electrode.

The addition of 10% of WG flakes into PLA allows obtaining an electrical conductive composite (σ = 2.9 S cm^{-1}, about 10 order of magnitude higher than pristine PLA, Figure 7.3a) capable to lit-on a LED (Figure 6b-c). At WG flakes loading below 1% the electrical conductivity of composites is similar to pristine PLA (~ 5 × 10^{-10} S cm^{-1}), since the percolation pathway between WG flakes is not achieved, as is evidenced by SEM analysis revelling isolated flakes dispersed into matrix for composite at 0.5% loadings (Figure 7.3a), and charge transfer is ruled by tunnelling effects [105,109]. Contrarily, above 1% loading, the percolation threshold, φ_c in volume fraction, is reached and a conductive path for charge carriers is generated [105], inducing an increase in electrical conductivity. The variation of electrical conductivity of composites *vs.* WG loading follows the classical percolation power-law relation (Eq. 1.13) [105].

Fitting the experimentally derived values of electrically conductivity (dotted grey lines in Figure 6a and inset), are derived φ_c = 0.019 (1.9 %), σ_0 = 115 S cm^{-1}, and t = 1.4, the last indicating a two-dimensional conductive pathway mainly. Finally, to understand the influence of an insulating filler into an electrically conductive composite, we monitored the changes on the electrically conductive composite by adding *h*-BN, thus having the sample W(G + *h*BN) 10% (green dot in Figure 7.3a, plotted in correspondence of WG relative loading, 5%). Comparing the conductivity of W(G + *h*BN) with the composite with the same amount of WG loading (5 %, $\sigma = 0.7$ S cm^{-1}), there is one order of magnitude reduction ($\sigma = 0.05$ S cm^{-1}), owing to the interruption of conductive pathways.

Anisotropic thermal conductivity of composites at 10% loaded composites (WG/PLA 10%, W*h*BN 10% and W(G + *h*BN)/PLA 10%) are shown in Figure 7.4a (in-plane conductivity in blue columns, through-plane conductivity in red columns), and compared with the thermal conductivity of PLA (black column of Figure 7.4a, 0.13 W m^{-1} K^{-1}). As expected, considering the orientation of fillers in the composite films, there is a large difference between the obtained in-plane and through-plane thermal conductivity values (*c.a.* 1 order of magnitude). A summary of thermal performances is reported in Table 7.1.

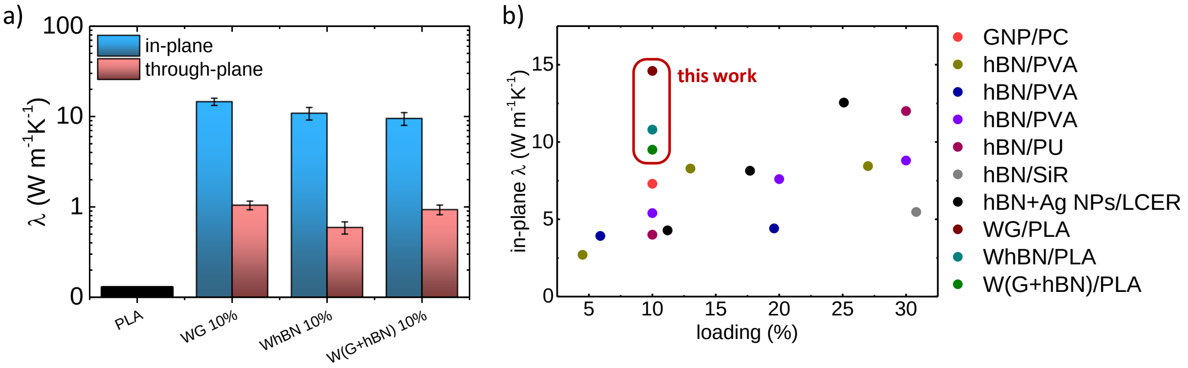

Figure 7.4. Thermal characterization of composites. a) in plane and through-plane thermal conductivities of PLA, WG/PLA 10%, W*h*BN/PLA 10% and W(G+*h*BN)/PLA 10%; b) comparison of obtained results with the state-of-the-art reports: red GNP/PC [297], dark yellow *h*-BN/PVA [298], royal *h*-BN/PVA [299], violet *h*-BN/PVA [300], magenta *h*-BN/polyurethane (PU) [301] grey *h*-BN/silicone rubber (SiR) [302], black *h*-BN+silver nanoparticles (Ag NPs)/liquid crystalline epoxy resin (LCER) [303]. The points inside the red square are this-work results.

The obtained values place the composites as the state-of-the-art of graphene-based or *h*-BN-based polymer composites in terms of thermal conductivity [287,299,304], evidencing the quality of the flakes obtained by the exfoliation with the WJM approach. The Figure 7.4b shows a plot obtained comparing in-plane thermal conductivity of herein produced composites together with relevant 2D crystals-based polymer composites reported in literature. The state-of-the-art for thermal conductivities of different composites reported is inferior to those achieved by our composites at comparable filler loadings. Noteworthy, a recent work describes the production of *h*-BN (95 wt %)/thermoplastic polyurethane (5%) composite with an in-plane thermal conductivity of

50.3 W m^{-1} K^{-1} [301], but considering loadings equal to this work (~ 10%) the thermal conductivity drops below 10 W m^{-1} K^{-1}[301]. The thermal synergistic effect is not observed in our composite. The synergistic effect, for non PLA matrixes, is usually attributed to the use of two different fillers [285,293,305–309]. Interestingly, the synergistic effect for thermal conductivity due to the use of bi-fillers and PLA has not been verified, as reported in the work of Mosanenzadeh et al. [310]. In fact, the composite prepared by using a 1:1 mixture of GNPs and *h*-BN (total loading 33.3%) has shown a thermal conductivity equal to that obtained with only the *h*-BN as filler (2.77 W m^{-1} K^{-1}) [310]. Moreover, when decreased the relative amount of GNPs compared to *h*-BN, the thermal conductivity of the overall composites is lower compared to the case of single-filler [310].

This could be addressed by the spatial arrangement of the two fillers inside the matrix or effects given by filler/filler or filler/matrix interfacial thermal resistances, due to phonon mismatch at the interfaces, lowering the efficiency of heat transfer [109,115,311].

Table 7.1. In-plane and through-plane thermal conductivity of composites with 10% total loading.

Filler(s)	**Thermal Conductivity (W m^{-1} K^{-1})**	
	in-plane	through-plane
WG 10%	14.6 ± 1.3	1.1 ± 0.1
W*h*BN 10%	10.8 ± 1.7	0.6 ± 0.1
W(G+*h*BN) 10%	9.5 ± 1.5	0.9 ± 0.1

7.4. Conclusions

2D crystal-based composites have been produced by solution blending using PLA as matrix, an environmentally friendly, cheap and biodegradable polymer, and fillers obtained by a production method developed in our lab, the wet-jet mill -assisted liquid phase exfoliation, which allows the production of large-scale, defect-free 2D crystals.

It is essential to highlight the importance of selecting the loadings and type of the fillers; it is possible to obtain composites with tuned on-demand mechanical, electric and/or thermal transport properties. Specifically, are found σ_U increasing of 20% and 30% (compared with neat PLA) with a loading of 0.1% of graphene and *h*-BN fillers, respectively. Moreover, at 10% of graphene loading, the composite shows an electrical conductivity (σ) of 2.9 S cm^{-1}, representing 10 orders of magnitude increment compared with the neat PLA ($\sigma = 10^{-11}$ S cm^{-1}). Furthermore, in-plane thermal conductivity of 14.6 W m^{-1} K^{-1}, that corresponds to a more than 100-fold increment with respect to neat PLA (λ = 0.13 W m^{-1} K^{-1}).

As matter of fact, I have demonstrated the composition of a broad portfolio of composites with specific properties:

(1) metal-grade electrical conductivity (σ = 2.9 S cm^{-1}) and composites with high thermal conductivity (*i.e.* in-plane ~ 10 W m^{-1} K^{-1}) by using 10% of WG/PLA,

(2) semiconductor-grade electrical conductivity (σ = 0.05 S cm^{-1}), selecting 10% of W-(G+*h*BN)/PLA, or

(3) insulating-grade conductivity ($\sigma = 10^{-10}$ S cm^{-1}), selecting 10% of W*h*BN/PLA.

These findings reveal that WJM is a promising method for the exfoliation of layered materials and their use as fillers in polymer-based composites.

Conclusions and perspectives

Up to date, the search for novel fillers is still one of the crucial quests for the development of high-performance polymer-based composites. In this context, 2D crystals have been recognized as promising, cost-effective, candidates to improve the mechanical, electrical, and thermal properties of polymers and have wide potential applications in many fields. However, as seen for CNT/polymer composites, the improvements are far from what is needed for many applications: many technical barriers involving structure control, dispersion of graphene in the matrix, interfacial interaction between graphene and matrix, and contact between individual graphene must be taken into account to realize the wide applications of these advanced composites.

The intrinsic properties of 2D crystals, in particular their stiffness and thermal and electrical conductivities, are one of the most important factors that determine the ultimate mechanical and other functional properties of 2D crystals/polymer composites. To meet the practical application for polymer composites, mass fabrication of 2D crystals is urgently required. Large quantities of 2D crystals are usually prepared by the LPE of their bulk layered counterparts. In this thesis it has been shown that LPE is a versatile synthesis technique that can be exploited for the production of several 2D crystals, in particular graphene, *h*-BN and WS_2. Moreover, the introduction of the WJM approach, presented in sections 2.2 and 3.2 allow an industrial scale production of 2D crystals with rates of 23.5 g h^{-1}, and a yield by weight of 100%.

Having a uniform dispersion of 2D crystals in polymer matrices for targeted applications is also a fundamental challenge because the properties of polymer-based composites strongly depend on the spatial distribution of fillers, as well as having strong interfacial interactions between fillers and host polymers. Superior mechanical properties, for example, can be achieved only when the filler is strongly bonded to the polymer matrix. Robust interfacial interactions can also contribute to the decrease of interfacial thermal resistance and T_g, thus leading to an increase of the thermal conductivity and thermal stability of the final composites. In this view, the presence of functional groups in functionalized 2D crystals, or oxidized and partially oxidized graphene (in form of GO or RGO), that can interact with polymer chains, facilitate uniform dispersion and restacking of the flakes. On the other hand, functionalizations usually hinder the pristine properties of 2D crystals, *e.g.*, stiffness of GO is 200 to 500 GPa lower than pristine graphene and it is both thermal and electrical insulator. For this reason, this thesis faces only with pristine 2D crystals, and a uniform dispersion is tried to be achieved acting on composite's production techniques, *i.e.* by exploiting solution blending.

Finally, as presented in the theoretical background in section 1.3, it is of extremely importance the morphology of the fillers for the determination of the final properties of composites, in particular their aspect ratio. The understanding of correlations between 2D crystals morphology and composite properties has been the main focus of the research presented in this thesis.

In the following, a brief summary of the most relevant results achieved.

Graphene/PC composites

The production of graphene/PC composites with improved mechanical and electrical properties has been achieved by using a simple and scalable solution blending method to disperse SLG/FLG flakes prepared by LPE in the polymer matrix. A solvent-exchange process is carried out to re-disperse the exfoliated SLG/FLG flakes from NMP, high boiling point and toxic solvent, in an environmentally friendly, low boiling point, solvent, *i.e.* 1,3-dioxolane, which is also used to dissolve the PC pellets, thus facilitating the mixing of the polymer dispersion with the SLG/FLG flakes. The loading of SLG/FLG flakes improves the mechanical, thermal properties, and electrical conductivity of the polymer, reaching a +26% improvement of E at 1 wt % loading, and an electrical conductivity 10^{-3} S m^{-1} at 10 wt % with a percolation threshold achieved at 0.55 vol%. The as-prepared PC/G composite with the aforementioned reinforced properties can be a promising material for 3D printing-based applications.

h-BN **/PC composites: looking for an environmentally friendly approach**

The LPE of bulk *h*-BN powder has been achieved following an environmentally friendly approach, avoiding the use of toxic solvent for the dispersion and exfoliation of flakes and instead using a water/surfactant solution. Moreover, by exploiting cascade ultra-centrifugation, two populations of flakes with aspect ratio, i.e., lateral size over thickness, equal to 250 and 350, respectively, have been obtained. The *h*-BN flakes with tuned aspect ratio are subsequently used as filler in a PC matrix by exploiting solution blending. The composite mechanical properties have been tested, finding that flakes with higher aspect ratio show superior reinforcements in terms of both E and σ_U, compared with their lower aspect ratio counterparts. As an example, at 0.1 wt % of loading, the increment of E, with respect to pristine PC, is of ~ 22 % for composites produced with higher aspect ratio fillers, whereas it is instead of ~ 17 % for lower aspect ratio fillers.

2D crystal/ABS composites: the role of surface area

A fine tuning of morphological properties of several 2D crystals, *i.e.*, graphene, *h*-BN and WS_2, previously obtained by LPE of their bulk counterparts, has been achieved by exploiting SBS and cascade ultra-centrifugations. TEM and AFM analyses revealed that the as-produced 2D crystals have surface area in the range 0.01 – 0.8 μm^2, and thicknesses in the range 0.9 – 4.2 nm. The 2D crystals have been used as filler in ABS matrix, obtaining composites in form of pellets, filaments and films. Mechanical properties of composites have been evaluated and linked with the morphological properties of fillers, in order to identify the key factor for mechanical reinforcement. The results obtained evidenced a linear correlation between the enhancements in Young's Modulus of composites and the parameter A/t^2, a novel and herein proposed representations of aspect ratio of 2D-shaped fillers.

As an example, by using graphene flakes of highest A/t^2 value (46×10^3) it is possible to enhance the Young's Modulus of the composite of 24% and 36%, compared to bare ABS, at filler loadings of 0.1 and 0.5 wt %, respectively.

Moreover, it has been shown the existence of an ultra-high efficiency regime emerging at 2D crystals loading below 0.1 wt % further expanding as A/t^2 increases. In these conditions, the mechanical reinforcement of the composite surprisingly exceeds that expected assuming the ideal stiffness of the corresponding 2D monolayers implying a synergic effect between the flake and the surrounding polymer matrix.

WJM-produced 2D crystals as fillers in PLA-based composites

The 2D crystals used as fillers in polymer composites is an attractive and interesting from the industrial point of view only if exists a scalable production method. The high-pressure WJM approach guarantees a production capability of 2.35 L h^{-1} of dispersions of 2D crystals, which can be subsequently dried, obtaining a powder. It has been shown that, large area, single- and few-layers graphene and *h*-BN flakes in powder form can been obtained by means of WJM and used as fillers in PLA matrix, exploiting solution blending. By tuning the concentration and type of the filler, we tune on-demand the mechanical, electric and thermic properties of the composites. Is has been therefore demonstrated the composition of a broad portfolio of composites with specific properties, *e.g.* composites with a thermal conductivity higher than 10 W m^{-1} K^{-1}, that can be either electrically conducting or electrically insulating by selecting graphene or *h*-BN as filler, respectively.

Future perspectives

The results presented in this thesis provide convincing evidence of the effective composite reinforcing capabilities of 2D crystals. While low quantities of fillers result in large increases in mechanical, thermal and electrical properties compared to neat matrix materials, there are still many challenges that need to be overcome in order to translate the lab-scale findings and evidences in industrially relevant products of everyday lives.

From this thesis, it has been noted that production of high-quality, large-area 2D crystals in a robust technique and mass scale remains the bottleneck that need to be overcome at the first instance to enable 2D crystals-based polymer composites practical applications. This has been tackled by the introduction of the WJM approach as 2D crystals production technique able to guarantee these characteristics.

Further improvements have to be done in a more precise structure control of 2D crystals, trying to obtain 2D crystals of known and monodisperse morphological properties, *i.e.*, surface area, lateral size and thickness. Moreover, the use of environmentally friendly, low-cost solvents for the exfoliation and stabilization of bulk layered materials is still one of the main challenges for researches exploiting LPE techniques.

References

[1] A.C. Ferrari, F. Bonaccorso, V. Falko, K.S. Novoselov, S. Roche, P. Bøggild, S. Borini, F. Koppens, V. Palermo, N. Pugno, J.A. Garrido, R. Sordan, A. Bianco, L. Ballerini, M. Prato, E. Lidorikis, J. Kivioja, C. Marinelli, T. Ryhänen, A. Morpurgo, J.N. Coleman, V. Nicolosi, L. Colombo, A. Fert, M. Garcia-Hernandez, A. Bachtold, G.F. Schneider, F. Guinea, C. Dekker, M. Barbone, C. Galiotis, A. Grigorenko, G. Konstantatos, A. Kis, M. Katsnelson, C.W.J. Beenakker, L. Vandersypen, A. Loiseau, V. Morandi, D. Neumaier, E. Treossi, V. Pellegrini, M. Polini, A. Tredicucci, G.M. Williams, B.H. Hong, J.H. Ahn, J.M. Kim, H. Zirath, B.J. van Wees, H. van der Zant, L. Occhipinti, A. Di Matteo, I. a. Kinloch, T. Seyller, E. Quesnel, X. Feng, K. Teo, N. Rupesinghe, P. Hakonen, S.R.T. Neil, Q. Tannock, T. Löfwander, J. Kinaret, Science and technology roadmap for graphene, related two-dimensional crystals, and hybrid systems, *Nanoscale* 7 (2014) 4598.

[2] K.S. Novoselov, D. Jiang, F. Schedin, T.J. Booth, V. V. Khotkevich, S. V. Morozov, A.K. Geim, Two-dimensional atomic crystals, *Proceedings of the National Academy of Sciences* 102 (2005) 10451.

[3] F. Bonaccorso, L. Colombo, G. Yu, M. Stoller, V. Tozzini, A.C. Ferrari, R.S. Ruoff, V. Pellegrini, 2D materials. Graphene, related two-dimensional crystals, and hybrid systems for energy conversion and storage, *Science* 347 (2015) 1246501.

[4] K.S. Novoselov, A.K. Geim, S. V Morozov, D. Jiang, Y. Zhang, S. V Dubonos, I. V Grigorieva, A.A. Firsov, Electric field effect in atomically thin carbon films, *Science* 306 (2004) 666.

[5] https://www.nobelprize.org/nobel_prizes/physics/laureates/2010/.

[6] C. Lee, X. Wei, J.W. Kysar, J. Hone, Measurement of the Elastic Properties and Intrinsic Strength of Monolayer Graphene, *Science* 321 (2008) 385.

[7] A.S. Mayorov, R. V. Gorbachev, S. V. Morozov, L. Britnell, R. Jalil, L.A. Ponomarenko, P. Blake, K.S. Novoselov, K. Watanabe, T. Taniguchi, A.K. Geim, Micrometer-scale ballistic transport in encapsulated graphene at room temperature, *Nano Letters* 11 (2011) 2396.

[8] A.K. Geim, K.S. Novoselov, The rise of graphene, *Nature Materials* 6 (2007) 183.

[9] A.A. Balandin, S. Ghosh, W. Bao, I. Calizo, D. Teweldebrhan, F. Miao, C.N. Lau, Superior thermal conductivity of single-layer graphene, *Nano Letters* 8 (2008) 902.

[10] A. Peigney, C. Laurent, E. Flahaut, R.R. Bacsa, A. Rousset, Specific surface area of carbon nanotubes and bundles of carbon nanotubes, *Carbon* 39 (2001) 507.

[11] L. Shi, T. Zhao, Recent advances in inorganic 2D materials and their applications in lithium and sodium batteries, *Journal of Materials Chemistry Chem. A* 5 (2017) 3735.

[12] Q.H. Wang, K. Kalantar-Zadeh, A. Kis, J.N. Coleman, M.S. Strano, Electronics and optoelectronics of two-dimensional transition metal dichalcogenides, *Nature Nanotechnology* 7 (2012) 699.

[13] H. Osterhage, J. Gooth, B. Hamdou, P. Gwozdz, R. Zierold, K. Nielsch, Thermoelectric properties of topological insulator Bi2Te3, Sb2Te3, and Bi2Se3 thin film quantum wells, *Applied Physics Letters* 105 (2014).

[14] Y. Lin, J.W. Connell, Advances in 2D boron nitride nanostructures: nanosheets, nanoribbons, nanomeshes, and hybrids with graphene, *Nanoscale* 4 (2012) 6908.

[15] B. Mortazavi, G. Cuniberti, Mechanical properties of polycrystalline boron-nitride nanosheets, *RSC Advances* 4 (2014) 19137.

[16] P. Samorì, I.A. Kinloch, X. Feng, V. Palermo, Graphene-based nanocomposites for structural and functional applications: Using 2-dimensional materials in a 3-dimensional world, *2D Materials* 2 (2015) 030205.

[17] A. Gamucci, V. Pellegrini, F. Bonaccorso, Body protection device, particularly a protective helmet, 2017.

[18] https://graphene-flagship.eu/graphene-motorcycle-helmet.

[19] https://head.com/sports/padel/technology/graphene/.

[20] M. Kotal, A.K. Bhowmick, Polymer nanocomposites from modified clays: Recent advances and challenges, *Progress in Polymer Science* 51 (2015) 127.

[21] D.R. Paul, L.M. Robeson, Polymer nanotechnology: Nanocomposites, *Polymer* 49 (2008) 3187.

[22] Y. Kojima, A. Usuki, M. Kawasumi, A. Okada, Y. Fukushima, T. Kurauchi, O. Kamigaito, Mechanical properties of nylon 6-clay hybrid, *Journal of Materials Research* 8 (1993) 1185.

[23] I. Zaman, B. Manshoor, A. Khalid, S. Araby, From clay to graphene for polymer nanocomposites-a survey, *Journal of Polymer Research* 21 (2014) 429.

[24] F. Gao, Clay/polymer composites: The story, *Materials Today* 7 (2004) 50.

[25] O.L. Manevitch, G.C. Rutledge, Elastic Properties of a Single Lamella of Montmorillonite by Molecular Dynamics Simulation, *The Journal of Physical Chemistry B* 108 (2004) 1428.

[26] F. Bonaccorso, A. Lombardo, T. Hasan, Z. Sun, L. Colombo, A.C. Ferrari, Production and processing of graphene and 2d crystals, *Materials Today* 15 (2012) 564.

[27] Z. Cai, B. Liu, X. Zou, H.-M. Cheng, Chemical Vapor Deposition Growth and Applications of Two-Dimensional Materials and Their Heterostructures, *Chemical Reviews* 118 (2018) 6091.

[28] X. Li, W. Cai, J. An, S. Kim, J. Nah, D. Yang, R. Piner, A. Velamakanni, I. Jung, E. Tutuc, S.K. Banerjee, L. Colombo, R.S. Ruoff, Large-area synthesis of high-quality and uniform graphene films on copper foils, *Science* 324 (2009) 1312.

[29] A. Nagashima, N. Tejima, Y. Gamou, T. Kawai, C. Oshima, Electronic dispersion relations of monolayer hexagonal boron nitride formed on the Ni(111) surface, *Physical Review B* 51 (1995) 4606.

[30] K.K. Kim, A. Hsu, X. Jia, S.M. Kim, Y. Shi, M. Hofmann, D. Nezich, J.F. Rodriguez-Nieva, M. Dresselhaus, T. Palacios, J. Kong, Synthesis of monolayer hexagonal boron nitride on Cu foil using chemical vapor deposition, *Nano Letters* 12 (2012) 161.

[31] B. Liu, M. Fathi, L. Chen, A. Abbas, Y. Ma, C. Zhou, Chemical Vapor Deposition Growth of Monolayer WSe2 with Tunable Device Characteristics and Growth Mechanism Study, *ACS Nano* 9 (2015) 6119.

[32] Y.-H.H. Lee, X.-Q.Q. Zhang, W. Zhang, M.-T.T. Chang, C.-T.T. Lin, K.-D.D. Chang, Y.-C.C. Yu, J.T.-W. Wang, C.-S.S. Chang, L.-J.J. Li, T.-W.W. Lin, Synthesis of Large-Area MoS2 Atomic Layers with Chemical Vapor Deposition, *Advanced Materials* 24 (2012) 2320.

[33] Y. Zhan, Z. Liu, S. Najmaei, P.M. Ajayan, J. Lou, Large-area vapor-phase growth and characterization of MoS2 atomic layers on a SiO2 substrate, *Small* 8 (2012) 966.

[34] S. Bae, H. Kim, Y. Lee, X. Xu, J.S. Park, Y. Zheng, J. Balakrishnan, T. Lei, H. Ri Kim, Y. Il Song, Y.J. Kim, K.S. Kim, B. Özyilmaz, J.H. Ahn, B.H. Hong, S. Iijima, Roll-to-roll production of 30-inch graphene films for transparent electrodes, *Nature Nanotechnology* 5 (2010) 574.

[35] J.N. Coleman, M. Lotya, A. O'Neill, S.D. Bergin, P.J. King, U. Khan, K. Young, A. Gaucher, S. De, R.J. Smith, I. V Shvets, S.K. Arora, G. Stanton, H.-Y. Kim, K. Lee, G.T. Kim, G.S. Duesberg, T. Hallam, J.J. Boland, J.J. Wang, J.F. Donegan, J.C. Grunlan, G. Moriarty, A. Shmeliov, R.J. Nicholls, J.M. Perkins, E.M. Grieveson, K. Theuwissen, D.W. McComb, P.D. Nellist, V. Nicolosi, Two-dimensional nanosheets produced by liquid exfoliation of layered materials, *Science* 331 (2011) 568.

[36] V. Nicolosi, M. Chhowalla, M.G. Kanatzidis, M.S. Strano, J.N. Coleman, Liquid Exfoliation of Layered Materials, *Science* 340 (2013) 1226419.

[37] Y. Hernandez, V. Nicolosi, M. Lotya, F.M. Blighe, Z. Sun, S. De, I.T. McGovern, B. Holland, M. Byrne, Y.K. Gun'Ko, J.J. Boland, P. Niraj, G. Duesberg, S. Krishnamurthy, R. Goodhue, J. Hutchison, V. Scardaci, A.C. Ferrari, J.N. Coleman, High-yield production of graphene by liquid-phase exfoliation of graphite., *Nature Nanotechnology* 3 (2008) 563.

[38] K.R. Paton, E. Varrla, C. Backes, R.J. Smith, U. Khan, A. O'Neill, C. Boland, M. Lotya, O.M. Istrate, P. King, T. Higgins, S. Barwich, P. May, P. Puczkarski, I. Ahmed, M. Moebius, H. Pettersson, E. Long, J. Coelho, S.E. O'Brien, E.K. McGuire, B.M. Sanchez, G.S. Duesberg, N. McEvoy, T.J. Pennycook, C. Downing, A. Crossley, V. Nicolosi, J.N. Coleman, Scalable production of large quantities of defect-free few-layer graphene by shear exfoliation in liquids, *Nature Materials* 13 (2014) 624.

[39] F. Bonaccorso, A. Bartolotta, J.N. Coleman, C. Backes, 2D-Crystal-Based Functional Inks, *Advanced Materials* 28 (2016) 6136.

[40] C. Hansen, Hansen Solubility Parameters: a User's Handbook, CRC Press, 2007.

[41] J.N. Coleman, Liquid-Phase Exfoliation of Nanotubes and Graphene, *Advanced Functional Materials* 19 (2009) 3680.

[42] J.H. Hildebrand, A Critique of the Theory of Solubility of Non-Electrolytes, *Chemical Reviews* 44 (1949) 37.

[43] A.F.M. Barton, Handbook of Polymer-Liquid Interaction Parameters and Solubility Parameters, CRC Press, 1990.

[44] Y. Hernandez, M. Lotya, D. Rickard, S.D. Bergin, J.N. Coleman, Measurement of Multicomponent Solubility Parameters for Graphene Facilitates Solvent Discovery, *Langmuir* 26 (2010) 3208.

[45] H.M. Solomon, B.A. Burgess, G.L. Kennedy, R.E. Staples, 1-Methyl-2-pyrrolidone (NMP): reproductive and developmental toxicity study by inhalation in the rat, *Drug and Chemical*

Toxicology 18 (1995) 271.

[46] A. Capasso, A.E. Del Rio Castillo, H. Sun, A. Ansaldo, V. Pellegrini, F. Bonaccorso, Ink-jet printing of graphene for flexible electronics: An environmentally-friendly approach, *Solid State Communications* 224 (2015) 53.

[47] E. Lago, P.S. Toth, G. Pugliese, V. Pellegrini, F. Bonaccorso, Solution blending preparation of polycarbonate/graphene composite: boosting the mechanical and electrical properties, *RSC Advances* 6 (2016) 97931.

[48] C. Liu, G. Hu, H. Gao, Preparation of few-layer and single-layer graphene by exfoliation of expandable graphite in supercritical N,N-dimethylformamide, *The Journal of Supercritical Fluids* 63 (2012) 99.

[49] S. Haar, M. El Gemayel, Y. Shin, G. Melinte, M.A. Squillaci, O. Ersen, C. Casiraghi, A. Ciesielski, P. Samorì, Enhancing the Liquid-Phase Exfoliation of Graphene in Organic Solvents upon Addition of n-Octylbenzene, *Scientific Reports* 5 (2015) 16684.

[50] R. Narayan, S.O. Kim, Surfactant mediated liquid phase exfoliation of graphene, *Nano Convergence* 2 (2015) 20.

[51] M. Lotya, Y. Hernandez, P.J. King, R.J. Smith, V. Nicolosi, L.S. Karlsson, F.M. Blighe, S. De, Z. Wang, I.T. McGovern, G.S. Duesberg, J.N. Coleman, W. Zhiming, I.T. McGovern, G.S. Duesberg, J.N. Coleman, Liquid phase production of graphene by exfoliation of graphite in surfactant/water solutions, *Journal of the American Chemical Society* 131 (2009) 3611.

[52] J.-W.T. Seo, A.A. Green, A.L. Antaris, M.C. Hersam, High-Concentration Aqueous Dispersions of Graphene Using Nonionic, Biocompatible Block Copolymers, *The Journal of Physical Chemistry Letters* 2 (2011) 1004.

[53] P. May, U. Khan, J.M. Hughes, J.N. Coleman, Role of Solubility Parameters in Understanding the Steric Stabilization of Exfoliated Two-Dimensional Nanosheets by Adsorbed Polymers, *The Journal of Physical Chemistry C* 116 (2012) 11393.

[54] A. Ciesielski, P. Samorì, Graphene via sonication assisted liquid-phase exfoliation, *Chemical Society Reviews* 43 (2014) 381.

[55] Y.T. Liang, M.C. Hersam, Highly concentrated graphene solutions via polymer enhanced solvent exfoliation and iterative solvent exchange, *Journal of the American Chemical Society* 132 (2010) 17661.

[56] L. Xu, J.W. McGraw, F. Gao, M. Grundy, Z. Ye, Z. Gu, J.L. Shepherd, Production of high-concentration graphene dispersions in low-boiling-point organic solvents by liquid-phase noncovalent exfoliation of graphite with a hyperbranched polyethylene and formation of graphene/ethylene copolymer composites, *Journal of Physical Chemistry C* 117 (2013) 10730.

[57] A.E. Del Rio Castillo, V. Pellegrini, H. Sun, J. Buha, D.A. Dinh, E. Lago, A. Ansaldo, A. Capasso, L. Manna, F. Bonaccorso, Exfoliation of Few-Layer Black Phosphorus in Low-Boiling-Point Solvents and Its Application in Li-Ion Batteries, *Chemistry of Materials* 30 (2018) 506.

[58] E. Petroni, E. Lago, S. Bellani, D.W. Boukhvalov, A. Politano, B. Gürbulak, S. Duman, M. Prato, S. Gentiluomo, R. Oropesa-Nuñez, J.-K. Panda, P.S. Toth, A.E. Del Rio Castillo, V. Pellegrini, F. Bonaccorso, Liquid-Phase Exfoliated Indium-Selenide Flakes and Their

Application in Hydrogen Evolution Reaction, *Small* 14 (2018) 1800749.

[59] O.M. Maragó, F. Bonaccorso, R. Saija, G. Privitera, P.G. Gucciardi, M.A. Iatì, G. Calogero, P.H. Jones, F. Borghese, P. Denti, V. Nicolosi, A.C. Ferrari, Brownian motion of graphene, *ACS Nano* 4 (2010) 7515.

[60] J. Hassoun, F. Bonaccorso, M. Agostini, M. Angelucci, M.G. Betti, R. Cingolani, M. Gemmi, C. Mariani, S. Panero, V. Pellegrini, B. Scrosati, An advanced lithium-ion battery based on a graphene anode and a lithium iron phosphate cathode., *Nano Letters* 14 (2014) 4901.

[61] C. Backes, B.M. Szydłowska, A. Harvey, S. Yuan, V. Vega-Mayoral, B.R. Davies, P.L. Zhao, D. Hanlon, E.J.G. Santos, M.I. Katsnelson, W.J. Blau, C. Gadermaier, J.N. Coleman, Production of highly monolayer enriched dispersions of liquid-exfoliated nanosheets by liquid cascade centrifugation, *ACS Nano* 10 (2016) 1589.

[62] W.S. Hummers, R.E. Offeman, Preparation of Graphitic Oxide, *Journal of the American Chemical Society* 80 (1958) 1339.

[63] D.R. Dreyer, S. Park, C.W. Bielawski, R.S. Ruoff, The chemistry of graphene oxide, *Chemical Society Reviews* 39 (2010) 228.

[64] W. Cai, R.D. Piner, F.J. Stadermann, S. Park, M.A. Shaibat, Y. Ishii, D. Yang, A. Velamakanni, S.J. An, M. Stoller, J. An, D. Chen, R.S. Ruoff, Synthesis and Solid-State NMR Structural Characterization of 13C-Labeled Graphite Oxide, *Science* 321 (2008) 1815.

[65] C. Mattevi, G. Eda, S. Agnoli, S. Miller, K.A. Mkhoyan, O. Celik, D. Mastrogiovanni, G. Granozzi, E. Carfunkel, M. Chhowalla, Evolution of electrical, chemical, and structural properties of transparent and conducting chemically derived graphene thin films, *Advanced Functional Materials* 19 (2009) 2577.

[66] S. Stankovich, D.A. Dikin, R.D. Piner, K.A. Kohlhaas, A. Kleinhammes, Y. Jia, Y. Wu, S.T.B.T. Nguyen, R.S. Ruoff, Synthesis of graphene-based nanosheets via chemical reduction of exfoliated graphite oxide, *Carbon* 45 (2007) 1558.

[67] S. Niyogi, E. Bekyarova, M.E. Itkis, J.L. McWilliams, M.A. Hamon, R.C. Haddon, Solution properties of graphite and graphene, *Journal of the American Chemical Society* 128 (2006) 7720.

[68] H.C. Schniepp, J.L. Li, M.J. McAllister, H. Sai, M. Herrera-Alonson, D.H. Adamson, R.K. Prud'homme, R. Car, D.A. Seville, I.A. Aksay, Functionalized single graphene sheets derived from splitting graphite oxide, *Journal of Physical Chemistry B* 110 (2006) 8535.

[69] C.Y. Su, Y. Xu, W. Zhang, J. Zhao, X. Tang, C.H. Tsai, L.J. Li, Electrical and spectroscopic characterizations of ultra-large reduced graphene oxide monolayers, *Chemistry of Materials* 21 (2009) 5674.

[70] D.A. Dikin, S. Stankovich, E.J. Zimney, R.D. Piner, G.H.B. Dommett, G. Evmenenko, S.T. Nguyen, R.S. Ruoff, Preparation and characterization of graphene oxide paper, *Nature* 448 (2007) 457.

[71] S.R. Graphene, O. Films, T. Conductors, H.A. Becerril, J. Mao, Z. Liu, R.M. Stoltenberg, Z. Bao, Y. Chen, Evaluation of Solution-Processed Reduced Graphene Oxide Films as Transparent Conductors, *ACS Nano* 2 (2008) 463.

[72] G. Eda, G. Fanchini, M. Chhowalla, Large-area ultrathin films of reduced graphene oxide as a

transparent and flexible electronic material, *Nature Nanotechnology* 3 (2008) 270.

[73] Y. Zhu, S. Murali, W. Cai, X. Li, J.W. Suk, J.R. Potts, R.S. Ruoff, Graphene and graphene oxide: synthesis, properties, and applications, *Advanced Materials* 22 (2010) 3906.

[74] P. Liu, A.L. Cottrill, D. Kozawa, V.B. Koman, D. Parviz, A.T. Liu, J. Yang, T.Q. Tran, M.H. Wong, S. Wang, M.S. Strano, Emerging trends in 2D nanotechnology that are redefining our understanding of "Nanocomposites," *Nano Today* 21 (2018) 18.

[75] V. Palermo, I.A. Kinloch, S. Ligi, N.M. Pugno, Nanoscale Mechanics of Graphene and Graphene Oxide in Composites: A Scientific and Technological Perspective, *Advanced Materials* 28 (2016) 6232.

[76] C. Vallés, A.M. Abdelkader, R.J. Young, I.A. Kinloch, The effect of flake diameter on the reinforcement of few-layer graphene-PMMA composites, *Composites Science and Technology* 111 (2015) 17.

[77] A.J. Marsden, D.G. Papageorgiou, C. Vallés, A. Liscio, V. Palermo, M.A. Bissett, R.J. Young, I.A. Kinloch, Electrical percolation in graphene–polymer composites, *2D Materials* 5 (2018) 032003.

[78] D.G. Papageorgiou, I.A. Kinloch, R.J. Young, Mechanical properties of graphene and graphene-based nanocomposites, *Progress in Materials Science* 90 (2017) 75.

[79] G. Kakavelakis, A.E. Del Rio Castillo, V. Pellegrini, A. Ansaldo, P. Tzourmpakis, R. Brescia, M. Prato, E. Stratakis, E. Kymakis, F. Bonaccorso, Size-Tuning of WSe2 Flakes for High Efficiency Inverted Organic Solar Cells, *ACS Nano* 11 (2017) 3517.

[80] T. Svedberg, K.O. Pedersen, The Ultracentrifuge, Oxford Univ. Press, London, 1940.

[81] S. Ahmed, F.R. Jones, A review of particulate reinforcement theories for polymer composites, *Journal of Materials Science* 25 (1990) 4933.

[82] R.M. Jones, Mechanics of composite materials, Taylor & Francis, 1998.

[83] R.J. Young, I.A. Kinloch, L. Gong, K.S. Novoselov, The mechanics of graphene nanocomposites: A review, *Composites Science and Technology* 72 (2012) 1459.

[84] P. May, U. Khan, A. O'Neill, J.N. Coleman, Approaching the theoretical limit for reinforcing polymers with graphene, *Journal of Materials Chemistry* 22 (2012) 1278.

[85] U. Khan, P. May, A. O'Neill, A.P. Bell, E. Boussac, A. Martin, J. Semple, J.N. Coleman, Polymer reinforcement using liquid-exfoliated boron nitride nanosheets, *Nanoscale* 5 (2013) 581.

[86] Z. Li, R.J. Young, N.R. Wilson, I.A. Kinloch, C. Vallés, Z. Li, Effect of the orientation of graphene-based nanoplatelets upon the Young's modulus of nanocomposites, *Composites Science and Technology* 123 (2016) 125.

[87] H. Krenchel, Fibre reinforcement: theoretical and practical investigations of the elasticity and strength of fibre-reinforced materials, 1964.

[88] J.C. Halpin Affdl, J.L. Kardos, The Halpin-Tsai equations: A review, *Polymer Engineering and Science* 16 (1976) 344.

[89] K. Hu, D.D. Kulkarni, I. Choi, V. V. Tsukruk, Graphene-polymer nanocomposites for structural and functional applications, *Progress in Polymer Science* 39 (2014) 1934.

[90] Y. Cui, S.I. Kundalwal, S. Kumar, Gas barrier performance of graphene/polymer nanocomposites, *Carbon* 95 (2016) 313.

[91] C. Lu, Y.W. Mai, Influence of aspect ratio on barrier properties of polymer-clay nanocomposites, *Physical Review Letters* 95 (2005) 088303.

[92] M.C. Carrera, E. Erdmann, H.A. Destéfanis, Barrier properties and structural study of nanocomposite of HDPE/montmorillonite modified with polyvinylalcohol, *Journal of Chemistry* (2013) 679567.

[93] H. Kim, Y. Miura, C.W. Macosko, Graphene/polyurethane nanocomposites for improved gas barrier and electrical conductivity, *Chemistry of Materials* 22 (2010) 3441.

[94] S. Xie, O.M. Istrate, P. May, S. Barwich, A.P. Bell, U. Khan, J.N. Coleman, Boron nitride nanosheets as barrier enhancing fillers in melt processed composites, *Nanoscale* 7 (2015) 4443.

[95] R.M. Barrer, J.H. Petropoulos, Diffusion in heterogeneous media: Lattices of parallelepipeds in a continuous phase, *British Journal of Applied Physics* 12 (1961) 691.

[96] L.E. Nielsen, Models for the Permeability of Filled Polymer Systems, *Journal of Macromolecular Science-Chemistry* 1 (1967) 929.

[97] R.K. Bharadwaj, Modeling the barrier properties of polymer-layered silicate nanocomposites, *Macromolecules* 34 (2001) 9189.

[98] T. V. Duncan, Applications of nanotechnology in food packaging and food safety: Barrier materials, antimicrobials and sensors, *Journal of Colloid and Interface Science* 363 (2011) 1.

[99] J. Kim, B. Yim, J. Kim, J. Kim, The effects of functionalized graphene nanosheets on the thermal and mechanical properties of epoxy composites for anisotropic conductive adhesives (ACAs), *Microelectronics Reliability* 52 (2012) 595.

[100] C.S. Boland, U. Khan, C. Backes, A. O'Neill, J. McCauley, S. Duane, R. Shanker, Y. Liu, I. Jurewicz, A.B. Dalton, J.N. Coleman, Sensitive, High-Strain, High-Rate Bodily Motion Sensors Based on Graphene–Rubber Composites, *ACS Nano* 8 (2014) 8819.

[101] C.S. Boland, U. Khan, G. Ryan, S. Barwich, R. Charifou, A. Harvey, C. Backes, Z. Li, M.S. Ferreira, M.E. Möbius, R.J. Young, J.N. Coleman, Sensitive electromechanical sensors using viscoelastic graphene-polymer nanocomposites, *Science* 354 (2016) 1257.

[102] R. Jan, A. Habib, M.A. Akram, I. Ahmad, A. Shah, M. Sadiq, A. Hussain, Flexible, thin films of graphene-polymer composites for EMI shielding, *Materials Research Express* 4 (2017) 035605.

[103] S. Kirkpatrick, Percolation and Conduction, *Reviews of Modern Physics* 45 (1973) 574.

[104] J.W. Essam, Percolation theory, *Reports on Progress in Physics* 43 (1980) 833.

[105] D. Stauffer, A. Aharony, Introduction To Percolation Theory, CRC Press, 1994.

[106] C.W. Nan, Y. Shen, J. Ma, Physical Properties of Composites Near Percolation, *Annual Review of Materials Research* 40 (2010) 131.

[107] G. Ambrosetti, C. Grimaldi, I. Balberg, T. Maeder, A. Danani, P. Ryser, Solution of the tunneling-percolation problem in the nanocomposite regime, *Physical Review B - Condensed Matter and Materials Physics* 81 (2010) 155434.

[108] D. Toker, D. Azulay, N. Shimoni, I. Balberg, O. Millo, Tunneling and percolation in metal-insulator composite materials, *Physical Review B - Condensed Matter and Materials Physics* 68 (2003) 041403.

[109] B. Guo, Z. Tang, L. Zhang, Transport performance in novel elastomer nanocomposites: Mechanism, design and control, *Progress in Polymer Science* 61 (2016) 29.

[110] J. Li, J.K. Kim, Percolation threshold of conducting polymer composites containing 3D randomly distributed graphite nanoplatelets, *Composites Science and Technology* 67 (2007) 2114.

[111] S.H. Xie, Y.Y. Liu, J.Y. Li, Comparison of the effective conductivity between composites reinforced by graphene nanosheets and carbon nanotubes, *Applied Physics Letters* 92 (2008) 243121.

[112] J. Hicks, A. Behnam, A. Ural, A computational study of tunneling-percolation electrical transport in graphene-based nanocomposites, *Applied Physics Letters* 95 (2009) 213103.

[113] Z. Zabihi, H. Araghi, Monte Carlo simulations of effective electrical conductivity of graphene/poly(methyl methacrylate) nanocomposite: Landauer-Buttiker approach, *Synthetic Metals* 217 (2016) 87.

[114] W. Rohsenow, J. Hartnett, Y. Cho, Microscale transport phenomena - Handbook of heat transfer, 3rd ed., McGraw-Hill, 1998.

[115] Z. Han, A. Fina, Thermal conductivity of carbon nanotubes and their polymer nanocomposites: A review, *Progress in Polymer Science* 36 (2011) 914.

[116] Y. Agari, A. Ueda, Y. Omura, S. Nagai, Thermal diffusivity and conductivity of PMMA/PC blends, *Polymer* 38 (1997) 801.

[117] N. Burger, A. Laachachi, M. Ferriol, M. Lutz, V. Toniazzo, D. Ruch, Review of thermal conductivity in composites: Mechanisms, parameters and theory, *Progress in Polymer Science* 61 (2016) 1.

[118] J.A. King, K.W. Tucker, B.D. Vogt, E.H. Weber, C. Quan, Electrically and thermally conductive nylon 6,6, *Polymer Composites* 20 (1999) 643.

[119] G. Wypych, Handbook of fillers: Physical properties of fillers and filled materials, Chem. Tech. Publishing, 2016.

[120] H.O. Pierson, Handbook of Carbon, Graphite, Diamonds and Fullerenes: Processing, Properties and Applications, Noyes Publications, 1993.

[121] A. Yu, P. Ramesh, M.E. Itkis, E. Bekyarova, R.C. Haddon, Graphite nanoplatelet-epoxy composite thermal interface materials, *Journal of Physical Chemistry C* 111 (2007) 7565.

[122] J.-B. Donnet, R.C. Bansal, M.-J. Wang, Carbon black: Science and Technology, Dekker, 1993.

[123] K.M.F. Shahil, A.A. Balandin, Graphene–Multilayer Graphene Nanocomposites as Highly Efficient Thermal Interface Materials, *Nano Letters* 12 (2012) 861.

[124] E. Hammel, X. Tang, M. Trampert, T. Schmitt, K. Mauthner, A. Eder, P. Pötschke, Carbon nanofibers for composite applications, *Carbon* 42 (2004) 1153.

[125] Y. Agari, A. Ueda, S. Nagai, Thermal conductivity of a polyethylene filled with disoriented short-cut carbon fibers, *Journal of Applied Polymer Science* 43 (1991) 1117.

[126] G.W. Lee, M. Park, J. Kim, J.I. Lee, H.G. Yoon, Enhanced thermal conductivity of polymer composites filled with hybrid filler, *Composites Part A: Applied Science and Manufacturing* 37 (2006) 737.

[127] Y.P. Mamunya, V. V. Davydenko, P. Pissis, E. V. Lebedev, Electrical and thermal conductivity of polymers filled with metal powders, *European Polymer Journal* 38 (2002) 1887.

[128] M.J. Biercuk, M.C. Llaguno, M. Radosavljevic, J.K. Hyun, A.T. Johnson, J.E. Fischer, Carbon nanotube composites for thermal management, *Applied Physics Letters* 80 (2002) 2767.

[129] F.H. Gojny, M.H.G. Wichmann, B. Fiedler, I.A. Kinloch, W. Bauhofer, A.H. Windle, K. Schulte, Evaluation and identification of electrical and thermal conduction mechanisms in carbon nanotube/epoxy composites, *Polymer* 47 (2006) 2036.

[130] F. Yavari, H.R. Fard, K. Pashayi, M.A. Rafiee, A. Zamiri, Z. Yu, R. Ozisik, T. Borca-Tasciuc, N. Koratkar, Enhanced thermal conductivity in a nanostructured phase change composite due to low concentration graphene additives, *Journal of Physical Chemistry C* 115 (2011) 8753.

[131] C.C. Teng, C.C.M. Ma, C.H. Lu, S.Y. Yang, S.H. Lee, M.C. Hsiao, M.Y. Yen, K.C. Chiou, T.M. Lee, Thermal conductivity and structure of non-covalent functionalized graphene/epoxy composites, *Carbon* 49 (2011) 5107.

[132] S.H. Song, K.H. Park, B.H. Kim, Y.W. Choi, G.H. Jun, D.J. Lee, B.S. Kong, K.W. Paik, S. Jeon, Enhanced thermal conductivity of epoxy-graphene composites by using non-oxidized graphene flakes with non-covalent functionalization, *Advanced Materials* 25 (2013) 732.

[133] C. Zhi, Y. Bando, C. Tang, H. Kuwahara, D. Golberg, Large-Scale Fabrication of Boron Nitride Nanosheets and Their Utilization in Polymeric Composites with Improved Thermal and Mechanical Properties, *Advanced Materials* 21 (2009) 2889.

[134] X. Wu, H. Liu, Z. Tang, B. Guo, Scalable fabrication of thermally conductive elastomer/boron nitride nanosheets composites by slurry compounding, *Composites Science and Technology* 123 (2016) 179.

[135] J. Yu, X. Huang, C. Wu, X. Wu, G. Wang, P. Jiang, Interfacial modification of boron nitride nanoplatelets for epoxy composites with improved thermal properties, *Polymer* 53 (2012) 471.

[136] Guoqing Zhang, Yanping Xia, Hui Wang, Yu Tao, Guoliang Tao, Shantung Tu, Haiping Wu, A Percolation Model of Thermal Conductivity for Filled Polymer Composites, *Journal of Composite Materials* 44 (2009) 963.

[137] J.N. Israelachvili, Intermolecular and Surface Forces: Revised Third Edition, Academic Press, 2011.

[138] M. Zhang, Y. Li, Z. Su, G. Wei, Recent advances in the synthesis and applications of graphene–polymer nanocomposites, *Polym. Chem.* 6 (2015) 6107.

[139] J.R. Potts, D.R. Dreyer, C.W. Bielawski, R.S. Ruoff, Graphene-based polymer

nanocomposites, *Polymer* 52 (2011) 5.

[140] H. Kim, A.A. Abdala, C.W. Macosko, Graphene/Polymer Nanocomposites, *Macromolecules* 43 (2010) 6515.

[141] T. Ramanathan, A.A. Abdala, S. Stankovich, D.A. Dikin, M. Herrera-Alonso, R.D. Piner, D.H. Adamson, H.C. Schniepp, X. Chen, R.S. Ruoff, S.T. Nguyen, I.A. Aksay, R.K. Prud'Homme, L.C. Brinson, Functionalized graphene sheets for polymer nanocomposites, *Nature Nanotechnology* 3 (2008) 327.

[142] S. Stankovich, D.A. Dikin, G.H.B. Dommett, K.M. Kohlhaas, E.J. Zimney, E.A. Stach, R.D. Piner, S.T. Nguyen, R.S. Ruoff, Graphene-based composite materials, *Nature* 442 (2006) 282.

[143] C. Gómez-Navarro, R.T. Weitz, A.M. Bittner, M. Scolari, A. Mews, M. Burghard, K. Kern, Electronic Transport Properties of Individual Chemically Reduced Graphene Oxide Sheets, *Nano Letters* 7 (2007) 3499.

[144] J.W. Suk, R.D. Piner, J. An, R.S. Ruoff, Mechanical properties of monolayer graphene oxide, *ACS Nano* 4 (2010) 6557.

[145] H.-B. Zhang, W.-G. Zheng, Q. Yan, Y. Yang, J.-W. Wang, Z.-H. Lu, G.-Y. Ji, Z.-Z. Yu, Electrically conductive polyethylene terephthalate/graphene nanocomposites prepared by melt compounding, *Polymer* 51 (2010) 1191.

[146] H. Kim, C.W. Macosko, Processing-property relationships of polycarbonate/graphene composites, *Polymer* 50 (2009) 3797.

[147] S. Vadukumpully, J. Paul, N. Mahanta, S. Valiyaveettil, Flexible conductive graphene/poly(vinyl chloride) composite thin films with high mechanical strength and thermal stability, *Carbon* 49 (2011) 198.

[148] E.L. Papadopoulou, F. Pignatelli, S. Marras, L. Marini, A. Davis, A. Athanassiou, I.S. Bayer, Nylon 6,6/graphene nanoplatelet composite films obtained from a new solvent, *RSC Adv.* 6 (2016) 6823.

[149] Z. Xu, C. Gao, In situ Polymerization Approach to Graphene-Reinforced Nylon-6 Composites, *Macromolecules* 43 (2010) 6716.

[150] L. Gong, B. Yin, L. Li, M. Yang, Nylon-6/Graphene composites modified through polymeric modification of graphene, *Composites Part B: Engineering* 73 (2015) 49.

[151] H. Kim, S. Kobayashi, M.A. AbdurRahim, M.J. Zhang, A. Khusainova, M.A. Hillmyer, A.A. Abdala, C.W. Macosko, Graphene/polyethylene nanocomposites: Effect of polyethylene functionalization and blending methods, *Polymer* 52 (2011) 1837.

[152] T. Kuilla, S. Bhadra, D. Yao, N.H. Kim, S. Bose, J.H. Lee, Recent advances in graphene based polymer composites, *Progress in Polymer Science* 35 (2010) 1350.

[153] A.E. Del Rio Castillo, A. Ansaldo, V. Pellegrini, F. Bonaccorso, Exfoliation of layered materials by wet-jet milling techniques, WO2017089987A1, 2017.

[154] A.E. Del Rio Castillo, V. Pellegrini, A. Ansaldo, F. Ricciardella, H. Sun, L. Marasco, J. Buha, Z. Dang, L. Gagliani, E. Lago, N. Curreli, S. Gentiluomo, F. Palazon, M. Prato, R. Oropesa-Nuñez, P.S. Toth, E. Mantero, M. Crugliano, A. Gamucci, A. Tomadin, M. Polini, F. Bonaccorso, R. Oropesa-Nunez, P.S. Toth, E. Mantero, M. Crugliano, A. Gamucci, A.

Tomadin, M. Polini, F. Bonaccorso, High-yield production of 2D crystals by wet-jet milling, *Materials Horizons* 5 (2018) 890.

[155] P.G. Karagiannidis, S.A. Hodge, L. Lombardi, F. Tomarchio, N. Decorde, S. Milana, I. Goykhman, Y. Su, S. V. Mesite, D.N. Johnstone, R.K. Leary, P.A. Midgley, N.M. Pugno, F. Torrisi, A.C. Ferrari, Microfluidization of Graphite and Formulation of Graphene-Based Conductive Inks, *ACS Nano* 11 (2017) 2742.

[156] https://natureworksllc.com/~/media/Files/NatureWorks/Technical-Documents/Technical-Data-Sheets/TechnicalDataSheet_4043D_3D-monofilament_pdf.pdf?la=en.

[157] W.C. Young, R.G. Budynas, Roark's formulas for stress and strain, McGraw-Hill, 2012.

[158] W.D. Callister, Materials Science and Engineering: an Introduction, Wiley, 2007.

[159] ASTM D 882-12, Standard Test Method for Tensile Properties of Thin Plastic Sheeting, ASTM International, (2012).

[160] M.B. Heaney, Electrical Conductivity and Resistivity, in: Electr. Meas. Signal Process. Displays, CRC Press, 2003.

[161] W.J. Parker, R.J. Jenkins, C.P. Butler, G.L. Abbott, Flash method of determining thermal diffusivity, heat capacity, and thermal conductivity, *Journal of Applied Physics* 32 (1961) 1679.

[162] J.C. Meyer, A.K. Geim, M.I. Katsnelson, K.S. Novoselov, T.J. Booth, S. Roth, The structure of suspended graphene sheets, *Nature* 446 (2007) 60.

[163] A. Gupta, G. Chen, P. Joshi, A. S. Tadigadapa, P.C. Eklund, Raman Scattering from High-Frequency Phonons in Supported n-Graphene Layer Films, *Nano Letters* 6 (2006) 2667.

[164] P. Nemes-Incze, Z. Osváth, K. Kamarás, L.P. Biró, Anomalies in thickness measurements of graphene and few layer graphite crystals by tapping mode atomic force microscopy, *Carbon* 46 (2008) 1435.

[165] A.C. Ferrari, J.C. Meyer, V. Scardaci, C. Casiraghi, M. Lazzeri, F. Mauri, S. Piscanec, D. Jiang, K.S. Novoselov, S. Roth, A.K. Geim, Raman Spectrum of Graphene and Graphene Layers, *Physical Review Letters* 97 (2006) 187401.

[166] A.A.C. Ferrari, D.D.M. Basko, Raman spectroscopy as a versatile tool for studying the properties of graphene, *Nature Nanotechnology* 8 (2013) 235.

[167] F. Bonaccorso, P.H. Tan, A.C. Ferrari, Multiwall Nanotubes, Multilayers, and Hybrid Nanostructures: New Frontiers for Technology and Raman Spectroscopy, *ACS Nano* 7 (2013) 1838.

[168] A.C. Ferrari, Raman spectroscopy of graphene and graphite: Disorder, electron-phonon coupling, doping and nonadiabatic effects, *Solid State Communications* 143 (2007) 47.

[169] A.C. Ferrari, J. Robertson, Resonant Raman spectroscopy of disordered, amorphous, and diamondlike carbon, *Physical Review B* 64 (2001) 075414.

[170] A.C. Ferrari, J. Robertson, Interpretation of Raman spectra of disordered and amorphous carbon, *Physical Review B* 61 (2000) 14095.

[171] P.S. Toth, M. Velický, M.A. Bissett, T.J.A. Slater, N. Savjani, A.K. Rabiu, A.M. Rakowski, J.R. Brent, S.J. Haigh, P. O'Brien, R.A.W. Dryfe, Asymmetric MoS_2 /Graphene/Metal Sandwiches: Preparation, Characterization, and Application, *Advanced Materials* 28 (2016) 8256.

[172] Y. Lin, T. V. Williams, T.-B. Xu, W. Cao, H.E. Elsayed-Ali, J.W. Connell, Aqueous Dispersions of Few-Layered and Monolayered Hexagonal Boron Nitride Nanosheets from Sonication-Assisted Hydrolysis: Critical Role of Water, *The Journal of Physical Chemistry C* 115 (2011) 2679.

[173] J. Kim, S. Kwon, D.-H. Cho, B. Kang, H. Kwon, Y. Kim, S.O. Park, G.Y. Jung, E. Shin, W.-G. Kim, H. Lee, G.H. Ryu, M. Choi, T.H. Kim, J. Oh, S. Park, S.K. Kwak, S.W. Yoon, D. Byun, Z. Lee, C. Lee, Direct exfoliation and dispersion of two-dimensional materials in pure water via temperature control, *Nature Communications* 6 (2015) 8294.

[174] G. Bepete, E. Anglaret, L. Ortolani, V. Morandi, K. Huang, A. Pénicaud, C. Drummond, Surfactant-free single-layer graphene in water, *Nature Chemistry* 9 (2016) 347.

[175] A.A. Green, M.C. Hersam, Solution phase production of graphene with controlled thickness via density differentiation, *Nano Letters* 9 (2009) 4031.

[176] R.J. Smith, P.J. King, M. Lotya, C. Wirtz, U. Khan, S. De, A. O'Neill, G.S. Duesberg, J.C. Grunlan, G. Moriarty, J. Chen, J. Wang, A.I. Minett, V. Nicolosi, J.N. Coleman, Large-scale exfoliation of inorganic layered compounds in aqueous surfactant solutions, *Advanced Materials* 23 (2011) 3944.

[177] J. Zhu, J. Kang, J. Kang, D. Jariwala, J.D. Wood, J.-W.T. Seo, K.-S. Chen, T.J. Marks, M.C. Hersam, Solution-Processed Dielectrics Based on Thickness-Sorted Two-Dimensional Hexagonal Boron Nitride Nanosheets, *Nano Letters* 15 (2015) 7029.

[178] I.R. Schmolka, US 3740421 A, 1973.

[179] F. Bonaccorso, T. Hasan, P.H. Tan, C. Sciascia, G. Privitera, G. Di Marco, P.G. Gucciardi, A.C. Ferrari, Density Gradient Ultracentrifugation of Nanotubes: Interplay of Bundling and Surfactants Encapsulation, *The Journal of Physical Chemistry C* 114 (2010) 17267.

[180] K. Kouroupis-Agalou, A. Liscio, E. Treossi, L. Ortolani, V. Morandi, N.M. Pugno, V. Palermo, Fragmentation and exfoliation of 2-dimensional materials: a statistical approach, *Nanoscale* 6 (2014) 5926.

[181] Q. Cai, D. Scullion, A. Falin, K. Watanabe, T. Taniguchi, Y. Chen, E.J.G. Santos, L.H. Li, Y. Shi, X. Wang, J.M. Tour, J.C. Idrobo, R. Vajtai, J. Lou, P.M. Ajayan, Raman signature and phonon dispersion of atomically thin boron nitride, *Nanoscale* 9 (2017) 3059.

[182] R. V. Gorbachev, I. Riaz, R.R. Nair, R. Jalil, L. Britnell, B.D. Belle, E.W. Hill, K.S. Novoselov, K. Watanabe, T. Taniguchi, A.K. Geim, P. Blake, Hunting for Monolayer Boron Nitride: Optical and Raman Signatures, *Small* 7 (2011) 465.

[183] A. Falin, Q. Cai, E.J.G. Santos, D. Scullion, D. Qian, R. Zhang, Z. Yang, S. Huang, K. Watanabe, T. Taniguchi, M.R. Barnett, Y. Chen, R.S. Ruoff, L.H. Li, Mechanical properties of atomically thin boron nitride and the role of interlayer interactions, *Nature Communications* 8 (2017) 15815.

[184] A. Pakdel, Y. Bando, D. Golberg, Nano boron nitride flatland, *Chemical Society Reviews* 43

(2014) 934.

[185] T. Kuzuba, K. Era, T. Ishii, T. Sato, A low frequency Raman-active vibration of hexagonal boron nitride, *Solid State Communications* 25 (1978) 863.

[186] T. Sainsbury, A. Satti, P. May, Z. Wang, I. McGovern, Y.K. Gun'ko, J.N. Coleman, Oxygen Radical Functionalization of Boron Nitride Nanosheets, *Journal of the American Chemical Society* 134 (2012) 18758.

[187] F.T. Johra, J.W. Lee, W.G. Jung, Facile and safe graphene preparation on solution based platform, *Journal of Industrial and Engineering Chemistry* 20 (2014) 2883.

[188] H. Sun, A.E. Del Rio Castillo, S. Monaco, A. Capasso, A. Ansaldo, M. Prato, D.A. Dinh, V. Pellegrini, B. Scrosati, L. Manna, F. Bonaccorso, Binder-free graphene as an advanced anode for lithium batteries, *Journal of Materials Chemistry A* 4 (2016) 6886.

[189] G.R. Bhimanapati, D. Kozuch, J.A. Robinson, Large-scale synthesis and functionalization of hexagonal boron nitride nanosheets, *Nanoscale* 6 (2014) 11671.

[190] W. Yang, J. Wang, C. Si, Z. Peng, J. Frenzel, G. Eggeler, Z. Zhang, [001] preferentially-oriented 2D tungsten disulfide nanosheets as anode materials for superior lithium storage, *Journal of Materials Chemistry A* 3 (2015) 17811.

[191] A. Avsar, J.Y. Tan, T. Taychatanapat, J. Balakrishnan, G.K.W. Koon, Y. Yeo, J. Lahiri, A. Carvalho, A.S. Rodin, E.C.T. O'Farrell, G. Eda, A.H. Castro Neto, B. Özyilmaz, Spin–orbit proximity effect in graphene, *Nature Communications* 5 (2014) 4875.

[192] A.T. Seyhan, Y. Göncü, O. Durukan, A. Akay, N. Ay, Silanization of boron nitride nanosheets (BNNSs) through microfluidization and their use for producing thermally conductive and electrically insulating polymer nanocomposites, *Journal of Solid State Chemistry* 249 (2017) 98.

[193] M. Buzaglo, M. Shtein, O. Regev, Graphene Quantum Dots Produced by Microfluidization, *Chemistry of Materials* 28 (2016) 21.

[194] J.C. Meyer, A.K. Geim, M.I. Katsnelson, K.S. Novoselov, D. Obergfell, S. Roth, C. Girit, A. Zettl, On the roughness of single- and bi-layer graphene membranes, *Solid State Communications* 143 (2007) 101.

[195] J.D. Bernal, The Structure of Graphite, *Proceedings of the Royal Society A: Mathematical, Physical and Engineering Sciences* 106 (1924) 749.

[196] A. Eckmann, A. Felten, A. Mishchenko, L. Britnell, R. Krupke, K.S. Novoselov, C. Casiraghi, Probing the nature of defects in graphene by Raman spectroscopy, *Nano Letters* 12 (2012) 3925.

[197] A. Das, B. Chakraborty, A.K. Sood, Raman spectroscopy of graphene on different substrates and influence of defects, *Bulletin of Materials Science* 31 (2008) 579.

[198] E.H. Martins Ferreira, M.V.O. Moutinho, F. Stavale, M.M. Lucchese, R.B. Capaz, C.A. Achete, A. Jorio, Evolution of the Raman spectra from single-, few-, and many-layer graphene with increasing disorder, *Physical Review B - Condensed Matter and Materials Physics* 82 (2010) 2010.

[199] W. Zhao, M. Fang, F. Wu, H. Wu, L. Wang, G. Chen, Preparation of graphene by exfoliation

of graphite using wet ball milling, *Journal of Materials Chemistry* 20 (2010) 5817.

[200] D. Ferrah, J. Penuelas, C. Bottela, G. Grenet, A. Ouerghi, X-ray photoelectron spectroscopy (XPS) and diffraction (XPD) study of a few layers of graphene on 6H-SiC(0001), *Surface Science* 615 (2013) 47.

[201] K. V. Emtsev, F. Speck, T. Seyller, L. Ley, J.D. Riley, Interaction, growth, and ordering of epitaxial graphene on SiC{0001} surfaces: A comparative photoelectron spectroscopy study, *Physical Review B - Condensed Matter and Materials Physics* 77 (2008) 155303.

[202] W. Konicki, M. Aleksandrzak, D. Moszyński, E. Mijowska, Adsorption of anionic azo-dyes from aqueous solutions onto graphene oxide: Equilibrium, kinetic and thermodynamic studies, *Journal of Colloid and Interface Science* 496 (2017) 188.

[203] C. Lee, H. Yan, L.E. Brus, T.F. Heinz, J. Hone, S. Ryu, Anomalous lattice vibrations of single- and few-layer MoS2, *ACS Nano* 4 (2010) 2695.

[204] H. Li, Q. Zhang, C.C.R. Yap, B.K. Tay, T.H.T. Edwin, A. Olivier, D. Baillargeat, From bulk to monolayer MoS2: Evolution of Raman scattering, *Advanced Functional Materials* 22 (2012) 1385.

[205] B. Bindhu, B.K. Sharu, M.S. Gopika, P.K. Praseetha, K. Veluraja, Molybdenum disulfide nanoflakes through Li-AHA assisted exfoliation in an aqueous medium, *RSC Advances* 6 (2016) 22026.

[206] L. Najafi, S. Bellani, B. Martín-García, R. Oropesa-Nuñez, A.E. Del Rio Castillo, M. Prato, I. Moreels, F. Bonaccorso, Solution-Processed Hybrid Graphene Flake/2H-MoS2 Quantum Dot Heterostructures for Efficient Electrochemical Hydrogen Evolution, *Chemistry of Materials* 29 (2017) 5782.

[207] W. Zhao, Z. Ghorannevis, K.K. Amara, J.R. Pang, M. Toh, X. Zhang, C. Kloc, P.H. Tan, G. Eda, Lattice dynamics in mono- and few-layer sheets of WS2 and WSe2, *Nanoscale* 5 (2013) 9677.

[208] A. Berkdemir, H.R. Gutiérrez, A.R. Botello-Méndez, N. Perea-López, A.L. Elías, C.-I. Chia, B. Wang, V.H. Crespi, F. López-Urías, J.-C. Charlier, H. Terrones, M. Terrones, Identification of individual and few layers of WS2 using Raman Spectroscopy, *Scientific Reports* 3 (2013) 1755.

[209] H. Sun, A. Varzi, V. Pellegrini, D.A.A. Dinh, R. Raccichini, A.E.E. Del Rio-Castillo, M. Prato, M. Colombo, R. Cingolani, B. Scrosati, S. Passerini, F. Bonaccorso, How much does size really matter? Exploring the limits of graphene as Li ion battery anode material, *Solid State Communications* 251 (2017) 88.

[210] M. V. Bracamonte, G.I. Lacconi, S.E. Urreta, L.E.F. Foa Torres, On the Nature of Defects in Liquid-Phase Exfoliated Graphene, *The Journal of Physical Chemistry C* 118 (2014) 15455.

[211] A.H. Castro Neto, N.M.R. Peres, K.S. Novoselov, A.K. Geim, The electronic properties of graphene, *Reviews of Modern Physics* 81 (2009) 109.

[212] K.S. Novoselov, A.K. Geim, S. V Morozov, D. Jiang, M.I. Katsnelson, I. V Grigorieva, S. V Dubonos, A.A. Firsov, Two-dimensional gas of massless Dirac fermions in graphene, *Nature* 438 (2005) 197.

[213] P. Cataldi, I.S. Bayer, G. Nanni, A. Athanassiou, F. Bonaccorso, V. Pellegrini, A.E. del Rio

Castillo, F. Ricciardella, S. Artyukhin, M.-A.A. Tronche, Y. Gogotsi, R. Cingolani, Effect of graphene nano-platelet morphology on the elastic modulus of soft and hard biopolymers, *Carbon* 109 (2016) 331.

[214] C.-C. Teng, C.-C.M. Ma, C.-H. Lu, S.-Y. Yang, S.-H. Lee, M.-C. Hsiao, M.-Y. Yen, K.-C. Chiou, T.-M. Lee, Thermal conductivity and structure of non-covalent functionalized graphene/epoxy composites, *Carbon* 49 (2011) 5107.

[215] P. Cataldi, I.S. Bayer, F. Bonaccorso, V. Pellegrini, A. Athanassiou, R. Cingolani, Foldable Conductive Cellulose Fiber Networks Modified by Graphene Nanoplatelet-Bio-Based Composites, *Advanced Electronic Materials* 1 (2015) 1500224.

[216] C. Berger, Z. Song, X. Li, X. Wu, N. Brown, C. Naud, D. Mayou, T. Li, J. Hass, A.N. Marchenkov, E.H. Conrad, P.N. First, W.A. de Heer, Electronic confinement and coherence in patterned epitaxial graphene, *Science (New York, N.Y.)* 312 (2006) 1191.

[217] G.D. Legrand, G.T. Bendler, Handbook of Polycarbonate Science and Technology, CRC Press, 1999.

[218] G. Abts, T. Eckel, R. Wehrmann, Polycarbonates, Ullmann’s Encyclopedia of Industrial Chemistry, Wiley, Weinheim, Germany, 2014.

[219] D. Li, A.E.A.E. Del Rio Castillo, H. Jussila, G. Ye, Z. Ren, J. Bai, X. Chen, H. Lipsanen, Z. Sun, F. Bonaccorso, Black phosphorus polycarbonate polymer composite for pulsed fibre lasers, *Applied Materials Today* 4 (2016) 17.

[220] T. Hasan, Z. Sun, F. Wang, F. Bonaccorso, P.H. Tan, A.G. Rozhin, A.C. Ferrari, Nanotube-Polymer Composites for Ultrafast Photonics, *Advanced Materials* 21 (2009) 3874.

[221] F. Fischer, Thermoplastics: The Best Choice for 3D Printing, *White Paper, Stratasys Inc., Edn Prairie, MN* (2011).

[222] Y. Wang, S.M. Chiao, T.-F. Hung, S.-Y. Yang, Improvement in toughness and heat resistance of poly(lactic acid)/polycarbonate blend through twin-screw blending: Influence of compatibilizer type, *Journal of Applied Polymer Science* 125 (2012) E402.

[223] R. Greco, M.F. Astarita, L. Dong, A. Sorrentino, Polycarbonate/ABS blends: Processability, thermal properties, and mechanical and impact behavior, *Advances in Polymer Technology* 13 (1994) 259.

[224] O. Olabisi, K. Adewale, Handbook of thermoplastics, CRC Press, 1997.

[225] J. V. Rutkowski, B.C. Levin, Acrylonitrile-butadiene-styrene copolymers (ABS): Pyrolysis and combustion products and their toxicity: a review of the literature, *Fire and Materials* 10 (1986) 93.

[226] B. Stephens, P. Azimi, Z. El Orch, T. Ramos, Ultrafine particle emissions from desktop 3D printers, *Atmospheric Environment* 79 (2013) 334.

[227] X. Wei, D. Li, W. Jiang, Z. Gu, X. Wang, Z. Zhang, Z. Sun, 3D Printable Graphene Composite, *Scientific Reports* 5 (2015) 11181.

[228] M. Yoonessi, J.R. Gaier, Highly conductive multifunctional graphene polycarbonate nanocomposites., *ACS Nano* 4 (2010) 7211.

[229] P.K. Sain, R.K. Goyal, Y.V.S.S. Prasad, K.B. Sharma, A.K. Bhargava, Few-layer-graphene/polycarbonate nanocomposites as dielectric and conducting material, *Journal of Applied Polymer Science* 132 (2015) 42443.

[230] M. Wegrzyn, A. Ortega, A. Benedito, E. Gimenez, Thermal and electrical conductivity of melt mixed polycarbonate hybrid composites co-filled with multi-walled carbon nanotubes and graphene nanoplatelets, *Journal of Applied Polymer Science* 132 (2015) 42536.

[231] B.Y. Lee, J.Y. Park, Y.C. Kim, Effect of polycarbonate structure and reduction time on graphene oxide dispersion, *Polymers for Advanced Technologies* 26 (2015) 1241.

[232] R.J. Golden, S.E. Holm, D.E. Robinson, P.H. Julkunen, E.A. Reese, Chloroform mode of action: implications for cancer risk assessment, *Regulatory Toxicology and Pharmacology : RTP* 26 (1997) 142.

[233] R.S. Chhabra, M.R. Elwell, B. Chou, R.A. Miller, R.A. Renne, Subchronic Toxicity of Tetrahydrofuran Vapors in Rats and Mice, *Toxicological Sciences* 14 (1990) 338.

[234] D.R. Lide, Handbook of organic solvents, CRC Press, 1995.

[235] E. Calvo, M. Pintos, A. Amigo, R. Bravo, Surface tension and density of mixtures of 1,3-dioxolane+alkanols at 298.15 K: Analysis under the extended Langmuir model, *Journal of Colloid and Interface Science* 272 (2004) 438.

[236] M.D. Lechner, C. Wohlfarth, B. Wohlfarth, Surface Tension of Pure Liquids and Binary Liquid Mixtures, Springer, 2015.

[237] F. Torrisi, T. Hasan, W. Wu, Z. Sun, A. Lombardo, T.S. Kulmala, G.-W. Hsieh, S. Jung, F. Bonaccorso, P.J. Paul, D. Chu, A.C. Ferrari, Inkjet-printed graphene electronics, *ACS Nano* 6 (2012) 2992.

[238] G. Weiss, Hazardous chemicals data book, 2nd ed., Noyes Data Corp., 1986.

[239] E.W. Flick, Industrial solvents handbook, Noyes Publications, 1985.

[240] J. Dybal, P. Schmidt, J. Baldrian, J. Kratochvíl, Ordered Structures in Polycarbonate Studied by Infrared and Raman Spectroscopy, Wide-Angle X-ray Scattering, and Differential Scanning Calorimetry, *Macromolecules* 31 (1998) 6611.

[241] Q. Su, S. Pang, V. Alijani, C. Li, X. Feng, K. Müllen, Composites of Graphene with Large Aromatic Molecules, *Advanced Materials* 21 (2009) 3191.

[242] T. Tsukamoto, K. Yamazaki, H. Komurasaki, T. Ogino, Effects of Surface Chemistry of Substrates on Raman Spectra in Graphene, *The Journal of Physical Chemistry C* 116 (2012) 4732.

[243] R. Anitha, S. Arunachalam, P. Radhakrishnan, Critical parameters influencing the quality of prototypes in fused deposition modelling, *Journal of Materials Processing Technology* 118 (2001) 385.

[244] S.. Masood, W.. Song, Development of new metal/polymer materials for rapid tooling using Fused deposition modelling, *Materials & Design* 25 (2004) 587.

[245] B.S. Banerjee, S.S. Khaira, K. Balasubramanian, Thin film encapsulation of nano composites of polycarbonate (PC) for thermal management systems, *RSC Adv.* 4 (2014) 63380.

[246] M. Karevan, S. Eshraghi, R. Gerhardt, S. Das, K. Kalaitzidou, Effect of processing method on the properties of multifunctional exfoliated graphite nanoplatelets/polyamide 12 composites, *Carbon* 64 (2013) 122.

[247] L. Gong, R.J. Young, I.A. Kinloch, I. Riaz, R. Jalil, K.S. Novoselov, Optimizing the reinforcement of polymer-based nanocomposites by graphene, *ACS Nano* 6 (2012) 2086.

[248] B. Shen, W. Zhai, M. Tao, D. Lu, W. Zheng, Enhanced interfacial interaction between polycarbonate and thermally reduced graphene induced by melt blending, *Composites Science and Technology* 86 (2013) 109.

[249] V. Mittal, A.U. Chaudhry, Polymer - Graphene nanocomposites: Effect of polymer matrix and filler amount on properties, *Macromolecular Materials and Engineering* 300 (2015) 510.

[250] E. Tkalya, M. Ghislandi, R. Otten, M. Lotya, A. Alekseev, P. van der Schoot, J. Coleman, G. de With, C. Koning, Experimental and theoretical study of the influence of the state of dispersion of graphene on the percolation threshold of conductive graphene/polystyrene nanocomposites, *ACS Applied Materials & Interfaces* 6 (2014) 15113.

[251] N. Johner, C. Grimaldi, I. Balberg, P. Ryser, Transport exponent in a three-dimensional continuum tunneling-percolation model, *Physical Review B - Condensed Matter and Materials Physics* 77 (2008) 174204.

[252] W. Bauhofer, J.Z. Kovacs, A review and analysis of electrical percolation in carbon nanotube polymer composites, *Composites Science and Technology* 69 (2009) 1486.

[253] L. He, S.C. Tjong, Low percolation threshold of graphene/polymer composites prepared by solvothermal reduction of graphene oxide in the polymer solution, *Nanoscale Research Letters* 8 (2013) 132.

[254] J. Liang, Y. Wang, Y. Huang, Y. Ma, Z. Liu, J. Cai, C. Zhang, H. Gao, Y. Chen, Electromagnetic interference shielding of graphene/epoxy composites, *Carbon* 47 (2009) 922.

[255] W. Meng, Y. Huang, Y. Fu, Z. Wang, C. Zhi, D. Golberg, K. Niihara, T. Nakayama, S.W. Lee, Y.H. Park, K. Niihara, L. Gao, G. Stanton, H.-Y. Kim, K. Lee, G.T. Kim, G.S. Duesberg, T. Hallam, J.J. Boland, J.J. Wang, J.F. Donegan, J.C. Grunlan, G. Moriarty, A. Shmeliov, R.J. Nicholls, J.M. Perkins, E.M. Grieveson, K. Theuwissen, D.W. McComb, P.D. Nellist, V. Nicolosi, Polymer composites of boron nitride nanotubes and nanosheets, *Journal of Materials Chemistry C* 2 (2014) 10049.

[256] R. Jan, P. May, A.P. Bell, A. Habib, U. Khan, J.N. Coleman, Enhancing the mechanical properties of BN nanosheet-polymer composites by uniaxial drawing, *Nanoscale* 6 (2014) 4889.

[257] T. Sainsbury, A. Satti, P. May, A. O’Neill, V. Nicolosi, Y.K. Gun’Ko, J.N. Coleman, Covalently functionalized hexagonal boron nitride nanosheets by nitrene addition, *Chemistry - A European Journal* 18 (2012) 10808.

[258] X. Huang, X. Qi, F. Boey, H. Zhang, Graphene-based composites, *Chemical Society Reviews* 41 (2012) 666.

[259] T.D. Fornes, D.R. Paul, Modeling properties of nylon 6/clay nanocomposites using composite theories, *Polymer* 44 (2003) 4993.

[260] X. Zhao, Q. Zhang, D. Chen, P. Lu, Enhanced Mechanical Properties of Graphene-Based

Poly(vinyl alcohol) Composites, *Macromolecules* 43 (2010) 2357.

[261] M.A. Rafiee, J. Rafiee, Z. Wang, H. Song, Z.-Z. Yu, N. Koratkar, Enhanced Mechanical Properties of Nanocomposites at Low Graphene Content, *ACS Nano* 3 (2009) 3884.

[262] L. Gong, I.A. Kinloch, R.J. Young, I. Riaz, R. Jalil, K.S. Novoselov, Interfacial Stress Transfer in a Graphene Monolayer Nanocomposite, *Advanced Materials* 22 (2010) 2694.

[263] J. Rosenthal, A model for determining fiber reinforcement efficiencies and fiber orientation in polymer composites, *Polymer Composites* 13 (1992) 462.

[264] M. Rubinstein, R.H. Colby, Polymer physics, Oxford University Press, 2003.

[265] J.N. Coleman, U. Khan, W.J. Blau, Y.K. Gun’ko, Small but strong: A review of the mechanical properties of carbon nanotube-polymer composites, *Carbon* 44 (2006) 1624.

[266] R.A. Vaia, J.F. Maguire, Polymer Nanocomposites With Prescribed Morphology: Going Beyond Nanoparticle- Filled Polymers, *Chemistry of Materials* 19 (2007) 2736.

[267] T. Kato, Polymer/Calcium Carbonate Layered Thin-Film Composites, *Advanced Materials* 12 (2000) 1543.

[268] G. Ozkoc, G. Bayram, E. Bayramli, Short glass fiber reinforced ABS and ABS/PA6 composites: Processing and characterization, *Polymer Composites* 26 (2005) 745.

[269] M.K. Akkapeddi, Glass fiber reinforced polyamide-6 nanocomposites, *Polymer Composites* 21 (2000) 576.

[270] P. Liu, Z. Jin, G. Katsukis, L.W. Drahushuk, S. Shimizu, C.-J. Shih, E.D. Wetzel, J.K. Taggart-Scarff, B. Qing, K.J. Van Vliet, R. Li, B.L. Wardle, M.S. Strano, Layered and scrolled nanocomposites with aligned semi-infinite graphene inclusions at the platelet limit, *Science* 353 (2016) 364.

[271] K. Kalaitzidou, H. Fukushima, L.T. Drzal, Mechanical properties and morphological characterization of exfoliated graphite-polypropylene nanocomposites, *Composites Part A: Applied Science and Manufacturing* 38 (2007) 1675.

[272] T. Morishita, H. Okamoto, Facile Exfoliation and Noncovalent Superacid Functionalization of Boron Nitride Nanosheets and Their Use for Highly Thermally Conductive and Electrically Insulating Polymer Nanocomposites, *ACS Applied Materials & Interfaces* 8 (2016) 27064.

[273] N. Gamze Karsli, T. Yilmaz, A. Aytac, G. Ozkoc, Investigation of erosive wear behavior and physical properties of SGF and/or calcite reinforced ABS/PA6 composites, *Composites Part B: Engineering* 44 (2013) 385.

[274] Y. Yoo, M.W. Spencer, D.R. Paul, Morphology and mechanical properties of glass fiber reinforced Nylon 6 nanocomposites, *Polymer* 52 (2011) 180.

[275] C. Yu, T. Zhu, X. Zhang, H. Liu, Influences of Lateral Size on the Properties of Graphene Based Materials and Poly(vinylbutyral)/Graphene Composite Materials, *Science of Advanced Materials* 7 (2015) 1213.

[276] N.M. Pugno, Mimicking nacre with super-nanotubes for producing optimized super-composites, *Nanotechnology* 17 (2006) 5480.

[277] J.-W. Jiang, J.-S. Wang, B. Li, Young's modulus of graphene: A molecular dynamics study, *Physical Review B* 80 (2009) 113405.

[278] K. Pearson, Note on Regression and Inheritance in the Case of Two Parents, *Proceedings of the Royal Society of London (1854-1905)* 58 (1895) 240.

[279] H.L. Cox, The elasticity and strength of paper and other fibrous materials, *British Journal of Applied Physics* 3 (1952) 72.

[280] R.J. Young, M. Liu, I.A. Kinloch, S. Li, X. Zhao, C. Vallés, D.G. Papageorgiou, The mechanics of reinforcement of polymers by graphene nanoplatelets, *Composites Science and Technology* 154 (2018) 110.

[281] K. Liu, Q. Yan, M. Chen, W. Fan, Y. Sun, J. Suh, D. Fu, S. Lee, J. Zhou, S. Tongay, J. Ji, J.B. Neaton, J. Wu, Elastic Properties of Chemical-Vapor-Deposited Monolayer MoS2, WS2, and Their Bilayer Heterostructures, *Nano Letters* 14 (2014) 5097.

[282] S.R. Ahmad, C. Xue, R.J. Young, The mechanisms of reinforcement of polypropylene by graphene nanoplatelets, *Materials Science and Engineering B: Solid-State Materials for Advanced Technology* 216 (2017) 2.

[283] A.M. Pinto, S. Moreira, I.C. Gonçalves, F.M. Gama, A.M. Mendes, F.D. Magalhães, Biocompatibility of poly(lactic acid) with incorporated graphene-based materials, *Colloids and Surfaces B: Biointerfaces* 104 (2013) 229.

[284] J. Hu, Y. Huang, X. Zeng, Q. Li, L. Ren, R. Sun, J.-B. Xu, C.-P. Wong, Polymer composite with enhanced thermal conductivity and mechanical strength through orientation manipulating of BN, *Composites Science and Technology* 160 (2018) 127.

[285] J. Zhang, W. Lei, D. Liu, X. Wang, Synergistic influence from the hybridization of boron nitride and graphene oxide nanosheets on the thermal conductivity and mechanical properties of polymer nanocomposites, *Composites Science and Technology* 151 (2017) 252.

[286] A. Ansaldo, P. Bondavalli, S. Bellani, A.E. Del Rio Castillo, M. Prato, V. Pellegrini, G. Pognon, F. Bonaccorso, High-power graphene–Carbon nanotube hybrid supercapacitors, *ChemNanoMat* 3 (2017) 436.

[287] H. Chen, V. V. Ginzburg, J. Yang, Y. Yang, W. Liu, Y. Huang, L. Du, B. Chen, Thermal conductivity of polymer-based composites: Fundamentals and applications, *Progress in Polymer Science* 59 (2016) 41.

[288] Z. Lin, A. Mcnamara, Y. Liu, K. Moon, C.-P. Wong, Exfoliated hexagonal boron nitride-based polymer nanocomposite with enhanced thermal conductivity for electronic encapsulation, *Composites Science and Technology* 90 (2014) 123.

[289] R. Prasher, Thermal Interface Materials: Historical Perspective, Status, and Future Directions, *Proceedings of the IEEE* 94 (2006) 1571.

[290] S. V. Garimella, A.S. Fleischer, J.Y. Murthy, A. Keshavarzi, R. Prasher, C. Patel, S.H. Bhavnani, R. Venkatasubramanian, R. Mahajan, Y. Joshi, B. Sammakia, B.A. Myers, L. Chorosinski, M. Baelmans, P. Sathyamurthy, P.E. Raad, Thermal challenges in next-generation electronic systems, *IEEE Transactions on Components and Packaging Technologies* 31 (2008) 801.

[291] X. Du, I. Skachko, A. Barker, E.Y. Andrei, Approaching ballistic transport in suspended

graphene, *Nature Nanotechnology* 3 (2008) 491.

[292] N. Karim, S. Afroj, S. Tan, P. He, A. Fernando, C. Carr, K.S. Novoselov, Scalable Production of Graphene-Based Wearable E-Textiles, *ACS Nano* 11 (2017) 12266.

[293] M. Shtein, R. Nadiv, M. Buzaglo, K. Kahil, O. Regev, Thermally Conductive Graphene-Polymer Composites: Size, Percolation, and Synergy Effects, *Chemistry of Materials* 27 (2015) 2100.

[294] H. Jiang, Z. Wang, H. Geng, X. Song, H. Zeng, C. Zhi, Highly Flexible and Self-Healable Thermal Interface Material Based on Boron Nitride Nanosheets and a Dual Cross-Linked Hydrogel, *ACS Applied Materials and Interfaces* 9 (2017) 10078.

[295] C. Xia, A.C. Garcia, S.Q. Shi, Y. Qiu, N. Warner, Y. Wu, L. Cai, H.R. Rizvi, N.A. D'Souza, X. Nie, Hybrid boron nitride-natural fiber composites for enhanced thermal conductivity, *Scientific Reports* 6 (2016) 34726.

[296] S. Ghaffari, S. Khalid, M. Butler, H.E. Naguib, Development of High Thermally Conductive and Electrically Insulative Polylactic Acid (PLA) and Hexagonal Boron Nitride (hBN) Composites for Electronic Packaging Applications, *Journal of Biobased Materials and Bioenergy* 9 (2015) 145.

[297] H.S. Kim, H.S. Bae, J. Yu, S.Y. Kim, Thermal conductivity of polymer composites with the geometrical characteristics of graphene nanoplatelets, *Scientific Reports* 6 (2016) 26825.

[298] J. Zhang, X. Wang, C. Yu, Q. Li, Z. Li, C. Li, H. Lu, Q. Zhang, J. Zhao, M. Hu, Y. Yao, A facile method to prepare flexible boron nitride/poly(vinyl alcohol) composites with enhanced thermal conductivity, *Composites Science and Technology* 149 (2017) 41.

[299] B.-H. Xie, X. Huang, G.-J. Zhang, High thermal conductive polyvinyl alcohol composites with hexagonal boron nitride microplatelets as fillers, *Composites Science and Technology* 85 (2013) 98.

[300] H. Shen, J. Guo, H. Wang, N. Zhao, J. Xu, Bioinspired Modification of h-BN for High Thermal Conductive Composite Films with Aligned Structure, *ACS Applied Materials & Interfaces* 7 (2015) 5701.

[301] C. Yu, W. Gong, W. Tian, Q. Zhang, Y. Xu, Z. Lin, M. Hu, X. Fan, Y. Yao, Hot-pressing induced alignment of boron nitride in polyurethane for composite films with thermal conductivity over 50 Wm−1 K−1, *Composites Science and Technology* 160 (2018) 199.

[302] Z. Kuang, Y. Chen, Y. Lu, L. Liu, S. Hu, S. Wen, Y. Mao, L. Zhang, Fabrication of Highly Oriented Hexagonal Boron Nitride Nanosheet/Elastomer Nanocomposites with High Thermal Conductivity, *Small* 11 (2015) 1655.

[303] F. Wang, Y. Yao, X. Zeng, T. Huang, R. Sun, J. Xu, C.-P. Wong, Highly thermally conductive polymer nanocomposites based on boron nitride nanosheets decorated with silver nanoparticles, *RSC Advances* 6 (2016) 41630.

[304] K.M.F. Shahil, A.A. Balandin, Thermal properties of graphene and multilayer graphene: Applications in thermal interface materials, *Solid State Communications* 152 (2012) 1331.

[305] K. Sa, P.C. Mahakul, S. Saha, D. Behara, P.N. Vishwakarma, P. Mahanandia, Investigation of Electrical and Thermal Properties of Reduced Graphene Oxide-Multiwalled Carbon Nanotubes/PMMA Hybrid Nanocomposite, *Physica Status Solidi (A)* 215 (2018) 1700476.

[306] M.K. Shin, B. Lee, S.H. Kim, J.A. Lee, G.M. Spinks, S. Gambhir, G.G. Wallace, M.E. Kozlov, R.H. Baughman, S.J. Kim, Synergistic toughening of composite fibres by self-alignment of reduced graphene oxide and carbon nanotubes, *Nature Communications* 3 (2012) 650.

[307] C.-C. Teng, C.-C.M. Ma, K.-C. Chiou, T.-M. Lee, Y.-F. Shih, Synergetic effect of hybrid boron nitride and multi-walled carbon nanotubes on the thermal conductivity of epoxy composites, *Materials Chemistry and Physics* 126 (2011) 722.

[308] S.Y. Pak, H.M. Kim, S.Y. Kim, J.R. Youn, Synergistic improvement of thermal conductivity of thermoplastic composites with mixed boron nitride and multi-walled carbon nanotube fillers, *Carbon* 50 (2012) 4830.

[309] L. Shao, L. Shi, X. Li, N. Song, P. Ding, Synergistic effect of BN and graphene nanosheets in 3D framework on the enhancement of thermal conductive properties of polymeric composites, *Composites Science and Technology* 135 (2016) 83.

[310] S.G. Mosanenzadeh, S. Khalid, Y. Cui, H.E. Naguib, High thermally conductive PLA based composites with tailored hybrid network of hexagonal boron nitride and graphene nanoplatelets, *Polymer Composites* 37 (2016) 2196.

[311] S. Colonna, O. Monticelli, J. Gomez, C. Novara, G. Saracco, A. Fina, Effect of morphology and defectiveness of graphene-related materials on the electrical and thermal conductivity of their polymer nanocomposites, *Polymer* 102 (2016) 292.

Appendix – Liquid-Phase Exfoliated Indium-Selenide Flakes and Their Application in Hydrogen Evolution Reaction

Alongside the activity devoted to the polymer composite field, during my research I have contributed to one of the first reports on production of few-layer indium selenide (InSe) by means of LPE [1] and its application in the field of electrocatalysis for water-splitting.

Considered out of topic for the scope of this Thesis, I will discuss the results that I have obtained in this appendix.

A.1 Introduction

As a result of the energy crisis and environmental pollution, one of the main challenges for today's society is to produce highly efficient and low-cost renewable energy sources [2]. Hydrogen is one of the most promising clean energy carriers, and it has consequently attracted an increasing amount of interest concerning both energy production and storage [3–5]. Specifically, electrochemical water splitting is viewed as an efficient and scalable method for viable H_2 production [6,7]. To date, Pt-based systems are the most efficient electrocatalysts for a hydrogen evolution reaction (HER) since they have an overpotential at a cathodic current density of 10 mA cm^{-2} (η_{10}) at nearly 50 mV [8–10]. Nevertheless, the high cost (> 30 USD g^{-1}) [11] and the limited availability (< 0.005 ppm) [12] of Pt make the quest to find alternative cheaper materials inevitable [9,10,13–15].

In this regard, layered materials such as transition-metal dichalcogenides (TMDs) [16–20], transition-metal carbides [21] and oxides [22–25] are promising Earth-abundant candidates as HER-electrocatalysts. Furthermore, the exfoliation of bulk layered materials in atomically thick flakes is effective for improving the HER efficiency compared to the bulk counterpart due to the increase in the number of exposed active sites, *i.e.*, the defects or vacancies that are mainly located at the edges of the 2D flakes [9,10,26–28]. According to theoretical predictions [29–32], the family of III−VI layered compounds, MX (M = Ga, In; X = S, Se, Te), are good candidates for hydrogen production [33]. MX compounds are wide bandgap semiconductors, with band gaps ranging from 1.2 to ~ 3.0 eV at room temperature (RT) [33–36], made of stacked quaternary layers of X–M–M–X atoms that are held together by van der Waals interactions [33,37]. Similarly to exfoliated TMDs, such as the most studied MoS_2 [16–20] and $MoSe_2$ [16–20], the unsaturated chalcogen-edges in the natural phase of MX compounds can be HER electrocatalytically active, with Gibbs free energy (ΔG) of adsorbed protons (H_{ads}) close to zero [16–20]. Notably, density functional theory (DFT) calculation evidenced that MX monolayers exhibit band edges located at energetically favourable positions for solar water splitting [29], *i.e.*, conduction band minimum energy higher than the standard reduction potential of H^+/H_2, which is –4.44 eV vs. vacuum energy level at pH = 0, and a valence band maximum energy lower than the standard oxidation potential of O_2/H_2O, which is –5.67 eV *vs.* vacuum energy level at pH = 0 [29]. Among these monolayers, indium selenide (InSe) has a conduction band edge energy of –4.14 eV *vs.* vacuum energy level,[29] which is closer to the HER standard reduction potential than that of other members of the III-VI family [29]. Based on this consideration, the investigation of the HER–electrocatalytic activity of InSe, as well as that on the other exfoliated MX compounds is of utmost interest. Early experiments carried out in acid electrolyte have been reported for gallium sulfide (GaS) flakes obtaining η_{10} ~ 570 mV [38].

Indium selenide, according to the stacking arrangements of quaternary layers, has four possible layered polytypes, β, ε, γ, and δ, where the β and γ-phases are two most viable forms [33,39]. For β-InSe, each primitive unit cell contains two quaternary layers, *i.e.*, eight atoms, while in the unit cell of γ-phase, there are three Se–In–In–Se monatomic layers, *i.e.*, twelve atoms [33,39,40]. Due to the quantum confinement effect [36,41], both β and γ-phases of InSe undergo a direct-to-indirect bandgap crossover with decreasing thickness [36,40–43], varying the bandgap value at room temperature from 1.3 eV in bulk [36,44] to ~ 2.1 eV in the single-layer limit [42].

Although mechanically-exfoliated InSe flakes, as well as their graphene heterostructures [45] have been used for devising optoelectronic devices (mostly photodetectors) [46–48], they have not been exploited yet in electrocatalytic applications [29]. Moreover, current InSe-based optoelectronic devices have been produced with mechanically exfoliated crystals [45–48]. However, micromechanical cleavage is not an industrially-relevant approach, especially for wide-scale technology transfer, since it suffers from a low-throughput [49,50]. Conversely, LPE is a scalable and cheap technique compared to other 2D crystal synthesis approaches [49,50] enabling the exfoliation of layered bulk materials in a liquid medium, *e.g.*, solvents[49,51–53] and surfactant or polymer solutions [49,51–53], by applying an external driving force such as ultra-sonication [49,51–53], as already discussed in section 1.2.1. Thus, LPE avoids the need for growing substrates or for a long processing time, which are typical constraints of the chemical vapour deposition (CVD) process, for example [49,54].

The most common solvent used to exfoliate layered crystals is NMP [52,55] because of its suitable surface energy and Hansen's solubility parameters (HSPs). Nevertheless, NMP is a teratogenic solvent (Health code ≥ 2, NFPA704) [56] with a high boiling point (202 °C) [57]. These two characteristics raise concerns for its applicability for the large-scale production of 2D crystals for technological applications. In particular, the boiling point of the solvent has to be taken into account with regard to the realization of high-performance devices [58–60]. The removal of the solvent is crucial, and this is achieved by heating up the sample or the entire device above its boiling point, but this process could either degrade the sample or damage the device [58–60]. Notably, when heated, NMP leaves contaminants as it degrades [61,62], which subsequently reduces the device performance [60,63]. For these reasons, non-toxic solvents that are easily handled (*i.e.* solvents that have a low boiling point) and that have a low environmental impact [58,59] are particularly attractive. This issue, however, has not been addressed yet with regard to InSe. In fact, a recent study reports the LPE of β-InSe from bulk powder into few-layered flakes [55], which have been used to develop a photodetector, by using NMP as a solvent.

In the next sections I will present the LPE of β-InSe in 2-propanol (IPA), a non-toxic solvent (Health code 1; NFPA704) [56] with a low boiling point (82.6 °C) [57], as an effective route for the exfoliation of β-InSe crystals in atomically thick flakes, without the formation of other chemical species, *i.e.* In_2Se_3 or In_2O_3. Therefore, is proposed the use of LPE InSe flakes as electrocatalysts for HER displaying pH-universal HER activity, which is dependent on the flakes morphology, *i.e.*, surface area and thickness.

A.2. Few-layer InSe flakes production and characterization

A.2.1 LPE of InSe and optical characterization

β-InSe single-crystals, produced by the modified Bridgman-Stockbarger method [44] (Figure A.1a), are exfoliated by means of LPE in IPA. The use of this solvent has significant advantages in material processing and analysis due to its nontoxicity and low boiling point [57]. Moreover, IPA has been successfully used to exfoliate layered compounds such as GaS [38,64], GaSe [64], and TMDs [52]. Sonication (Figure A.1c) and ultra-centrifugation (Figure A.1d) of β-InSe single-crystals are performed to obtain a stable pale orange dispersion of exfoliated β-InSe flakes (Figure A.1e and bottom inset of Figure A.1f). In order to investigate the HER activity dependence on the β-InSe flakes' morphology, I prepared three different samples, which were selected by varying the ultra-centrifugation speeds, *i.e.* 200*g* (ex-InSe 200*g*), 1000*g* (ex-InSe 1000*g*) and 4000*g* (ex-InSe 4000*g*). In the following text, structural and morphological analyses refer mostly to the ex-InSe 1000*g* sample, simply named 'ex-InSe', which was expected to be a trade-off in the physicochemical properties between the slower and the higher ultra-centrifugation speeds.

In order to evaluate the concentration of the dispersed ex-InSe flakes, optical extinction measurements were performed. Figure A.1f shows a typical ex-InSe extinction spectrum which is characterized by two features at ~ 275 nm and at ~ 360 nm that are related to the maxima in the imaginary part of the dielectric function that is connected to the direct transitions from the valence band to the conduction band [65]. The corresponding wavelength of both peaks is shifted toward lower values by decreasing the average flake thickness (Figure A.2a) according to the planar quantum confinement of photo-excited carriers [36].

The concentration of the dispersion is estimated by the Beer-Lambert law: [66]:

$$E = \varepsilon c l \tag{A.1}$$

in which E is the extinction, ε is the optical extinction coefficient, c is the concentration and l is the path length. Optical extinction measurements, at known concentrations of ex-InSe dispersed flakes in IPA, allow the optical extinction coefficient to be estimated. The slope of this curve provides ε = 580 L g^{-1} m^{-1} at 600 nm (top inset to Figure A.1f). At this wavelength, the extinction coefficient is found to be size-independent, as optical extinction spectra of samples sorted by different ultra-centrifugation speeds overlap above 550 nm (Figure A.2b). By using the experimentally derived ε value, the concentration of ex-InSe is 0.11 g L^{-1}.

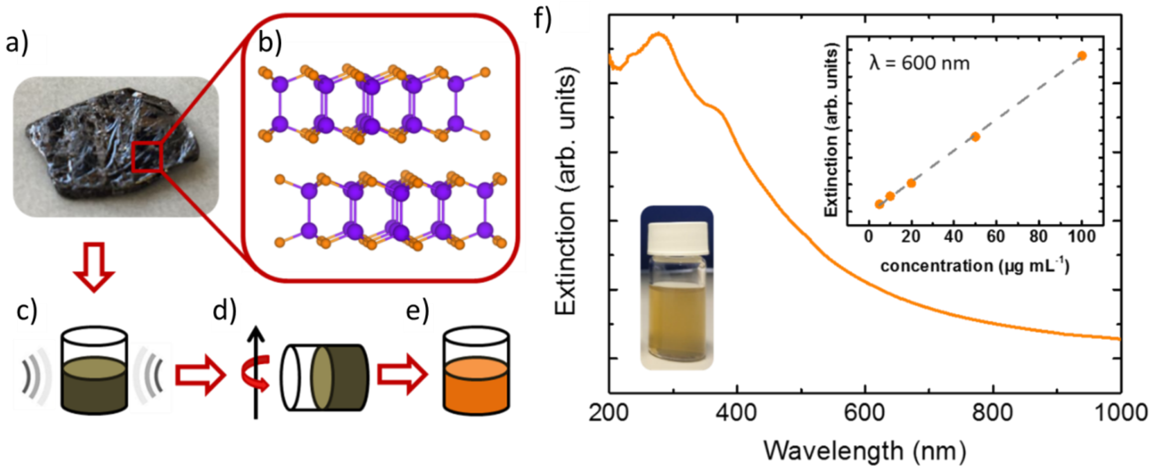

Figure A.1. Production of β-InSe ultrathin flakes by LPE. a) β-InSe single crystal, grown by the modified Bridgman-Stockbarger method; b) atomic structure of β-InSe; c), d) and e) schematics of the LPE process: sonication; ultra-centrifugation; and stable dispersion of exfoliated β-InSe flakes, respectively. f extinction spectrum of the ex-InSe sample. Top inset: optical extinction at 600 nm *vs*. concentration for ex-InSe. Bottom inset: photograph of ex-InSe dispersion in IPA. Adapted from [1].

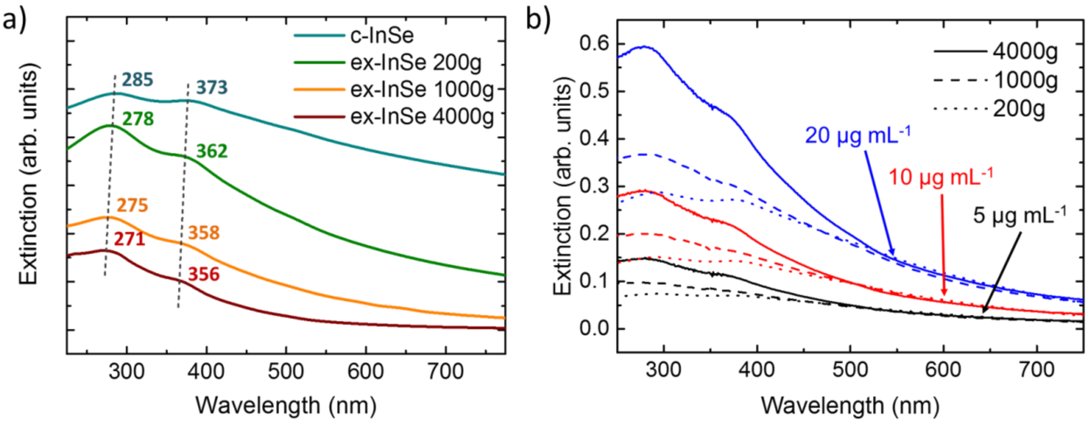

Figure A2. a) Extinction spectra of c-InSe (cyan curve), ex-InSe 200*g* (green curve), ex-InSe 1000*g* (orange curve) and ex-InSe 4000*g* (red curve). The dashed lines highlight the blue shift in position of direct transition peaks from bulk to the exfoliated InSe samples. b) Extinction spectra of ex-InSe samples at different centrifugation speeds (200*g*, dotted curves, 1000*g*, dashed curves, and 4000*g*, continue curves) and different concentrations (5µg mL^{-1}, black curves, 10µg mL^{-1}, red curves, 20µg mL^{-1}, blue curves). It is worth noting that the curves of the samples with the same concentration overlap below 550 nm. Adapted from [1].

A.2.2 Morphological and structural characterization of few-layer InSe

The effective exfoliation of β-InSe in IPA is evaluated by means of morphological, chemical and structural analyses (Figure A.3) in order to confirm the production of few-layers β-InSe flakes together with the preserved elemental composition and lattice structure. Representative TEM and AFM images for ex-InSe are reported in Figure A.3a and b, respectively. Statistical analysis, fitted by a log-normal distribution [67] (Figure A.3c), indicates that ex-InSe have a typical lateral size of ~ 113 nm (with a log-normal standard deviation of 0.84), a corresponding average surface area of ~ $6.1 \cdot 10^{-3}$ µm^2 (see the surface area statistical analysis in the inset to Figure A.3c), and a most probable thickness of 4 nm (with a log-normal standard deviation of 0.54). Thus, according to a β-InSe monolayer thickness of about 0.9 nm [42,68], single/few-layer β-InSe flakes are effectively produced, resulting in a distribution peak at ~ 4 quaternary Se–In–In–Se layers. For what concerns the morphological characterization of ex-InSe 200*g* and ex-InSe 4000*g*, as expected, the slower (higher) ultra-centrifugation speed has a larger (smaller) overall flake size than the ex-InSe 1000*g* sample, and has an average lateral size of ~ 160 nm (75 nm), surface area of ~ $11.2 \cdot 10^{-3}$ µm^2 ($2.6 \cdot 10^{-3}$ µm^2) and thickness of ~ 6.85 nm (2.61 nm). Figure A.3d shows XPS spectra of crystalline β-InSe dispersed in IPA (c-InSe) and ex-InSe for both the In and Se 3d core levels. Both the c-InSe and ex-InSe spectra show two peaks in the In 3d spectral range, which relate to the spin-orbit splitting of the d orbitals

($3d_{5/2}$ at 444.2 eV and $3d_{3/2}$ at 451.8 eV) [69], and four peaks in the Se 3d spectral range, which are associated to the spin-orbit splitting of Se^{2-} and Se^0 ($3d_{5/2}$ at 53.7/54.5 eV and $3d_{3/2}$ at 54.6/55.3 eV) [69]. The high binding energy components of Se are ascribed to surface modifications due to exposure to ambient conditions [42,70]. Nevertheless, the exfoliation process in IPA causes a slight oxidation of selenium (9.3 %), as is indicated by the features located at 58.6 and 59.5 eV, which are ascribed to the $3d_{5/2}$ and $3d_{3/2}$ core levels, respectively, in the spin-orbit splitting of Se^{4+} [69].

The acquired X-ray diffraction (XRD) patterns (Figure A.3e) demonstrate, for both the bulk (cyan trace) and the exfoliated samples (orange trace), the presence of a β-InSe hexagonal structure (D^4_{6h} symmetry, P63/mmc space group) with calculated lattice parameters of $a = b = 4.005 \pm 0.004$ Å and $c = 16.660 \pm 0.004$ Å. These findings are in agreement with the International Centre of Diffraction Data [ICDD 98-018-5172]. In particular, in the case of c-InSe, only peaks belonging to the (00*l*) plane family were observed, indicating that there are highly oriented crystalline flakes along the *c*-axis. On the other hand, for the XRD pattern of the ex-InSe sample, planes with different orientations are visible (*e.g.* 010, 011 and 110).

Raman spectroscopy measurements were also carried out with the aim of unambiguously demonstrating the absence of other chemical species, *e.g.* In_2Se_3 or In_2O_3 [71,72], during the exfoliation process or during exposure to ambient gases. Accordingly to the aforementioned β-InSe unit cell structure, counting three degrees of freedom for each atom, β-InSe has 24 vibrational modes at the centre Γ of the Brillouin zone [73]. Of these 24 modes, six are Raman active ($2A_{1g}$, $2E_{1g}$, E^1_{2g}, A_{2u}) [72,73] and their corresponding atomic vibrations are shown as an inset to Figure A.3f. As evidenced by measuring the Raman spectra at RT (Figure 3.Af), the six first-order modes are visible in both the c-InSe and ex-InSe samples. They are classified as E^1_{1g} at 40 cm^{-1}, A^1_{1g} at 117 cm^{-1}, E^2_{1g} at 178 cm^{-1}, E^1_{2g} at 200 cm^{-1}, A_{2u} at 210 cm^{-1}, A^2_{1g} at 227 cm^{-1}, which is in agreement with previous theoretical [74] and experimental works [72]. Second-order modes are also visible at RT and result from overtones of E^1_{2g} (402 cm^{-1}) and A_{2u} (423 cm^{-1}) [75]. It is worth noting that the peak positions of all modes have no significant energy shift in the ex-InSe sample as is the case for c-InSe (Figure A.4), which is in agreement with previous experimental studies [72,76]. Interestingly, no modes relating to other InSe-based compounds are observed, confirming that the stoichiometry is preserved without the formation of other chemical species during the exfoliation process [71,72]. These conclusions are further supported by XRD patterns, displayed in Figure A.3e.

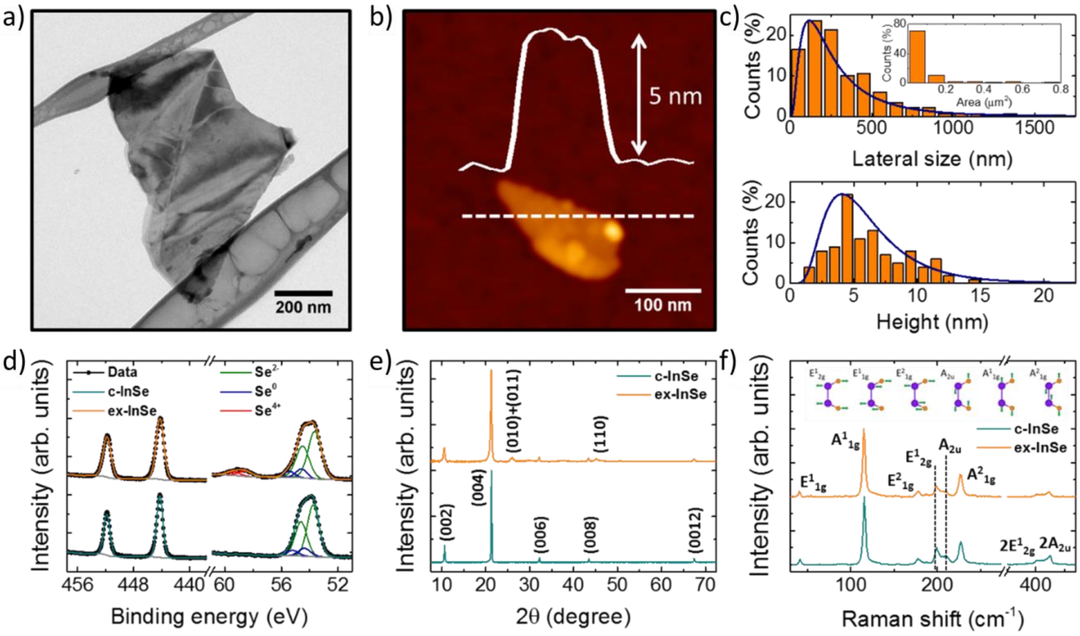

Figure A.3. Morphological, chemical and structural characterization of ex-InSe flakes. a) Representative TEM image of an isolated ex-InSe flake; b) Representative AFM image of an isolated ex-InSe flake. Height profile (solid white lines) of the indicated section (white dashed lines) is also shown; c) Lateral size and thickness statistical analyses for ex-InSe flake dispersion. Inset: statistical analysis for ex-InSe surface area; d) In-3d and Se-3d core-level spectra for c-InSe (cyan trace) and ex-InSe (orange trace) samples; e) XRD spectra for c-InSe (cyan trace) and ex-InSe (orange trace) samples; f) Raman spectra for c-InSe (cyan trace) and ex-InSe (orange trace) samples. Inset: schematic of atomic vibrations for β-InSe Raman active modes. Adapted from [1].

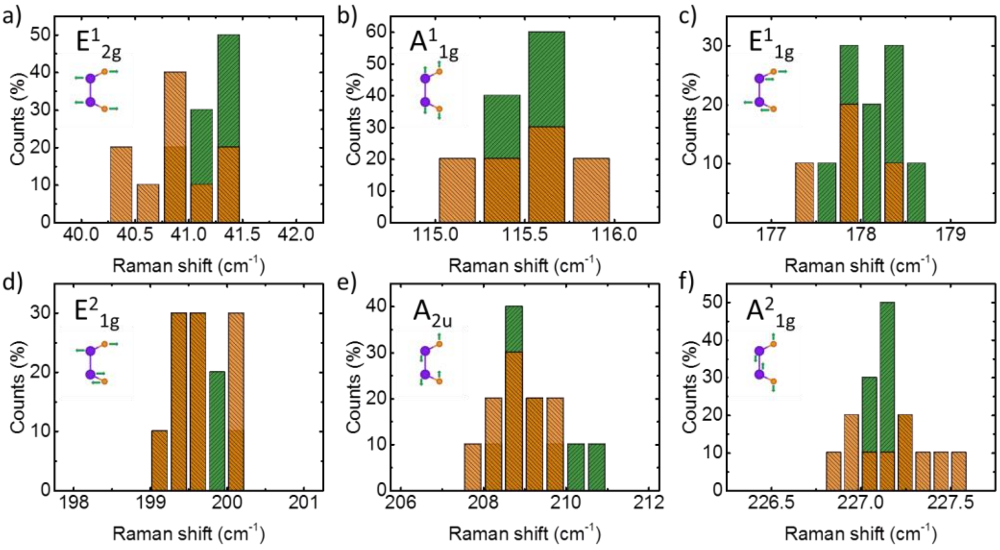

Figure A.4 Raman statistical analysis of c-InSe (green bars) and ex-InSe (orange bars) samples. a) Pos(E^1_{2g}); b) Pos(A^1_{1g}); c) Pos(E^1_{1g}); d) Pos(E^2_{1g}); e) Pos(A_{2u}); f) Pos(A^2_{1g}). No energy shifts between the bulk (c-InSe) and exfoliated (ex-InSe) samples are observed. Detail of Raman active atomic vibrations of InSe in insets of each graph. Adapted from [1].

A.3. Use of InSe flakes as electrocatalysts for water splitting

A.3.1 InSe/SWCNTs electrocatalysts fabrication and characterization

To evaluate the HER activity of β-InSe, both bulk and flake dispersions, purified at different ultra-centrifugation speeds (*i.e.* 200*g*, 1000*g* and 4000*g*), were tested. The β-InSe samples were deposited on single wall carbon nanotube (SWCNTs)-based films, which are used as flexible current collectors. As demonstrated by recent studies on carbon-based hybrid heterostructures [77–82], SWCNTs-based films can increase the electron accessibility to the HER-active sites, speeding up the HER-kinetics [83–85] compared to glassy carbon (GC) rigid electrodes. In our studies, we observed that the low adhesion of deposited β-InSe atop GC electrodes does not allow for a proper evaluation of the electrocatalytic properties of the material, *i.e.* the deposited β-InSe becomes detached from the substrate during the measurements, especially in the exfoliated samples. Additionally, the use of SWCNT-based buckypaper provides stability for the electrocatalysts in aqueous electrolytes. This permits to avoid the use of ion conducting catalyst binders (typically Nafion® [86] in acid solution and Tokuyama AS-4® [87] in the alkaline one), which can be expensive [88,89] or detrimental to the electrocatalytic activity of the catalyst [90,91]. The hybrid heterostructures formed by commercial SWCNTs (mass loading 1.2 mg cm^{-2}) and β-InSe samples (mass loading 1.2 mg cm^{-2} for each sample) were produced through a sequential vacuum filtration deposition on nylon membranes with flexible binder-free active electrodes, which are compatible with high-throughput scalable industrial manufacturing. Figure A.5a-b displays HR-SEM cross-sectional images of the as-produced c-InSe and ex-InSe based heterostructures (SWCNT/c-InSe and SWCNT/ex-InSe), respectively. Both the SWCNT/c-InSe and the SWCNT/ex-InSe electrocatalysts show a bilayered-like architecture with a distinct separation between the SWCNT-based collector and the β-InSe-based active film (~ 3 µm film thickness for ex-InSe sample). Thus, as is also evidenced by top-view images (insets to Figure A.5a-b), no penetration of β-InSe within the SWCNT-based buckypaper was observed, suggesting that the role of SWCNT film is that of a bare current collector. The HER-activities of the as-produced InSe-based electrocatalysts were evaluated in both acid (0.5 M H_2SO_4, pH = 1) and alkaline (1 M KOH, pH = 14) electrolytes (Figure A.5c-f). The HER under acidic conditions consists of two steps: H_{ads} at the catalytic sites of the electrode (Volmer reaction, $H_3O^+ + e^- \rightleftarrows H_{ads} + H_2O$), and either an electrochemical desorption step (Heyrovsky reaction, $H_{ads} + H_3O^+ + e^- \rightleftarrows H_2 + H_2O$) or a recombination step (Tafel reaction, $2H_{ads} \rightleftarrows H_2$) [92,93]**.** The occurrence of the two reactions depends on the Gibbs free energy of the process; the one which has the energy value closer to 0 eV is promoted [92,93]**.** In alkaline media, the H_{ads} is formed by the discharge of H_2O (Volmer reaction, $H_2O + e^- \rightleftarrows H_{ads} + OH^-$) [92,93]**.** Then, either the Heyrovsky step ($H_2O + H_{ads} + e^- \rightleftarrows H_2 + OH^-$) or the chemical

Tafel step ($2H_{ads} \rightleftarrows H_2$) occurs, depending on the Gibbs free energy value of the two steps [92,93]. The overpotential at a 10 mA cm^{-2} cathodic current density (η_{10}), the Tafel slope and the exchange current density (j_0) are typical figures of merit (FoM) to evaluate the HER performance of electrocatalysts.[92,93] In detail, the Tafel slope and j_0 are estimated from the linear portion of the Tafel plots (overpotential vs. current density curves) according to the Tafel equation (see the Experimental Section for further details) [92,93]**.** In particular, the Tafel slope is used to evaluate the HER mechanism at the electrode/electrolyte interface, while j_0 relates to the amount of the available active sites for HER [92,93]**.** In fact, for insufficient H_{ads} surface coverage, the Volmer reaction is the rate-limiting step of HER, and a theoretical Tafel slope of 120 mV dec^{-1} is expected [92,93]**.** Conversely, in the limit of high H_{ads} surface coverage, the HER-kinetics is dominated by Heyrovsky or Tafel reactions, and has Tafel slopes of 40 or 30 mV dec^{-1}, respectively [92,93]**.**

To relate the morphology of β-InSe flakes to HER performance, both c-InSe and samples ultra-centrifuged at different speeds, *i.e.*, ex-InSe 200*g*, ex-InSe 1000*g* and ex-InSe 4000*g*, were tested. The current density *vs.* potential relative to reversible hydrogen electrode (RHE) curves of β-InSe based electrocatalysts under both acidic and alkaline conditions are reported in Figures A.5c and A.5d, respectively. As it has been previously observed on layered crystals [94,95]**,** including GaS [38], the HER-activity of β-InSe flakes increases when the flakes' size (lateral size and thickness) decreases. Indeed, the η_{10} value scales from 581 mV (540 mV) for c-InSe, to 561 mV (483 mV) for ex-InSe 200*g*, to 556 mV (471 mV) for ex-InSe 1000*g*, to 549 mV (451 mV) for ex-InSe 4000*g* in an acid (alkaline) solution. As it has been theoretically [96,97] and experimentally[38,94,95,98] demonstrated, this effect is mostly due to the increased number of HER-active sites. In fact, the reduction in the lateral size and thickness of the flake, which occurs when the ultra-centrifugation speed is enhanced, exposes the liquid electrolyte to a larger amount of active edge defects and vacancies than those of the bulk counterpart [96–98]**.** A rigorous kinetic analysis of the HER, *i.e.* the establishment of the Tafel slope and j_0, is not conducted here because of the unambiguous results that were obtained in the presence of high-surface area SWCNT buckypaper, which gives a capacitive current density even for a low voltage scan rate ($\leq$ 5 mV s^{-1}) [99]. Nevertheless, it is worth noting that the calculated j_0 value for the exfoliated β-InSe samples increased from 0.18 µA cm^{-2} (0.45 µA cm^{-2}) for ex-InSe 200*g* to 0.42 µA cm^{-2} (5.8 µA cm^{-2}) for ex-InSe 4000*g* in an acid (alkaline) solution, suggesting that the catalytic activity is dominated by the edge sites. Experimental Tafel slopes, reported together with their corresponding Tafel plots for which pH = 1 (Figure A.5e) and pH = 14 (Figure A.5f), have values higher than 120 mV dec^{-1} for all the β-InSe samples in both an acid and alkaline solution, indicating that the Volmer reaction step determines the rate of the HER.

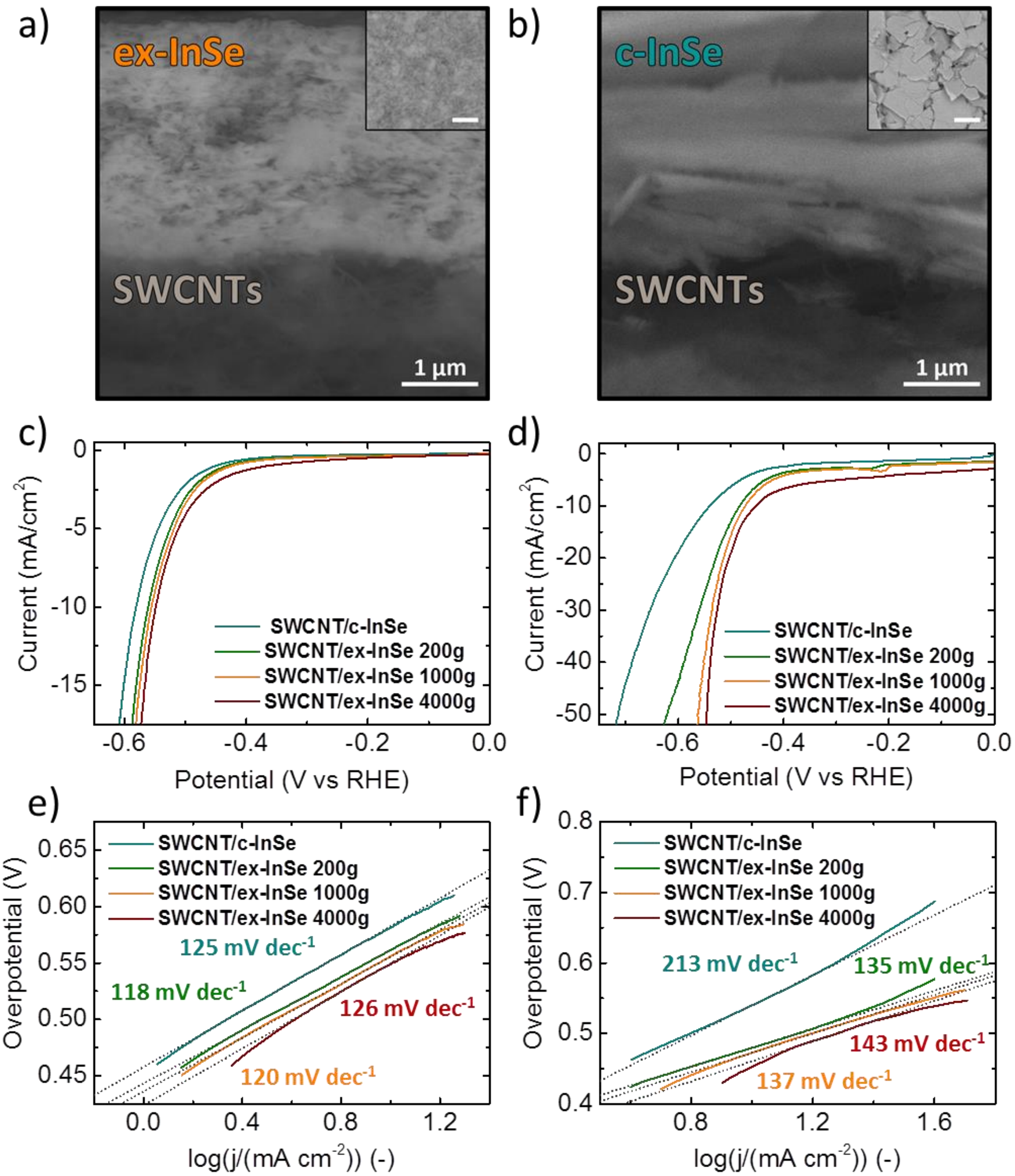

Figure A.5. Morphological and electrochemical characterization of SWCNT/β-InSe hybrid electrocatalysts. a) Cross-sectional HR-SEM image of SWCNT/c-InSe heterostructure (top view in inset, scale bar is 1 µm); b) Cross-sectional HR-SEM image of SWCNT/ex-InSe 1000*g* heterostructure (top view in inset, scale bar is 1 µm); c Current density vs. potential relative to RHE curves for SWCNT/c-InSe, SWCNT/ex-InSe 200*g* and SWCNT/ex-InSe 1000*g* samples at pH = 1; d) Current density *vs.* potential relative to RHE curves for SWCNT/c-InSe, SWCNT/ex-InSe 200*g* and SWCNT/ex-InSe 1000*g* samples at pH = 14; e) Tafel plots of the same β-InSe based electrocatalysts shown in panel c. Linear fits (dashed lines) and corresponding Tafel slope values are reported; f) Tafel plots of the same β-InSe based electrocatalysts shown in panel d. Linear fits (dashed lines) and corresponding Tafel slope values are reported. Adapted from [1].

Moreover, Tafel slope values exceeding the Volmer slope of 120 mV dec^{-1} have been previously described in theoretical studies as not having ideal behaviour due to the anion adsorption or non-uniform distribution of the surface electric field on rugged electrodes [100–102]. Previous electrochemical characterizations of MX compounds have been performed on GaS [38] and GaSe [103]. The latter, tested in its bulk form, has a poor electrocatalytic activity; $\eta_{10} > 1V$ on GC in an acid solution [103]. Conversely, exfoliated GaS deposited on pyrolytic carbon reaches a Tafel slope value of 85 mV dec^{-1} and an overpotential $\eta_{10} \sim 570$ mV under acidic conditions [38]. Thus, LPE-produced atomically thick layers of InSe exhibit the lowest η_{10} value among the MX family.

A.3.2 Insights on catalytic activity of InSe

In order to unveil the origin of the catalytic activity of InSe, DFT calculations were carried out based on a theoretical model using a 64-atom supercell ($In_{32}Se_{32}$). The energy of the reactions that rule the adsorption of water fragments (*i.e.* H^+ and OH^-), as well as the energy barriers of the H_2O dissociation (*i.e.* $H_2O + e^- \rightarrow H_{ads} + OH^-$) on InSe monolayer were calculated (Table AT.1). Notably, the latter reaction coincides with the Volmer step in alkaline environment. This step could also be concomitant with the adsorption of OH^-, whose desorption is effective in promoting HER [104]. To estimate the differential enthalpy (ΔH) that is associated to the Volmer step, the total energy of the InSe monolayer with two physisorbed water molecules (Figure A.6a) is compared to the total energy of the same system with chemisorbed H, *e.g.* H_{ads} (Figure A.6b). The presence of a second water molecule represents a minimalistic model of the water environment. Moreover, in order to have a complete representation of the HER process in an alkaline environment, the differential enthalpy associated to the adsorption of OH^- (OH_{ads}) is evaluated (Figure A.6c). The differential Gibbs free energy is evaluated using the formula:

$$\Delta G = \Delta H - T\Delta S + ZPE - eU \tag{A.2}$$

in which T is the RT and ΔS is the changes of entropy of the system, ZPE is the zero point energy and U is the overpotential (0.83 V for reaction under alkaline conditions and 1.23 V for reaction under acidic conditions) [105–107].

The results of the DFT calculations (Table AT.1) for pristine InSe monolayers indicate that the energy required for an H^+ adsorption is unfavourable ($\Delta G > 2$ eV) in both acidic and alkaline environments. Nevertheless, the presence of thermodynamically unavoidable lattice defects, such as Stone-Wales defects or Se vacancies, makes the adsorption of water fragments exothermic. In particular, the HER activity can be mainly addressed to the Se vacancies, which are naturally present in β-InSe single crystals [37,44,108]. In fact, taking into account the Se vacancies, the ΔG for H_{ads} in both acidic and alkaline environments is closer than those of the un-defected and Stone-Wales defected InSe monolayer; they have the ideal value of ΔG = 0 eV, which is an energetically feasible HER condition [109,110]. A differential Gibbs free energy close to 0 eV indicates that the H_{ads} free energy is close to that of the reactant or product. Low ΔG suggests that there is a strong bonding of H_{ads}, while a high ΔG implies that H_{ads} are weakly bonded to the catalyst surface. Both conditions negatively affect the HER kinetics [110]. In addition, the ΔG for OH^- adsorption is reduced in presence of Se vacancies (–0.84 eV) with respect to the pristine case (+2.47 eV). Thus, the beneficial OH^- desorption in an alkaline environment is favoured by the defected InSe monolayer. The reduction of ΔG for H_{ads} in presence of Se vacancies is compatible with the η_{10} downward trend that was observed in both the acid and alkaline environments when the flakes' lateral size is reduced. As a result, the edge-related HER activity is therefore linked to an increase in the number of exposed Se vacancies, which are mostly placed at the edge of the exfoliated flakes.

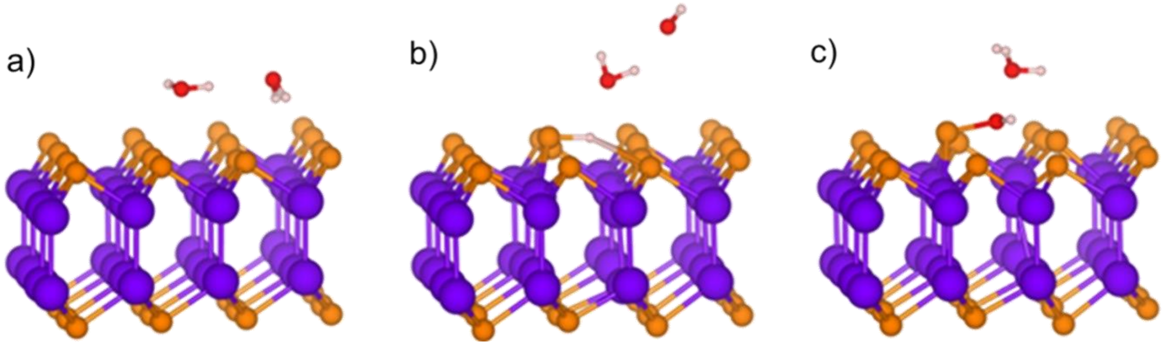

Figure A.6. Scheme of the DFT models used for investigating InSe catalytic activity. a) InSe supercell with a physisorbed pair of water molecules; b) and c) chemisorption on InSe monolayer of H_{ads} and OH_{ads}, respectively. Adapted from [1].

Table AT.1. Calculated values of the differential enthalpy (ΔH) and Gibbs free energy (ΔG) for H_{ads} and OH_{ads} in both acidic and alkaline environments.

	ΔH (eV)		ΔG (eV)		
Condition	H_{ads}	OH_{ads}	H_{ads} acid	H_{ads} alkali	OH_{ads} alkali
InSe-monolayer	+3.34	+2.95	+2.23	+2.63	+2.47
Stone-Wales defect	-1.05	-0.41	-2.16	-1.76	-0.89
Se-vacancy	+0.65	-0.36	-0.46	-0.06	-0.84

A.4. Conclusions

In conclusion, effective exfoliation of InSe single crystals by means of LPE in a non-toxic solvent has been demonstrated, obtaining a stable dispersion of atomically thick InSe flakes with an IPA concentration up to 0.11 g L^{-1}. Transmission electron and atomic force microscopy analyses allowed the exfoliated flakes' morphology to be evaluated; they had an average thickness of ~ 5 nm, corresponding to ~ 4 InSe layers, and a maximum lateral size of ~ 113 nm. Moreover, Raman, XPS and XRD analyses confirm the preservation of the crystal structural and chemical properties in the exfoliated flakes, revealing that there was not any formation of spurious compounds (*i.e.* In_2Se_3 or In_2O_3). Thus, LPE in IPA has been demonstrated to produce InSe flakes with thickness at the atomic scale, confirming its crucial role in the application and technological fields as a competitive and environmentally friendly production technique. In particular, electrochemical H_2 production was evaluated here as a possible application for InSe flakes. Hybrid and flexible heterostructures composed by SWCNTs and InSe flakes with different morphologies (*i.e.*, different lateral size and thickness) were tested under both acidic and alkaline conditions, and the smallest InSe flakes obtained a promising overpotential η_{10} of 549 mV and 471 mV, respectively. In particular it corresponds to the lowest reported values of η_{10} among the MX compounds [38,103]. These results pave the way for the use of InSe flakes in water splitting and for further optimization as flexible and cost-effective (photo)electrocatalysts. Moreover, a clear size effect is observed in the InSe HER-performance, suggesting that the active sites are located at the edges of the InSe flakes. This observation is related to the presence of Se vacancies at the edges of the flakes and is demonstrated by means of DFT calculations. In fact, theoretical results show a reduction in the exothermic ΔG in the defected InSe monolayer in comparison with its pristine counterpart. These results prove that InSe flakes are feasible materials for different types of catalytic reactions such as oxidation and reduction.

A.5. Experimental Section

Exfoliation of bulk β-InSe

β-InSe single crystals were grown by the modified Bridgman-Stockbarger method (details on the growth in Supporting Information) [44]. Exfoliated β-InSe flakes were produced through LPE [52], followed by SBS [49], in IPA (ACS Reagent, ≥ 99.8%, Sigma Aldrich). In short, 40 mg of β-InSe single crystals are pulverized in a mortar and, once added to 20 mL of IPA, ultra-sonicated in a sonicator bath (Branson® 5800 cleaner, Branson Ultrasonics) for 6 h, keeping the bath temperature in the range of 25 °C – 35 °C. The resulting dispersion was ultra-centrifuged at 200*g*, 1000*g* or 4000*g* (in a Beckman Coulter Optima™ XE-90 with a SW32Ti rotor) for 30 min at 15 °C in order to separate un-exfoliated and thick β-InSe flakes (collected as sediment) from the as-prepared dispersion. Then, 80% of the supernatant, containing small and thin β-InSe flakes, was collected by pipetting.

Material characterization

Optical extinction spectroscopy was carried out by a Cary Varian 5000UV-Vis. In order to measure the extinction spectra, exfoliated β-InSe flake dispersions in IPA were diluted 1:10 with the pure solvent. For each sample, the extinction spectra (absorbed plus scattered light) of the pure IPA were subtracted from the sample spectrum. The optical extinction coefficient was determined by using the Beer-Lambert law ($E = \varepsilon c l$, in which E is the optical extinction at 600 nm, ε is the extinction coefficient, c is the concentration of the exfoliated β-InSe flakes and l is the path length of the quartz cuvette, 0.01 m).

TEM imaging was carried out on a JEOL JEM 1400Plus microscope, operating at 120 kV, equipped with a LaB_6 thermionic source, a Gatan CCD camera Orius 830 and a JEOL Dry SD30GV silicon-drift detector (SDD). Samples for the TEM measurements were prepared by drop-casting the exfoliated β-InSe flake dispersions onto carbon-coated Cu grids with successive drying under vacuum overnight.

Atomic force microscopy images were acquired using a Nanowizard III (JPK Instruments, Germany) mounted on an Axio Observer D1 (Carl Zeiss, Germany) inverted optical microscope. The AFM measurements were carried out using PPP-NCHR cantilevers (Nanosensors, USA) with a nominal tip diameter of 10 nm. A drive frequency of ~ 295 kHz is used. Intermittent contact mode AFM images (512×512 data points) of 5×5 μm^2, 2.5×2.5 μm^2, and 500×500 nm^2 are collected by keeping the working set point above 65% of the free oscillation amplitude. The scan rate for the acquisition of images was 0.6 Hz. Height profiles of ~ 100 flakes were processed by using JPK Data Processing software (JPK Instruments, Germany). The samples were prepared by drop-casting the exfoliated β-InSe flake dispersions onto mica sheets (G250-1, Agar Scientific Ltd., Essex, U.K.) and subsequently drying them under vacuum overnight.

Raman spectroscopy measurements were carried out using a Renishaw micro-Raman InVia with a 100× objective, an excitation wavelength of 514.5 nm and an incident power of 1 mW. For each sample, 20 spectra are collected. The samples were prepared by drop casting exfoliated β-InSe flake dispersions on Si/SiO_2 substrates and drying them under vacuum. The spectra were fitted with Lorentzian functions.

The crystal structure was characterized by XRD using a PANalytical Empyrean with Cu K_α radiation. The samples for XRD were prepared by drop-casting exfoliated β-InSe flake dispersions onto Si substrates and drying them under vacuum.

X-ray photoelectron spectroscopy characterization was carried out on a Kratos Axis UltraDLD spectrometer, using a monochromatic Al Kα source (15 kV, 20 mA). The spectra were acquired over an area of 300 µm x 700 µm. Wide scans were collected with a constant pass energy of 160 eV and an energy step of 1 eV. High-resolution spectra were acquired at a constant pass energy of 10 eV and an energy step of 0.1 eV. The binding energy scale was calibrated to the C 1s peak at 284.8 eV. The spectra were analysed using CasaXPS software (version 2.3.17). The fitting of the spectra was performed by using a Shirley background and Voigt profiles. The samples were prepared by drop-casting exfoliated β-InSe flake dispersions onto Si substrates and drying them under vacuum.

Electrode fabrication

Hybrid heterostructures were fabricated by the vacuum filtration of SWCNT (> 90% purity, Cheap Tubes) dispersions in 1-Methyl-2-pyrrolidinone (Reagent Grade, 99%, Sigma Aldrich) and exfoliated β-InSe flake dispersions on nylon membranes (Whatman® membrane filters nylon, pore size 0.2 µm). The mass fraction for both materials was kept constant at 1.2 mg cm^{-2}. The SWCNT dispersion was prepared by dispersing SWCNTs in NMP at a concentration of 0.4 g L^{-1} using ultra-sonication based de-bundling [111]. The dispersion was sonicated using a horn probe sonic tip (Vibra-cell 75185, Sonics) with a vibration amplitude set to 45% and a sonication time of 30 min. The sonic tip was pulsed at a rate of 5 s on and 2 s off to avoid damage to the processor and to reduce any solvent heating. An ice bath was used during sonication in order to minimize heating effects.

Electrode characterization

High resolution scanning electron microscopy analysis was performed with a field-emission scanning electron microscope FE-SEM (Jeol JSM-7500 FA) in a high vacuum, with an acceleration voltage of 15 kV. Images were collected acquiring the backscattered electrons. A carbon coating of 10 nm on the sample is required to prevent charging effects.

Electrochemical measurements on the as-prepared hybrid heterostructures were carried out at RT in a flat-bottomed fused silica cell under a three-electrode configuration using a CompactStat potentiostat/galvanostat station (Ivium), controlled via IviumSoft. A Pt-wire was used as the counter electrode and saturated KCl Ag/AgCl was used as the reference electrode. Measurements were carried out in 0.5 M H_2SO_4 (99.999% purity, Sigma Aldrich) or 1 M KOH (≥ 85% purity, ACS reagent, pellets, Sigma Aldrich) aqueous electrolytes (pH = 1 and pH = 14, respectively). The potential difference between the working electrode and the Ag/AgCl reference electrode was converted to the reversible hydrogen electrode (RHE) scale via the Nernst equation: $E_{RHE} = E_{Ag/AgCl} + 0.059pH + E^0_{Ag/AgCl}$, in which E_{RHE} is the converted potential versus RHE, $E_{Ag/AgCl}$ is the measured potential versus the Ag/AgCl reference electrode, and $E^0_{Ag/AgCl}$ is the standard potential of Ag/AgCl at 25 °C (0.1976 V). Linear sweep voltammetry curves were acquired at a scan rate of 5 mV/s and iR-corrected, in which i is the current and the R is the series resistance that arises from the substrate and electrolyte resistance. R is measured by electrochemical impedance spectroscopy (EIS) at an open circuit potential and frequency of 10^4 Hz.

The linear portions of the Tafel plots fit the Tafel equation $\eta = m\log(j) + A$, in which η is the overpotential with respect to RHE, j is the current density, m is the Tafel slope and A is the intercept of the linear regression. The j_0 was calculated from the Tafel equation by setting $\eta = 0$.

Theoretical methods

The atomic structure and energetics of water splitting on InSe monolayers were studied by DFT using the QUANTUM-ESPRESSO code[112] and the GGA–PBE + van der Waals approximation, which are feasible for the description of the adsorption of molecules on surfaces [113,114]. Energy cut-offs of 25 Ry and 400 Ry were used for the plane-wave expansion of the wave functions and the charge density, respectively, and the 4×4×1 Monkhorst-Pack k-point grid for the Brillouin sampling [115]. Optimizations of both atomic positions and lattice vectors were performed for all calculations.

A.6. Appendix references

[1] E. Petroni, E. Lago, S. Bellani, D.W. Boukhvalov, A. Politano, B. Gürbulak, S. Duman, M. Prato, S. Gentiluomo, R. Oropesa-Nuñez, J.-K. Panda, P.S. Toth, A.E. Del Rio Castillo, V. Pellegrini, F. Bonaccorso, Liquid-Phase Exfoliated Indium-Selenide Flakes and Their Application in Hydrogen Evolution Reaction, *Small* 14 (2018) 1800749.

[2] B. Obama, The irreversible momentum of clean energy., *Science* 355 (2017) 126.

[3] I. Vamvasakis, B. Liu, G.S. Armatas, Size Effects of Platinum Nanoparticles in the Photocatalytic Hydrogen Production Over 3D Mesoporous Networks of CdS and Pt Nanojunctions, *Advanced Functional Materials* 26 (2016) 8062.

[4] G. Liu, G. Zhao, W. Zhou, Y. Liu, H. Pang, H. Zhang, D. Hao, X. Meng, P. Li, T. Kako, J. Ye, In Situ Bond Modulation of Graphitic Carbon Nitride to Construct p-n Homojunctions for Enhanced Photocatalytic Hydrogen Production, *Advanced Functional Materials* 26 (2016) 6822.

[5] V. Tozzini, V. Pellegrini, Prospects for hydrogen storage in graphene, *Phys. Chem. Chem. Phys.* 15 (2013) 80.

[6] H. Li, Y. Zhou, W. Tu, J. Ye, Z. Zou, State-of-the-Art Progress in Diverse Heterostructured Photocatalysts toward Promoting Photocatalytic Performance, *Advanced Functional Materials* 25 (2015) 998.

[7] Y. Wu, G.-D. Li, Y. Liu, L. Yang, X. Lian, T. Asefa, X. Zou, Overall Water Splitting Catalyzed Efficiently by an Ultrathin Nanosheet-Built, Hollow Ni_3S_2-Based Electrocatalyst, *Advanced Functional Materials* 26 (2016) 4839.

[8] K. Maeda, K. Teramura, D. Lu, T. Takata, N. Saito, Y. Inoue, K. Domen, Photocatalyst releasing hydrogen from water, *Nature* 440 (2006) 295.

[9] X. Zou, Y. Zhang, Noble metal-free hydrogen evolution catalysts for water splitting, *Chem. Soc. Rev.* 44 (2015) 5148.

[10] P.C.K. Vesborg, B. Seger, I. Chorkendorff, Recent Development in Hydrogen Evolution Reaction Catalysts and Their Practical Implementation, *The Journal of Physical Chemistry Letters* 6 (2015) 951.

[11] R. Sarı, S. Hammoudeh, U. Soytas, Energy economics, *Energy Economics* 32 (2010) 351.

[12] S.R. Taylor, Abundance of chemical elements in the continental crust: a new table, *Geochimica et Cosmochimica Acta* 28 (1964) 1273.

[13] J.A. Turner, Sustainable hydrogen production, *Science* 305 (2004) 972.

[14] Y. Kim, D.H.K. Jackson, D. Lee, M. Choi, T.W. Kim, S.Y. Jeong, H.J. Chae, H.W. Kim, N. Park, H. Chang, T.F. Kuech, H.J. Kim, In Situ Electrochemical Activation of Atomic Layer Deposition Coated MoS2 Basal Planes for Efficient Hydrogen Evolution Reaction, *Advanced Functional Materials* 27 (2017) 1701825.

[15] Y. Zhang, Q. Zhou, J. Zhu, Q. Yan, S.X. Dou, W. Sun, Nanostructured Metal Chalcogenides for Energy Storage and Electrocatalysis, *Advanced Functional Materials* 27 (2017) 1702317.

[16] M. Pumera, Z. Sofer, A. Ambrosi, Layered transition metal dichalcogenides for electrochemical energy generation and storage, *J. Mater. Chem. A* 2 (2014) 8981.

[17] M. Chhowalla, H.S. Shin, G. Eda, L.-J. Li, K.P. Loh, H. Zhang, The chemistry of two-dimensional layered transition metal dichalcogenide nanosheets, *Nature Chemistry* 5 (2013) 263.

[18] Q. Lu, Y. Yu, Q. Ma, B. Chen, H. Zhang, 2D Transition-Metal-Dichalcogenide-Nanosheet-Based Composites for Photocatalytic and Electrocatalytic Hydrogen Evolution Reactions, *Advanced Materials* 28 (2016) 1917.

[19] J. Shi, X. Wang, S. Zhang, L. Xiao, Y. Huan, Y. Gong, Z. Zhang, Y. Li, X. Zhou, M. Hong, Q. Fang, Q. Zhang, X. Liu, L. Gu, Z. Liu, Y. Zhang, Two-dimensional metallic tantalum disulfide as a hydrogen evolution catalyst, *Nature Communications* 8 (2017) 958.

[20] L. Najafi, S. Bellani, R. Oropesa-Nuñez, A. Ansaldo, M. Prato, A.E. Del Rio Castillo, F. Bonaccorso, Engineered MoSe2-Based Heterostructures for Efficient Electrochemical Hydrogen Evolution Reaction, *Advanced Energy Materials* 8 (2018) 1703212.

[21] Y. Zhong, X. Xia, F. Shi, J. Zhan, J. Tu, H.J. Fan, Transition Metal Carbides and Nitrides in Energy Storage and Conversion, *Advanced Science* 3 (2016) 1500286.

[22] M.T. Greiner, L. Chai, M.G. Helander, W.M. Tang, Z.H. Lu, Transition metal oxide work functions: The influence of cation oxidation state and oxygen vacancies, *Advanced Functional Materials* 22 (2012) 4557.

[23] X. Liu, W. Liu, M. Ko, M. Park, M.G. Kim, P. Oh, S. Chae, S. Park, A. Casimir, G. Wu, J. Cho, Metal (Ni, Co)-Metal Oxides/Graphene Nanocomposites as Multifunctional Electrocatalysts, *Advanced Functional Materials* 25 (2015) 5799.

[24] Y.H. Li, P.F. Liu, L.F. Pan, H.F. Wang, Z.Z. Yang, L.R. Zheng, P. Hu, H.J. Zhao, L. Gu, H.G. Yang, Local atomic structure modulations activate metal oxide as electrocatalyst for hydrogen evolution in acidic water, *Nature Communications* 6 (2015) 8064.

[25] Y. Chen, K. Yang, B. Jiang, J. Li, M. Zeng, L. Fu, Emerging two-dimensional nanomaterials for electrochemical hydrogen evolution, *J. Mater. Chem. A* 5 (2017) 8187.

[26] D. Merki, X. Hu, Recent developments of molybdenum and tungsten sulfides as hydrogen evolution catalysts, *Energy & Environmental Science* 4 (2011) 3878.

[27] D. Voiry, M. Salehi, R. Silva, T. Fujita, M. Chen, T. Asefa, V.B. Shenoy, G. Eda, M. Chhowalla, Conducting MoS2 nanosheets as catalysts for hydrogen evolution reaction, *Nano Letters* 13 (2013) 6222.

[28] L. Najafi, S. Bellani, B. Martín-García, R. Oropesa-Nuñez, A.E. Del Rio Castillo, M. Prato, I. Moreels, F. Bonaccorso, Solution-Processed Hybrid Graphene Flake/2H-MoS2 Quantum Dot Heterostructures for Efficient Electrochemical Hydrogen Evolution, *Chemistry of Materials* 29 (2017) 5782.

[29] H.L. Zhuang, R.G. Hennig, Single-Layer Group-III Monochalcogenide Photocatalysts for Water Splitting, *Chemistry of Materials* 25 (2013) 3232.

[30] Q. Peng, R. Xiong, B. Sa, J. Zhou, C. Wen, B. Wu, M. Anpo, Z. Sun, Computational mining of photocatalysts for water splitting hydrogen production: two-dimensional InSe-family monolayers, *Catalysis Science & Technology* 7 (2017) 2744.

[31] C. Chowdhury, S. Karmakar, A. Datta, Monolayer Group IV–VI Monochalcogenides: Low-Dimensional Materials for Photocatalytic Water Splitting, *The Journal of Physical Chemistry C* 121 (2017) 7615.

[32] Y. Li, Y.-L. Li, B. Sa, R. Ahuja, Review of two-dimensional materials for photocatalytic water splitting from a theoretical perspective, *Catalysis Science & Technology* 7 (2017) 545.

[33] K. Xu, L. Yin, Y. Huang, T.A. Shifa, J. Chu, F. Wang, R. Cheng, Z. Wang, J. He, C. Liu, C. Chen, J. Zou, W.D. Hu, F.X. Xiu, F.X. Xiu, T. Hyeon, J.N. Coleman, C.T. Chen, Z.Y. Xu, J.P. Hu, X. Chen, X.C. Ma, Q.K. Xue, X.J. Zhou, Synthesis, properties and applications of 2D layered $M^{III}X^{VI}$ (M = Ga, In; X = S, Se, Te) materials, *Nanoscale* 8 (2016) 16802.

[34] D.J. Late, B. Liu, H.S.S.R. Matte, C.N.R. Rao, V.P. Dravid, Rapid Characterization of Ultrathin Layers of Chalcogenides on SiO2/Si Substrates, *Advanced Functional Materials* 22 (2012) 1894.

[35] A. Yamamoto, A. Syouji, T. Goto, E. Kulatov, K. Ohno, Y. Kawazoe, K. Uchida, N. Miura, Excitons and band structure of highly anisotropic GaTe single crystals, *Physical Review B* 64 (2001) 035210.

[36] G.W. Mudd, S.A. Svatek, T. Ren, A. Patanè, O. Makarovsky, L. Eaves, P.H. Beton, Z.D.

Kovalyuk, G. V. Lashkarev, Z.R. Kudrynskyi, A.I. Dmitriev, Tuning the Bandgap of Exfoliated InSe Nanosheets by Quantum Confinement, *Advanced Materials* 25 (2013) 5714.

[37] D. Boukhvalov, B. Gürbulak, S. Duman, L. Wang, A. Politano, L. Caputi, G. Chiarello, A. Cupolillo, The Advent of Indium Selenide: Synthesis, Electronic Properties, Ambient Stability and Applications, *Nanomaterials* 7 (2017) 372.

[38] A. Harvey, C. Backes, Z. Gholamvand, D. Hanlon, D. McAteer, H.C. Nerl, E. McGuire, A. Seral-Ascaso, Q.M. Ramasse, N. McEvoy, S. Winters, N.C. Berner, D. McCloskey, J.F. Donegan, G.S. Duesberg, V. Nicolosi, J.N. Coleman, Preparation of Gallium Sulfide Nanosheets by Liquid Exfoliation and Their Application As Hydrogen Evolution Catalysts, *Chemistry of Materials* 27 (2015) 3483.

[39] P. Gomes de Costa, R.G. Dandrea, R.F. Wallis, M. Balkanski, First-principles study of the electronic srtucture of γ-InSe and β-InSe, *Physical Review B* 48 (1993) 14135.

[40] S. Lei, L. Ge, S. Najmaei, A. George, R. Kappera, J. Lou, M. Chhowalla, H. Yamaguchi, G. Gupta, R. Vajtai, A.D. Mohite, P.M. Ajayan, Evolution of the Electronic Band Structure and Efficient Photo-Detection in Atomic Layers of InSe, *ACS Nano* 8 (2014) 1263.

[41] G.W. Mudd, M.R. Molas, X. Chen, V. Zólyomi, K. Nogajewski, Z.R. Kudrynskyi, Z.D. Kovalyuk, G. Yusa, O. Makarovsky, L. Eaves, M. Potemski, V.I. Fal'ko, A. Patanè, The direct-to-indirect band gap crossover in two-dimensional van der Waals Indium Selenide crystals, *Scientific Reports* 6 (2016) 39619.

[42] J. Lauth, F.E.S.S. Gorris, M. Samadi Khoshkhoo, T. Chassé, W. Friedrich, V. Lebedeva, A. Meyer, C. Klinke, A. Kornowski, M. Scheele, H. Weller, Solution-Processed Two-Dimensional Ultrathin InSe Nanosheets, *Chemistry of Materials* 28 (2016) 1728.

[43] M.A. Airo, S. Gqoba, F. Otieno, M.J. Moloto, N. Moloto, Structural modification and band-gap crossover in indium selenide nanosheets, *RSC Adv.* 6 (2016) 40777.

[44] B. Gürbulak, M. Şata, S. Dogan, S. Duman, A. Ashkhasi, E.F. Keskenler, Structural characterizations and optical properties of InSe and InSe:Ag semiconductors grown by Bridgman/Stockbarger technique, *Physica E: Low-Dimensional Systems and Nanostructures* 64 (2014) 106.

[45] G.W. Mudd, S.A. Svatek, L. Hague, O. Makarovsky, Z.R. Kudrynskyi, C.J. Mellor, P.H. Beton, L. Eaves, K.S. Novoselov, Z.D. Kovalyuk, E.E. Vdovin, A.J. Marsden, N.R. Wilson, A. Patanè, High Broad-Band Photoresponsivity of Mechanically Formed InSe-Graphene van der Waals Heterostructures, *Advanced Materials* 27 (2015) 3760.

[46] W. Feng, W. Zheng, W. Cao, P. Hu, Back Gated Multilayer InSe Transistors with Enhanced Carrier Mobilities via the Suppression of Carrier Scattering from a Dielectric Interface, *Advanced Materials* 26 (2014) 6587.

[47] W. Feng, J.-B. Wu, X. Li, W. Zheng, X. Zhou, K. Xiao, W. Cao, B. Yang, J.-C. Idrobo, L. Basile, W. Tian, P. Tan, P. Hu, Ultrahigh photo-responsivity and detectivity in multilayer InSe nanosheets phototransistors with broadband response, *J. Mater. Chem. C* 3 (2015) 7022.

[48] S. Lei, F. Wen, L. Ge, S. Najmaei, A. George, Y. Gong, W. Gao, Z. Jin, B. Li, J. Lou, J. Kono, R. Vajtai, P. Ajayan, N.J. Halas, An Atomically Layered InSe Avalanche Photodetector, *Nano Letters* 15 (2015) 3048.

[49] F. Bonaccorso, A. Lombardo, T. Hasan, Z. Sun, L. Colombo, A.C. Ferrari, Production and processing of graphene and 2d crystals, *Materials Today* 15 (2012) 564.

[50] F. Bonaccorso, A. Bartolotta, J.N. Coleman, C. Backes, 2D-Crystal-Based Functional Inks, *Advanced Materials* 28 (2016) 6136.

[51] A. Ciesielski, P. Samorì, Graphene via sonication assisted liquid-phase exfoliation, *Chemical Society Reviews* 43 (2014) 381.

[52] J.N. Coleman, M. Lotya, A. O'Neill, S.D. Bergin, P.J. King, U. Khan, K. Young, A. Gaucher, S. De, R.J. Smith, I. V Shvets, S.K. Arora, G. Stanton, H.-Y. Kim, K. Lee, G.T. Kim, G.S. Duesberg, T. Hallam, J.J. Boland, J.J. Wang, J.F. Donegan, J.C. Grunlan, G. Moriarty, A. Shmeliov, R.J. Nicholls, J.M. Perkins, E.M. Grieveson, K. Theuwissen, D.W. McComb, P.D. Nellist, V. Nicolosi, Two-dimensional nanosheets produced by liquid exfoliation of layered materials, *Science* 331 (2011) 568.

[53] A.C. Ferrari, F. Bonaccorso, V. Falko, K.S. Novoselov, S. Roche, P. Bøggild, S. Borini, F. Koppens, V. Palermo, N. Pugno, J.A. Garrido, R. Sordan, A. Bianco, L. Ballerini, M. Prato, E. Lidorikis, J. Kivioja, C. Marinelli, T. Ryhänen, A. Morpurgo, J.N. Coleman, V. Nicolosi, L. Colombo, A. Fert, M. Garcia-Hernandez, A. Bachtold, G.F. Schneider, F. Guinea, C. Dekker, M. Barbone, C. Galiotis, A. Grigorenko, G. Konstantatos, A. Kis, M. Katsnelson, C.W.J. Beenakker, L. Vandersypen, A. Loiseau, V. Morandi, D. Neumaier, E. Treossi, V. Pellegrini, M. Polini, A. Tredicucci, G.M. Williams, B.H. Hong, J.H. Ahn, J.M. Kim, H. Zirath, B.J. van Wees, H. van der Zant, L. Occhipinti, A. Di Matteo, I. a. Kinloch, T. Seyller, E. Quesnel, X. Feng, K. Teo, N. Rupesinghe, P. Hakonen, S.R.T. Neil, Q. Tannock, T. Löfwander, J. Kinaret, Science and technology roadmap for graphene, related two-dimensional crystals, and hybrid systems, *Nanoscale* 7 (2014) 4598.

[54] X. Li, W. Cai, J. An, S. Kim, J. Nah, D. Yang, R. Piner, A. Velamakanni, I. Jung, E. Tutuc, S.K. Banerjee, L. Colombo, R.S. Ruoff, Large-area synthesis of high-quality and uniform graphene films on copper foils, *Science* 324 (2009) 1312.

[55] Z. Li, H. Qiao, Z. Guo, X. Ren, Z. Huang, X. Qi, S.C. Dhanabalan, J.S. Ponraj, D. Zhang, J. Li, J. Zhao, J. Zhong, H. Zhang, High-Performance Photo-Electrochemical Photodetector Based on Liquid-Exfoliated Few-Layered InSe Nanosheets with Enhanced Stability, *Advanced Functional Materials* 28 (2018) 1705237.

[56] NFPA 704: Standard System for the Identification of the Hazards of Materials for Emergency Response.

[57] W.M. Haynes, CRC Handbook of Chemistry and Physics, CRC Press, 2016.

[58] A.E. Del Rio Castillo, V. Pellegrini, H. Sun, J. Buha, D.A. Dinh, E. Lago, A. Ansaldo, A. Capasso, L. Manna, F. Bonaccorso, Exfoliation of Few-Layer Black Phosphorus in Low-Boiling-Point Solvents and Its Application in Li-Ion Batteries, *Chemistry of Materials* 30 (2018) 506.

[59] G. Kakavelakis, A.E. Del Rio Castillo, V. Pellegrini, A. Ansaldo, P. Tzourmpakis, R. Brescia, M. Prato, E. Stratakis, E. Kymakis, F. Bonaccorso, Size-Tuning of WSe2 Flakes for High Efficiency Inverted Organic Solar Cells, *ACS Nano* 11 (2017) 3517.

[60] H. Sun, A.E. Del Rio Castillo, S. Monaco, A. Capasso, A. Ansaldo, M. Prato, D.A. Dinh, V. Pellegrini, B. Scrosati, L. Manna, F. Bonaccorso, Binder-free graphene as an advanced anode for lithium batteries, *Journal of Materials Chemistry A* 4 (2016) 6886.

[61] C. Berrueco, P. Álvarez, S. Venditti, T.J. Morgan, A.A. Herod, M. Millan, R. Kandiyoti, Sample Contamination with NMP-oxidation Products and Byproduct-free NMP Removal from Sample Solutions, *Energy & Fuels* 23 (2009) 3008.

[62] H.C. Yau, M.K. Bayazit, J.H.G. Steinke, M.S.P. Shaffer, Sonochemical degradation of N-methylpyrrolidone and its influence on single walled carbon nanotube dispersion, *Chemical Communications* 51 (2015) 16621.

[63] M. Nikolka, I. Nasrallah, B. Rose, M.K. Ravva, K. Broch, A. Sadhanala, D. Harkin, J. Charmet, M. Hurhangee, A. Brown, S. Illig, P. Too, J. Jongman, I. McCulloch, J.-L. Bredas, H. Sirringhaus, High operational and environmental stability of high-mobility conjugated polymer field-effect transistors through the use of molecular additives, *Nature Materials* 16 (2017) 356.

[64] C.J. Zhang, S.-H. Park, O. Ronan, A. Harvey, A. Seral-Ascaso, Z. Lin, N. McEvoy, C.S. Boland, N.C. Berner, G.S. Duesberg, P. Rozier, J.N. Coleman, V. Nicolosi, Enabling Flexible Heterostructures for Li-Ion Battery Anodes Based on Nanotube and Liquid-Phase Exfoliated 2D Gallium Chalcogenide Nanosheet Colloidal Solutions, *Small* 13 (2017) 1701677.

[65] L. Debbichi, O. Eriksson, S. Lebègue, Two-Dimensional Indium Selenides Compounds: An Ab Initio Study, *The Journal of Physical Chemistry Letters* 6 (2015) 3098.

[66] C. Hansen, Hansen Solubility Parameters: a User's Handbook, CRC Press, 2007.

[67] K. Kouroupis-Agalou, A. Liscio, E. Treossi, L. Ortolani, V. Morandi, N.M. Pugno, V. Palermo, Fragmentation and exfoliation of 2-dimensional materials: a statistical approach, *Nanoscale* 6 (2014) 5926.

[68] Z. Chen, K. Gacem, M. Boukhicha, J. Biscaras, A. Shukla, Anodic bonded 2D semiconductors: from synthesis to device fabrication, *Nanotechnology* 24 (2013) 415708.

[69] D. Briggs, Handbook of X-ray Photoelectron Spectroscopy C. D. Wanger, W. M. Riggs, L. E. Davis, J. F. Moulder and G. E.Muilenberg Perkin-Elmer Corp., Physical Electronics Division, Eden Prairie, Minnesota, USA, 1979. 190 pp. $195, *Surface and Interface Analysis* 3 (1981) v.

[70] G. Brojerdi, G. Tyuliev, D. Fargues, M. Eddrief, M. Balkanski, Ion Beam Modification of InSe Surfaces, *Surface and Interface Analysis* 25 (1997) 111.

[71] K. Kambas, C. Julien, M. Jouanne, A. Likforman, M. Guittard, Raman Spectra of α- and γ-In2Se3, *Physica Status Solidi (B)* 124 (1984) K105.

[72] M. Osman, Y. Huang, W. Feng, G. Liu, Y. Qiu, P. Hu, Modulation of opto-electronic properties of InSe thin layers via phase transformation, *RSC Adv.* 6 (2016) 70452.

[73] S. Jandl, C. Carlone, Raman spectrum of crystalline InSe, *Solid State Communications* 25 (1978) 5.

[74] V. Zólyomi, N.D. Drummond, V.I. Fal'Ko, Electrons and phonons in single layers of hexagonal indium chalcogenides from ab initio calculations, *Physical Review B - Condensed Matter and Materials Physics* 89 (2014) 205416.

[75] C. Carlone, S. Jandl, Second order Raman spectrum and phase transition in InSe, *Solid State Communications* 29 (1979) 31.

[76] R. Schwarcz, M.A. Kanehisa, M. Jouanne, J.F. Morhange, M. Eddrief, Evolution of Raman spectra as a function of layer thickness in ultra-thin InSe films, *J. Phys.: Condens. Matter* 14 (2002) 967.

[77] D. McAteer, Z. Gholamvand, N. McEvoy, A. Harvey, E. O’Malley, G.S. Duesberg, J.N. Coleman, Thickness Dependence and Percolation Scaling of Hydrogen Production Rate in MoS_2 Nanosheet and Nanosheet–Carbon Nanotube Composite Catalytic Electrodes, *ACS Nano* 10 (2016) 672.

[78] B. Qu, C. Li, C. Zhu, S. Wang, X. Zhang, Y. Chen, Growth of $MoSe_2$ nanosheets with small size and expanded spaces of (002) plane on the surfaces of porous N-doped carbon nanotubes for hydrogen production, *Nanoscale* 8 (2016) 16886.

[79] Z. Liu, N. Li, H. Zhao, Y. Du, Colloidally synthesized $MoSe_2$/graphene hybrid nanostructures as efficient electrocatalysts for hydrogen evolution, *Journal of Materials Chemistry A* 3 (2015) 19706.

[80] Y. Huang, H. Lu, H. Gu, J. Fu, S. Mo, C. Wei, Y.-E. Miao, T. Liu, A CNT@$MoSe_2$ hybrid catalyst for efficient and stable hydrogen evolution, *Nanoscale* 7 (2015) 18595.

[81] L. Jia, X. Sun, Y. Jiang, S. Yu, C. Wang, A Novel $MoSe_2$-Reduced Graphene Oxide/Polyimide Composite Film for Applications in Electrocatalysis and Photoelectrocatalysis Hydrogen Evolution, *Advanced Functional Materials* 25 (2015) 1814.

[82] H. Tang, K. Dou, C.-C. Kaun, Q. Kuang, S. Yang, $MoSe_2$ nanosheets and their graphene hybrids: synthesis, characterization and hydrogen evolution reaction studies, *J. Mater. Chem. A* 2 (2014) 360.

[83] H. Yu, X. Yu, Y. Chen, S. Zhang, P. Gao, C. Li, A strategy to synergistically increase the number of active edge sites and the conductivity of MoS_2 nanosheets for hydrogen evolution, *Nanoscale* 7 (2015) 8731.

[84] Q. Liu, Q. Fang, W. Chu, Y. Wan, X. Li, W. Xu, M. Habib, S. Tao, Y. Zhou, D. Liu, T. Xiang, A. Khalil, X. Wu, M. Chhowalla, P.M. Ajayan, L. Song, Electron-Doped 1T-MoS_2 via Interface Engineering for Enhanced Electrocatalytic Hydrogen Evolution, *Chemistry of Materials* 29 (2017) 4738.

[85] J. Yang, D. Voiry, S.J. Ahn, D. Kang, A.Y. Kim, M. Chhowalla, H.S. Shin, Two-Dimensional Hybrid Nanosheets of Tungsten Disulfide and Reduced Graphene Oxide as Catalysts for Enhanced Hydrogen Evolution, *Angewandte Chemie International Edition* 52 (2013) 13751.

[86] K.A. Mauritz, R.B. Moore, State of understanding of Nafion, *Chemical Reviews* 104 (2004) 4535.

[87] P.S. Khadke, U. Krewer, Mass-Transport characteristics of oxygen at pt/anion exchange ionomer interface, *Journal of Physical Chemistry C* 118 (2014) 11215.

[88] Y. Wang, K.S. Chen, J. Mishler, S.C. Cho, X.C. Adroher, A review of polymer electrolyte membrane fuel cells: Technology, applications, and needs on fundamental research, *Applied Energy* 88 (2011) 981.

[89] K.M. Nouel, P.S. Fedkiw, Nafion®-based composite polymer electrolyte membranes, *Electrochimica Acta* 43 (1998) 2381.

[90] K. Shinozaki, B.S. Pivovara, S.S. Kocha, Enhanced Oxygen Reduction Activity on Pt/C for

Nafion-free, Thin, Uniform Films in Rotating Disk Electrode Studies, *ECS Transactions* 58 (2013) 15.

[91] H. Tu, W. Wang, C. Wan, Y.-Y. Wang, Novel Method for the Synthesis of Hydrophobic Pt - Ru Nanoparticles and Its Application to Preparing a Nafion-Free Anode for the Direct Methanol Fuel Cell, *The Journal of Physical Chemistry B* 110 (2006) 15988.

[92] B.E. Conway, B. V. Tilak, Interfacial processes involving electrocatalytic evolution and oxidation of H2, and the role of chemisorbed H, *Electrochimica Acta* 47 (2002) 3571.

[93] M. Boudart, Turnover Rates in Heterogeneous Catalysis, *Chemical Reviews* 95 (1995) 661.

[94] J. Kibsgaard, Z. Chen, B.N. Reinecke, T.F. Jaramillo, Engineering the surface structure of MoS2 to preferentially expose active edge sites for electrocatalysis, *Nature Materials* 11 (2012) 963.

[95] J. Xie, H. Zhang, S. Li, R. Wang, X. Sun, M. Zhou, J. Zhou, X.W.D. Lou, Y. Xie, Defect-rich MoS2 ultrathin nanosheets with additional active edge sites for enhanced electrocatalytic hydrogen evolution, *Advanced Materials* 25 (2013) 5807.

[96] B. Hinnemann, P.G. Moses, J. Bonde, K.P. Jørgensen, J.H. Nielsen, S. Horch, I. Chorkendorff, J.K. Nørskov, Biomimetic hydrogen evolution: MoS2 nanoparticles as catalyst for hydrogen evolution, *Journal of the American Chemical Society* 127 (2005) 5308.

[97] J. Wang, J. Liu, B. Zhang, X. Ji, K. Xu, C. Chen, L. Miao, J. Jiang, The mechanism of hydrogen adsorption on transition metal dichalcogenides as hydrogen evolution reaction catalyst, *Phys. Chem. Chem. Phys.* 19 (2017) 10125.

[98] T.F. Jaramillo, K.P. Jorgensen, J. Bonde, J.H. Nielsen, S. Horch, I. Chorkendorff, Identification of Active Edge Sites for Electrochemical H2 Evolution from MoS2 Nanocatalysts, *Science* 317 (2007) 100.

[99] T. Shinagawa, A.T. Garcia-Esparza, K. Takanabe, Insight on Tafel slopes from a microkinetic analysis of aqueous electrocatalysis for energy conversion, *Scientific Reports* 5 (2015) 13801.

[100] P. Rüetschi, Overvoltage and Catalysis, *Journal of The Electrochemical Society* 106 (1959) 819.

[101] W.H. Mulder, J.H. Sluyters, T. Pajkossy, L. Nyikos, Tafel current at fractal electrodes: Connection with admittance spectra, *Journal of Electroanalytical Chemistry and Interfacial Electrochemistry* 285 (1990) 103.

[102] M. Filoche, B. Sapoval, Shape-dependency of current through non-linear irregular electrodes, *Electrochimica Acta* 46 (2000) 213.

[103] S.M. Tan, C.K. Chua, D. Sedmidubský, Z. Sofer, M. Pumera, Electrochemistry of layered GaSe and GeS: applications to ORR, OER and HER, *Phys. Chem. Chem. Phys.* 18 (2016) 1699.

[104] J. Zhang, T. Wang, P. Liu, S. Liu, R. Dong, X. Zhuang, M. Chen, X. Feng, Engineering water dissociation sites in MoS $_2$ nanosheets for accelerated electrocatalytic hydrogen production, *Energy & Environmental Science* 9 (2016) 2789.

[105] P.W. Atkins, Physical Chemistry, 6th ed., Oxford University Press, 1998.

[106] S. Kandoi, A.A. Gokhale, L.C. Grabow, J.A. Dumesic, M. Mavrikakis, Why Au and Cu Are More Selective Than Pt for Preferential Oxidation of CO at Low Temperature, *Catalysis Letters* 93 (2004) 93.

[107] J.K. Nørskov, J. Rossmeisl, A. Logadottir, L. Lindqvist, J.R. Kitchin, T. Bligaard, H. Jónsson, Origin of the overpotential for oxygen reduction at a fuel-cell cathode, *Journal of Physical Chemistry B* 108 (2004) 17886.

[108] A. Politano, G. Chiarello, R. Samnakay, G. Liu, B. Gürbulak, S. Duman, A.A. Balandin, D.W. Boukhvalov, The influence of chemical reactivity of surface defects on ambient-stable InSe-based nanodevices, *Nanoscale* 8 (2016) 8474.

[109] S.A. Vilekar, I. Fishtik, R. Datta, Kinetics of the Hydrogen Electrode Reaction, *Journal of The Electrochemical Society* 157 (2010) B1040.

[110] Q. Tang, D. Jiang, Mechanism of Hydrogen Evolution Reaction on 1T-MoS2 from First Principles, *ACS Catalysis* 6 (2016) 4953.

[111] T. Hasan, P.H. Tan, F. Bonaccorso, A.G. Rozhin, V. Scardaci, W.I. Milne, A.C. Ferrari, Polymer-Assisted Isolation of Single Wall Carbon Nanotubes in Organic Solvents for Optical-Quality Nanotube−Polymer Composites, *The Journal of Physical Chemistry C* 112 (2008) 20227.

[112] P. Giannozzi, S. Baroni, N. Bonini, M. Calandra, R. Car, C. Cavazzoni, D. Ceresoli, G.L. Chiarotti, M. Cococcioni, I. Dabo, A. Dal Corso, S. de Gironcoli, S. Fabris, G. Fratesi, R. Gebauer, U. Gerstmann, C. Gougoussis, A. Kokalj, M. Lazzeri, L. Martin-Samos, N. Marzari, F. Mauri, R. Mazzarello, S. Paolini, A. Pasquarello, L. Paulatto, C. Sbraccia, S. Scandolo, G. Sclauzero, A.P. Seitsonen, A. Smogunov, P. Umari, R.M. Wentzcovitch, QUANTUM ESPRESSO: a modular and open-source software project for quantum simulations of materials, *Journal of Physics: Condensed Matter* 21 (2009) 395502.

[113] V. Barone, M. Casarin, D. Forrer, M. Pavone, M. Sambi, A. Vittadini, Role and effective treatment of dispersive forces in materials: Polyethylene and graphite crystals as test cases, *Journal of Computational Chemistry* 30 (2009) 934.

[114] J.P. Perdew, K. Burke, M. Ernzerhof, Generalized Gradient Approximation Made Simple, *Physical Review Letters* 77 (1996) 3865.

[115] H.J. Monkhorst, J.D. Pack, Special points for Brillouin-zone integrations, *Physical Review B* 13 (1976) 5188.